UNIVERSIDADE FEDERAL DO CEARÁ

CENTRO DE TECNOLOGIA

DEPARTAMENTO DE ENGENHARIA METALÚRGICA E DE MATERIAIS

PROGRAMA DE PÓS-GRADUAÇÃO EM ENGENHARIA E CIÊNCIA DE MATERIAIS

ÉMERSON MENDONÇA MINÁ

NEW APPROACH DEVELOPMENT FOR COMPLEX DISSIMILAR GIRTH WELDING OF HIGH STRENGTH LOW ALLOY STEEL PIPES CLADDED WITH NI-BASED ALLOY

FORTALEZA

2019

ÉMERSON MENDONÇA MINÁ

NEW APPROACH DEVELOPMENT FOR COMPLEX DISSIMILAR GIRTH WELDING OF HIGH STRENGTH LOW ALLOY STEEL PIPES CLADDED WITH NI-BASED ALLOY

Tese apresentada ao Programa de Pós-Graduação em Engenharia e Ciência de Materiais da Universidade Federal do Ceará, como requisito parcial à obtenção do título de Doutor em Engenharia e Ciência de Materiais. Área de concentração: Propriedades Físicas e Mecânicas dos Materiais.

Orientador: Prof. Dr. Cleiton Carvalho Silva.
Coorientador: Prof. Dr. Hélio Cordeiro de Miranda

FORTALEZA

2019

Dados Internacionais de Catalogação na Publicação
Universidade Federal do Ceará
Biblioteca Universitária
Gerada automaticamente pelo módulo Catalog, mediante os dados fornecidos pelo(a) autor(a)

M564n Miná, Émerson Mendonça.
New approach development for complex dissimilar girth welding of high strength low alloy steel pipes cladded with Ni-based alloy / Émerson Mendonça Miná. – 2019.
285 f. : il. color.

Tese (doutorado) – Universidade Federal do Ceará, Centro de Tecnologia, Programa de Pós-Graduação em Engenharia e Ciência de Materiais, Fortaleza, 2019.
Orientação: Prof. Dr. Cleiton Carvalho Silva.
Coorientação: Prof. Dr. Hélio Cordeiro de Miranda.

1. Soldagem dissimilar circunferencial; . 2. Reel lay. 3. Overmatch. 4. Aço baixa liga. 5. Ligas de Ni. I. Título.

CDD 620.11

ÉMERSON MENDONÇA MINÁ

NEW APPROACH DEVELOPMENT FOR COMPLEX DISSIMILAR GIRTH WELDING OF HIGH STRENGTH LOW ALLOY STEEL PIPES CLADDED WITH NI-BASED ALLOY

Thesis Submitted to the Post-Graduate Program in Engineering and Materials Science of the Universidade Federal do Ceará, In Partial fulfillment of the requirements for the Degree of Doctor in Materials Science and Engineering. Concentration area: Physical and Mechanical Properties of Materials.

Approved at: 07/11/2019.

EXAMINING COMMISSION

_____

Prof. Dr. Cleiton Carvalho Silva (Advisor)
Universidade Federal do Ceará (UFC)

_____

Prof. Dr. Hélio Cordeiro de Miranda (Coadvisor)
Universidade Federal do Ceará (UFC)

_____

Prof. Dr. Marcelo Ferreira Mota
Universidade Federal do Ceará (UFC)

_____

Prof. Dr. Afonso Reguly
Universidade Federal do Rio Grande do Sul (UFRGS)

_____

Prof. Dr. Giovani Dalpiaz
Centro de Pesquisas Leopoldo Américo Miguez de Mello (CENPES/Petrobras)

To god.

To my parents, Giovanni and Rosali.

ACKNOWLEDGMENTS

To my father and my mother by huge love, education and support gave to me. It is incredible how two persons choose to live for children, adapting their dreams for the children dreams. I love you so much. I also would like to thank my lovely sister who inspires me with her lightness way to lead her life.

To my wife by all love and patience to understand that doctoral course was important for my personal gratification. I love you my princess.

I would like to thank the Universidade Federal do Ceará in special the Professors of the Departamento de Engenharia e Ciência de Materials, which gave to me the opportunity to be a Metallurgical Engineering, at first moment, and now a Materials Scientist.

I would like to thank the CENPES/ANP/PETROBRAS by the funding of all resources need to this thesis including the scholarships. I also would like to thank the funding agencies that give support to department like CAPES, CNPq and PIBIC system.

I would like to thank the Central Analítica-UFC/CT-INFRA/MCTI-SISANO/Pró-Equipamentos that allowed use of microscope so important to this thesis.

I would like express my sincere gratitude to my supervisor Professor Cleiton Carvalho Silva that teach me along of these years how to be a researcher. The rigor with work, motivated me to improve day by day and made me grew as professional. You will ever be an example of researcher to take for my journey.

I would like thank my co-supervisor Professor Hélio Cordeiro de Miranda by indispensable support gave to this thesis. I also appreciate the lessons about welding and, specially, the advice of how to conduct of a research line with so hard goals to be obtained.

I would like thank the Professor Willys Machado Aguiar by patience to teach me even for the most basic concepts. Your humility and self-motivation to keep learning something new every day inspires me to follow by the same way.

To engineering students, Gabriel, Fernando, Victor, Karine, Gilvâniva that gave me support for produce this thesis. Without your help it would not have been possible conclude this study. I also would like thank to Rafaella by full support to necessary for conclude this researcher.

To persons of LPTS in especial to Bruno, Edson and Mário that gave support manufacturing and performing the mechanical tests.

To my friends Yuri, Tathiane, Davi, Átila, Caroliny, Pedro, Salvador, Kamilla, Paulo, Alexandre, Edileusa and Roger that made the days of this journey lighter.

“Remember to look up at the stars and not down at your feet. Try to make sense of what you see and wonder about what makes the universe exist. Be curious. And however difficult life may seem, there is always something you can do and succeed at. It matters that you don’t just give up.”

Stephen Hawking

RESUMO

Na presente foi realizado um estudo sistemático para desenvolver um procedimento especial para a soldagem dissimilar circunferencial de tubo de aço API 5L X65 revestido com a Liga 625. O principal objetivo foi produzir juntas sem trincas de solidificação, que apresentem o *overmatch* mínimo de limite de escoamento (LE) requerido para a posterior instalação de dutos pelo método *reel lay*. Para atingir o objetivo foi proposto o uso de dois materiais de adição: uma liga de níquel para oferecer uma resistência a corrosão similar ao revestimento e, um aço baixa liga (ABL) para fornecer o *overmatch* de LE. Estudos de simulação termodinâmica foram realizadas para selecionar ligas para a soldagem dissimilar proposta. A solidificação das ligas de níquel 625, 686, C-276, 22, 59, 680 e 617 foram investigadas quando misturadas com os aços API 5L X65 e AWS ER100S-G (ABL) para verificar compatibilidade metalúrgica, em termos de trincas de solidificação. Dentre as ligas investigadas, as ligas 22, 686 e 59 apresentaram a menor suscetibilidade a trincas de solidificação quando misturadas com os aços conforme simulação termodinâmica. Um estudo experimental avaliando o efeito da mistura do aço AWS ER100S-G com as ligas 625, 22, 686 e 59 foi realizado. Apenas poucas e pequenas descontinuidades foram observadas para as ligas 22, 686 e 59, enquanto a Liga 625 apresentou trincas com a presença de fases eutéticas ricas em Nb. Quatro juntas dissimilares foram produzidas com diferentes ligas (625, 22, 686 e 59) para os dois primeiros passes, enquanto os demais passes foram realizados com o aço AWS ER100S-G. A junta produzida com a Liga 625 apresentou diversas trincas ao longo dos dois primeiros passes de ABL, que prejudicaram as propriedades mecânicas. As três juntas produzidas com as ligas 22, 686 e 59 não apresentaram trincas de solidificação. Além disso, essas juntas apresentaram um limite escoamento suficiente para o *overmatch* mínimo requerido não somente para o aço API 5L X65 como também para os aços API 5L X70 e X80 conforme DNVGL-ST F101. A mistura entre o ABL e as ligas de níquel originou uma microestrutura complexa, na qual os dois passes de liga de níquel apresentaram uma matriz γ-FCC, enquanto os dois primeiros passes ABL apresentou uma matriz martensítica com austenita retida (A_{ret}) e carbonetos cúbicos. O terceiro passe ABL apresentou uma matriz bainítica com martensita, microconstituinte martensita-austenita (MA) e carbonetos e, os demais passes ABL apresentou uma matriz composta por ferrita acicular e MA. A tenacidade a -15°C foi insatisfatório devido a característica frágil das juntas.

Palavras-chave: Soldagem dissimilar circunferencial; reel lay; overmatch; aço baixa liga; ligas de Ni.

ABSTRACT

In the present thesis, a systematic study to develop a special welding procedure for dissimilar girth welding of API 5L X65 steel pipe cladded with Alloy 625 is presented. The main objective was to join the pipes without solidification cracking and achieve the minimum yield strength overmatch required for subsequent installation of the pipeline by reel lay method. To achieve this goal, it was proposed to use two different fillers metals: a Ni-based alloy to offer a corrosion resistance, similar to the cladding, and a low alloy steel (LAS) to provide the YS overmatch. Thermodynamic simulation studies were performed to select the alloys for the dissimilar welding proposed. The solidification of Ni-based alloys 625, 686, C-276, 22, 59, 680 and 617 when mixed with API 5L X65 and AWS ER100S-G steels (LAS) were investigated using thermodynamic simulation, in order to investigate the metallurgical compatibility for dissimilar welding, in terms of solidification cracking. Among all alloys investigated, the alloys 22, 686 and 59 presented the lowest solidification crack susceptibility when mixed with the steels. An experimental study evaluating the mix effect of AWS ER100S-G steel with alloys 625, 22, 686 and 59 also was performed. The results shown that alloys 22, 686 and 59 presented few small discontinuities, while the Alloy 625 exhibited large cracks with presence of Nb-rich eutectic phases. Four dissimilar girth welds were produced with different alloys (625, 22, 686 and 59) for the first two weld passes, while the other weld passes used the AWS ER100S-G steel (LAS). The welded joint produced with Alloy 625 exhibited numerous cracks along of the first two LAS weld passes that detrimental mechanical properties. The three welded joints produced with alloys 22, 686 and 59 did not presented solidification cracks. Moreover, these welded joints achieved the minimum YS overmatch required by DNVGL-ST F101 for subsequent installation by reel lay method, not only for API 5L X65 steel, but also for API 5L X70 and X80 steels. The mixture between the LAS and Ni-based alloys created a complex microstructure, where the two Ni-based weld passes showed a γ-FCC matrix, while the first two LAS weld passes showed a martensitic matrix with retained austenite (Aret) and cubic carbonitrides. The third LAS weld pass exhibited a bainitic matrix with martensite, martensite-austenite (MA) microconstituent and carbides, and the others LAS weld passes showed an acicular ferrite (AF) matrix with MA particles. The toughness of the welded joints at -15°C was unsatisfactory due to brittle fracture.

Keywords: Dissimilar girth welding; reel lay; overmatch; low alloy steel; Ni-based alloys.

LIST OF FIGURE

LIST OF TABLES

SUMMARY

Chapter 1

Overview of the problematics concerning dissimilar girth welding of high strength low alloy steel pipes with an internal CRA cladding

1.1 Introduction

The discovery of huge oil reserves in the pre-salt layer, located in the Brazilian continental shelf, changed the economic and technological scenario of the oil & gas industry. This discovery created the perspective of a massive increase of oil and gas production and began a sudden demand for the development of new technologies to exploit these pre-salt reserves; technologies that represented an enormous engineering challenge. One of the major barriers to overcome is fluid transportation, due to the extensive distance from the offshore unit to the oil reservoirs in the pre-salt layer. Usually, these reservoirs are located in ultra-deep waters, with depths of at least 2 km. Besides this, there are another 6-8 kms of post-salt and salt layers until the oil reservoir itself. Furthermore, the location of some of these oil reserves are about 300 km from the Brazilian coast, which represents another challenge for the installation of offshore units and the transportation of the oil and gas production.

The initial production of the oil from the reservoir to the offshore unit is conducted through the riser which is a fundamental component that connects the offshore unit to the wellhead. This large pipeline can be manufactured at an onshore unit or offshore, depending on the installation method chosen. There are currently three main methods of installing risers: the S-lay, J-lay and reel lay methods (Figure 1-1).

The S-lay method represents the traditional method and is frequently used for installations in shallow waters. This process requires the transport of pipes by large supply vessels to the offshore unit, where the pipeline is manufactured by girth welding with the pipes in a horizontal position. The laying of the pipeline occurs as soon as the joint welding and inspection are complete. The name of this process is related to the S shape formed by pipeline, between the pipe-laying ship and the seabed. The process offers a high laying rate of about 3-5 km per day. On the other hand, a high tension is imposed on the pipeline, especially at the stinger and sagbend.

The main feature of the J-lay method is the position of the pipes during installation. In the J-lay method, the welding and inspection of the joints takes place with the pipes in a

vertical position. This drastically reduces the load on the offshore unit, since the pipeline laying occurs simultaneously in the vertical position. Moreover, this method ensures a shorter distance between the pipe laying ship and the wellhead, minimizing efforts. Although the J-lay method offers better component integrity, the process is more expensive and more importantly it is inconvenient for the welding and inspection procedures. In addition, the laying rate is approximately 1-1.5 km per day, which is lower than the S-lay process.

Figure 1-1. Installation processes: S-lay, J-lay and reel lay [1].

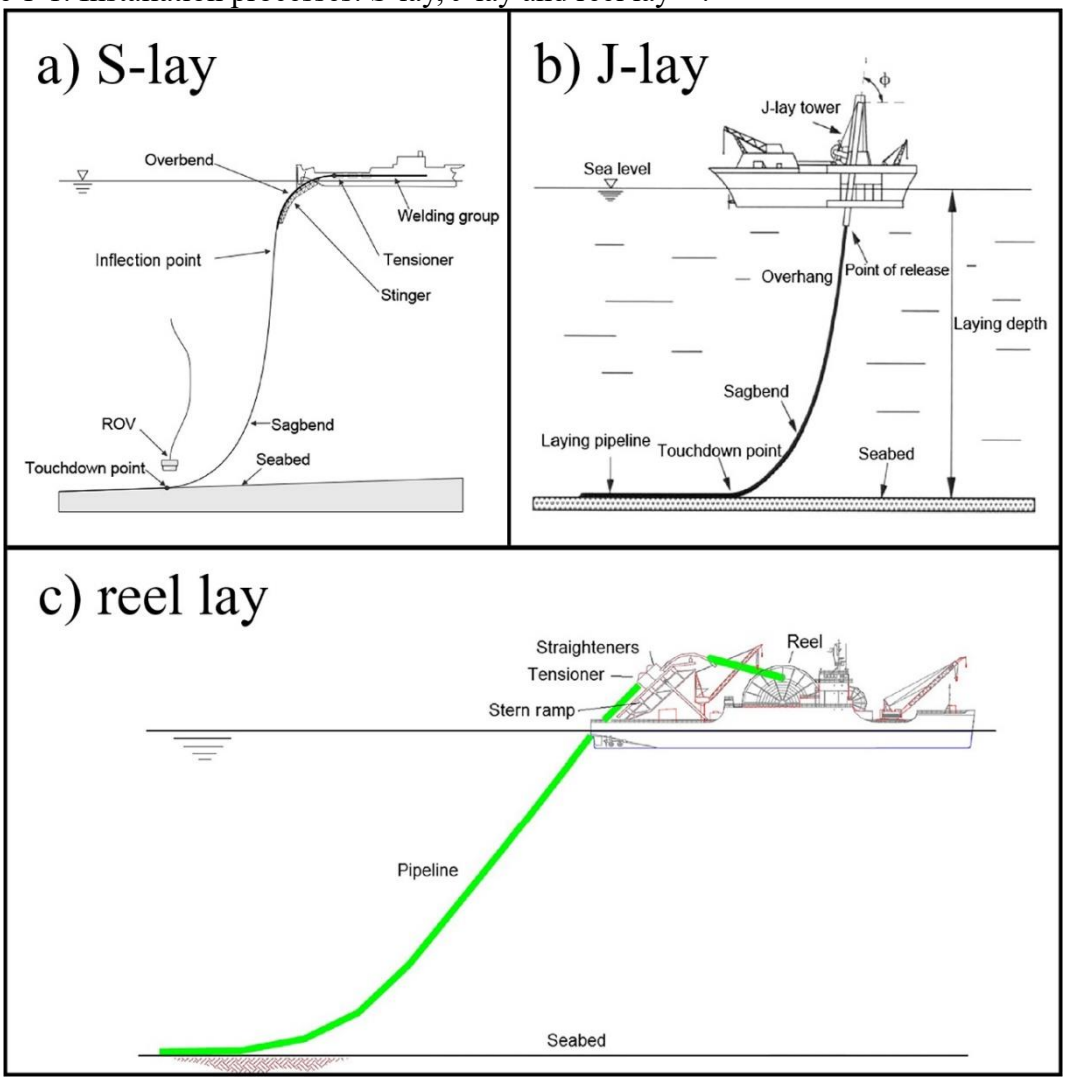

Source: Adapted from Bai and Bai[1]

The third installation method, the reel lay method, is the most efficient. The laying rate is very high compared to other two methods, and can reach an incredible 12-24 km per day.

[1] BAI, Qiang; BAI, Yong. Installation Design. *In*: **Subsea Pipeline Design, Analysis, and Installation**. Boston: Gulf Professional Publishing, 2014. p. 707-751.

This is because much of the procedure takes place at an onshore unit, which also reduces costs and increases productivity. In this case, the girth welding and inspection of the joints are performed on land, which allows optimum welding quality, increases safety and productivity. The pipeline is then spooled onto large drums on a pipe laying ship. On arrival at the location for installation the pipeline is unspooled and it straightens during the laying process. Nonetheless, with the reel lay method, the welded joints requires high strength, since they are subjected to at least 2% of strain during the spooling, unspooling and straightening steps.

The DNVGL-ST F101 standard defines the requirements for materials used in the manufacturing of pipelines to be installed by the reel lay method. The joint welding of these pipes should exhibit a good overmatch of yield strength (YS) to increase component safety. The maximum value of the YS of the steel pipe is taken as a reference, minus 20 MPa. This huge overmatch makes it difficult to weld these pipes, especially for welding high strength steel pipes. Currently, steels are manufactured according to specifications proposed by the American Petroleum Institute (API). Applications for ultra-deep waters commonly use steels with a YS above 450 MPa, such as API 5L X65 steel. High strength steels allow a reduction of pipeline wall thickness and consequently the weight of the riser, which represent one of the challenges for exploration of oil reservoirs in ultra-deep waters.

The American Welding Society (AWS) specifies the characteristics of low alloy steel (LAS) filler metals for a wide range of materials with a YS varying between 400 and 750 MPa that allow the joint welding of API 5L X65 steel. This welding procedure is well established for joining steel pipes without corrosion resistant alloy (CRA) claddings. Unfortunately, the use of materials with high corrosion resistance is required on most pipeline systems, since petroleum and its impurities are an aggressive corrosive environment, making the use of CRA cladding almost indispensable. Nickel-based alloys are a class of materials most commonly used as CRA claddings, due to their superior corrosion and oxidation resistance in a wide range of harsh environments. Alloy 625 represents the most commonly used Ni-based alloy as the CRA cladding, as it offers great corrosion and oxidization resistance and is becoming cost effective.

Unfortunately, the inner layer of the CRA cladding increases the dissimilar girth welding complications with high strength steel pipes for subsequent reel lay installation. This is because the filler metal to be used must maintain corrosion resistance at least equal to the Alloy 625 cladding. A common procedure is to recommend the use of the same material as the CRA cladding to weld the pipes, thus, avoiding metallurgical problems related to dissimilar welding. However, when Alloy 625 is used as the filler metal for joining API 5L X65 steel pipes

it cannot offer the minimum YS necessary to ensure a sufficient overmatch for the reel lay installation method, which is 580 MPa. This is also true for welding higher strength steels like API 5L X70 and X80 grade, where it is necessary to achieve a minimum YS of 615 MPa and 685 MPa, respectively. These requirements limit the choice of Ni-based commercial alloys that offers both high corrosion resistance and high strength in the as-welded condition, without a long heat treatment after welding.

The simplest solution to this problem is the use of two filler metals, one to provide the corrosion resistance needed for the region next to the CRA cladding and a second to provide the high strength, necessary to confer the overmatch. Nevertheless, this simpler solution represents a major challenge from a metallurgical point of view. The mix of steel with the Ni-based alloys can result in weldability issues related to the formation of solidification cracks. The combination of alloying elements such as Ni, Cr, Mo, Nb and Ti from Alloy 625 with the Fe, Si, Mn and C present in the steel, can induce the formation of secondary phases, which have detrimental effects on weldability. Laves phase is a common phase observed in such dissimilar welds. Rich in Fe, Si and Nb, the Laves phase is known for its low melting point, which provides the initial conditions for the formation of solidification cracks. To have a successful weld, without solidification cracking, a careful selection of alloys needs to be made, in order to find the most suitable Ni-based alloys to mix with the low alloy steel.

A solution to this problematic would not only represents a major technological breakthrough for the oil and gas industry, but it could also have a huge economic impact in the order of millions of dollars. Advances along these lines of research will affect the technical and economic aspects of the oil and gas industry. These advances would allow the use of stronger steels, reducing the weight of rigid risers. The cost of materials for installation and repair/replacement would be reduced and allow access to extremely difficult ultra-deep water reserves from the technical point of view. Furthermore, component life is extended, structural integrity is improved, operational reliability increases, thus making facilities safer.

Among the many advantages of the reel lay installation method, the main ones are a better weld quality that improves the safety, increased productivity gain, avoiding any reworking and reduced costs associated with vessel rental and manpower. This represents a major economic impact for such ventures. A single day without producing petroleum from a new reservoir represents a loss of hundreds of thousands of dollars.

Petrobras, the Brazilian oil & gas company, is a pioneer in many technological innovations related to petroleum production in ultra-deep waters, especially in pre-salt reserves. The company has invested in new manufacturing technologies regarding rigid risers. The

present thesis represents the beginning of a line of research at the Welding Research Technology Laboratory of the Universidade Federal do Ceará and is part of a research project that is in partnership with the Petrobras Research Center.

1.2 Objective

The main objective of the present thesis is to develop a special welding procedure for a complex dissimilar girth welding. This procedure which is designed to join rigid risers of API 5L X65 steel with Alloy 625 cladding requires the use of two different filler metals. The first is a Ni-based alloy to assure corrosion resistance (of the weld) and the second is a low alloy steel filler metal to provide a minimum yield strength of 580 MPa, which is required for the reel lay installation technique. This latter filler metal also ensures the structural integrity of the riser, in terms of solidification cracking.

1.2.1 Specific objectives

- To determine, through thermodynamic simulation, the effect of mixing between Ni-based alloys and low alloy steels on solidification, in terms of solidification temperature range, nucleation of secondary phases, microsegregation and the behavior of the alloying elements;
- To assess the physical metallurgy of the Ni-based alloys and steel when mixed by welding by evaluating the effect of welding parameters on dilution, distribution of the alloying elements, resultant microstructure and its relationship with solidification cracking;
- To manufacture dissimilar girth welding of API 5L X65 steel pipes with alloy 625 cladding without solidification cracking based on the proposed approach.
- To achieve the minimum yield strength overmatch (580 MPa) required for girth welding of API 5L X65 steel for installation by the reel lay method.
- To correlate the microstructure of dissimilar welding with its toughness.

Chapter 2

Logical steps adopted to carry out this study

2.1 Methodology

The thesis was developed in three stages: Selection of materials, Metallurgical compatibility and Girth welding of pipes. Each stage was fundamental to the next stage and consequently to the evolution of the study. The flowchart displayed in Figure 2-1 shows the main stages.

The ‘Selection of materials’ stage was divided into three chapters. The first chapter discusses the selection of the Ni-based alloys to perform the proposed welding based on a literature review. The following two chapters investigated the mixture of the selected alloys with steel pipe and low alloy steel, respectively. Thermodynamic simulations of the solidification process were performed in order the verify the best Ni-based alloys to be used for the girth welding proposed, especially in terms of solidification cracking susceptibility.

The second stage concerns the ‘Metallurgical compatibility’ of the Ni-based alloys pre-selected with low alloy steel. Here, an experimental study investigated the microstructure and solidification crack susceptibility for deposits of single weld beads of low alloy steel on claddings of the Ni-based alloys selected. This chapter investigates the results of the dissimilar welding between steel and Ni-based alloy selected in this study.

The third and last stage gathers the results obtained from the ‘Girth welding’ of API 5L X65 steel pipe with an internal cladding of Alloy 625. The weldability, microstructure and mechanical properties of the welded joints and consequently the innovate girth welding procedures were assessed in this stage.

Figure 1-2. Flowchart of this study.

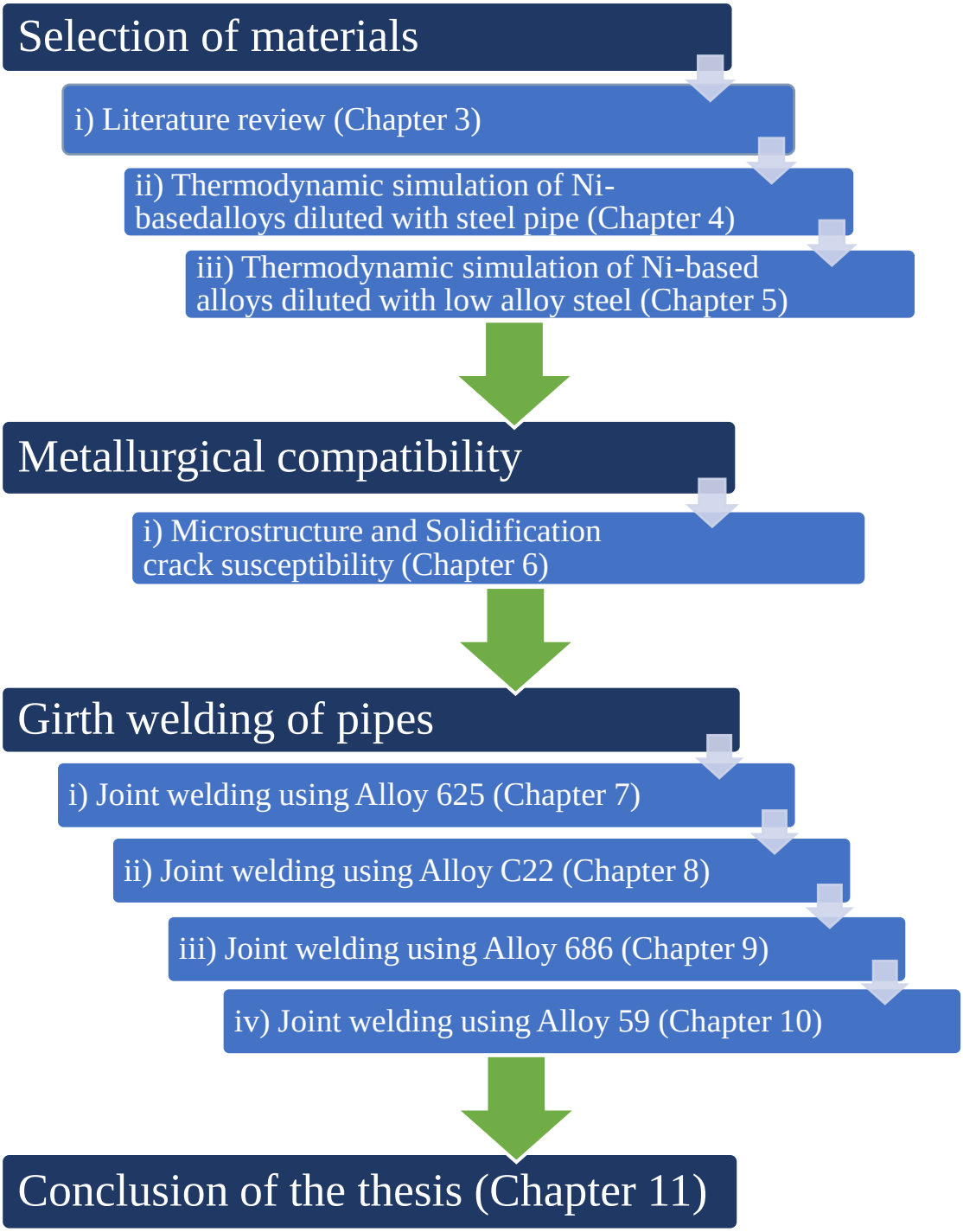

Source: Developed by the author.

Chapter 3

A fundamental literature review to begin the study

3.1 Literature review

In this section, some basic concepts related to Ni-based alloys and weldability will be introduced in order to preselect materials, which will be evaluated using thermodynamic simulations in Section 4.

3.1.1 Ni-based alloys

Ni-based alloys are a class of materials that offer a wide range of applications for different goals. Their capacity to solubilize a large fraction of alloying elements makes them extremely versatile[1]. Among the many alloys available, it is possible to find an alloy for various complex applications. There are alloys with high strength, resistance to corrosion and oxidization, high toughness and fatigue strength as well as alloys able to resist high or cryogenic working temperatures[2]. Consequently, this special class of materials are widely used in applications related to the aerospace, arms, nuclear, petrochemical, automotive and biochemical industries[3].

The class of Ni-based alloys may be divided according to their strengthening mechanism, which can be by solid solution or precipitation of secondary phases[4]. There is another special subdivision related to alloy strengthening by dispersion of oxides, but this strengthening mechanism follows the same fundamentals as precipitation strengthening alloys. More details about these materials are presented below.

3.2.1.1 Solid solution strengthened alloys

Nickel matrixes have a great capacity to solubilize a large fraction of alloying elements, especially Al, Co, Cr, Fe, Hf, Mn, Mo, Nb, Ta and W[1]. The face centered cubic (FCC) crystal lattice structure furnishes the material with tough and ductile characteristics[5] as well as a big atomic packing factor enabling several alloying elements to be solubilized in the same alloy. Naturally, each element has its own physical and chemical properties that will

influence the general properties of the alloy. In terms of mechanical behavior, the addition of alloying elements with appreciably different atomic numbers causes a distortion of the crystal lattice. The misfit of the atomic radii among the Ni matrixes and the solid solution elements inhibit a dislocation movement[6]. Figure 3-1 shows the effect of solid solution in dislocation motion[7] and, the strengthening effect of some elements on the yield strength in Cu-FCC alloys[8].

Figure 3-1. The effect of solid solution in a) dislocation motion[7] and b) the effect of Be, Si, Sn, Al, Ni and Zn addition on solid solution strengthening of Cu-FCC alloys[8].

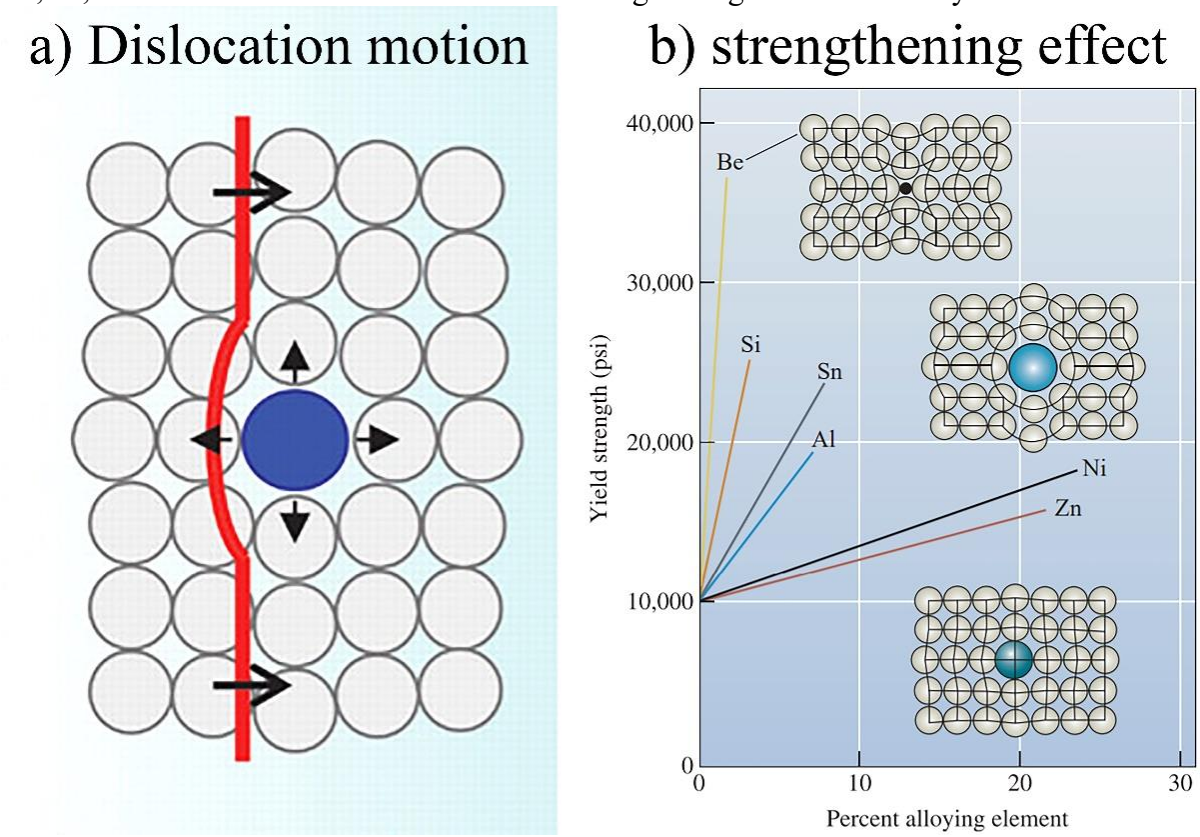

Source: Adapted from LU *et al.*[7] and Askeland *et al.*[8].

Another important effect of solid solution hardening is related to stacking fault energy (SFE). In general, the addition of solid solution elements decreases the SFE of a crystal lattice structure and consequently hinders the dislocation cross slip, which is responsible for the continuous motion of dislocations along the crystal lattice[9]. This dislocation motion mechanism is one of the most important in FCC materials[10].

The concentration of elements such as Mo, W, Cr, Al, and Rh as clusters also impedes the dislocation motion, causing a strengthening of the alloy[11]. This hardening effect decreases at high temperatures, especially for service temperatures above 60% of the melting

temperature of the alloy, since at these temperatures diffusion occurs easily causing the dissolution of clusters.

Although strength at high temperatures is very important for most industrial applications, corrosion resistance of a material is considered fundamental for severe environments. There is a special family of solid solution strengthening Ni-based alloys called Ni-Cr-Mo. The alloys from this family usually have a Cr and Mo content varying from 10 to 30 wt% and 0 to 15 wt%, respectively[4]. These alloys are typically used in severe corrosion environments, with high levels of impurities, especially halides. Ni-based alloys with low Mo cannot prevent localized corrosion[12]; however, massive addition of Cr and Mo provides good resistant to a wide range of aggressive corrosive mechanisms such as pitting and crevice corrosion at low pH, high chloride oxidizing and stress corrosion cracking[13]. There are several commercial alloys suitable for different environments, in which the Alloy 625 (62Ni-21Cr-9Mo-3.7Nb) and Alloy C-276 (59Ni-16Cr-16Mo-4W-5Fe) have been used extensively since their introduction onto the market.

3.1.1.2 Precipitate strengthened alloys

The family of precipitate strengthened (PS) alloys is of great importance in the aerospace industry. Commonly known by ‘superalloys’ due to their extremely high toughness, these alloys may easily pass 1000 MPa of yield strength with an adequate addition of alloying elements and heat treatment[4]. In this case, the main hardening mechanism is related to the precipitation of coherent phases well distributed throughout the material. In order to induce the nucleation of precipitates solid solution elements are intentionally inserted above to solubility of the γ-FCC matrix.

To achieve the excellent properties of precipitation strengthened alloys several alloying elements are added into the γ-FCC matrix; each one with its own specific goal. Al, Ti and Nb are the most important elements for these alloys, since they are responsible for the hardening by precipitation of the coherent phases. The solubility of these elements by the γ-FCC matrix is drastically reduced at low temperatures. Thus, the precipitation of the coherent γ′-Ni_3(Ti,Al) and γ″ Ni_3Nb phases occurs during heat treatments.

The hardening mechanism is complex and concerns several phenomena related to the dislocation motion. There are two ways for the dislocation to progress through a particle into the matrix: shearing or looping particle[6,10]. Figure 3-2 shows these two interactions [14–16].

Naturally, the dislocation will choose the mechanism that offers the least resistance[10]. In the case of coherent phases both mechanisms are more difficult than with incoherent phases, since there are no broken bonds between the coherent phase and the matrix and, the bond strength of such an intermetallic coherent phase is very high[17].

Figure 3-2. Schematic and transmission electron images for both mechanisms: a) shearing and b) looping the particle[14–16].

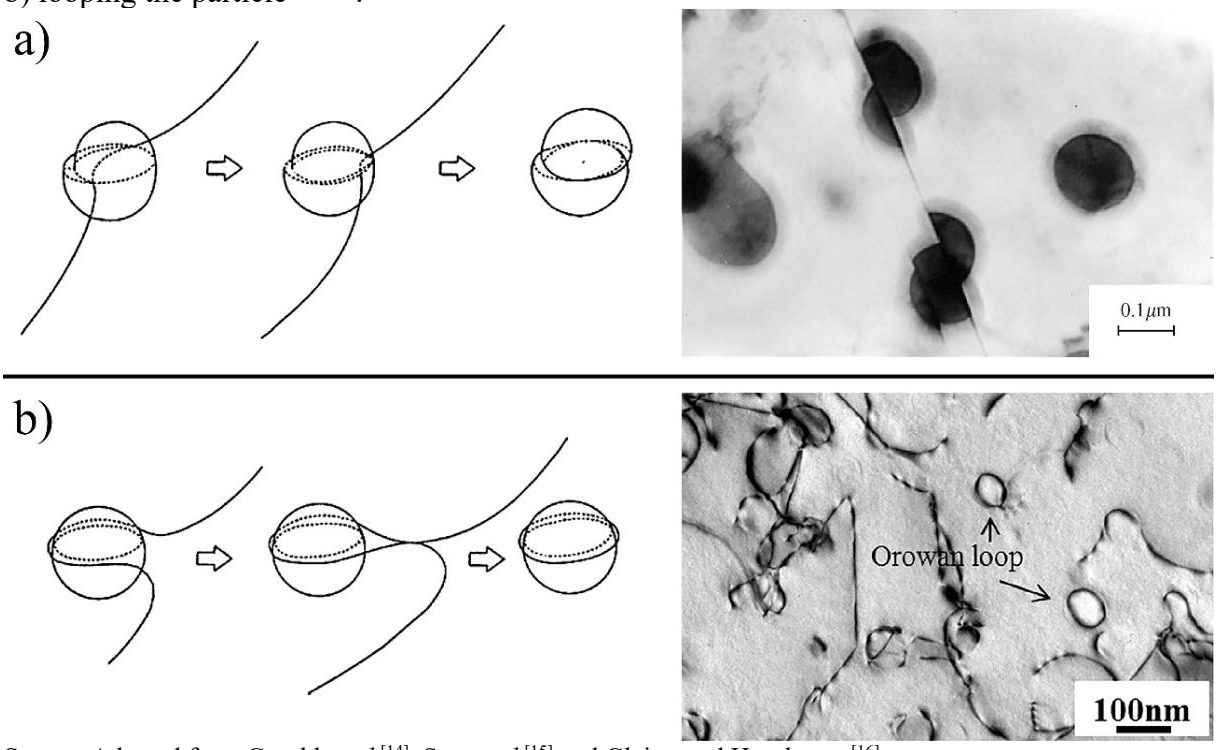

Source: Adapted from Gerold *et al*.[14], Sun *et al*.[15] and Gleiter and Hornbogen[16].

The hardening effect is only achieved after a heat treatment. The procedure is divided in two main steps: solubilization and aging. The solubilization step is necessary to homogenize the solute elements, eliminating any eventual coarse particles nucleated during solidification, especially for the as welded condition, in which the microsegregation of alloying elements represents a phenomenon inherent to the welding processes[18]. The time and temperature required for solubilization treatment will depend on the alloy and its thermomechanical conditions. The treatments to solubilize Alloy 80A and Alloy 718, both in the as wrought condition, require temperatures of 1080°C for 8 h and 980°C for 1 h, respectively, while to solubilize Alloy 718 in the as cast condition, a temperature of 1095°C is needed for 1 h[9]. The aging treatments, in turn, need a long time for precipitation and for the growth of the coherent phases; in general, at least 16h is necessary to achieve the desired hardening effect.

The effects of the heat treatment, especially for welded alloys, is extremely complex, as strain-age cracking can occur during the solubilization step. During the heating, for the solubilization step, a precipitate strengthening of the γ' and/or γ" phases may lead to the formation of these strain-age cracks. The cracking occurs during stress relief step, since the stress concentrates in the weld metal strengthened by precipitates causing cracks, especially in high constraint components[18].

There are other general considerations that must be taken into account for these heat treatments. These treatments are expensive due to the long hours required to achieve the aging and consequently the strength desired. Besides, components with complex geometries present certain practical difficulties [19]. Furthermore, in the present case, there is a special impediment for the use of heat treatments that is relate to the base metal. API steels are considered to be high strength low alloy (HSLA) steels and, as such, their toughness has been achieved mainly by thermal-mechanical processes that are responsible for grain refinement[20]. In addition, a long period at the aging temperature will cause the nucleation and growth of the γ-FCC of the HSLA steel[21]. Moreover, the heat treatment also leads to the diffusion of the alloying elements that causes precipitation phases along the interface.

According to Lalam *et al.*[22] the post weld heat treatment of dissimilar welding between Alloy 718 and EN24 structural steel by continuous drive friction caused the nucleation of several precipitates such as Fe_3Mn_7, Ni_3Al_4 and AlNi, and this drastically reduced the toughness of the material by about 4J, even at room temperature[22]. Moreover, the yield strength of the joint in the as welded condition was approximately 376 MPa[22], which is far from the YS required for joining such HSLA steels desired by the present study. Consequently, these above mentioned difficulties and specifics make the use of precipitate strengthened alloys for girth welding of API steels impracticable.

3.1.1.3 Oxide dispersion strengthened alloys

As previously mentioned, the oxide dispersion strengthened alloys (ODS) are a family of Ni-based alloys with a focus on high toughness and their hardening mechanism is quite similar to the hardening mechanism of the precipitate strengthened alloys. In this case, nanometric oxide particles are introduced into the bulk of the material, providing a physical barrier to dislocation motion. The hardening mechanism is not so effective as in precipitate hardened alloys, since the incoherent particles have several broken bonds, therefore, the

progress of the dislocation motion will be achieved lopping the particles by the Orowan mechanism[10].

The main advantage of this hardening mechanism is related to the high thermal stability of oxides in comparison to the γ' and γ" precipitates. This allows the use of oxide dispersion strengthened alloys in temperatures above 1000°C, when for example, the solubilization of the hardening precipitates commonly occurs. New ODS alloys that combine the oxide dispersion and precipitate hardening mechanisms have been developed to be used in PS applications, especially those for high temperature service conditions. Nganbe and Heilmaier[23] investigated the creep resistance of two ODS alloys, PM 1000 and PM 3030, at 600°C, 850°C and 1000°C. Both alloys were strengthened by Y_2O_3, but the PM 3030 alloy was also strengthened by the γ' precipitates. The creep resistance of PM 3030 at 600°C was higher than PM 1000 due to the γ' hardening effect, while at 1000°C the creep resistance of PM 3030 decreased drastically as a consequence of solid solution softening, γ' dissolution and coarsening[23]. This combination of ODS with precipitate strengthening is not restricted to Ni-based alloys; it has been used with ferritic and austenitic stainless steels by mechanical alloying processes[24,25]. A recent study manufactured ODS 316L steel by powder metallurgy in order to increase the toughness of the austenitic steel and a 458 MPa of yield strength was obtained; this represented an increase of about 50% in comparison with a conventional 316L steel[26].

There are some disadvantages like loss of toughness with the ODS method. The ODS alloys are normally manufactured by powder metallurgy; however, the low density of the oxide particles hinders the homogenization of the particles throughout the material, especially for conventional manufacturing methods such as welding. According to Dupont *et al*.[4] it is virtually impossible to weld ODS alloys without losing toughness, since the oxide particles float and agglomerate on the surface of weld. The authors also pointed out that the use of the high energy density fusion welding processes may improve the mechanical properties, considering the fast solidification of these welding processes. Nonetheless, it remains impracticable to obtain similar properties of such materials manufactured by powder metallurgy processes.

Considering the basic features of the Ni-based alloys presented here, this study will continue to focus on solid solution strengthened alloys, since they are more compatible with the welding applications proposed. Furthermore, conventional welding, without the need for post weld heat treatments can be applied to these alloys; and there is a large choice of suitable alloys with high corrosion resistance.

3.1.1.4 Historical evolution of main solid solution alloys

Since early last century, there has been significant developments in the design of solid solution alloys with a focus on corrosion resistance. Industries have always been interested in versatile alloys with good corrosion resistance and a high thermal stability. In the 1930's the first alloy with such features called Alloy C was developed. Further developments with the combination of Ni-Cr and Ni-Mo gave birth to the design of the first Ni-Cr-Mo alloy[13]. Table 3-1 shows the chemical composition of Alloy C and other solid solution strengthened alloys.

Until the middle of 60's, Alloy C was the still the best corrosion resistant alloy on the market. Nonetheless, Alloy C in the as welded condition exhibited serious problems in terms of intergranular corrosion. The recommendation to overcome this was post weld heat treatment to homogenized the elements and thus avoid degradation. However, this inconvenient heat treatment reduced the fields of application for this material[13]. Therefore, in the mid 60's two alloys were developed that are used until today: Alloy C-276 and Alloy 625[12,13].

Table 3-1. Chemical composition of the main solid solution strengthened alloys with high corrosion resistance.

Chemical composition of alloys												
Alloys	**Ni**	**Cr**	**Mo**	**W**	**Fe**	**Co**	**C**	**Si**	**Nb**	**Al**	**Ti**	**Ano**
Alloy C	55	16	16	4	6	-	0.05	0.7	-			1934
Alloy 625	63	20	8	-	5	-	0.005	0.04	3.6			1964
Alloy C-276	57	16	16	4	5	-	0.005	0.04	-			1965
Alloy C4	66	16	16	-	2	-	0.005	0.04	-			1970
Alloy 617	54	22	9			12.5		0.07		1		70's
Alloy C22	57	21	13	3	3	-	0.005	0.04	-			1982
Alloy 59	59	23	16	-	1<	-	0.005	0.04	-			1990
Alloy 686	56	21	16	4	2	-	0.005	0.04	-			1993
Alloy 680		20.5	6.5	6.5		-			3.5		1.5	2015

The design of Alloy 625 actually started in the 50's, but was only patented later. The conception of Alloy 625 took into consideration the weldability, high creep resistance and non-age strengthened in order to attend a specific problem related to steam power plants at the time. The first attempts to use a high content of Nb resulted in prototypal alloys hardened by age treatment that lead to the design of Alloy 718 in 1958, which, represents one of the most important PS alloys, even today. The project was focused on a non-age hardening material with a high strength at room temperature. So, a large amount of Cr and Mo were intentionally added

in order to increase hardening by solid solution; moreover this also greatly increased the potential application of Alloy 625 in the field of corrosion resistance [27].

Ruther and Greenberg[28] carried out one of the first studies on Alloy 625. They investigated the corrosion resistance of stainless steels and Ni-based alloys to resist the superheated steam in the nuclear industry. Alloy 625 exhibited a superior corrosion resistance in short static and dynamic tests at 650°C than 304 stainless steel under the same conditions.

Later, Cieslak *et al*.[29] investigated the solidification mechanism of Alloy 625, considering the particular aspects of welding processes. Using differential thermal analysis (DTA), the authors evaluated the formation of secondary phases in Alloy 625, including experimental alloys by varying the Nb, Si and C contents in Alloy 625. The thermograms showed the eutectic reactions at the final stage of solidification such as γ/Laves, γ/NbC and γ/M_6C due to the microsegregation of Nb, Si and C. Using a high content of C, the NbC reaction was favored over the Laves reaction. While with a low C content, the Si favored the Laves reaction, consuming almost all the C, which eventually resulted in the nucleation of M_6C carbide[29].

Innumerable studies with Alloy 625 have been done until now due to its versatility. Other important studies investigated the weldability[30], microstructure[31,32], microsegregation[31,32], solidification path[31,32], aging effect[33] and its application in early manufacturing processes such as additive manufacturing[34] and friction stir welding[35,36]. Below is the solidification path for Alloy 625 after improvements to its chemical composition over the years[32]:

$$L+(TiN) \rightarrow L+ \gamma + (TiN) \rightarrow L + \gamma + (TiN) + (NbTi)C[shell] \rightarrow L + \gamma + (TiN) + (NbTi)C[shell] + Laves \rightarrow \gamma + (TiN)[core]/(NbTi)C[shell] + Laves$$

The evolution of solid solution strengthened alloys continued with a focus on corrosion resistance, and in 1965 the Alloy C-276 was designed; which was at the same period as Alloy 625. However, significant changes were occurring in metallurgy at this time, and therefore, Alloy C-276 was considered to be one of first alloys of the second generation of solid solution strengthened Ni-based alloys for use in corrosion resistant services[12]. Also new technologies in the decarburization process were introduced, which made the reduction of Si and C possible [12,13]. Thus, Alloy C-276 was developed almost equal to Alloy C, but this time with residual Si and C contents, in order to improve the intergranular corrosion resistance. The

result was a significant reduction of carbides rich in Cr and Mo along the grain boundaries. Leonard[37] investigated the time temperature transformation curves for Alloy C-276 and compared them with curves from Alloy C. Taking the most favorable temperature for the nucleation of precipitates, which is 871°C, the author pointed out that Alloy C only need a few seconds to precipitate the deleterious phase, in terms of corrosion resistance; while Alloy C-276 need at least 5 min to nucleate the P phase and 1 h to nucleate Ni_7Mo_6[37].

Despite great advances in intergranular corrosion resistance and weldability, since post weld heat treatment was no longer indispensable for Alloy C-276 as it was for Alloy C, there have been reports concerning the precipitation of phases rich in Cr and Mo that make this alloy sensitive to localized corrosion[38]. DTA analyses have revealed that the P phase nucleated at the final stage of solidification of Alloy C-276 due to the microsegregation of Mo and W[39]. Besides, the P phase rich in Mo and W may decompose in the μ phase[39]. Both phases are rich in Mo and W in which are responsible to prevent localized and crevice corrosion[40–42]. Below is the solidification path proposed for Alloy C-276[39]:

$$L \rightarrow L + \gamma \rightarrow L + \gamma + P \rightarrow \gamma + P \rightarrow \gamma + P + \mu$$

Studies for the development of Ni-based alloys that focused on corrosion resistance were also interested in increasing the thermal stability of the alloys, in other words, these studies sought alloys with high susceptibility to nucleation of precipitates during solidification and ones that were able to give service at high temperatures. Thus, in 1970 Alloy C4 was designed with a focus to minimize the precipitation of topologically closed packed (TCP) phases and carbides. Therefore, Ti was intentionally introduced with aim to stabilize C by nucleation of Ti carbides[43], and thus avoid the nucleation of Cr and Mo rich in carbides.

Hodge and Kirchner[43] investigated the time temperature transformation of Alloy C4 and compared it to Alloy C-276. The authors observed that Alloy C-276 nucleated M_6C in 5 min at 800°C, while Alloy C4 needed at least 4 h. After 100h at the same temperature, a μ phase was observed but only for Alloy C-276. The authors also highlighted the good thermal stability at the aging regime of between 600 and 1000°C, as no significant changes in corrosion resistance were observed.

Cieslak *et al*.[39] also evaluated the solidification path of Alloy C4 by DTA analysis. On cooling a single exothermic peak that corresponds to a γ phase was observed, and this indicates no precipitation occurred. The microsegregation profile revealed a concentration of

Ti at the interdendritic region and electron diffraction patterns of particles confirmed the presence of TiC carbides[39]. Notably, Alloy C4 has an excellent thermal stability due to the absence of TCP phases and carbides rich in Cr and Mo. The solidification path proposed by literature is shown below:

$$L \rightarrow L + \gamma \rightarrow L + \gamma + TiC \rightarrow \gamma + TiC$$

The absence of the P and μ phases, even at high temperatures, is most probably related to the absence of W in its chemical composition, considering the previous studies concerning Alloy C, Alloy C-276 and Alloy C4[37,39,43]. This may be due to the reduction of Mo solubility by the Ni-based matrix rich in W and, may also be related to the difficulty of Mo to diffuse into the matrix.

In the early 70's, Alloy 617 was designed. Alloy 617 is considered a Ni-Cr-Mo alloy, even though it has at least 10% Co present in solution. The chemical composition of Alloy 617 is quite similar to Alloy 625, considering the Cr and Mo fractions above 20% and 9%, respectively. The major difference between them is related to the substitution of Ni for Co, and the fact that it has good solubility in the Ni matrix.

This resemblance of Alloy 617 with Alloy 625 is seen in its properties and consequently in the applications Alloy 617 is used for. Both alloys are designed for use in nuclear components that need high creep properties and oxidization at high working temperatures[44]. According to the literature, the addition of 1% Al gives Alloy 617 the possibility to be strengthened by precipitation of γ'[45]. Nevertheless, it maintains its good corrosion resistance for different corrosive environments.

Olson *et al.*[46] compared the corrosion resistance of Alloy 617 with other Ni-based alloys commonly used in heat exchangers for nuclear reactors, under severe molten fluoride salt solution. The anions of molten salts commonly increase the corrosion rates, since stable complexes react with Cr and Fe present in the alloys. Among the high Cr Ni-based alloys, the 617 and 800H alloys showed a similar corrosion resistance, while Alloy 230 exhibited the worst corrosion resistance among the alloys tested [46].

Recently, the use of Alloy 617 was investigated for a new generation of fossil fuel power plants based on supercritical water under temperatures and pressures up to 650°C and 34.5 MPa, respectively. The authors compared the 617, 625, 718 alloys, and Alloy 617 exhibited the best corrosion resistance. Few submicron pits were observed for Alloy 617, while Alloy 718 exhibited the poorest pitting resistance, which was attributed to the Nb and/or Ti

precipitates such as the γ" phase, since a galvanic corrosion occurs considering the high compositional differences between the precipitates and Ni matrix[47].

The weldability of Alloy 617 was compared with 625, 59, 600H and 800H alloys by the PVR test (deformation crack test)[48]. Alloy 617 showed a susceptibility to solidification cracks quite similar to Alloy 625, considering the standard deviation. The study reported the occurrence of liquation cracks in the heat affected zone (HAZ) due to the high Mo present in the liquid film between grains. Ductility dip-cracking was also observed in the HAZ of Alloy 617, outlining the grain boundaries.

In the 80's, a new alloy called Alloy C22 was developed based on the C4 and C-276 alloys. The development took into account the excellent thermal stability of Alloy C4 and limitations of both alloys, in terms of corrosion resistance. First, the Cr fraction was increased considerably in order to improve the oxidizing resistance in non-halide solutions, as this was one of the main problems of the C4 and C-276 alloys[13]. In this case, the good oxidizing resistance of Alloy 625 was also considered for this [49].

In order to improve the localized corrosion resistance, the Mo fraction was reduced to 13% and W was added for compensation. Nonetheless, the combination of Mo, W and Fe provided nucleation of the TCP phases during solidification and cooling of Alloy C-276. Thus, for Alloy C22 a reduction of these elements in comparison to Alloy C-276 was proposed, whilst taking into consideration the electron vacancy of the W and Fe solid solution elements[13]. The result was an alloy with superior corrosion resistance, which include oxidization and localized corrosion, with an excellent thermal stability even at high temperatures[50].

Lloyd *et al*.[41] investigated the effect of Cr, Mo and W on the passivity of several solid solution strengthened alloys including Alloy C22. The high Cr alloys such as C22, 625 and 2000 exhibited a lower passive current density compared to alloys C4 and C-276. The authors also pointed out that only the high Cr and Mo alloys, C22 and 2000 did not undergo crevice corrosion between specimen and resin used to manufacture the specimen. Moreover, the lower passivity current of Alloy C22 compared to Alloy 2000 under the same conditions, suggested that W, which was only present in Alloy C22, was responsible for the superior corrosion resistance[41].

The solidification of Alloy C22 was evaluated by DTA measurements and compared with alloys C4 and C-276 by Cieslak *et al*.[39]. A small peak was observed at the end of the solidification that was attributed to the σ reaction. The high Cr content led to the nucleation of the σ phase, while for Alloy C-276 this was characterized as a P phase, it is favored strongly by Mo and Ni. Alloy C4 did not exhibited any TCP due to the reasons

previously mentioned. The P and μ phases also were identified in thin foils of Alloy C22 by electron diffraction patterns, which the authors attributed to the solid transformations that occurred during cooling. The solidification path proposed by the literature is shown below [39]:

$$L \rightarrow L + \gamma \rightarrow L + \gamma + P \rightarrow L + \gamma + P + \sigma \rightarrow \gamma + P + \sigma \rightarrow \gamma + P + \sigma + \mu$$

Weldability problems are not expected for these Ni-Cr-Mo alloys, even with the presence of TCP phases, since the σ and P phases did not significantly increase their solidification temperature ranges[39], differently from what was observed for the Laves reaction at the end of the solidification of Alloy 625[29–31].

In the early 90's, two new alloys were introduced to work under severe corrosion conditions because conventional alloys such as the 625, C-276 and C22 alloys were not able to provide sufficient corrosion resistance. Thus, in 1990 and 1992 the Alloy 59 and Alloy 686 were designed, respectively. Both alloys were developed with a superior addition of alloying elements, especially Alloy 686 that contained at least 41% of solid solution elements in the Ni matrix.

In the case of Alloy 59 its conception was based on the New Phacomp model, introduced by Morinaga[51]. The proposed simulation model successfully predicted the phase stability of the TCP phases in the γ-FCC, considering the physical features that are related to the solubility of the solute, such as electronegativity, atomic size and average energy of the d orbitals of the alloying transition metals. The benchmark of the simulator was done by 25 ternary systems, which included Ni-Co-Cr, Ni-Cr-Mo, Fe-Ni-Cr, Co-Ni-Mo, Ni-Al-Ti and Ni-Cr-Ti[51]. Thus, an Ni-Cr-Mo alloy was designed with minor additions of other alloying elements that conferred the best thermal stability offered by alloys from the Ni-Cr-Mo family to Alloy 59 [13].

Lou *et al*.[52] evaluated Alloy 59 under severe H_2SO_4 acid solution. According to these authors Alloy 59 exhibited a fast and stable passivation film, even for different potentials, from 0 to 0.9V. Based on the x-ray photoelectron spectroscopy (XPS) measurements, the passive layer was made up of Cr_2O_3, $Cr(OH)_3$ and $Ni(OH)_2$ with support of Mo oxides from a range of Mo(VI) and Mo(IV). Mishra and Shoesmith[40] also investigated the corrosion resistance of Alloy 59 and compared it against other Ni-Cr-Mo alloys, in order to assess the effect of Cr, Mo and W on corrosion resistance. The authors pointed out that the crevice corrosion of Alloy 59 was quite similar to Alloy C22, despite the fact that Alloy 59 does not have 3% W as is present in Alloy C22, and considering that W has an important role in

preventing the initiation of crevice corrosion. On the other hand, Alloy 59 has a larger Mo fraction that is well solubilized due to its good thermal stabilization.

The weldability of Alloy 59 was compared to that of the 625, 617, 600H and 800H alloys. The PVR test (deformation crack test) showed that Alloy 59 exhibited only small liquation cracks and some solidification cracks in the partially mixed zones. Among the alloys evaluated, Alloy 59 was ranked as having the lowest susceptible to solidification, liquation and ductility dip cracking[48].

There is no experimental report describing the solidification path of Alloy 59; however, a recent thermodynamical study predicted the simulation of Alloy 59 based on the Scheil-Gulliver model[53]. The study predicted the formation σ, P and Cr_2Si at the end of solidification, because the thermodynamic model of Scheil-Gulliver[54,55] assumes that there is no solid back diffusion during solidification, which enhances the microsegregation during cooling. However, the predicted phases only took into account the solidification and, therefore, other solid transformations may lead to the dissolution of these phases and the nucleation of others like the μ phase.

With respect to Alloy 686, it was mentioned about the superior addition of alloying elements present in its chemical composition. This overcome of Mo, for example, impairs its thermal stability. Currently, there some studies assessing the welding metallurgy and microstructure of precipitates nucleated during solidification of Alloy 686[56–59]. One recent study quantified almost 2% of precipitates nucleated in Alloy 686 cladding. The precipitate phases showed an average chemical composition of 27.1Ni-20.0Cr-38.2Mo-6.2W-8.5Fe-0.1Mn[60].

Miná *et al*.[61] assessed the effect of iron dilution on the partitioning coefficient of alloying elements in clad welding of Alloy 686. A small increase in the Mo partitioning coefficient was observed as dilution increased and, this was attributed to a possible solubility reduction caused by addition of Fe into solid solution. According to the study, at least 20% of Mo was segregated to the liquid portion.

Silva *et al*.[62] investigated the solidification path of Alloy 686 when diluted with ASTM A516 Gr60 steel in clad welding. Selected area diffraction of thin foils detected σ, P and μ π phases. The authors suggested that during solidification the high Cr content associated with the segregation of Mo caused the nucleation of the s and P phases at the final stage of solidification. After the reheating of the Alloy 686 weld metal caused by multi pass welding, the temperature crossed the γ + μ biphasic field, and this caused the partial solid transformation

of P phase in μ phase. Thus, it is reasonable to propose, according to the study mentioned[62] and also based on other studies that investigated Ni-Cr-Mo-W alloys[39,63,64] that the solidification path is:

$$L \rightarrow L + \gamma \rightarrow L + \gamma + P \rightarrow L + \gamma + P + \sigma \rightarrow \gamma + P + \sigma \rightarrow \gamma + P + \sigma + \mu$$

A new solid solution, called Alloy 680, derived from the Ni-Cr-Mo family was designed and patented in 2010[65]. Alloy 680 was directly linked to a new challenge from the oil and gas industries. The challenge was to reach the high strength required for joint welding of complex steel pipes with internal CRA cladding and it was designed in a partnership between Petrobras (Brazilian oil and gas company) and Special Metals company. The new filler metal would have to exhibit high strength, good impact toughness at subzero temperatures and a corrosion resistance comparable to Alloy 625, since CRA claddings are commonly cladded with this alloy. These requirements required the addition of a large amount of solid solution elements: Ni-20.5Cr-6.5Mo-6.5W-3.5Nb-1.5Ti[66]. Besides the effect of solid solution strengthening, Alloy 680 may also be strengthened by the precipitation of coherent phases, since there is a high Nb and Ti content like in other PS alloys; nonetheless, until now no study has investigated this possibility.

According to Mannan *et al*.[67], who introduced a new high strength filler metal, Alloy 680 may exhibit a yield strength varying from 550 MPa to 655 MPa, depending on the welding heat input adopted and the Fe dilution achieved. However, the authors did not detail the phenomenon behind this strengthening mechanism. On the other hand they obtained and compared the critical crevice temperature (CCT) to traditional high corrosion/oxidization resistant alloys and Alloy 680 exhibited a good performance compared to Alloy 625. The CCTs for 680, 625 and 686 were 45°C, 25°C and 65°C[67], respectively. Alloy 686 showed high resistance, due to the large amount of Cr, Mo and W added, as well as excellent resistance to localized corrosion.

The Laboratório de Pesquisa e Tecnologia em Soldagem at the Universidade Federal do Ceará has been carrying out research in partnership with Petrobras. One of these projects, among others related to welding technology that this group has been developing, is the use and evaluation of Alloy 680 for joint welding of high strength steels. A recent master thesis investigated the joint welding of API 5L X65 steel with internal cladding of Alloy 625 using Alloy 680 as the filler metal[68]. The investigation showed that Alloy 680 provided sufficient yield strength to overmatch the strength of the steel pipe. The impact toughness of

the welded joint at -15°C was on average approximately 76J. However, in terms of weldability there were some solidification cracks for weld passes with high Fe dilution and high depth-to-width (D/W) ratio[68].

3.1.2 Solidification cracking

Solidification cracking is one of the more serious problems related to welding. The solidification cracking phenomenon is very complex, since many other metallurgical and mechanical phenomena are occurring simultaneously. The welding parameters also contribute to the complexity of the solidification cracking phenomenon; this is because even a single specific welding parameter may induce more than one metallurgical and/or mechanical effect, which in turn, may minimize or contribute to the solidification cracking phenomenon. Among the controversies and effects that are not well understood, the scientific community agree on some factors that define the base of the phenomenon[69]:

- Metallurgical;
- Mechanical;
- Restraint.

These factors interact among themselves and, the solidification-cracking phenomenon depends on each of them. In most cases, the absence of one of these factors is enough to prevent the formations of cracks. The following section presents the main aspects of each of these factors in detail.

3.1.2.1 Metallurgical factor

Probably, the metallurgical factor has the strongest effect on the solidification-cracking phenomenon and consequently, the weldability of alloys is frequently associated to metallurgical factors. The chemical composition of a material is what really defines the metallurgical factor. The elements present define the orderly arrangement of atoms and the crystal lattice as well as the equilibrium of phases, thermal expansion coefficient, solidus temperature, solubility of elements, microsegregation and nucleation of secondary phases. Some of these metallurgical effects also interact among themselves, as well as with the mechanical and restraint factors.

Initially, it is important to define the basic concepts concerning solidification. In the arc welding process, solidification occurs out of equilibrium, since the fast cooling does not

allow the elements to diffuse and organize for the lowest energy of the system, in terms of thermodynamic equilibrium. The absence or almost negligible diffusion of the elements at the solid-liquid (liquid-solid) interface, towards the solid, causes the enrichment of the liquid (phase) by solute. The fast cooling hinders the diffusion of the elements to the solid portion, even in cases where the solid has the ability to solubilize those elements. Moreover, as the cooling advances the solubilization ability of the solid decreases, which causes the rejection of the solute by the solid phase, contributing to an even greater solute rich liquid. This phenomenon is called microsegregation and, it has an important role in the solidification cracking susceptibility of materials.

Microsegregation of the solute or alloying elements that remained liquid make the nucleation of secondary phases thermodynamically possible and different from the solid matrix phase at the final stage of solidification. In the case of Ni-based alloys, these secondary phases can be MC, M_6C M_7C_3 $M_{23}C_6$ carbides and TCP phases like σ, P, μ, δ, η and Laves [1]. Some of these phases have low solidus temperatures that cause the solidification temperature range of the material to widen. In general, alloys with a large solidification temperature range are more susceptible to solidification cracking.

An argument to explain this proposition is related to the time and temperature range that the remaining liquid will be submitted to before the solidification is complete. As solidification progresses, two principal stresses appear that are due to the contraction of the liquid-to-solid transformation and to the solid thermal contraction. The larger the solidification time the longer the remaining liquid will be submitted to the above mentioned stresses. Depending on the restraint and ability of the solid and grain boundaries to absolve the stress, the solidification cracking may occur or not. This demonstrates a convergent point among metallurgical, mechanical and restraint factors.

The microsegregation can be predicted by the classical model proposed by Gulliver[55] and posteriorly equated by Scheil[54]. In a non-equilibrium solidification process, especially in welding, the solidification is concluded in a few seconds. The Scheil-Gulliver model represents this fast solidification processes very well, since the model induces an intense microsegregation. The model assumes that no solid back diffusion occurs during solidification. Therefore, there is no homogenization of the solid phase as in equilibrium model (lever rule). Moreover, the Scheil-Gulliver model also assumes that the solute is fully homogenized in the liquid portion. Besides, as solidification progresses, the solubility of the solid phase decreases along with the temperature decrease. This causes banding in the chemical profile of the solid, as well as enriching the solute in the remaining liquid. This solute enriched remaining liquid in

turn favors the thermodynamic nucleation of other phases differently from the solid matrix phase that may have a low solidus temperature. Figure 3-3 illustrates the microsegregation phenomenon proposed by Scheil-Gulliver[70].

Figure 3-3. Graph representing the Scheil-Guilliver solidification model. As the solidification progresses the remaining liquid has a new chemical composition until it converges with the eutectic point at the final stage of solidification[70].

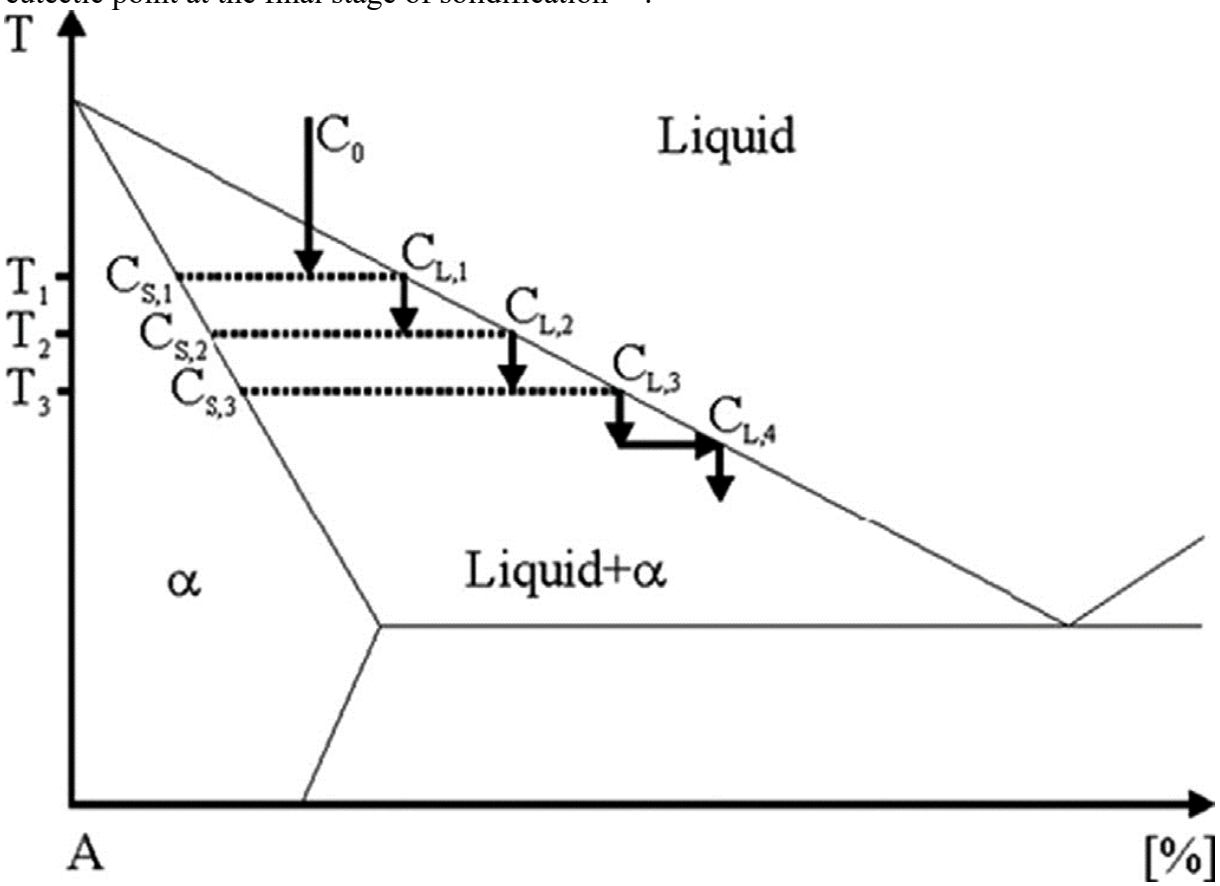

Source: Adapted from MatCalc[70].

Other studies have proposed complex models to describe solidification and microsegregation. Brody and Flemings[71] developed a model taking into account the solid back diffusion of some elements, especially for interstitial elements. This model is particularly important to predict the solidification of steels, since their microstructure and properties are strongly influenced by interstitial elements such as C. In slow solidification processes this model that considers the solid back diffusion has a notably better accuracy in predicting solidification. Clyne and Kurz[72] also proposed a model with important contributions in this field. On the other hand, in fast solidification processes, the Scheil-Gulliver model predicts the solidification very well and with considerable ease. Dupont[31] and Miná *et al*.[61] investigated the microsegregation when welding 625 and 686 alloys, respectively. In both studies the

microsegregation was calculated based on the Brody and Flemings model; however, the solid back diffusion of the alloying elements like Cr, Mo, Nb and W were almost zero[31,61], reducing the equation to the Scheil-Gulliver model. This was attributed to very low time available for the elements to diffuse during solidification, which was about 1s[61]. Moreover, these elements have a low diffusion coefficient into the Ni matrix, since they are considered solid solution elements.

Currently, there are commercial software packages based on the Calphad method that implemented the Scheil-Gulliver model. Information resulting from these models can help to understand and investigate the solidification crack susceptibility by predicting the secondary phases, the volume fraction and their chemical composition. However, with so much thermodynamic information, the interpretation is complex and it must also take into consideration other phenomena.

As mentioned, there are secondary phases in Ni-based alloys that can nucleate due to microsegregation. Nonetheless, some of these are more deleterious, in terms of solidification cracking than others. The eutectic phases such as Laves, Nb and/or Ti carbides have a greater deleterious effect if compared with other TCP phases like the σ, P and μ phases[29,39]. Therefore, some considerations must be taken concerning the volume fraction of secondary phases. In general, a large fraction of non-eutectic phases is less deleterious than a small fraction of eutectic phases. On the other hand, a large fraction of eutectic phases may also lead to a reduction of solidification cracking susceptibility due to a phenomenon called back-filling.

The back-filling phenomenon is about filling or the healing of intercellular, interdendritic, porosities and solidification cracks with the remaining liquid fraction (Figure 3-4). Through a capillary mechanism the remaining liquid fills the discontinuities and thus avoids or minimizes this metallurgical factor of the solidification cracking phenomenon[73]. Back-filling may explain some controversies concerning the Alloy 625 results in weldability tests[74]. As previously presented, Alloy 625 has a tendency to nucleate a large fraction of eutectic phases. Under severe restraint Alloy 625 tends not to have good weldability, since the back-filling phenomenon is suppressed, whereas under low restraint the alloy shows good weldability.

Figure 3-4. The backfilling of intergranular cracking by eutectic phases.

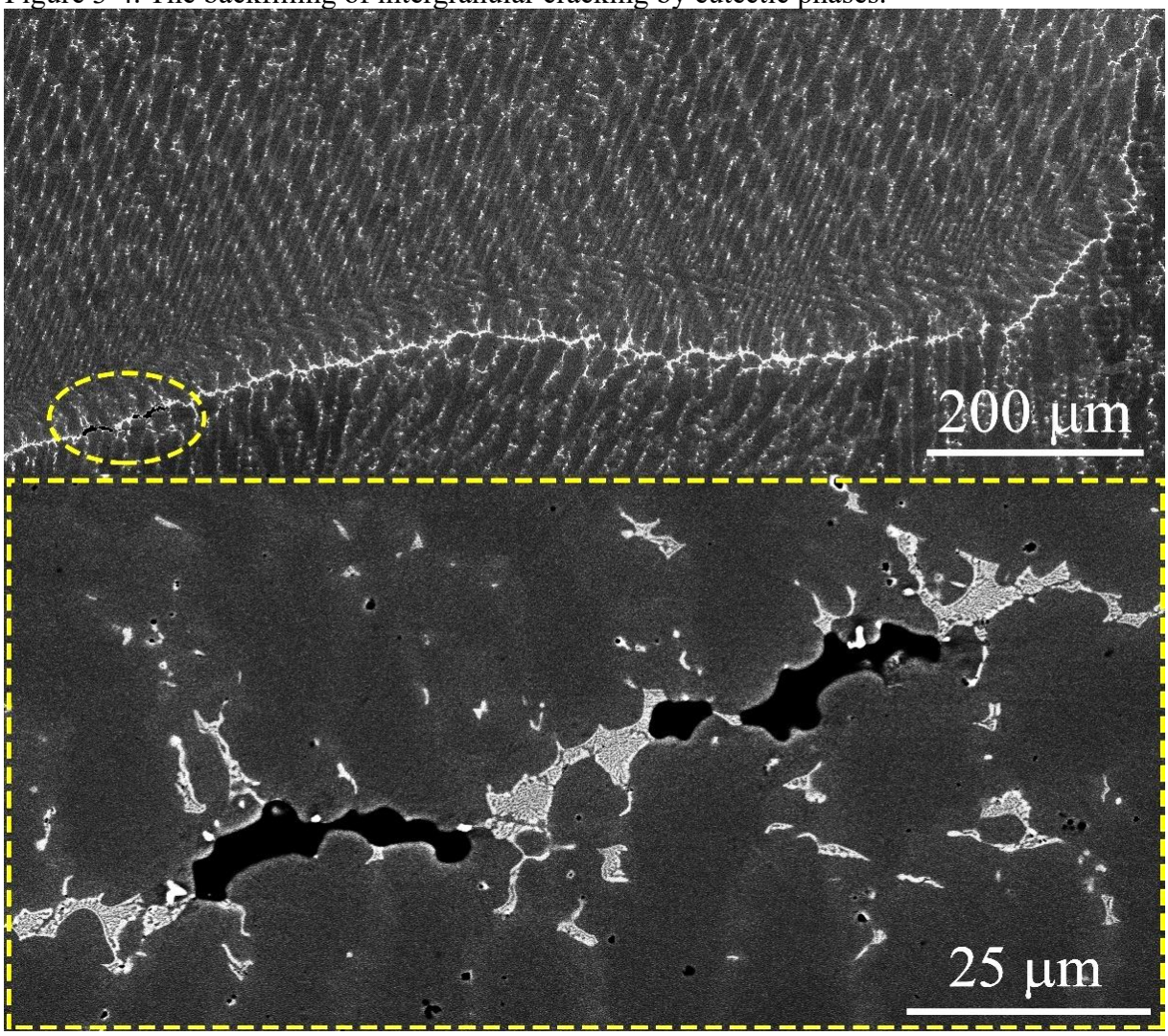

Source: Developed by the author.

Wheeling and Lippold[75] investigated the effect of the volume fraction of eutectic phases on healing solidification cracks. They evaluated the Ni-30Cr alloy with changes in the Nb and Mo fractions, 2-8% and 2-4%, respectively. The authors correlated the eutectic phases predicted by Scheil-Gulliver model and by metallographic analysis with a weldability test called cast pin tear test (CPTT)[76]. Figure 3-5 shows a summary of the most important results obtained by these authors. The volume fraction of the eutectic phases that were predicted showed greater accuracy when compared to the metallographic analysis. This reinforces the accuracy of the Scheil-Gulliver model to predict the solidification in welding processes. Low susceptibility to solidification cracking was observed for low (~1.5%) and very high fractions (~15%) of eutectic phases due to the healing/back-filling effect, while for moderate fractions (~7.5%) a high susceptibility to solidification cracking was observed. The authors not only highlighted that the

addition of Nb increased the eutectic volume fraction and the healing effect, but also adverted that under high stress there is a drastic reduction of the healing effect[75].

Figure 3-5. Effect of Nb addition on the eutectic volume fraction and solidification cracking susceptibility[75].

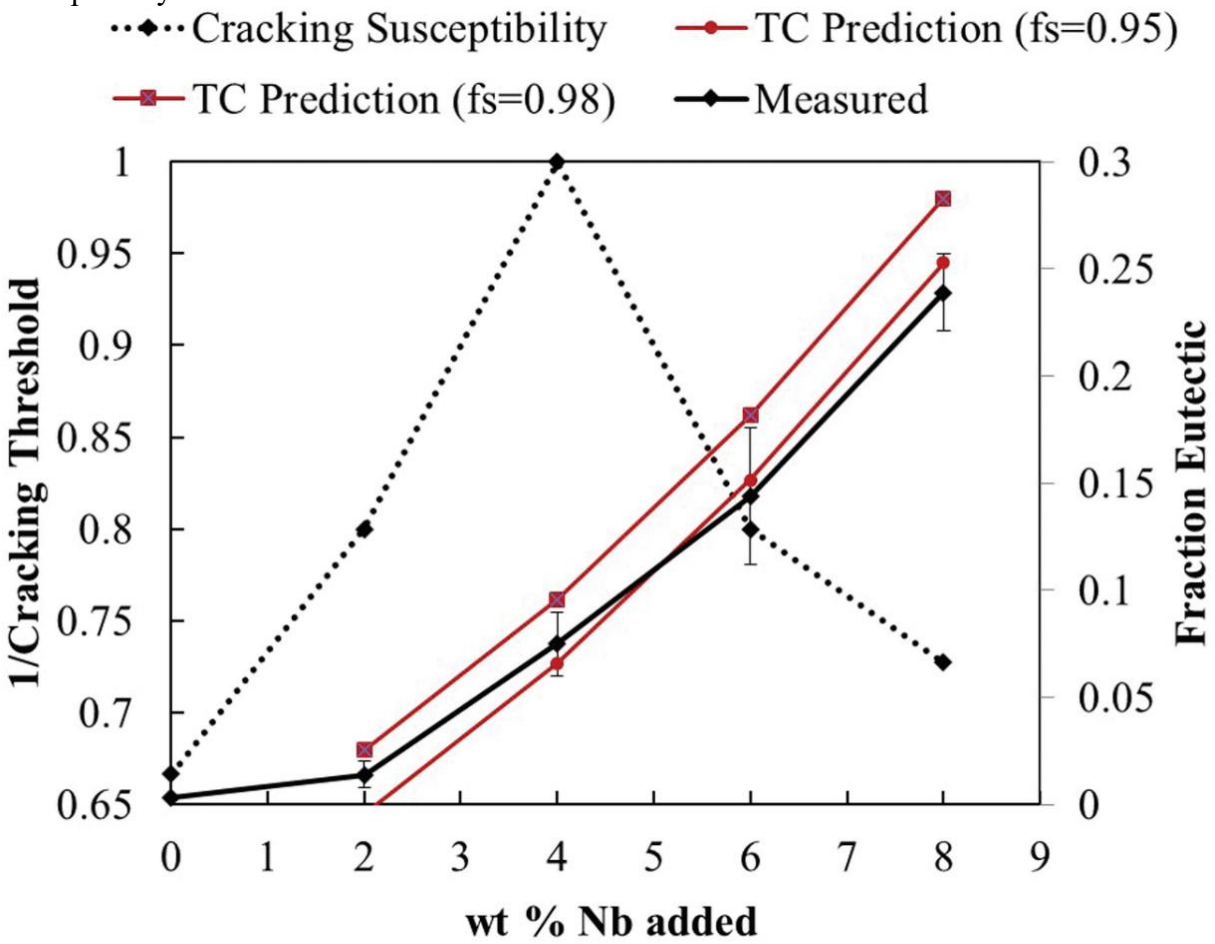

Source: Adapted from Wheeling and Lippold[75].

The characteristics of the liquid also have a significant influence on solidification cracking. The surface tension between the eutectic liquid film and solid phase is directly related to the wettability of the remaining liquid. According to Liu and Kou[77] when a liquid film has a high surface tension and consequently a low wettability, the grains establish bridging among them with the remaining liquid concentrated at triple points among the grains. The opposite condition causes the wetting of grain boundaries, which drastically reduces the resistance between grains. Figure 3-6 exhibits the effect of wettability of eutectic liquid for solidification cracking susceptibility.

Figure 3-6. The effect of eutectic liquid wettability in solidification cracking susceptibility. For a) a low wettability condition, the eutectic liquid concentrates in few regions, whereas for b) a high wettability condition, the eutectic liquid around the solidification grains, drastically reducing the mechanical resistance[77].

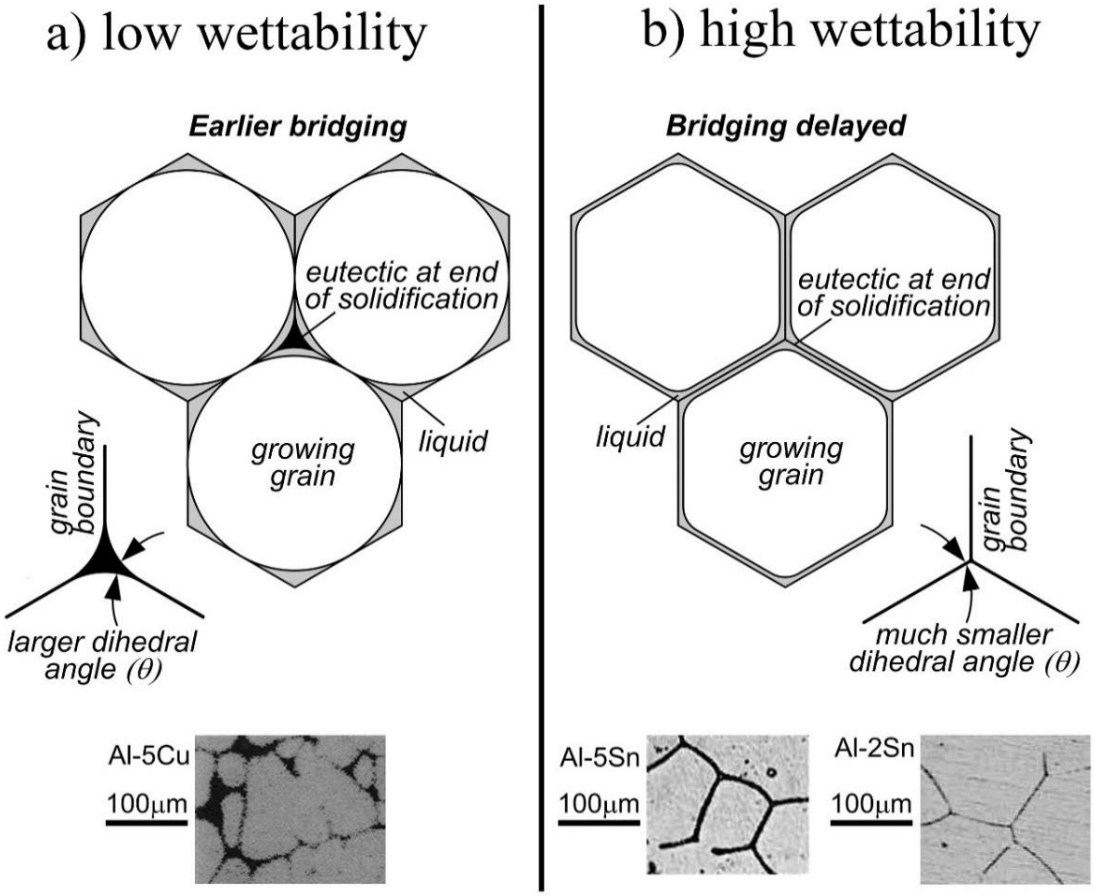

Source: Adapted from Liu and Kou[77].

3.1.2.2 Mechanical factor

The mechanical factor has a significant influence on the solidification-cracking phenomenon. The inherent stress that occurs during solidification is also responsible for the growth of the discontinuities or defects created by metallurgical factor described. The contraction due to the state transformation is commonly called shrinkage, especially in casting processes, where similar cracks occur and are called hot tears. The shrinkage is due, in part, to changes in the density of the liquid as cooling advances, but mainly by volume differences between the solid and liquid phases[78].

The stress due to the solid thermal contraction also has an important role in the mechanical factor. This physical feature is influenced by the crystal lattice of the material. In general, body centered cubic (BCC) materials have a linear expansion coefficient (α) lower than FCC materials. This partly explains why BCC materials have lower solidification cracking

susceptibility than FCC materials. Figure 3-7 shows the α coefficient of pure elements, which confirms this physical feature[79]. This phenomenon is evident for Fe allotropy, since γ-Fe-FCC shows a larger α coefficient compared to δ-Fe-FCC, although the latter only occurs at high temperatures. Furthermore, there is the strong variation of the α-Al coefficient as the temperature increases. This reinforces the important role of solid thermal contraction, since Al alloys are known for their high susceptibility to solidification cracking.

Figure 3-7. The linear expansion coefficient (α) for pure elements are divided by a) BCC and b) FCC[79].

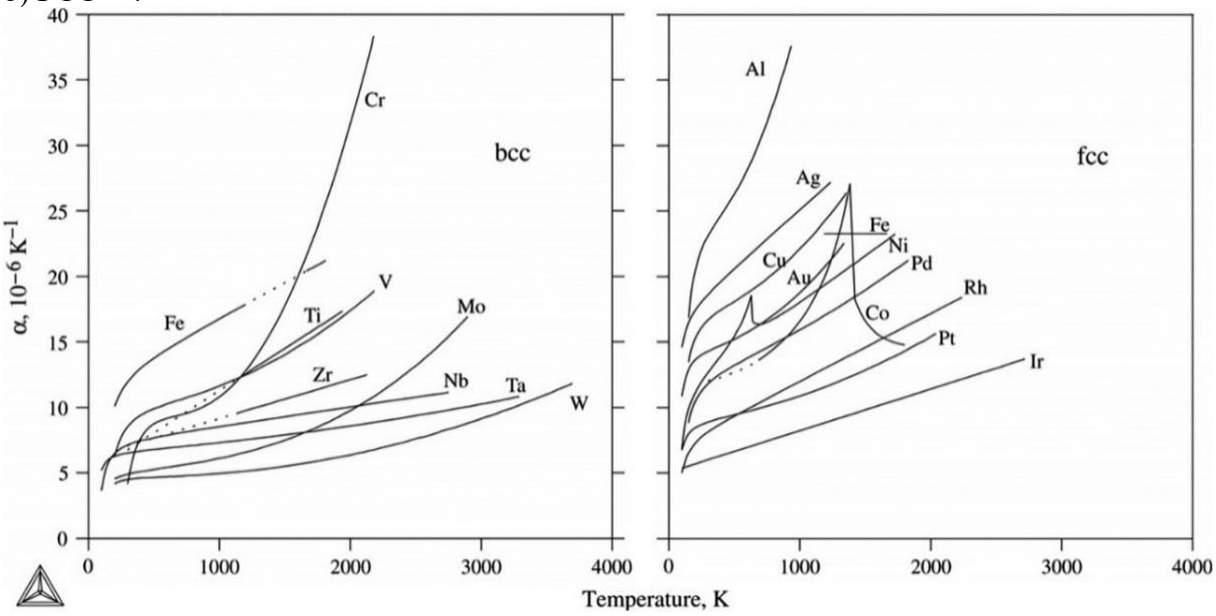

Source: Adapted from Lu *et al.*[79].

As a metallurgical and mechanical factor, restraints have a fundamental role in the evolution of solidification cracks. Normally, a high restraint level prevents material strain, which causes the growth of defects that evolve into cracks. The fishbone test developed by Houldcroft[80] makes the effect of the restraint level in solidification cracking clear. The test evaluates the solidification cracking susceptibility of weld beads deposited on sheet with different restraint levels provided by different groove sizes that allow the strain to dissipate during welding.

3.1.2.3 Welding parameters

The welding parameters have a strong influence on the metallurgical phenomena described. The welding heat input (HI_w) affects the cooling rate and consequently

microsegregation and back-filling. A high HI_w reduces the cooling rate, causing the rejection of elements by the solid phase during solidification. This increase in microsegregation causes an increase of the eutectic fraction, which in turn, increases the back-filling effect. Moreover, back-filling is also favored by an increase of time made available to fill the cracks. On the other hand, microsegregation and back-filling are reduced by a fast cooling rate due to a low HI_w.

The oscillation or weaving of arc welding causes the deflection of the grain growth direction. This prevents the concentration of segregated elements in a few grain boundaries. This distribution of the remaining liquid prevents the formation of large solidification cracks, especially along the centerline of the weld bead. This can also cause the distribution of heat, thus increasing the cooling rate. As discussed previously, fast cooling reduces microsegregation.

Another important welding parameter is related to the weld bead geometry. Single weld beads with low depth-to-width (D/W) ratios have a lower solidification cracking susceptibility compared to high D/W ratios[4,81,82]. This is because a low D/W ratio prevents columnar grains meeting at the center of the weld[18], and thus provides the distribution of the segregated alloying elements along the solidification grain boundaries and not at the weld centerline.

3.1.3 Final considerations

The Ni-based alloys represent a universe of different alloys for a wide range of applications. To select a candidate for the present study is not an easy task. The review was focused on solid solution alloys, since other families of Ni-based alloys have particularities that hinder or invalidate the project from a technical and/or economical point of view. Thus, several high corrosion and oxidization resistant alloys were presented, demonstrating their principal metallurgical aspects. Therefore, based on this the candidate alloys chosen were the 625, 686, C-276, 22, 59, 617 and 680 alloys.

A low alloy steel was selected to make up the major part of the girth welding proposed based on a yield strength that was sufficient to overmatch not only API 5L X65 steel but also the API 5L X70 and X80 steels. Thus, based on the AWS A5.28/A5.28M standard[82] the AWS ER 100S-G steel was chosen.

In order for the study to obtain the most adequate welding procedures for the girth welding proposed all the pre-selected alloys were assessed by thermodynamic simulation.

REFERENCES

1 SIMS, C. T.; STOLOFF, N. S.; HAGEL, W. C. **Superalloys II: high-temperature materials for aerospace and industrial power**. 2nd ed. New York: John Wiley & Sons Inc., 1987.

2 PEREPEZKO, J. H. The Hotter the Engine, the Better. **Science**, New York, v. 326, n. 5956, p. 1068-1069, nov. 2009.

3 POLLOCK, T. M.; TIN, S. Nickel-based superalloys for advanced turbine engines: Chemistry, microstructure, and properties. **Journal of Propulsion and Power**, v. 22, n. 2, p. 361-374, 2006.

4 DUPONT, J. N.; LIPPOLD, J. C.; KISER, S. D. **Welding metallurgy and weldability of nickel-base alloys**. Hoboken, New Jersey: John Wiley & Sons Inc., 2009.

5 REED, R. C. **The Superalloys: fundamentals and applications**. New York: Cambridge University Press, 2008.

6 GEDDES, B.; LEON, H.; HUANG, X. **Superalloys: alloying and performance**. Ohio: ASM International, 2010.

7 LU, K.; LU, L.; SURESH, S. Strengthening Materials by Engineering Coherent Internal Boundaries at the Nanoscale. **Science**, v. 324, n. 5925, p. 349-352, apr. 2009.

8 ASKELAND, D. R.; FULAY, P. P.; WRIGHT, W. J. **The science and engineering of materials**. 6. ed. Stamford: Cengage Learning, 2011.

9 DONACHIE, M. J.; DONACHIE, S. J. **Superalloys: a technical Guide**. 2nd ed. Ohio: ASM International, 2002.

10 HULL, D.; BACON, D. J. **Introduction to dislocations**. 5th ed. Kidlington: Elsevier, 2011.

11 DURAND-CHARRE, M. **The microstructure of superalloys**. Boca Raton: CRC Press, 1998.

12 HODGE, F. G. The history of solid-solution-strengthened Ni alloys for aqueous corrosion service. **JOM**, v. 58, n. 9, p. 28-31, 2006.

13 AGARWAL, D. C.; HERDA, W. R. The “C” family of Ni-Cr-Mo alloys’ partnership with the chemical process industry: the last 70 years. **Materials and Corrosion**, v. 48, n. 8, p. 542–548, 1 ago. 1997.

14 GEROLD, V. Precipitation hardening. *In*: NABARRO, F. R. N. **Dislocations in solids**. New York: North-Holland, 1979. v. 4, p. 222.

15 SUN, F. *et al*. Dislocation motion in a NI-Fe-based superalloy during creep–rupture beyond 700°C. **Materials Letters**, v. 159, p. 241-244, 2015.

16 GLEITER, H.; HORNBOGEN, E. Beobachtung der wechselwirkung von versetzungen mit kohärenten geordneten Zonen (II). **Physica Status Solidi (b)**, v. 12, n. 1, p. 251-264, jan. 1965.

17 PORTER, D. A.; EASTERLING, K. E.; SHERIF, M. **Phase Transformations in Metals and Alloys**. 3rd ed. Boca Raton: CRC Press, feb. 2009.

18 KOU, S. **Welding Metallurgy**. 2nd ed. Hoboken, New Jersey: John Wiley & Sons, Inc., 2003.

19 ALORAIER, A. *et al*. Weld repair practices without post weld heat treatment for ferritic alloys and their consequences on residual stresses: A review. **International Journal of Pressure Vessels and Piping**, v. 87, n. 4, p. 127-133, 2010.

20 SHAO, Y. *et al*. Formation mechanism and control methods of acicular ferrite in HSLA steels: A review. **Journal of Materials Science & Technology**, v. 34, n. 5, p. 737-744, 2018.

21 ZHU, Z. *et al*. The effect of chemical composition on microstructure and properties of intercritically reheated coarse-grained heat-affected zone in X70 steels. **Metallurgical and Materials Transactions B**, v. 45, n. 1, p. 229–235, 2014.

22 LALAM, S. V. *et al*. Continuous drive friction welding of Inconel 718 and EN24 dissimilar metal combination. **Materials Science and Technology**, v. 25, n. 7, p. 851-861, jul. 2009.

23 NGANBE, M.; HEILMAIER, M. Creep behavior and damage of Ni-base superalloys PM 1000 and PM 3030. **Metallurgical and Materials Transactions A**, v. 40, n. 12, p. 2971, 2009.

24 MURTY, K. L.; CHARIT, I. Structural materials for Gen-IV nuclear reactors: challenges and opportunities. **Journal of Nuclear Materials**, v. 383, n. 1, p. 189-195, 2008.

25 XU, Y. *et al*. Fabrication and characterization of ODS austenitic steels. **Journal of Nuclear Materials**, v. 417, n. 1, p. 283-285, 2011.

26 KIM, D. W. Influence of nitrogen-induced grain refinement on mechanical properties of nitrogen alloyed type 316LN stainless steel. **Journal of Nuclear Materials**, v. 420, n. 1, p. 473-478, 2012.

27 EISELSTEIN, H. L.; TILLACK, D. J. The invention and definition of alloy 625. **Superalloys**, v. 718, n. 625, p. 1-14, 1991.

28 RUTHER, W. E.; GREENBERG, S. Corrosion of steels and nickel alloys in superheated steam. **Journal of the Electrochemical Society**, v. 111, n. 10, p. 1116-1121, 1964.

29 CIESLAK, M. J. *et al*. A melting and solidification study of alloy 625. **Metallurgical Transactions A**, v. 19, n. 9, p. 2319-2331, 1988.

30 CIESLAK, M. J.; HEADLEY, T. J.; FRANK, R. B. Welding metallurgy of custom age 625 PLUS alloy. **Welding Journal (Miami, Fla)**, v. 68, n. 12, p. 473s-482s, 1989.

31 DUPONT, J. N. Solidification of an alloy 625 weld overlay. **Metallurgical and Materials Transactions A**, v. 27, n. 11, p. 3612-3620, nov. 1996.

32 SILVA, C. C. *et al*. New insight on the solidification path of an alloy 625 weld overlay. **Journal of Materials Research and Technology**, v. 2, n. 3, p. 228-237, 2013.

33 SILVA, C. C. *et al*. Mechanical properties and microstructural characterization of aged nickel-based Alloy 625 weld metal. **Metallurgical and Materials Transactions A: Physical Metallurgy and Materials Science**, v. 49, n. 5, p. 1653-1673, may. 2018.

34 MURR, L. E. *et al*. Metal fabrication by additive manufacturing using laser and electron beam melting technologies. **Journal of Materials Science and Technology**, v. 28, n. 1, p. 1-14, 2012.

35 SONG, K. H.; NAKATA, K. Effect of precipitation on post-heat-treated Inconel 625 alloy after friction stir welding. **Materials and Design**, v. 31, n. 6, p. 2942-2947, 2010.

36 SONG, K. H.; NAKATA, K. Mechanical properties of friction-stir-welded inconel 625 alloy. **Materials Transactions**, v. 50, n. 10, p. 2498-2501, 2009.

37 LEONARD, R. B. Thermal stability of Hastelloy Alloy C-276. **Corrosion**, v. 25, n. 5, p. 222–232, 1 maio 1969.

38 SRIKANTH, A.; MANIKANDAN, M. Development of welding technique to avoid the sensitization in the Alloy 600 by conventional gas tungsten arc welding method. **Journal of Manufacturing Processes**, v. 30, p. 452-466, 2017.

39 CIESLAK, M. J.; HEADLEY, T. J.; ROMIG, A. D. The welding metallurgy of HASTELLOY alloys C-4, C-22, and C-276. **Metallurgical Transactions A**, v. 17, n. 11, p. 2035-2047, nov. 1986.

40 MISHRA, A. K.; SHOESMITH, D. W. Effect of alloying elements on crevice corrosion inhibition of nickel-chromium-molybdenum-tungsten alloys under aggressive conditions: an electrochemical study. **Corrosion**, v. 70, n. 7, p. 721-730, fev. 2014.

41 LLOYD, A. C. *et al*. Cr, Mo and W alloying additions in Ni and their effect on passivity. **Electrochimica Acta**, v. 49, n. 17, p. 3015-3027, 2004.

42 LUTTON CWALINA, K. *et al*. Revisiting the effects of molybdenum and tungsten alloying on corrosion behavior of nickel-chromium alloys in aqueous corrosion. **Current Opinion in Solid State and Materials Science**, v. 23, n. 3, p. 129-141, 2019.

43 HODGE, F. G.; KIRCHNER, R. W. Improved Ni-Cr-Mo alloy for corrosion service. **Corrosion**, v. 32, n. 8, p. 332-336, 1976.

44 YVON, P.; CARRÉ, F. Structural materials challenges for advanced reactor systems. **Journal of Nuclear Materials**, v. 385, n. 2, p. 217-222, 2009.

45 MANKINS, W. L.; HOSIER, J. C.; BASSFORD, T. H. Microstructure and phase stability of INCONEL alloy 617. **Metallurgical Transactions**, v. 5, n. 12, p. 2579-2590, 1974.

46 OLSON, L. C. *et al*. Materials corrosion in molten LiF-NaF-KF salt. **Journal of Fluorine Chemistry**, v. 130, n. 1, p. 67-73, 2009.

47 TAN, L. *et al*. Corrosion behavior of Ni-base alloys for advanced high temperature water-cooled nuclear plants. **Corrosion Science**, v. 50, n. 11, p. 3056-3062, 2008.

48 FINK, C.; ZINKE, M.; KEIL, D. Evaluation of hot cracking susceptibility of nickel-based alloys by the PVR test. **Welding in the World**, v. 56, n. 7, p. 37-43, 2012.

49 MANNING, P. E.; SCHOEBEL, J.-D. HASTELLOY Alloy C-22 - a new and versatile material for the chemical process industries. **Werkstoffe und Korrosion**, v. 37, n. 3, p. 137-145, 1986.

50 SRIDHAR, N.; WU, J. B. C.; MANNING, P. E. Corrosion Resistant Ni-Cr-Mo Alloys. **JOM**, v. 37, n. 11, p. 51-53, 1985.

51 MORINAGA, M. *et al*. New PHACOMP and its application to alloy design. *In*: SUPERALLOYS, 4., 1984, Seven Springs. **Proceedings**. Englewood: Metallurgical Society of AIME, 1984. p. 523-532.

52 LUO, H. *et al*. Characterization of electrochemical and passive behaviour of Alloy 59 in acid solution. **Electrochimica Acta**, v. 135, p. 412-419, 2014.

53 TURCHI, P. E. A.; KAUFMAN, L.; LIU, Z. K. Modeling of Ni-Cr-Mo based alloys: part I-phase stability. **Calphad**, v. 30, n. 1, p. 70-87, 2006.

54 SCHEIL, E. No Title. **Z. Metallkd.**, v. 34, p. 70-72, 1942.

55 GULLIVER, G. H. The quantitative effect of rapid cooling upon the constitution of binary alloys. **J. Inst. Met**, v. 9, n. 1, p. 120-157, 1913.

56 MINÁ, E. M. *et al*. Effect of dilution on the microstructure of AWS ERNiCrMo-14 alloy in overlay welding by the TIG process with cold wire feed. **Welding International**, v. 32, n. 2, p. 130-138, 2018.

57 MALTIN, C. A.; GALLOWAY, A. M.; MWEEMBA, M. Microstructural evolution of Inconel 625 and Inconel 686CPT weld metal for clad carbon steel linepipe joints: a comparator study. **Metallurgical and Materials Transactions A**, v. 45, n. 8, p. 3519-3532, jul. 2014.

58 MINÁ, É. M. *et al*. Efeito da diluição sobre a microestrutura da liga AWS ERNiCrMo-14 na soldagem de revestimentos pelo processo TIG com alimentação de arame frio. **Soldagem & Inspeção**, v. 21, n. 3, p. 317-329, 2016.

59 ARULMURUGAN, B.; MANIKANDAN, M. Development of welding technology for improving the metallurgical and mechanical properties of 21st century nickel based superalloy 686. **Materials Science and Engineering: A**, v. 691, p. 126-140, 2017.

60 MINÁ, É. M. *et al*. Electron detection modes comparison for quantification of secondary phases of Inconel 686 weld metal. **Materials Characterization**, v. 133, p. 10-16, nov. 2017.

61 MINÁ, É. M. *et al*. The effect of dilution on microsegregation in AWS ER NiCrMo-14 alloy welding claddings. **Metallurgical and Materials Transactions A: Physical Metallurgy and Materials Science**, v. 47, n. 12, 2016.

62 SILVA, C. C. *et al*. Assessment of microstructure of alloy Inconel 686 dissimilar weld claddings. **Journal of Alloys and Compounds**, v. 684, p. 628-642, 2016.

63 PERRICONE, M. J.; DUPONT, J. N.; CIESLAK, M. J. Solidification of hastelloy alloys: an alternative interpretation. **Metallurgical and Materials Transactions A**, v. 34, n. 5, p. 1127-1132, 2003.

64 PAN, Y.-M.; DUNN, D. S.; CRAGNOLINO, G. A. Topologically close-packed phase precipitation and thermal stability in alloy 22. **Metallurgical and Materials Transactions A**, v. 36, n. 5, p. 1143-1151, 2005.

65 KISER, S. D.; GOLLIHUE, R. D.; MANNAN, S. K. **High strength ni-cr-mo-w-nb-ti welding product and method of welding and weld deposit using the same**, EP3126090A1, 4 apr. 2014, 8 feb. 2017.

66 IANNUZZI, M.; BARNOUSH, A.; JOHNSEN, R. Materials and corrosion trends in offshore and subsea oil and gas production. **npj Materials Degradation**, v. 1, n. 1, p. 2, 2017.

67 MANNAN, S. *et al*. A new nickel alloy filler metal designed for welding high strength ID-clad steels. *In*: THE EUROPEAN CORROSION CONGRESS. 2016, Montpellier. **Anais...** Frankfurt: Eurocorr, 2016, v. 2, p. 1114-1129.

68 SILVA, R. DE S. **Alternative nickel alloy study on the union of internally-coated API 5L X65 tubes with Inconel 625**. Dissertação, Mestrado em Engenharia e Ciência de Materiais – Departamento de Engearia e Metalúrgica e de Materiais, Universidade Federal do Ceará, Fortaleza, 2018.

69 CROSS, C. E. On the origin of weld solidification cracking. *In*: BÖLLINGHAUS, T.; HEROLD, H. **Hot Cracking Phenomena in Welds**. Heidelberg: Springer Berlin Heidelberg, 2005. p. 3-18.

70 MATCALC ENGINEERING. MatCalc User Manual. Vienna: MatCalc, 2019.

71 BRODY, H. D.; FLEMINGS, M. C. **Transactions TMS-AIME**, v. 236, p. 615, 1966.

72 CLYNE, T. W.; KURZ, W. Solute redistribution during solidification with rapid solid state diffusion. **Metallurgical Transactions A**, v. 12, n. 6, p. 965-971, 1981.

73 LUNDIN, C.; QIAO, C.; LEE, C. Evaluation of backfilled solidification cracks in austenitic stainless welds in relationship to evaluation of hot cracking. **Welding Journal**, v. 72, p. 321-328, jan. 1993.

74 LIPPOLD, J. C. *et al*. Weld solidification cracking in solid-solution strengthened ni-base filler metals BT. *In*: BÖLLINGHAUS, T. *et al*. **Hot Cracking Phenomena in Welds II**. Heidelberg: Springer Berlin Heidelberg, 2008. p. 147-170.

75 WHEELING, R. A.; LIPPOLD, J. C. Solidification cracking susceptibility of Ni-30Cr weld metals with variable niobium and molybdenum. **Welding Journal**, v. 95, n. 7, p. 229S-238S, 2016.

76 ALEXANDROV, B. T.; LIPPOLD, J. C. Use of the cast pin tear test to study solidification cracking. **Welding in the World**, v. 57, n. 5, p. 635-648, 2013.

77 LIU, J.; KOU, S. Crack susceptibility of binary aluminum alloys during solidification. **Acta Materialia**, v. 110, p. 84-94, 2016.

78 ESKINE, D.; ZUIDEMA, J.; KATGERMAN, L. Linear solidification contraction of binary and commercial aluminium alloys. **International Journal of Cast Metals Research**, v. 14, n. 4, p. 217-223, jan. 2002.

79 LU, X.-G.; SELLEBY, M.; SUNDMAN, B. Assessments of molar volume and thermal expansion for selected BCC, FCC and HCP metallic elements. **Calphad**, v. 29, n. 1, p. 68-89, 2005.

80 HOULDCROFT, P. T. A simple cracking test for use with argon-arc welding. **British Welding Journal**, v. 2, n. 10, p. 471-475, 1955.

81 LIPPOLD, J. C. Centerline cracking in deep penetration electron beam welds in type 304L stainless steel. **Welding Journal (Miami, Fla)**, v. 64, n. 5, p. 127-136s, 1985.

82 SUN, Y. *et al*. Characterization and formation mechanism of periodic solidification defects in deep-penetration laser welding of NiCrMoV steel with heavy section. **The International Journal of Advanced Manufacturing Technology**, v. 100, n. 9, p. 2857–2866, 2019.

83 AMERICAN WELDING SOCIETY. AWS A5.28/A5.28M: **Specification for Low-Alloy Steel Electrodes and Rods for Gas Shielded Arc Welding**. Miami. p. 40. 2015.

Chapter 4

Thermodynamic simulation of dissimilar joint weld solidification of API 5L X65 steel pipe using Ni-based alloys

4.1 Abstract

Dissimilar welding is an important manufacturing technique from the economic and technological point of view. This technique enables the production of complex components by welding and/or cladding of dissimilar materials. Using this technique Ni-based alloys can be combined with structural steel providing a great number of applications in oil & gas industries. Nonetheless, there are numerous problems relating to the solidification of Ni-based alloys. The aim of the present study is to understand the solidification process of Ni-based alloys for several dilution levels with the API 5L X65 steel pipe through thermodynamic simulation. The JMatPro® software performed solidification simulations based on the classical solidification model of Scheil-Gulliver. The alloys selected were 625, 686, C-276, 22, 59, 617 and 680, from the classes Ni-Cr-Mo, Ni-Cr-Co-Mo and Ni-Cr-Mo-W-Nb-Ti. The alloys 625 and 680, which contain Nb, showed a solidification temperature range (ΔT) superior to 200°C. The solidification range of these alloys was more strongly influenced by the increase of the iron content than the other alloys. The alloys C-276 and 617 demonstrated an intermediate solidification temperature range in comparison with the other alloys evaluated. The alloys 686, 22 and 59 showed the best results even with an increase in the dilution levels.

4.2 Introduction

Dissimilar welding, which represents a versatile manufacturing process, makes the joining and/or cladding of different classes of materials possible and gives equipment and/or components specific properties depending on the alloys selected[1–4]. Thus internal claddings for risers, valves, pressure vessels and other complex components can be manufactured for the naval, nuclear, chemical, oil and gas industries, among others[5–8].

In the oil & gas industry the use of Ni-based alloys as the filler metal for joints and claddings of high strength low alloy steel pipes is common[9,10]. This special class of materials have been used in girth welding of steel pipes due to its excellent mechanical properties,

allowing an overmatch the mechanical properties of steel pipes commonly used on oil and gas industries[9,11,12]. In addition, Ni-based alloys are frequently used as corrosion resistance alloy (CRA) for cladding of risers due to its great oxidization and corrosion resistance in widely corrosive environments[8,13–15].

Even with the economic and technological advantages provided by dissimilar welding using Ni-based alloys, the metallurgical aspects of the welding is a critical point of this technique[10]. The result of mixing two different material classes is of great importance as deleterious phases may be formed, which makes the application of the technique unviable[16]. Thus, it is necessary to understand the metallurgical aspects of the mixture of the selected alloys such as, the crystalline structure of the mixture, the possible phases in equilibrium, the mechanical properties, and others[16,17]. All these characteristics must be clearly understood so that the dissimilar welding technique is successful for each application.

One of main metallurgical difficulties related to the use of these Ni-based alloys is the susceptibility to solidification cracking. These cracks most commonly occur during solidification, and are normally the consequences of the nucleation of low melting point phases[18–20]. Various studies have pointed out that the main cause for the formation of these phases is related to the presence of Nb, Si, Fe and C; because some of these elements are strongly segregated during solidification[18]. The high concentration of these elements in the remaining liquid makes the nucleation of secondary phases at the final stage of solidification thermodynamically favorable. Therefore, the chemical composition of the fusion zone, which is a consequence of dilution among the selected alloys for dissimilar welding, is directly related to solidification cracking. According to Kou[21], the metallurgical factors that have been frequently point out as the most responsible to affect the solidification cracking susceptibility of weld metals are: solidification temperature range, the fraction and distribution of liquid metal at the final stage of solidification, the primary solidification phase, the surface tension and consequently the wetting of liquid metal on solidification grain boundary and, the grain structure. The chemical composition of weld metal affect directly or indirectly all metallurgical factors above mentioned, being especially critical for solidification temperature range and the reminiscent liquid, which are affected by microsegregation of alloying elements during solidification[21]. In this context, thermodynamic simulation represents a powerful tool in materials selection field, which allows the prediction of several physical and chemical properties of these materials, without the need to perform experiments, requiring time and expenses with valuable materials, especially in the case of Ni-based alloys[22,23]. Thermodynamic simulations can provide intrinsic features of these materials such as their

solidification range, phases in equilibrium, thermal and electrical properties, among others[22]. Thus, with such a set of known properties the most suitable alloys can be selected for the project in hand, and thus avoid any possible metallurgical problems.

In order to propose new solutions to girth welding problems related to dissimilar welding of steel pipes in the oil & gas industry, the present study simulated the solidification of Ni-based alloys from the classes Ni-Cr-Mo, Ni-Cr-Co-Mo and Ni-Cr-Mo-W-Nb-Ti, in order to evaluate the susceptibility to solidification cracking. Thus, the solidification of the alloys 625, 686, C-276, 22, 59, 617 and 680 were simulated under various conditions by varying the dilution levels with API 5L X65 steel pipe.

4.3 Experimental procedure

The present study was carried out to select alloys to execute the welding joints of API 5L X65 steel pipes. Several solidification simulations were performed to evaluate the mixture of Ni-based alloy with API 5L X65 steel pipe. The nickel alloy will dilute with the steel pipe, promoting an increase of iron in the pass weld bead, while the other alloying elements such as Ni, Cr and Mo will be reduced. In practice, the root pass (1st pass) has dilution bigger than other passes. As the other passes are deposited, the percentual fraction of steel pipe on pass decreases, reducing the dilution level. Figure 4-1 shows the schematic of the joint welding.

Figure 4-1. Schematic of the joint welding.

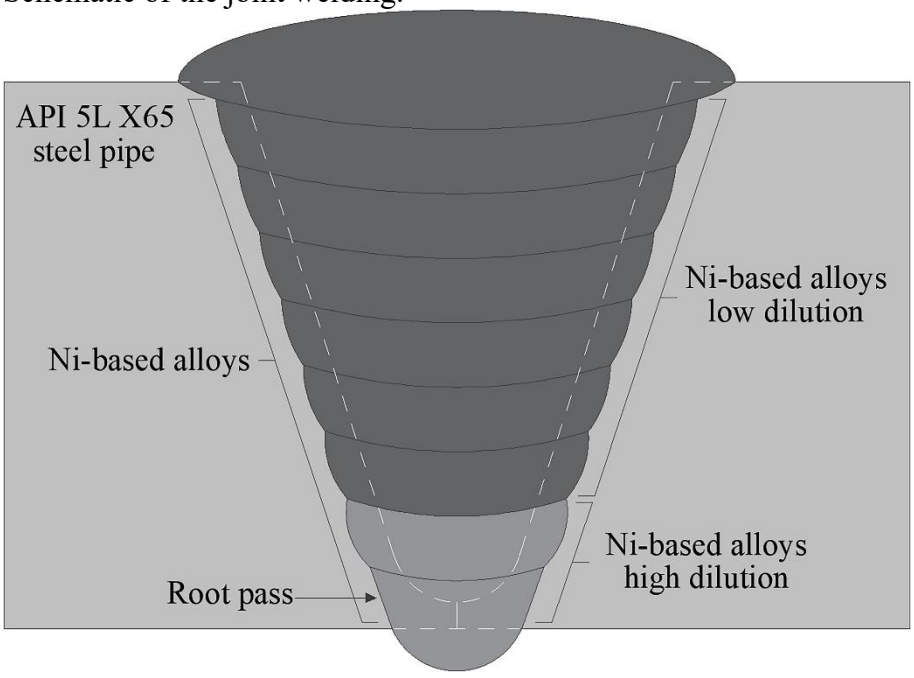

Source: Developed by the author.

The Ni-based alloys 625, 686, C-276, 22 and 59 were selected to simulate the joint. These alloys belong to the Ni-Cr-Mo class, which have great corrosion resistance under various corrosive environments. Two other alloys (617 and 680) were also chosen as they belong to the family of Ni-based alloys strengthened through precipitation hardening and solid solution and have excellent resistance to a wide range of corrosive environments similar to the Ni-Cr-Mo alloys. Among the alloys chosen, the new alloy named 680 is considered the alloy with the most complex composition, as it contains significant amounts of the alloying elements such as Cr, Mo, W, Nb and Ti. Table 4-1 shows the chemical composition of all the alloys used in this study. The composition of each wire filler metal was obtained from claddings produced according to the AWS A5.34 standard. Optical emission spectroscopy measurements were carried out on the claddings, in order to obtain the chemical composition of welded materials. Only the composition of alloys C-276 and 617 were obtained from results reported in the literature[24,25].

Table 4-1. Chemical composition of alloys used in the study.

Chemical composition of alloys								
	API 5L X65 steel pipe	Alloy 625 (AWS ER NiCrMo-3)	Alloy 686 (AWS ER NiCrMo-14)	Alloy C-276 (AWS ER NiCrMo-4)	Alloy 22 (AWS ER NiCrMo-10)	Alloy 59 (AWS ER NiCrMo-13)	Alloy 617 (AWS ER NiCrCoMo-1)	Alloy 680 (AWS ER NiCrMoWNbTi-1)
Al	0.04	-	-	-	-	-	1.25	-
C	0.11	0.1	0.01	0.20	0.015	0.01	0.06	0.05
Co	-	0.06	0.05	0.12	0.25	0.03	12.45	-
Cr	0.12	21.67	20.66	15.50	21.05	22.78	21.80	19.94
Cu	0.18	-	-	0.35	-	0.05	-	-
Fe	97.51	0.09	0.38	6.50	4.96	0.77	0.75	0.55
Hf	-	0.01	-	-	0.01	-	-	-
Mn	1.17	-	0.24	0.85	0.12	0.23	-	-
Mo	0.14	8.81	16.4	15.20	13.15	15.4	9.05	6.32
Nb	0.03	3.73	-	-	-	0.06	-	3.58
Ni	0.34	65.22	58.07	58.00	57.35	60.42	54.28	61.20
P	0.012	0.02	0.02	-	0.02	0.015	-	-
Re	-	-	0.05	-	0.06	-	-	-
S	0.004	0.015	0.02	-	0.01	0.005	-	-
Si	0.28	-	-	0.05	-	-	0.11	-
Ta	-	0.02	-	-	0.06	0.01	-	-
Ti	-	0.17	0.06	-	-	-	0.25	1.46
V	0.06	0.05	0.05	0.13	0.03	0.15	0.06	0.04
W	-	-	3.98	3.10	2.97	-	-	6.91
Zn	-	0.05	0.06	-	-	0.07	-	-

Source: Developed by the author.

Seven dilution levels: 5%, 10%, 15%, 20%, 30%, 40% and 50% were simulated for both the root and filling passes. The dilution level is the ration of the amount of base metal melted to the total amount of weld metal (fusion zone). Thereby, a high dilution level such as 40%, means that a high portion of base metal is part of the chemical composition of the fusion zone. High dilution levels such as 40% and 50% are uncommon in practice, but they are

theoretically important to understand the tendency of metallurgical phenomena. Equation 1 describes the dilution, *D*, as a function of the chemical composition of the fusion zone (C_{FZ}), base metal (C_{BM}) and filler metal (C_{FM}). Thus, it is possible estimate the chemical composition of the fusion zone for each dilution level.

$$C_{FZ} = D(C_{BM} - C_{FM}) + C_{FM} \quad (1)$$

All the thermodynamic simulation results were based on the classical solidification model of Scheil-Gulliver, and performed using the commercial software JMatPro®. The Scheil-Gulliver model does not consider the diffusion of elements in the solid phases. This mean that the model assumes a fast solidification and, consequently assumes a high segregation of elements during the solidification[26]. In addition, the model assumes the total mixture of elements in the liquid phase, and that in the solid/liquid interface all physical conditions necessary for equilibrium have been established[26]. Equation 2 shows the mathematical model proposed by Scheil-Gulliver, where C_s, f_s, C_o and k represent the chemical composition of the solid part, the fraction of solid, the nominal chemical composition of the alloy and the partition coefficient, respectively[26]. Another more complex model, which considers the diffusion in the solid, was proposed by Brody and Fleming[27]. However, in experimental studies performed by Dupont[20] and Miná[28], in which the microsegregation in welding of the 625 alloy and 686 alloy, respectively, were evaluated, the authors highlighted that for a high cooling rate, the diffusion of elements such as Cr, Mo, Nb, W, and others was practically zero. Therefore, the Scheil-Gulliver model represents an acceptable model with a good precision to describe the solidification of alloys for welding processes.

$$C_s = kC_0(1 - f_s)^{k-1} \quad (2)$$

Equation 2 can provide the partition coefficient k for all elements present in the alloy. Elements that have a $k>1$, have a tendency to be incorporated by the solid phase during the solidification[20,28–30]. Elements that have a $k<1$, have a tendency to be segregated by the solid phase, making the remaining liquid rich in the alloying elements[20,28–30]. When there is a local concentration of alloying elements in the liquid, a new phase different from matrix phase may nucleate at the final stage of solidification. In the case of Ni-based alloys, the nucleation of eutectic phases is common, and this normally increases susceptibility to solidification cracking due to the low melting point of these phases.

4.4 Results and Discussion

4.4.1 Solidification simulation of the Ni-based alloys

Figure 4-2 shows the simulation of the solidification based on the Scheil-Gulliver model for all Ni-based alloys. Each graph demonstrates the evolution of the solid fraction as a consequence of cooling, detailing the phase nucleation reactions during solidification. Naturally, all the Ni-based alloys showed the γ-FCC as the first and largest solidified phase. Although γ-FCC has a high capacity to solubilize alloying elements[31], the segregation of elements such as S, P, Si, Nb and Ti is often reported in the literature. This phenomenon is the main reason that Ni-based alloys are slightly more susceptible to solidification cracking than other alloys[21]. Several studies have pointed out that the segregation of these elements is responsible for the formation of many secondary phases such as MC, M_6C and $M_{23}C_6$ carbides, and topologically close-packed phases such as σ, δ, η, P and Laves phases[18–20,28–30,32]

In terms of carbides, the alloy 625 was the first to show carbides in equilibrium with γ phase during the solidification. This is probably due to the high carbon content in the alloy in comparison to the other alloys. The carbon showed a low solubility in this alloy due to its high affinity with the other alloying elements such as Cr and Mo, which favor the nucleation of carbides at high temperatures[33–35].

Figure 4-2 confirms that alloy 680 was the only alloy to show the Laves phase during the solidification process. The Laves phase is frequently reported in the literature as the main eutectic phase responsible for the formation of solidification cracks in Ni-based alloys[36]. The σ phase was also observed in all Ni-based alloys evaluated, since it is normally composed of the alloying elements commonly found in these alloys such as, Cr, Mo and Fe. According to a recent study, besides Cr, Mo also enhances the field stability of σ phase and the P phase[37]. In all cases, the nucleation of σ phase was observed in the final stage of solidification. The P phase, on the other hand, was only predicted in the 680, 686 and C-276 alloys. Possibly, the nucleation of the P phase was influenced by the high W content present in these alloys, which may reduce the solubility of the other elements by the γ matrix or by the simple segregation of W during solidification. A detailed study concerning the P phase in Ni-based alloys reported that elements such as Cr, Mo, W and Re were frequently observed in concentrations greater than the nominal chemical composition of the alloys evaluated[38,39]. Probably the approximate

3% of W present in alloy 22 was not enough to promote the nucleation of the P phase during the solidification, despite the similar chemical compositions of alloys 22 and 686.

Figure 4-2. Simulation of the solidification of the Ni-based alloys a) 625, b) 686, c) C-276, d) 22, e)59, f) 617 and g) 680.

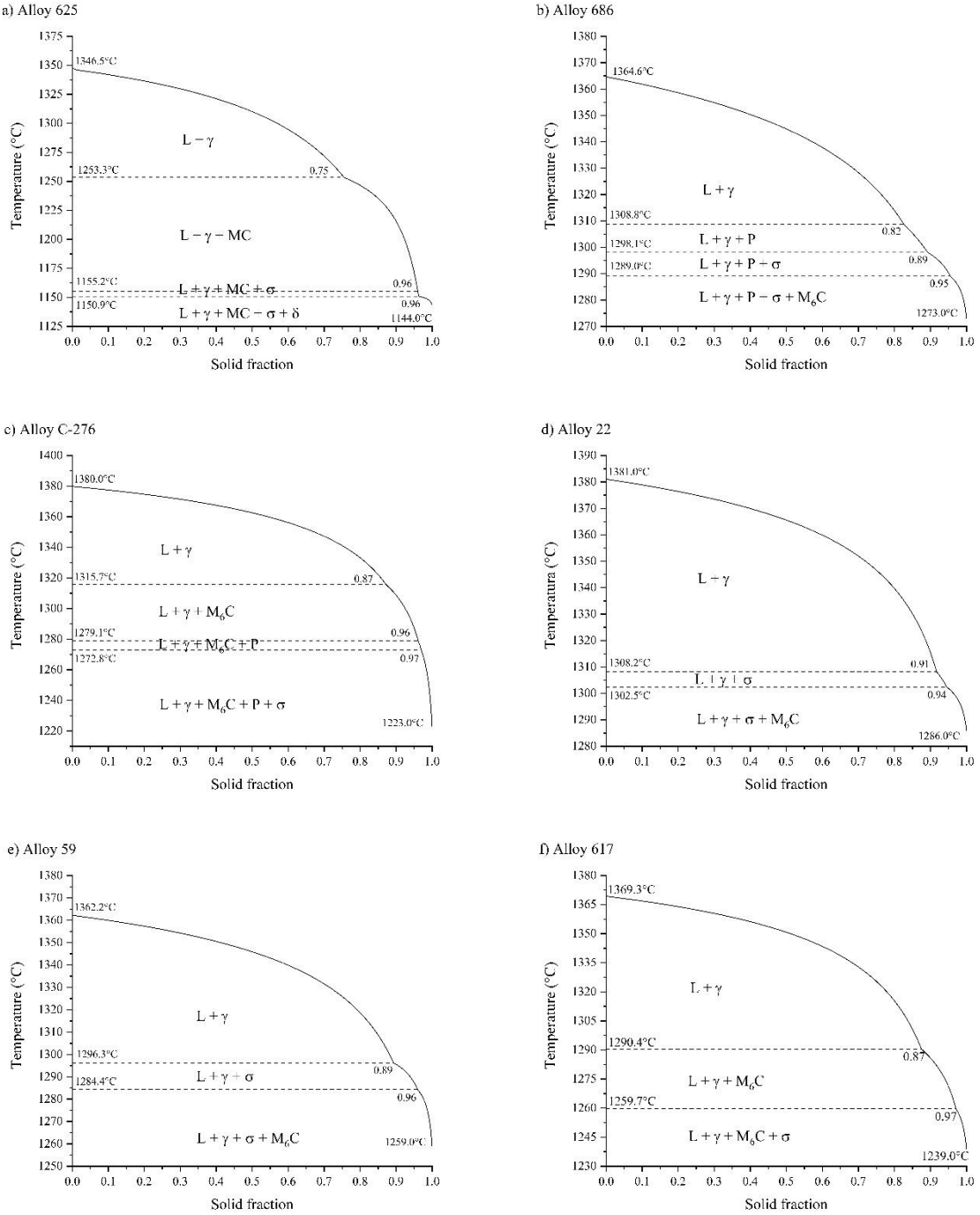

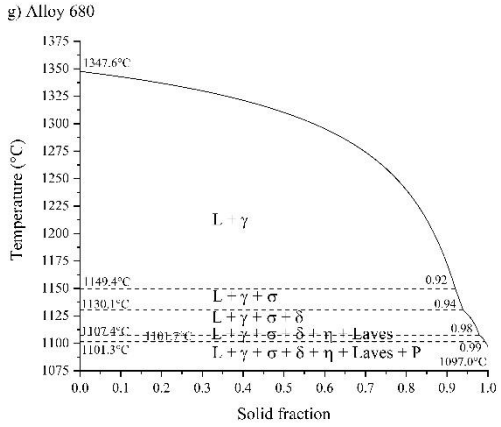

Source: Developed by the author.

Concerning the initial solidification temperatures (T_{Si}), the alloys assessed did not show any significant differences, and varied from 1,346°C to 1,381°C. The alloys 22 and C-276 had the highest T_{Si} values, which probably was influenced by the almost 5% iron content in these alloys, since the melting point of pure Fe is only slightly higher than pure Ni. The final solidification temperature (T_{Sf}) were on the other hand significantly different among the alloys evaluated. The alloys 625 and 680, which have a significant Nb content in the nominal chemical composition, demonstrated the lowest values, always less than 1150°C, while the other alloys gave values superior to 1223°C. Naturally, all these phenomena are reflected in the solidification temperature range (ΔT) of these alloys, making it possible to differentiate which alloy may show the highest susceptibility to solidification cracking, based on the ΔT estimated for each one. Figure 4-3 summarizes the ΔT of all Ni-based alloys simulated.

Among the alloys evaluated, alloy 680 had the highest solidification temperature range, approximately 250°C. Followed by alloy 625, which had a high ΔT of approximately 200°C. These results corroborate with simulation results reported by Hu *et al*.[15]. In terms of experimental results, Dupont[20] measured the solidification temperature range of alloy 625 using the differential thermal analysis (DTA) and obtained a result close to the simulated reported here, approximately 170°C. The alloys C-276 and 617 in turn, had intermediate values of ΔT, 130°C and 156°C respectively, while the alloys 686, 22 and 59 showed the best results, with ΔTs between 91°C and 103°C. Among all alloys evaluated, alloy 686 demonstrated the lowest solidification temperature range. Turchi *et al*.[40] simulated the solidification of several Ni-based alloys, including alloy 22, and obtained a result similar to the one presented in Figure 4-2. Cieslak *et al*.[19] using DTA presented a result similar to this study, approximately 105°C.

Figure 4-3. Solidification range of all Ni-based alloys 625, 686, C-276, 22, 59, 617 and 680.

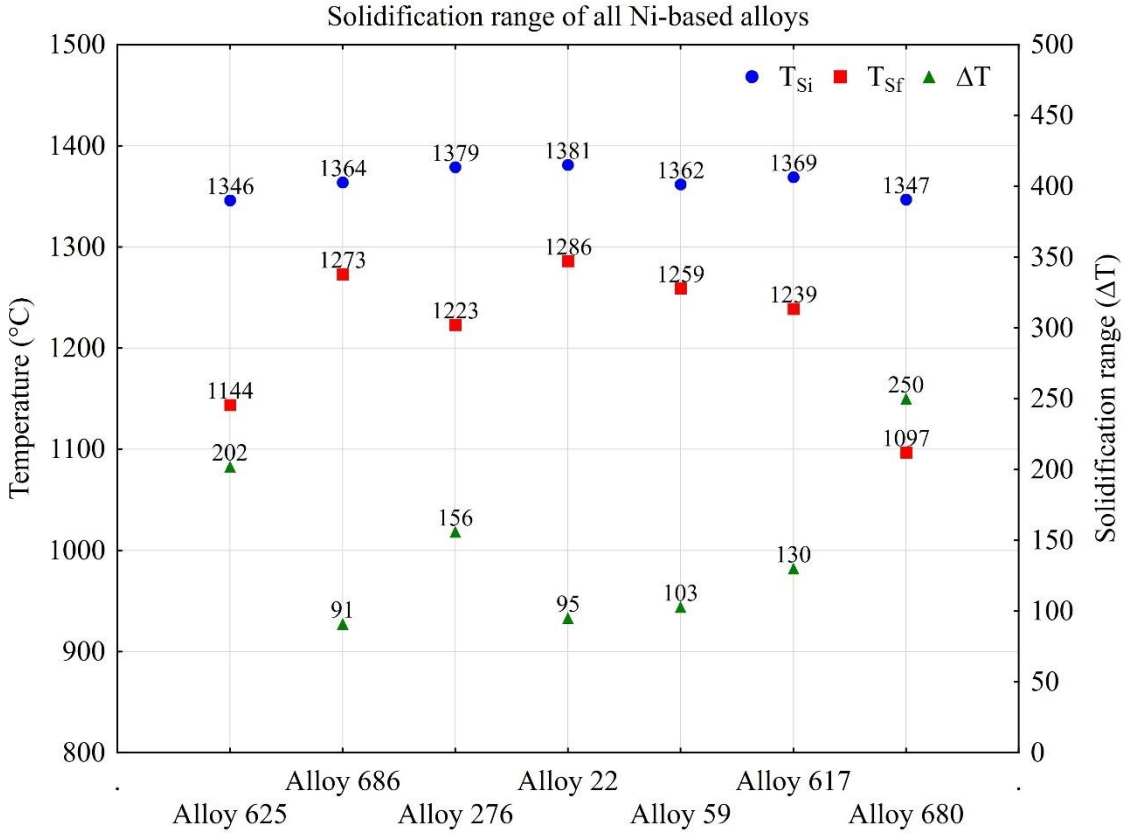

Source: Developed by the author.

Based on the simulated results shown here and confronted with the simulated and experimental results from the literature[9,19,34,35], alloy 680 will almost certainly follow the same tendency as alloy 625, with ΔT results always close to or high than 200°C due to the high Nb content in the alloy. Furthermore, the other alloys will show similar results to those reported for alloy 22. These results demonstrate the high potential of the classical solidification model of Scheil-Gulliver to describe studies for welding Ni-based alloys, and furthermore they give support to the next step of study, which is to simulate these Ni-based alloys under different levels of dilution with selected steels.

4.4.2 Dilution effect on solidification simulation

Seven chemical compositions of the fusion zone were simulated according to the dilution level desired. The chemical compositions were based on Equation 2. The different dilutions produced for each alloy deposited on the API 5L X65 steel are given in Tables 4-2 to 4-8, corresponding to the alloys 625, 686, C-276, 22, 59, 617 and 680, respectively.

Table 4-2. Dilution conditions of alloy 625 with API 5L X65 steel pipe.

Dilution conditions of alloy 625 with API 5L X65 steel pipe								
Ele/Dil	0%	5%	10%	15%	20%	30%	40%	50%
Al	0.000	0.002	0.004	0.007	0.009	0.013	0.018	0.022
C	0.100	0.100	0.101	0.101	0.101	0.102	0.102	0.103
Co	0.061	0.057	0.054	0.051	0.048	0.042	0.036	0.030
Cr	21.665	20.588	19.511	18.433	17.356	15.202	13.047	10.893
Cu	0.000	0.009	0.018	0.028	0.037	0.055	0.073	0.092
Fe	0.086	4.957	9.828	14.700	19.571	29.313	39.056	48.798
Hf	0.008	0.007	0.007	0.006	0.006	0.005	0.005	0.004
Mn	0.000	0.059	0.117	0.176	0.235	0.352	0.469	0.587
Mo	8.808	8.374	7.941	7.507	7.074	6.207	5.340	4.473
Nb	3.733	3.547	3.362	3.177	2.992	2.622	2.251	1.881
Ni	65.303	62.055	58.807	55.558	52.310	45.814	39.317	32.821
Si	0.000	0.014	0.028	0.042	0.056	0.083	0.111	0.139
Ta	0.022	0.021	0.020	0.018	0.017	0.015	0.013	0.011
Ti	0.169	0.161	0.153	0.144	0.136	0.120	0.103	0.086
V	0.047	0.047	0.048	0.048	0.049	0.050	0.051	0.052

Source: Developed by the author.

Table 4-3. Dilution conditions of alloy 686 with API 5L X65 steel pipe.

Dilution conditions of alloy 686 with API 5L X65 steel pipe								
Ele/Dil	0%	5%	10%	15%	20%	30%	40%	50%
Al	0.000	0.002	0.004	0.007	0.009	0.013	0.018	0.022
Co	0.054	0.051	0.049	0.046	0.043	0.038	0.032	0.027
Cr	20.655	19.628	18.602	17.575	16.548	14.495	12.441	10.388
Cu	0.000	0.009	0.018	0.028	0.037	0.055	0.073	0.092
Fe	0.377	5.233	10.090	14.947	19.803	29.517	39.230	48.943
Mn	0.240	0.287	0.333	0.380	0.427	0.520	0.613	0.707
Mo	16.403	15.589	14.776	13.963	13.150	11.524	9.897	8.271
Nb	0.000	0.001	0.003	0.004	0.006	0.009	0.012	0.015
Ni	58.066	55.180	52.294	49.407	46.521	40.748	34.975	29.203
Re	0.055	0.052	0.049	0.047	0.044	0.038	0.033	0.027
Si	0.000	0.014	0.028	0.042	0.056	0.083	0.111	0.139
Ta	0.055	0.052	0.050	0.047	0.044	0.039	0.033	0.028
Ti	0.057	0.054	0.051	0.049	0.046	0.041	0.035	0.030
V	0.054	0.054	0.054	0.054	0.054	0.055	0.055	0.055
W	3.975	3.776	3.578	3.379	3.180	2.783	2.385	1.988
C	0.010	0.015	0.020	0.024	0.029	0.039	0.048	0.058

Source: Developed by the author.

Figure 4-4 shows the results of simulation for solidification of alloy 625. The solidification temperature range increased as the dilution was increased, as consequence of two effects. The first is related to the final solidification temperature, which showed a significant decrease with the greater participation of steel composition in the weld metal. While the second effect is related to T_{si}. Probably, this phenomenon involving the T_{Si} is a result of increase in Fe content due to dilution. As previously discussed in the simulated results of alloy 22, iron has a tendency to increase the T_{Si}. Therefore, for the same T_{Sf}, the dilution showed a tendency to increase the ΔT due to the impact of a more Fe concentration in the T_{Si}. The second effect is

related to T_{SF}, which showed a highest impact in ΔT, tightly influenced by phases nucleated at the final stage of solidification.

Table 4-4. Dilution conditions of alloy C-276 with API 5L X65 steel pipe.

Dilution conditions of alloy C-276 with API 5L X65 steel pipe								
Ele/Dil	0%	5%	10%	15%	20%	30%	40%	50%
Al	0.000	0.002	0.004	0.007	0.009	0.013	0.018	0.022
Co	0.120	0.114	0.108	0.102	0.096	0.084	0.072	0.060
Cr	15.500	14.731	13.962	13.193	12.424	10.886	9.348	7.811
Cu	0.350	0.342	0.333	0.325	0.317	0.300	0.283	0.267
Fe	6.500	11.051	15.601	20.152	24.702	33.803	42.904	52.005
Mn	0.850	0.866	0.882	0.899	0.915	0.947	0.979	1.012
Mo	15.200	14.447	13.694	12.941	12.188	10.682	9.176	7.670
Nb	0.000	0.001	0.003	0.004	0.006	0.009	0.012	0.015
Ni	58.200	55.307	52.414	49.521	46.628	40.842	35.056	29.269
Si	0.050	0.061	0.073	0.084	0.096	0.118	0.141	0.164
Ti	0.000	0.000	0.000	0.001	0.001	0.001	0.001	0.002
V	0.130	0.126	0.123	0.119	0.115	0.108	0.101	0.093
W	3.100	2.945	2.790	2.635	2.480	2.170	1.860	1.550
C	0.020	0.024	0.029	0.033	0.037	0.046	0.054	0.063

Source: Developed by the author.

Table 4-5. Dilution conditions of alloy 22 with API 5L X65 steel pipe.

Dilution conditions of alloy 22 with API 5L X65 steel pipe								
Ele/Dil	0%	5%	10%	15%	20%	30%	40%	50%
Al	0.000	0.002	0.004	0.007	0.009	0.013	0.018	0.022
Co	0.250	0.237	0.225	0.212	0.200	0.175	0.150	0.125
Cr	21.048	20.001	18.955	17.909	16.862	14.770	12.677	10.584
Cu	0.000	0.009	0.018	0.028	0.037	0.055	0.073	0.092
Fe	4.955	9.583	14.211	18.838	23.466	32.722	41.977	51.233
Hf	0.007	0.007	0.006	0.006	0.006	0.005	0.004	0.004
Mn	0.119	0.172	0.224	0.277	0.330	0.435	0.541	0.646
Mo	13.145	12.495	11.844	11.194	10.544	9.243	7.943	6.642
Nb	0.000	0.001	0.003	0.004	0.006	0.009	0.012	0.015
Ni	57.350	54.499	51.649	48.798	45.948	40.247	34.545	28.844
Re	0.057	0.054	0.051	0.048	0.046	0.040	0.034	0.029
Si	0.000	0.014	0.028	0.042	0.056	0.083	0.111	0.139
Ta	0.061	0.058	0.055	0.052	0.049	0.043	0.037	0.031
Ti	0.000	0.000	0.000	0.001	0.001	0.001	0.001	0.002
V	0.030	0.031	0.032	0.034	0.035	0.038	0.040	0.043
W	2.965	2.817	2.669	2.520	2.372	2.076	1.779	1.483
C	0.015	0.020	0.024	0.029	0.033	0.042	0.051	0.061

Source: Developed by the author.

The lowest and highest ΔT, in terms of dilution, of alloy 625 were selected and the evolution of their solid fractions during solidification were discussed in greater detail. Figure 4-5 shows the dilutions of 5% and 40%. The nucleated phases are pointed out as the main reason that the highest dilution produced the worst result; however, the Laves phases nucleated at the final stage of solidification, which enlarged the ΔT considerably. After the nucleation of the

Laves phases a temperature of approximately 100°C was necessary to solidify a very small portion of liquid, from 94% to 100%. This result corroborated with literature, which indicate that the Laves phase is a low melting point phase, and is responsible for the formation of solidification cracks[18,20,35,36]. According to studies, the Laves phase is rich in Nb, Ni, Fe, C and Si. Therefore, an increase of dilution with steel promotes an increase of Fe, C and Si, which increases the stability field of the Laves phase, and this then favors nucleation and consequently increases the ΔT considerably[36,41]. On the other hand, the carbides nucleated earlier with high dilution due to the additional carbon from the dilution of the Ni-based alloy with the steel, considering that the base metal has a higher carbon content.

Table 4-6. Dilution conditions of alloy 59 with API 5L X65 steel pipe.

Dilution conditions of alloy 59 with API 5L X65 steel pipe								
Ele/Dil	0%	5%	10%	15%	20%	30%	40%	50%
Al	0.000	0.002	0.004	0.007	0.009	0.013	0.018	0.022
Co	0.030	0.029	0.027	0.026	0.024	0.021	0.018	0.015
Cr	22.775	21.642	20.510	19.377	18.244	15.979	13.713	11.448
Cu	0.052	0.058	0.065	0.071	0.078	0.091	0.104	0.117
Fe	0.766	5.603	10.440	15.277	20.115	29.789	39.463	49.138
Hf	0.005	0.005	0.004	0.004	0.004	0.003	0.003	0.002
Mn	0.231	0.278	0.325	0.372	0.419	0.513	0.608	0.702
Mo	15.400	14.637	13.874	13.111	12.348	10.822	9.296	7.770
Nb	0.064	0.062	0.060	0.059	0.057	0.053	0.050	0.047
Ni	60.510	57.501	54.492	51.484	48.475	42.458	36.441	30.424
Si	0.000	0.014	0.028	0.042	0.056	0.083	0.111	0.139
Ta	0.012	0.011	0.011	0.010	0.009	0.008	0.007	0.006
Ti	0.000	0.000	0.000	0.001	0.001	0.001	0.001	0.002
V	0.148	0.143	0.138	0.134	0.129	0.120	0.111	0.102
C	0.010	0.015	0.020	0.024	0.029	0.039	0.048	0.058

Source: Developed by the author.

Table 4-7. Dilution conditions of alloy 617 with API 5L X65 steel pipe.

Dilution conditions of alloy 617 with API 5L X65 steel pipe								
Ele/Dil	0%	5%	10%	15%	20%	30%	40%	50%
Al	1.250	1.190	1.129	1.069	1.009	0.888	0.768	0.647
Co	12.450	11.828	11.205	10.583	9.960	8.715	7.470	6.225
Cr	21.800	20.716	19.632	18.548	17.464	15.296	13.128	10.961
Cu	0.000	0.009	0.018	0.028	0.037	0.055	0.073	0.092
Fe	0.750	5.588	10.426	15.264	20.102	29.778	39.454	49.130
Mn	0.000	0.059	0.117	0.176	0.235	0.352	0.469	0.587
Mo	9.050	8.604	8.159	7.713	7.268	6.377	5.486	4.595
Nb	0.000	0.001	0.003	0.004	0.006	0.009	0.012	0.015
Ni	54.280	51.583	48.886	46.189	43.492	38.098	32.704	27.309
Si	0.110	0.118	0.127	0.135	0.144	0.160	0.177	0.194
Ti	0.250	0.238	0.225	0.213	0.201	0.176	0.151	0.127
V	0.000	0.003	0.006	0.008	0.011	0.017	0.023	0.028
C	0.060	0.062	0.065	0.067	0.069	0.074	0.078	0.083

Source: Developed by the author.

Table 4-8. Dilution conditions of alloy 680 with API 5L X65 steel pipe.

Dilution conditions of alloy 680 with API 5L X65 steel pipe								
Ele/Dil	0%	5%	10%	15%	20%	30%	40%	50%
Al	0.000	0.002	0.004	0.007	0.009	0.013	0.018	0.022
Cr	19.935	18.944	17.954	16.963	15.972	13.991	12.009	10.028
Cu	0.000	0.009	0.018	0.028	0.037	0.055	0.073	0.092
Fe	0.547	5.395	10.244	15.092	19.940	29.636	39.332	49.029
Mn	0.000	0.059	0.117	0.176	0.235	0.352	0.469	0.587
Mo	6.320	6.011	5.702	5.393	5.084	4.466	3.848	3.230
Nb	3.580	3.402	3.225	3.047	2.870	2.515	2.160	1.805
Ni	61.204	58.161	55.118	52.074	49.031	42.945	36.858	30.772
Si	0.000	0.014	0.028	0.042	0.056	0.083	0.111	0.139
Ti	1.458	1.385	1.312	1.239	1.167	1.021	0.876	0.731
V	0.041	0.042	0.043	0.043	0.044	0.046	0.047	0.049
W	6.905	6.560	6.215	5.869	5.524	4.834	4.143	3.453
C	0.005	0.010	0.015	0.020	0.025	0.035	0.045	0.056

Source: Developed by the author.

Figure 4-4. The results of solidification simulation for all dilution levels of the alloy 625 deposited on the API 5L X65 steel.

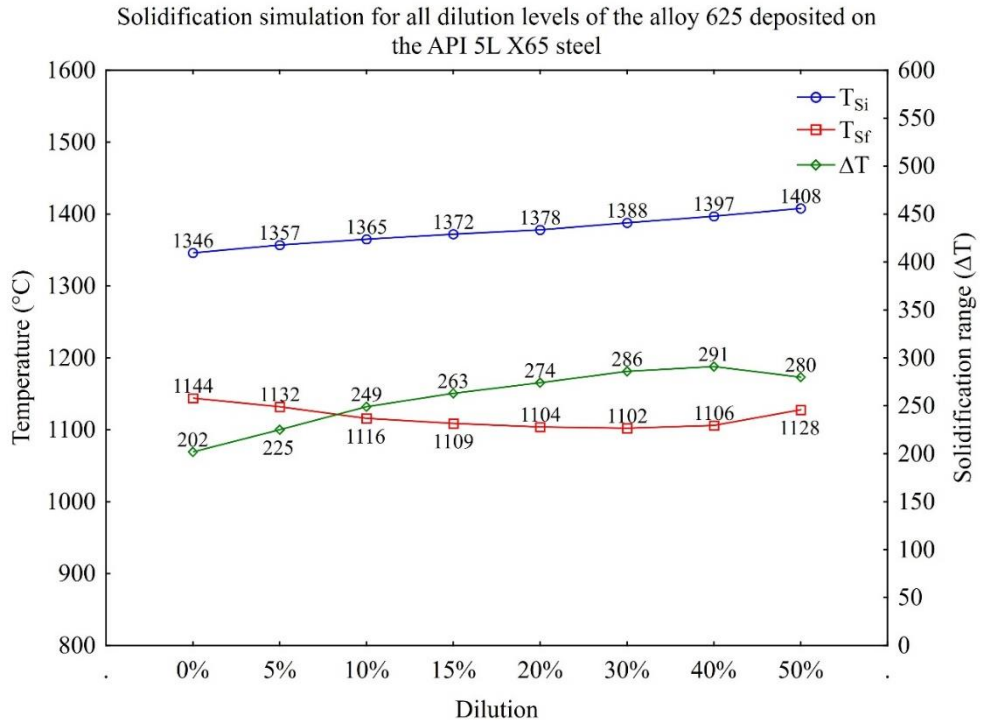

Source: Developed by the author.

Figure 4-6 describes the simulated effect of dilution on the solidification of alloy 686. This alloy has a relative stability, in terms of solidification temperature range, as it gives values varying from 91°C to 119°C. The slight increase in the ΔT with the increase in dilution was attributed to the iron effect, which pushes the T_{Si} to higher temperatures. In comparison with the results for alloy 625, the ΔT of alloy 686 under all conditions was very small, which is because the alloy 625 contains Nb in its chemical composition, which increases ΔT to more

than 200°C. Figure 4-7 shows the solidification diagrams of alloy 686 for the 5% and 50% dilutions, which had the lowest and highest ΔTs, in terms of dilution levels, respectively. Notably there was no P-phase in the high dilution level, which is probably due to the reduction in the concentration of important alloying elements in its composition, such as Cr, Mo and W that is a consequence of the high dilution level[38,39]. The same dilution effect was observed for the σ phase, which just nucleated at the final stage of solidification, when the remaining liquid fraction was almost zero. The M_6C carbide was present in both dilution level, showing an early nucleation at high temperatures for the 50% of dilution level, which was naturally stimulated by the additional C with the increase of dilution.

Figure 4-5. Solidification simulation of alloy 625 for the dilution levels of a) 5% and b) 40%.

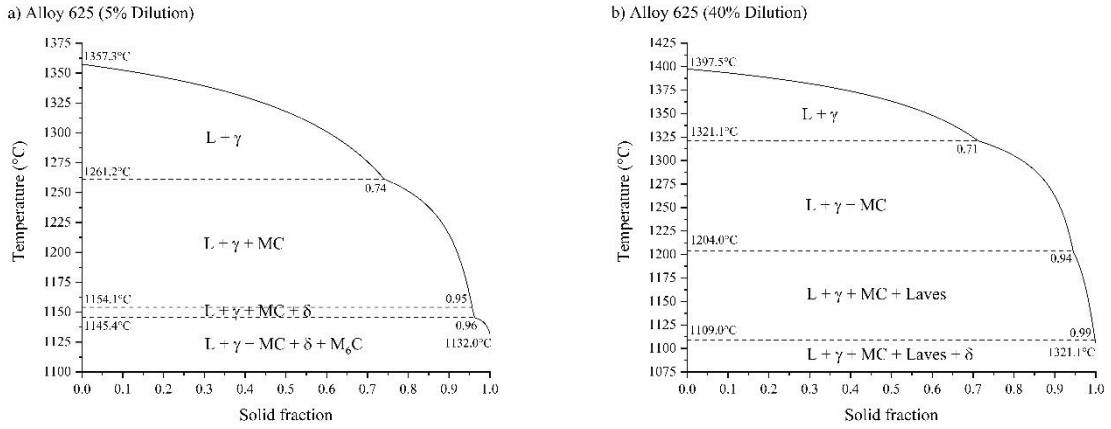

Source: Developed by the author.

Figure 4-8 shows the results related to the dilution effect on the solidification of alloy C-276. Alloy C-276 shows an intermediate behavior in terms of solidification temperature range. In most cases the ΔT had values greater than those presented by alloy 686 and smaller than those by alloy 625. Furthermore, the dilution effect was different for the ΔT if compared with the other alloys. This time, dilution caused a reduction of the ΔT that was influenced by the increase of T_{Sf}. Figure 4-9 highlights the 5% and 50% dilution levels. The low dilution level shows secondary phases such as P and σ phases, which enlarged the ΔT at the end of the solidification process. The high dilution level in turn, showed only M_6C carbides in equilibrium with the γ matrix. This was due to the low Cr fraction present, which implies a low Cr fraction able to segregate to liquid. Probably there was not enough Cr present in the remaining liquid to nucleate the P and σ phases, considering that Cr has a higher solubility in the γ phase.

Figure 4-6. The results of solidification simulation for all dilution levels of the alloy 686 deposited on the API 5L X65 steel.

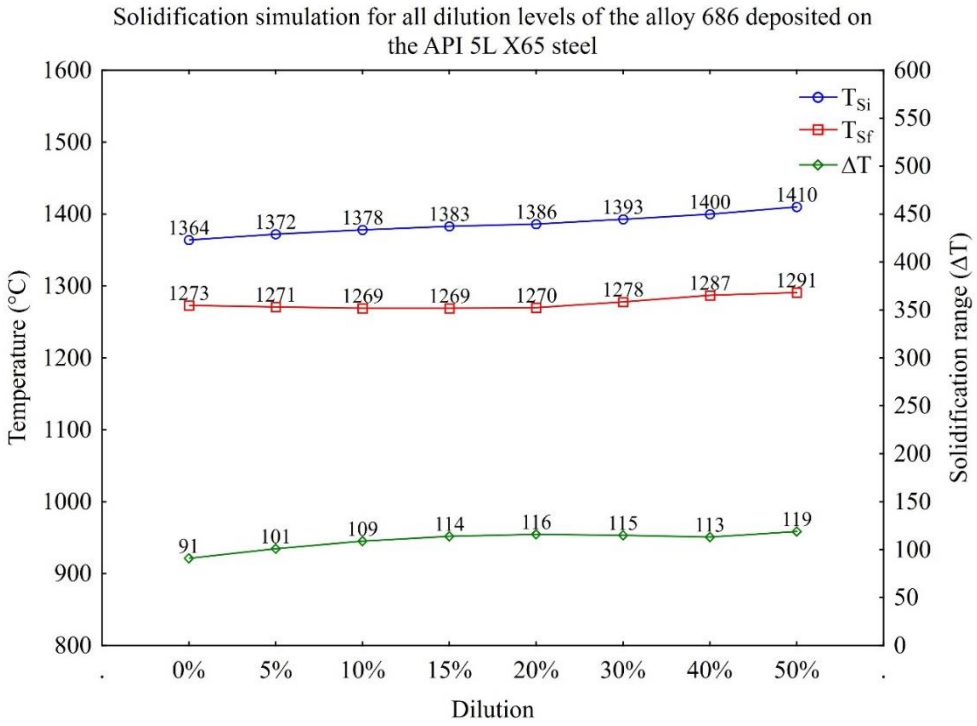

Source: Developed by the author.

Figure 4-7. Solidification simulation of alloy 686 for the dilution level conditions of a) 5% and b) 50%.

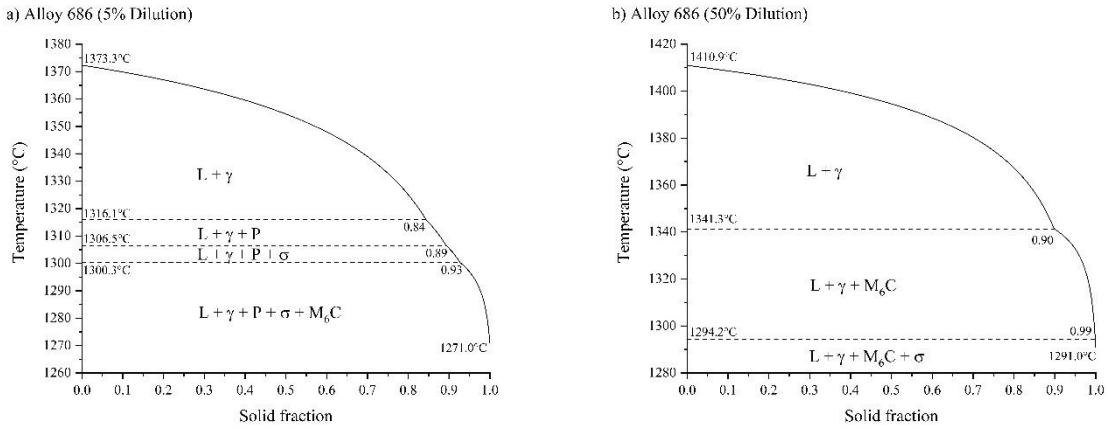

Source: Developed by the author.

Figure 4-10 shows the solidification results of alloy 22 diluted with steel pipe. Alloy 22 gave low values of ΔT as was observed for alloy 686, in which the solidification temperature range presented quite low values compared to the alloys which contain significant amounts of Nb. Figure 4-11 indicates the dilution levels, which have the lowest and highest ΔT. The phase evolution during solidification indicated a lack of the σ phase for the highest dilution level, which is probably due to the low Cr content present. In addition, the nucleation of the MC

carbide at the final stage of the solidification process must have consumed the Cr content, making the nucleation of σ phase more difficult.

Figure 4-8. The results of solidification simulation for all dilution levels of the alloy C-276 deposited on the API 5L X65 steel.

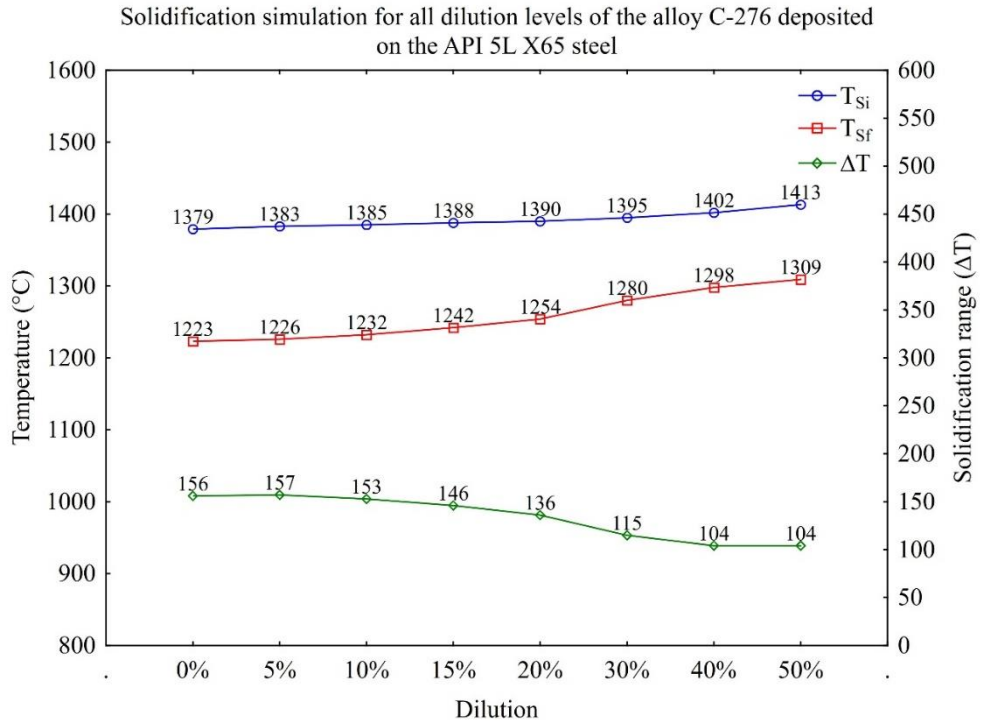

Source: Developed by the author.

Figure 4-9. Solidification simulation of alloy C-276 for the dilution levels of a) 5% and b) 50%.

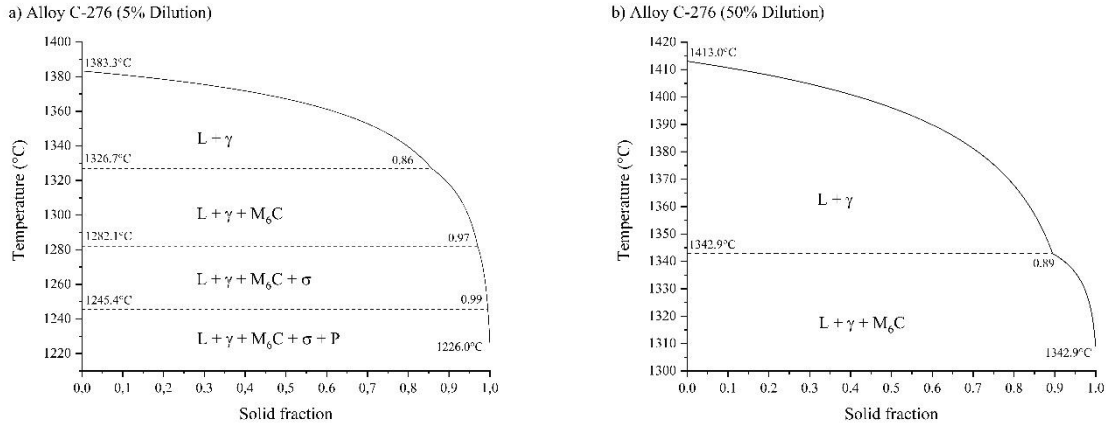

Source: Developed by the author.

Another alloy evaluated within the Ni-Cr-Mo system was the alloy 59. The main differential of this alloy is that it has no W. Figure 4-12 shows the solidification results of alloy 59 for several dilution levels with the steel. The ΔT values obtained for alloy 59 as a function of dilution were slightly higher than those observed for the alloys 686 and 22, but in all cases

much smaller in comparison to the alloy 625. Figure 4-13 shows the solidification diagrams for the 5% and 20% levels, which presented the lowest and highest ΔTs, respectively. The nucleated phases were similar to those observed in alloys 686 and 22. The σ phase tended to nucleate at the end of the solidification process as dilution increased. The carbides were observed in the both cases.

Figure 4-10. The results of solidification simulation for all dilution levels of the alloy 22 deposited on the API 5L X65 steel.

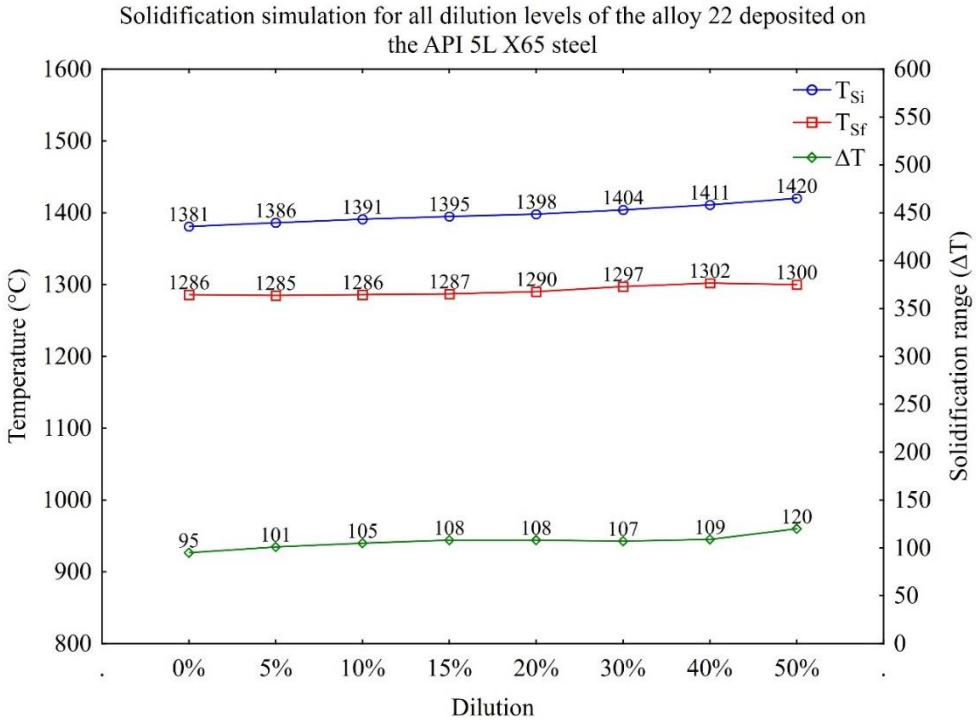

Source: Developed by the author.

Figure 4-11 Solidification simulation of alloy 22 for the dilution levels of a) 5% and b) 50%.

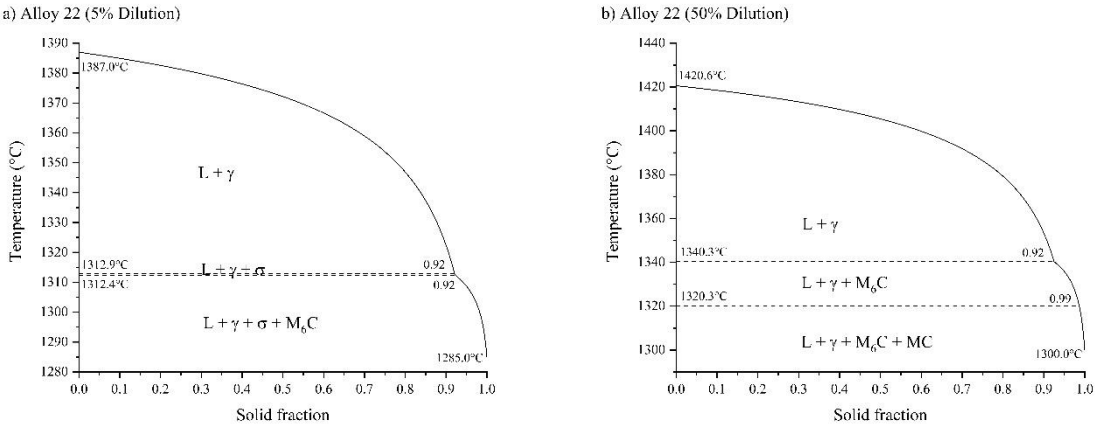

Source: Developed by the author.

Figure 4-12. The results of solidification simulation for all dilution levels of the alloy 59 deposited on the API 5L X65 steel.

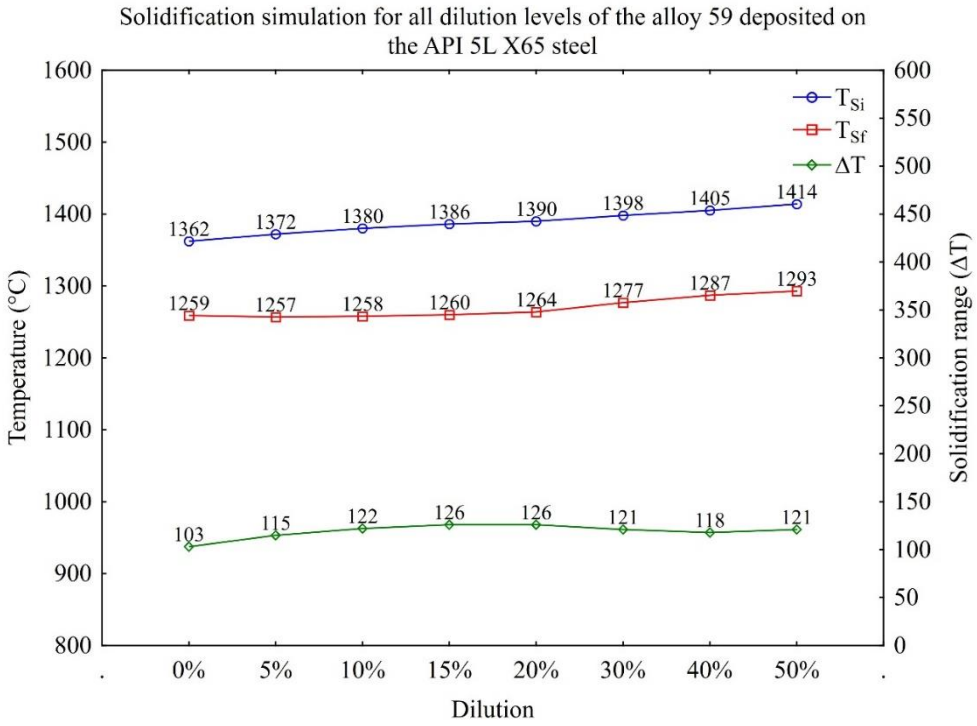

Source: Developed by the author.

Figure 4-13. Solidification simulation of alloy 59 for the dilution levels of a) 5% and b) 20%.

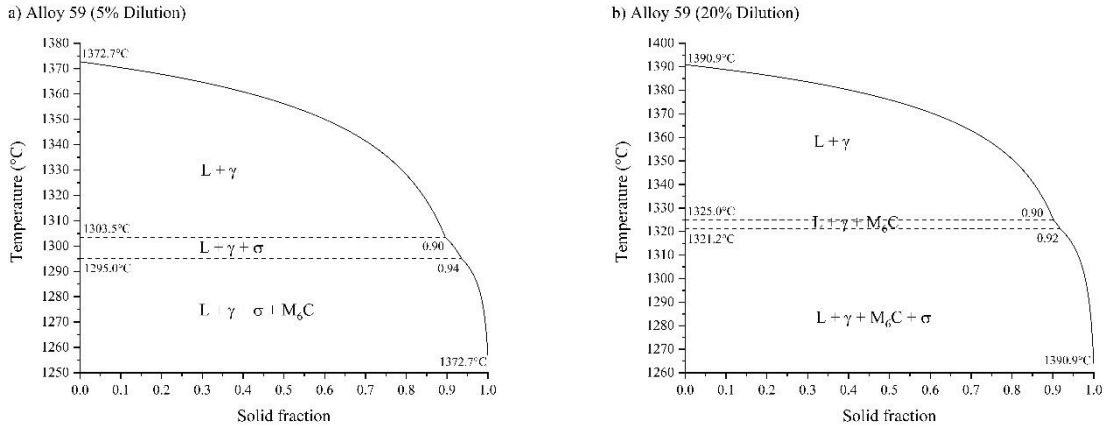

Source: Developed by the author.

Another alloy assessed was alloy 617, which belongs to the Ni-Cr-Co-Mo family. The main chemical features of this Ni-based alloy is its high Cr and Mo content, similar to alloy 625, which has as its main difference additional Co in at least 10%. Co has a great affinity for the Ni matrix, and promotes an effect of solid solution strengthening similar to that produced by other alloying elements such as Nb and W. Figure 4-14 shows the simulated results related to the solidification of alloy 617 in several dilution levels with the pipe. There was an increase in the solidification temperature range as dilution increased. In this case, the T_{si} temperature

was principally responsible for this effect, probably as a result of an increase of Fe in the chemical composition of the weld metal alloy.

Figure 4-14. The results of solidification simulation for all dilution levels of the alloy 617 deposited on the API 5L X65 steel.

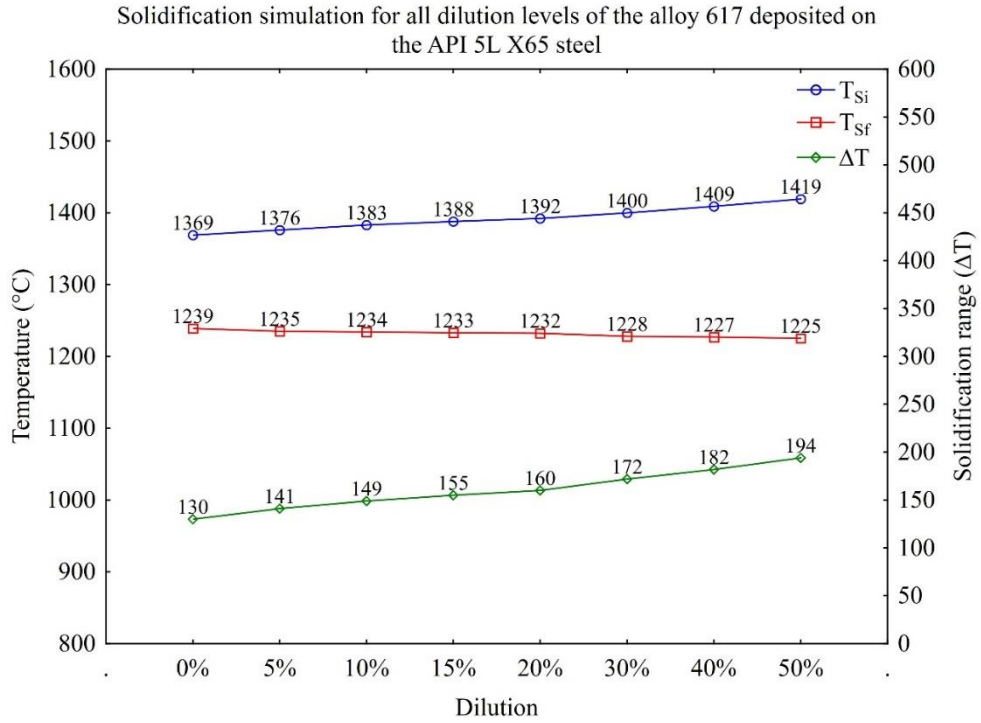

Source: Developed by the author.

Figure 4-15 shows the simulation of the solidification process for dilution levels of 5% and 50%. The difference between the lowest (5%) dilution level and the simulation results for the alloy 617 without any dilution effect was the nucleation of the MC carbides at the final stage of solidification. Naturally, this occurred due to the increase of carbon from the mixture with the steel pipe. While for the high dilution level the simulation predicted that there would be no σ nucleation reaction; this is due to a reduction in the alloying elements, such as Cr and Mo, that are responsible for its stability[38,39]. In addition, the γ-FCC solidification rate from 80% of solid phases in the system was reduced drastically. This occurred due to changes in the chemical composition of the γ-phase, evidencing the combined influence of the γ-phase and carbides enlarging the ΔT at the final stage of solidification. Nonetheless, even with the relatively high ΔT for the 50% dilution level, it is believed that the phases predicted by the solidification simulation are not likely to promote solidification defects in practice[42].

Figure 4-15. Solidification simulation of alloy 617 for the dilution levels of a) 5% and b) 50%.

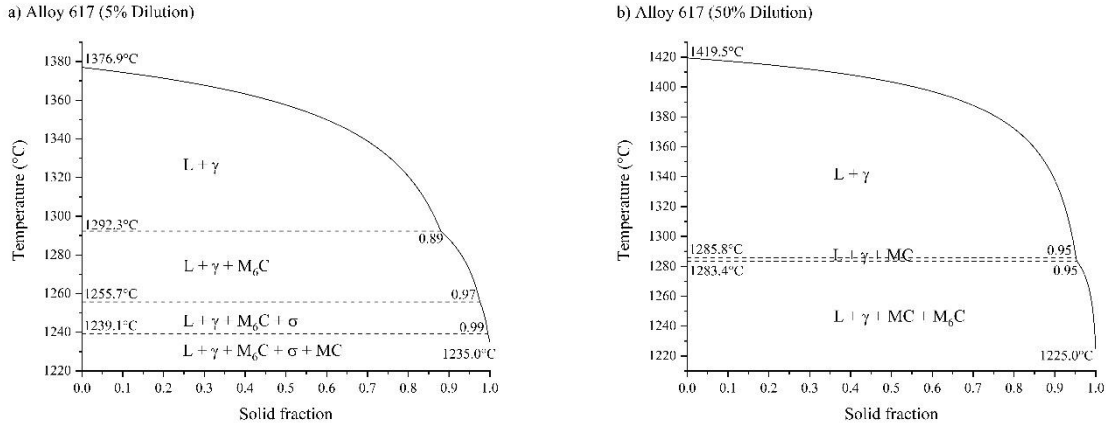

Source: Developed by the author.

The last Ni-based alloy evaluated in this study was the alloy 680, which differs from all alloys previously evaluated in terms of the combined addition of Nb, W and Ti in high concentrations. Figure 4-16 highlights the effects of dilution on the solidification temperature range of alloy 680. Similar to what was observed for alloy 625, as the dilution was increased the ΔT was significantly enlarged. In this case, the T_{Si} showed a more significant effect on the ΔT with an increase of dilution greater than observed for T_{Sf}. In all cases, the T_{Sf} values were very low, indicating the possible formation of low melting point phases at the final stage of the solidification process. Figure 4-17 details the evolution of the solidification fraction as a function of the nucleated phases for the dilution levels of 5% and 50%. In all cases the nucleation of Laves phases was noted, and more significantly this behavior indicates the harmful effect of iron dilution on the solidification behavior of this particular alloy. The Laves phase, in the high dilution level, nucleated earlier at high temperatures, indicating a more favorable nucleation of this deleterious phase under this thermodynamic condition. The δ phase was not predicted for the highest dilution level (50%). This is probably a consequence of a reduction of Nb due to the high dilution level, and by the strong nucleation of Laves phase, which must have consumed the majority of the Nb segregated from the remaining liquid. Another phase not observed for the high dilution level was the σ phase, which probably did not nucleate due to the low Cr content in this case, which is a consequence of the dilution level, taking into account the high solubility of Cr by the γ matrix and the very low segregation potential of this alloying element[35,38,39].

The solidification simulation results of the selected Ni-based alloys, diluted with the API 5L X65 steel, were able to indicate, which alloys will show a high or a low susceptibility to solidification cracks, taking into account the solidification temperature range. Figure 4-18

summarizes all the ΔT results of the alloys evaluated for all the dilution levels considered. The alloys containing Nb in their chemical compositions have the highest ΔT values. In many cases, these alloys presented ΔT values superior to twice the solidification range observed for the alloys that did not contain Nb in solution. In addition, the presence of low melting point phases predict a greater tendency to form solidification cracks in practice. Thus, the alloys 625 and 680 have a higher susceptibility to solidification cracks in comparison to all the other Ni-based alloys evaluated in this study. The alloys 617 and C-276 showed intermediate values of ΔT. The alloys 686, 22 and 59, showed the lowest susceptibility to solidification cracks, since their ΔTs did not exceed 130°C.

Figure 4-16. The results of solidification simulation for all dilution levels of the alloy 680 deposited on the API 5L X65 steel.

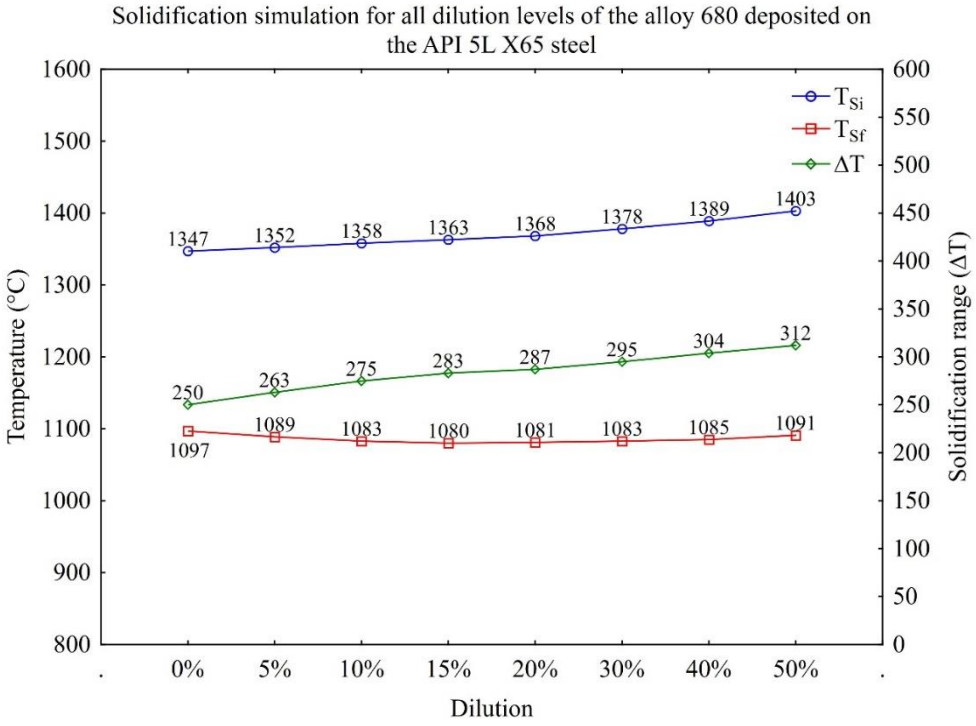

Source: Developed by the author.

The Laves phases were only observed in the alloys containing Nb, such as 625 and 680. This phase is known as a low melting point phase, which promotes a significant increase in the solidification temperature range of Ni-based alloys. Several studies, which have evaluated alloy 625 related to the solidification cracking phenomenon, described the nucleation of Laves phase at the final stage of the solidification process[15,20].

Among the alloys evaluated, alloy 22 must be emphasized as it had the lowest solidification temperature range for most of the dilution levels evaluated in this study. However,

the different results in terms of ΔT among the alloys 686, 22 and 59 were low, almost imperceptible. Thus, it is difficult to indicate which of these three alloys will present in practice the lowest susceptibility to solidification cracking. Nevertheless, the literature reports low evidence of solidification cracks in these alloys[29,43–46], including the alloys 617 and C-276[42,46].

Figure 4-17. Solidification simulation of alloy 680 for the dilution levels of a) 5% and b) 50%.

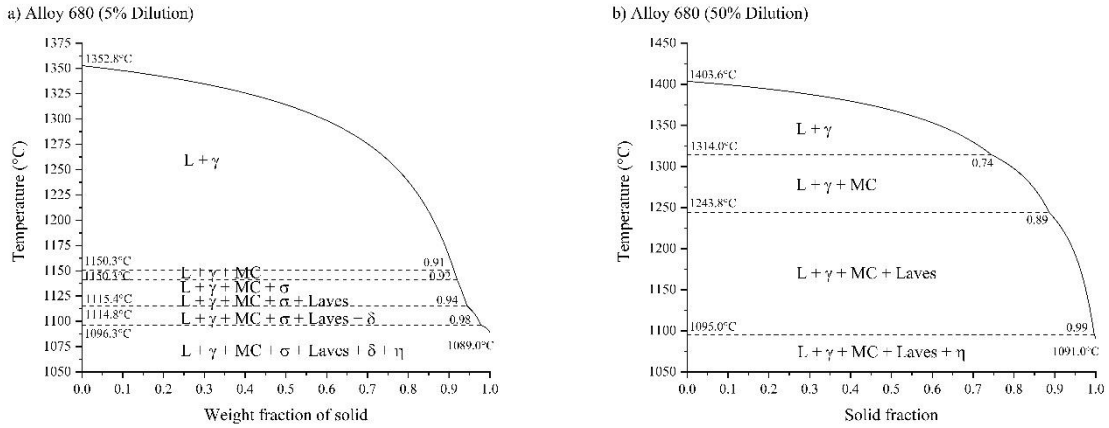

Source: Developed by the author.

Figure 4-18. Summary of all the results of the simulated solidification ranges for all the dilution levels of all the Ni-based alloys analyzed here.

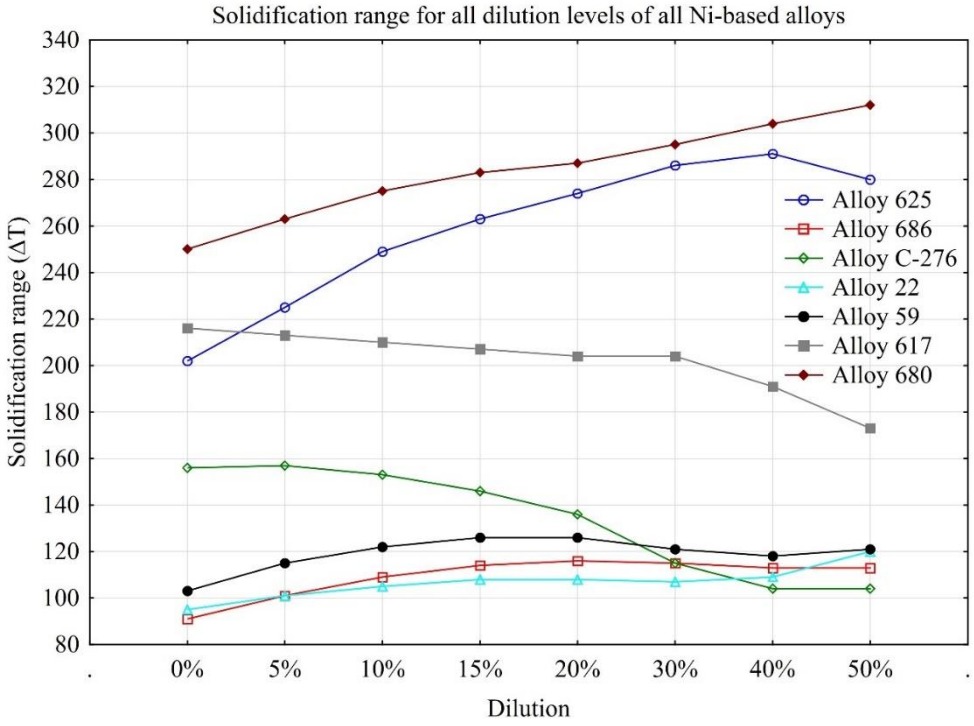

Source: Developed by the author.

4.5 Conclusion

Based on the simulated results produced and discussed in the present study entitle "Thermodynamic simulation of dissimilar joint welding solidification of API 5L X65 steel pipe using Ni-based alloys", it was possible to conclude that:

- The thermodynamic simulation of alloy solidification based on the classical model of Scheil-Gulliver, was able to describe the solidification temperature range of alloys, only taking into account the chemical composition of those alloys. The simulated results, when confronted with simulated and experimental results reported in the literature, showed a good agreement as well as similar tendencies.
- Carbide nucleation was predicted for all simulations, since carbon has a strong affinity for the alloying elements such as Cr, Mo and W. The nucleation of Laves phase was predicted only for the alloys containing Nb in their chemical composition, and the dilution with steel, promoted their nucleation due the additional Fe, Si and C. The δ phase was also observed only in alloys with Nb content, and its nucleation was suppressed at the high dilution level. The σ phase was predicted in all alloys and like the P phase, their nucleation was unfavorable for high dilution levels due to a reduction of the alloying elements such as Cr, Mo and W. The P phase was only observed in alloys containing high amounts of W.
- The alloys 625 and 680, which contain Nb, showed the highest solidification temperature range. Therefore, among the Ni-based alloys evaluated, these alloys were the most susceptible to solidification cracks, considering just the solidification temperature range. The Laves phase was observed only in these alloys and their nucleation was the main reason to enlarge the ΔT, increasing the possibility to observe solidification cracks in practice.
- The alloys 686, 22 and 59 showed considerably better results, in terms of ΔT. The alloys 617 and C-276 in turn, showed an intermediate result, without any evidence of low melting point phases. The alloy 686 had the smallest ΔT for the no dilution level with the base metal. Alloy 22 showed the best result in the majority of the dilution cases evaluated. Nonetheless, among the alloys 686, 22 and 59, it is not possible to point out the alloy with the least susceptibility to

solidification cracking by only following the methodology performed in this study. However, the alloys 686, 22 and 59 will show low evidence of solidification crack in practice, and the same is expected for the alloys 617 and C-276.

REFERENCES

1 SUN, Z.; ION, J. C. Laser welding of dissimilar metal combinations. **Journal of Materials Science**, v. 30, n. 17, p. 4205-4214, 1995.

2 SAEDI, A. H.; HAJJARI, E.; SADROSSADAT, S. M. Microstructural characterization and mechanical properties of TIG-welded API 5L X60 HSLA steel and AISI 310S stainless steel dissimilar joints. **Metallurgical and Materials Transactions A**, v. 49, n. 11, p. 5497-5508, 2018.

3 KOURDANI, A.; DERAKHSHANDEH-HAGHIGHI, R. Evaluating the properties of dissimilar metal welding between Inconel 625 and 316L stainless steel by applying different welding methods and consumables. **Metallurgical and Materials Transactions A**, v. 49, n. 4, p. 1231-1243, 2018.

4 DUPONT, J. N.; BABU, S.; LIU, S. Welding of materials for energy applications. **Metallurgical and Materials Transactions A**, v. 44, n. 7, p. 3385-3410, 2013.

5 SILVA, C. C. *et al*. A study on the effect of the interpass temperatures in properties and microstructures of the Alloy 625 dissimilar fusion zone. **Materials Science Forum**, v. 783-786, p. 2816-2821, 2014.

6 SARAIVA, D. L. *et al*. Application of low Ms temperature consumable to dissimilar welded joint. **Materials Science and Technology**, v. 30, n. 9, p. 1057-1062, 1 jul. 2014.

7 SILVA, C. C. *et al*. Austenitic and ferritic stainless steel dissimilar weld metal evaluation for the applications as-coating in the petroleum processing equipment. **Materials & Design**, v. 47, p. 1-8, 2013.

8 BALDRIDGE, T. *et al*. Laser cladding of Inconel 690 on Inconel 600 superalloy for corrosion protection in nuclear applications. **Optics and Lasers in Engineering**, v. 51, n. 2, p. 180-184, 2013.

9 CHONG, T.-V. S. *et al*. Effects of elevated temperatures on the mechanical properties of nickel-based alloy clad pipelines girth welds. **Engineering Fracture Mechanics**, v. 152, p. 174-192, 2016.

10 IANNUZZI, M.; BARNOUSH, A.; JOHNSEN, R. Materials and corrosion trends in offshore and subsea oil and gas production. **npj Materials Degradation**, v. 1, n. 1, p. 2, 2017.

11 SOUZA, R. F.; RUGGIERI, C. Fracture assessments of clad pipe girth welds incorporating improved crack driving force solutions. **Engineering Fracture Mechanics**, v. 148, p. 383-405, 2015.

12 JONES, R. L. *et al*. Reeled clad SCR weld fatigue qualification. *In*: OFFSHORE TECHNOLOGY CONFERENCE, 2011, Houston. **Proceedings**. Houston: Offshore Technology Conference, 2011. p 1-13.

13 LLOYD, A. C. *et al*. Cr, Mo and W alloying additions in Ni and their effect on passivity. **Electrochimica Acta**, v. 49, n. 17, p. 3015-3027, 2004.

14 MOHAMMADI ZAHRANI, E.; ALFANTAZI, A. M. Hot corrosion of Inconel 625 Overlay Weld Cladding in Smelting Off-Gas Environment. **Metallurgical and Materials Transactions A**, v. 44, n. 10, p. 4671-4699, 2013.

15 HU, Y. L. *et al*. Effect of Ti addition on cracking and microhardness of Inconel 625 during the laser solid forming processing. **Journal of Alloys and Compounds**, v. 711, p. 267-277, 2017.

16 MAI, T. A.; SPOWAGE, A. C. Characterisation of dissimilar joints in laser welding of steel-kovar, copper-steel and copper-aluminium. **Materials Science and Engineering: A**, v. 374, n. 1, p. 224-233, 2004.

17 JOSEPH, A. *et al*. Evaluation of residual stresses in dissimilar weld joints. **International Journal of Pressure Vessels and Piping**, v. 82, n. 9, p. 700-705, 2005.

18 CIESLAK, M. J. The welding and solidification metallurgy of Alloy 625. **Welding Journal**, v. 70, n. 2, p. 49-56, 1991.

19 CIESLAK, M. J.; HEADLEY, T. J.; ROMIG, A. D. The welding metallurgy of HASTELLOY alloys C-4, C-22, and C-276. **Metallurgical Transactions A**, v. 17, n. 11, p. 2035-2047, nov. 1986.

20 DUPONT, J. N. Solidification of an alloy 625 weld overlay. **Metallurgical and Materials Transactions A**, v. 27, n. 11, p. 3612-3620, nov. 1996.

21 KOU, S. **Welding Metallurgy**. 2nd ed. ed. Hoboken, New Jersey: John Wiley & Sons, Inc., 2003.

22 KATTNER, U. R. The thermodynamic modeling of multicomponent phase equilibria. **JOM**, v. 49, n. 12, p. 14-19, 1997.

23 SZELIGA, D. *et al*. Investigation of casting–ceramic shell mold interface thermal resistance during solidification process of nickel based superalloy. **Experimental Thermal and Fluid Science**, v. 87, p. 149-160, 2017.

24 REN, W. *et al*. Effects of the long-time thermal exposure on the microstructure and mechanical properties of laser weldings of Inconel 617. **Journal of Materials Processing Technology**, v. 247, p. 296-305, 2017.

25 RAMKUMAR, K. D. *et al*. Characterization of weld strength and impact toughness in the multi-pass welding of super-duplex stainless steel UNS 32750. **Materials & Design**, v. 60, p. 125-135, 2014.

26 SCHEIL, E. No Title. **Z. Metallkd.**, v. 34, p. 70-72, 1942.

27 BRODY, H. D.; FLEMINGS, M. C. **Transctions TMS-AIME**, v. 236, p. 615, 1966.

28 MINÁ, É. M. *et al*. The effect of dilution on microsegregation in AWS ER NiCrMo-14 alloy welding claddings. **Metallurgical and Materials Transactions A: Physical Metallurgy and Materials Science**, v. 47, n. 12, 2016.

29 SILVA, C. C. *et al*. Assessment of microstructure of alloy Inconel 686 dissimilar weld claddings. **Journal of Alloys and Compounds**, v. 684, p. 628-642, 2016.

30 SILVA, C. C. *et al*. New insight on the solidification path of an alloy 625 weld overlay. **Journal of Materials Research and Technology**, v. 2, n. 3, p. 228-237, 2013.

31 SIMS, C. T.; STOLOFF, N. S.; HAGEL, W. C. **Superalloys II: high-temperature materials for aerospace and industrial power**. 2nd ed. New York: John Wiley & Sons Inc., 1987.

32 MINÁ, É. M. *et al*. Electron detection modes comparison for quantification of secondary phases of Inconel 686 weld metal. **Materials Characterization**, v. 133, p. 10-16, nov. 2017.

33 XU, F. *et al*. Microstructural evolution and mechanical properties of Inconel 625 alloy during pulsed plasma arc deposition process. **Journal of Materials Science & Technology**, v. 29, n. 5, p. 480-488, 2013.

34 LI, C. *et al*. Microstructure evolution characteristics of Inconel 625 alloy from selective laser melting to heat treatment. **Materials Science and Engineering: A**, v. 705, p. 20-31, 2017.

35 SILVA, C. C. *et al*. Mechanical properties and microstructural characterization of aged nickel-based Alloy 625 weld metal. **Metallurgical and Materials Transactions A: Physical Metallurgy and Materials Science**, v. 49, n. 5, p. 1653-1673, may. 2018.

36 DUPONT, J. N.; ROBINO, C. V.; MARDER, A. R. Solidification and weldability of Nb-bearing superalloys. **Welding Journal (Miami, Fla)**, v. 77, n. 10, p. 417-431, 1998.

37 PERRICONE, M. J.; DUPONT, J. N. Effect of composition on the solidification behavior of several Ni-Cr-Mo and Fe-Ni-Cr-Mo alloys. **Metallurgical and Materials Transactions A**, v. 37, n. 4, p. 1267-1280, 2006.

38 POPP, R. *et al*. Determination of solubility limits of refractory elements in TCP phases of the Ni-Mo-Cr ternary system using diffusion multiples. **Journal of Alloys and Compounds**, v. 788, p. 67-74, 2019.

39 HUO, J. *et al*. Microstructural characteristics of σ phase and P phase in Ru-containing single crystal superalloys. **Materials Characterization**, v. 124, p. 73-82, 2017.

40 TURCHI, P. E. A.; KAUFMAN, L.; LIU, Z.-K. Modeling of Ni–Cr–Mo based alloys: part I-phase stability. **Calphad**, v. 30, n. 1, p. 70-87, 2006.

41 CIESLAK, M. J.; HEADLEY, T. J.; FRANK, R. B. Welding metallurgy of custom age 625 PLUS alloy. **Welding Journal (Miami, Fla)**, v. 68, n. 12, p. 473s-482s, 1989.

42 HOSSEINI, H. S.; SHAMANIAN, M.; KERMANPUR, A. Characterization of microstructures and mechanical properties of Inconel 617/310 stainless steel dissimilar welds. **Materials Characterization**, v. 62, n. 4, p. 425-431, 2011.

43 MALTIN, C. A.; GALLOWAY, A. M.; MWEEMBA, M. Microstructural evolution of Inconel 625 and Inconel 686CPT weld metal for clad carbon steel linepipe joints: A Comparator Study. **Metallurgical and Materials Transactions A**, v. 45, n. 8, p. 3519–3532, jul. 2014.

44 MINÁ, É. M. *et al*. Efeito da diluição sobre a microestrutura da liga AWS ER NiCrMo-14 na soldagem de revestimentos pelo processo TIG com alimentação de arame frio. **Soldagem & Inspeção**, v. 21, n. 3, p. 317-329, 2016.

45 MINÁ, E. M. *et al*. Effect of dilution on the microstructure of AWS ERNiCrMo-14 alloy in overlay welding by the TIG process with cold wire feed. **Welding International**, v. 32, n. 2, p. 130-138, 2018.

46 ROWE, M. D.; CROOK, P.; HOBACK, G. L. Weldability of a corrosion-resistant Ni-Cr-Mo-Cu alloy. **Welding Journal (Miami, Fla)**, v. 82, n. 11, p. 313s-320s, 2003.

Chapter 5

Thermodynamic simulation of joint welding solidification of API 5L X65 steel pipe using low alloy steel and Ni-based alloys

5.1 Abstract

The present study assessed the solidification process of low alloy steel (LAS) filler metal for various dilution levels with Ni-based alloys, through thermodynamic simulation, in order to select the best mixture conditions for welding, in terms of solidification crack susceptibility. The software Thermo Calc® performed the solidification simulations based on the classical solidification model of Scheil-Gulliver. Various different combinations of AWS ER100S-G steel with the Ni-based alloys 625, 686, C276, 22, 59, 617 and 680, from the Ni-Cr-Mo, Ni-Cr-Co-Mo and Ni-Cr-Mo-W-Nb-Ti classes were used. The thermodynamic simulations predicted for the dilution levels with the Ni-based alloys without Nb and/or Ti a low solidification range (ΔT) and no evidence of low melting point phases were found. The alloys 625 and 680, on the other hand, showed deleterious phases, especially Laves phases. The Ni-based alloys 686, 22 and 59 were elected as the best alloys to mixture with LAS to perform dissimilar weld joints with API 5L X65 steel pipe to attend the new challenges of the Oil & Gas industries.

5.2 Introduction

Dissimilar welding is a powerful manufacturing technique that allow combine materials from different classes, combining the best properties of selected materials, in order to manufacture an equipment and/or component[1–7]. Industries, such as oil & gas, have been using dissimilar welding on manufacturing of risers based on steel pipes with internal CRA cladding[8–11]. The CRA cladding is commonly manufactured by Ni-based alloy, and the alloy 625 is the most used for this welding overlay[12–14], providing a life extension of component keeping a good cost-benefit[10]. Initially designed for weldability and high creep resistance at high thermal service, the alloy 625 shown a great corrosion resistance in different corrosive environments since its development on 60's decade[15]. Nonetheless, the welding overlay procedure to perform the dissimilar cladding of steel pipe with Ni-based alloy is well established. The challenge begins on welding procedure to join the risers.

Usually, the join procedure recommends the same nickel-based alloy used on internal cladding of pipe for performing the join, in order to avoid metallurgical problems due mixture of different materials[16–18]. In addition, for the same reason is recommended a lowest dilution with steel pipe[16]. Thus, it is possible to perform the join of pipe avoiding solidification defects, especially cracks[16]. Naturally, the mechanical properties of the joint shall be similar to the nickel-based alloy used. However, this will reduce the field of application of these pipes, especially for welding of HSLA steel pipes, such as API 5L X65, X70 and X80 steels[16,18].

Nowadays, the most attractive riser installation process is reel lay. Different from traditional methods such as S-lay and J-lay, the reel lay allow the joint of pipes in an onshore unit close to dock. This provides a high quality of weldments with great productivity and allow the easy inspection of weldments. After join welding of pipes, the pipeline is spooled onto a large diameter drum on a pipe-laying vessel for transportation. Subsequently the pipeline is unspooled into subsea during installation of the riser. Nonetheless, during the bending and unbending deformation of spooled and unspooled steps, about 2% of plastic deformation is introduced on pipe, including weldment region[19]. Considering that welding process may introduce some defects such as porosity, shrink porosity, solidification cracks and reheat cracks as well[20], the reel lay process require a welding with a high quality and great mechanical properties.

The DNVGL ST F101 standard established some requirements to installation of risers by reel lay process[21]. The most severe requirement is about yield strength (YS), since welded joint must exhibit a YS at least equal to the maximum YS defined for base metal by standard minus 20 MPa. This requirement aims guarantee the safety of operation, once riser failure leads to an environmental pollution and material loss. In this context, it is necessary a judicious selection of materials to provide the mechanical properties required, that also offer a great weldability. According with the literature, the dissimilar welds using alloy 625 as filler metal only show a YS overmatching for API 5L X65 steel after bending and unbending steps on reel lay process[16]. A DNV report classify this kind of girth welds as a ‘partially overmatch’ and recommend take into account this assumption on calculations[22]. In addition, the alloy 625 is reported as critical alloy with a high solidification crack susceptibility[23], especially for dissimilar welding. The incorporation of Fe by dilution with steel pipe makes possible the nucleation of eutetic phases such as Laves, that impair the weld metal by formation of solidification cracks[12]. Therefore, it is evident the necessity of new solutions to make viable the use of reel lay process on installation of rigid riser with internal clad.

An alternative to perform the girth welding of steel pipes with internal CRA cladding, it is use low alloy steel (LAS) filler metals, in order to give the overmatch of mechanical properties. Nonetheless, a mixture of alloys from different classes of materials may promote metallurgical defects. It is necessary a good metallurgical compatibility of LAS with the Ni-based alloy cladding. In general, the mixture of steel and nickel-based alloy may cause solidification cracking due to nucleation of eutetic phases at the final stage of solidification, especially for the case of alloy 625[12,13,23–25]. Cieslak *et al*. evaluated the solidification crack of alloy 625 weld metal varying the fraction of Si, C and Nb[25]. The author highlighted a high solidification crack susceptibility characterized by wider fusion/solidification due to nucleation of eutetic phases such as NbC, Laves and M_6C at final of solidification[25]. In this case, the Nb shown a more deleterious consequences than observed for Si and C addition[25]. Therefore, a concise selection of materials is necessary for mixture with LAS aiming to avoid solidification defects.

There are some Ni-based alloys strengthened by solid solution from the same class of alloy 625, that may figure as alternative to solve this challenge. The alloy C276, as alloy 625, was equally developed on 60's decade[15,26]. This alloy was designed with residual fraction of Si and C, in order to avoid solidification cracks[15,26]. The alloy 686, from the third generation of Ni-Cr-Mo has a great corrosion resistance without reports concerning solidification cracks[11,15,26–32]. The alloy 22, similar to alloy 686 was designed as a new insight of alloy C276, where they were combined a higher Cr content, a lower quantity of Mo and with W addition, in order to improve the localized corrosion resistance[33,34]. The alloy 59 considered a 'pure' alloy from the Ni-Cr-Mo class, considering its chemical composition[26]. It was designed to show a great thermal stability, low tendency to nucleation of secondary phases and, consequently, a great corrosion resistance[15,26]. The alloy 617 is another option for this application, considering its great hot corrosion resistance[35]. This alloy has been widely used in nuclear industries because of its exceptional properties of high temperature strength and creep resistance, due to high Cr, Co and Mo content[35]. Finally, the new alloy 680 figure as a high strength alloy, designed especially to girth welding of high strength steel riser internally cladded with alloy 625. The massive addition of alloying elements such as Cr, Mo, W, Nb and Ti, provides an overmatch on mechanical properties, including yield strength.

Even with few alloys, it is necessary refine the material selection before to perform an experimental study. In this context, thermodynamic simulations represents a powerful tool in materials selection field, which allows to predict several physical and chemical properties of these materials[36,37]. Based on classical solidification model of Scheil-Gulliver is possible

predict details of material characteristics such as the solidification range, phase nucleation reactions, the composition and amount of each predicted phase, all of which gave support to select the most appropriate alloys for a specific welding application, in terms of solidification cracking susceptibility.

In order to propose new solutions to girth welding problems related to dissimilar welding of API 5L X65 steel pipes, used in the oil & gas industry as submarine risers and flowlines, the present study simulated the solidification of mixture of AWS ER 100S-G with Ni-based alloys from Ni-Cr-Mo, Ni-Cr-Co-Mo and Ni-Cr-Mo-W-Nb-Ti classes, in order to evaluate the susceptibility to solidification cracking. Thus, the solidification of AWS ER 100S-G was simulated under various conditions by varying the dilution levels with the alloys 625, 686, C276, 22, 59, 617 and 680, aim to the selection the better alloys and the most suitable dilution level for this application.

5.3 Experimental procedure

The present study is focused on evaluating the dilution effect of the AWS ER100S-G steel, named here as low alloy steel (LAS) filler metal. For the 1st and 2nd passes were defined as filler metal one of the Ni-based alloys selected in this study, in order to guarantee a corrosion resistance similar to alloy 625 cladding of pipe on the root region. Thus, when LAS is deposited on 2nd Ni-based alloy pass, it will dilute and change its chemical composition, originating a novel alloy with chemistry and mechanical properties very specific. Figure 5-1 shows, in details, the sequence of the deposition of the welding passes to fill the joint. The LAS will dilute with nickel alloy present on 2nd pass, which is the same of cladding. The mixture cause addition of alloying elements, such as Ni, Cr, Mo, W, Nb and Ti, typically presents on Ni-based alloys. As the other LAS passes are deposited, the effect of dilution with nickel-based alloys will decrease, leading the subsequent passes more and more to LAS chemical composition. The dilution effect with steel pipe was not take into account, considering the similarity with LAS.

Table 5-1 shows the chemical compositions of all the alloys used in this study. The chemical composition of each alloy was obtained following the recommendations of the AWS A5.34 standard and the measurements were performed by optical emission spectroscopy, except for the alloys C276 and 617, where the chemical composition was based on results reported in the literature[38,39].

Figure 5-1. Schematic of joint welding.

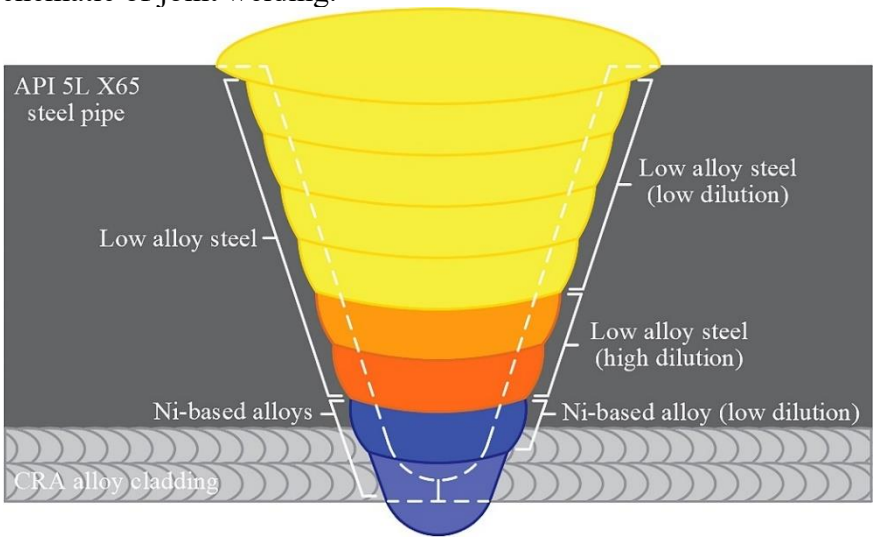

Source: Developed by the author.

Table 5-1. Chemical composition of the alloys used in this study.

Chemical composition of alloys								
Elements	Alloy 625 ER NiCrMo-3	Alloy 686 ER NiCrMo-14	Alloy C276 ER NiCrMo-4	Alloy 22 ER NiCrMo-10	Alloy 59 ER NiCrMo-13	Alloy 617 ER NiCrCoMo-1	Alloy 680 ER NiCrMoWNbTi-1	AWS ER 100S-G steel
Fe	0.09	0.38	6.50	4.96	0.77	0.75	0.55	97.47
C	0.1	0.01	0.20	0.015	0.01	0.06	0.05	0.11
Mn	-	0.24	0.85	0.12	0.23	-	-	1.17
Si	-	-	0.05	-	-	0.11	-	0.28
P	0.02	0.02	-	0.02	0.015	-	-	0.012
S	0.015	0.02	-	0.01	0.005	-	-	0.004
Ni	65.22	58.07	58.00	57.35	60.42	54.28	61.20	0.34
Cr	21.67	20.66	15.50	21.05	22.78	21.80	19.94	0.12
Mo	8.81	16.4	15.20	13.15	15.4	9.05	6.32	0.14
W	-	3.98	3.10	2.97	-	-	6.91	-
Re	-	0.05	-	0.06	-	-	-	-
Cu	-	-	0.35	-	0.05	-	-	0.18
Nb	3.73	-	-	-	0.06	-	3.58	0.03
Al	-	-	-	-	-	1.25	-	0.04
V	0.05	0.05	0.13	0.03	0.15	0.06	0.04	0.06
Ti	0.17	0.06	-	-	-	0.25	1.46	-
Co	0.06	0.05	0.12	0.25	0.03	12.45	-	0.04
Hf	0.01	-	-	0.01	-	-	-	-
Ta	0.02	-	-	0.06	0.01	-	-	-
Zn	0.05	0.06	-	-	0.07	-	-	-

Source: Developed by the author.

The dilution levels of: 5%, 10%, 15%, 20%, 30%, 40% and 50% were used for the simulation of the LAS pass. The dilution level is related to the amount of base metal that melted and mixed with the filler metal to produce the fusion zone. Thereby, a dilution level of 30%. means that 30% of base metal is included in the chemical composition of the fusion zone. High dilution levels such as 40% and 50% are uncommon in practice, but they are important to understand this tendency of this metallurgical phenomenon. Equation 1 estimates the chemical composition of the fusion zone considering the different levels of dilution (D), the chemical compositions of the base metal (C_{BM}) and the filler metal (C_{FM}).

$$C_{FZ} = D(C_{BM} - C_{FM}) + C_{FM} \quad (1)$$

The thermodynamic simulations were based on the classical solidification model of Scheil-Gulliver, performed using the commercial software ThermoCalc®. The Scheil-Gulliver model assumes there is no diffusion of elements in the solid phases, which means that there is a fast solidification with a high segregation of elements during the solidification[40]. On the other hand, the model considers the total mixture of elements in the liquid phase, and that in the solid/liquid interface there is equilibrium[40]. Solidification in welding processes occurs quickly, and various studies in the literature have confirmed the accuracy of Scheil-Gulliver models to simulate solidification of alloys for welding processes[11,12]. Equation 2 shows the mathematical model proposed by Scheil-Gulliver, where C_s, f_s, C_o and k represent the solid chemical composition, the solid fraction, the nominal chemical composition of the alloy and the partition coefficient, respectively[5].

$$C_s = kC_0(1 - f_s)^{k-1} \quad (2)$$

The partition coefficient k of all elements during the solidification can be found using Equation 2. An element that has $k>1$ means that this element has a tendency to be incorporated by the solid phase during the solidification[11–13,29]. On the other hand an element with $k<1$, indicates that this element will probably be segregated by the solid phase, thus making the liquid rich in this alloying element[11–13,29]. Thus, this phenomenon favors the transformation of the remaining liquid into secondary phases as its chemical composition differs from the alloy. In the case of Ni-based alloys, the nucleation of eutectic phases is common, and this normally increases the susceptibility to solidification cracking due to the low melting point of these phases.

5.4 Results and Discussion

5.4.1 Simulation of the solidification of the LAS

Initially, steel without dilution was simulated to obtain the solidification of the pure filler metal, which corresponds to the 0% dilution level. Figure 5-2 shows the solid evolution in function of temperature, and predicted that the δ ferrite would be the first solid phase. As the δ ferrite volume grew, some elements were solubilized by its body centered cubic (BCC)

structure, while other elements, such as Ni, Mn, Mo, Si and C, were rejected enriching the liquid portion. Thus, after 85% of the solid phase had nucleated in equilibrium with the liquid phase, the γ phase nucleated, naturally with a face centered cubic (FCC) structure.

After the nucleation reaction of the γ phase the solidification rate of the system was seen to fall drastically. During the reaction of L + δ the solidification rate was approximately 2.5 X 10^{-2} f_s/°C, while the solidification rate after the L + δ + γ reaction fell approximately one order of magnitude, solidifying at 8.4 X 10-4 f_s/°C. Thus, the solidification was most likely increased by the γ phase nucleation. Table 5-2 shows the fraction of each phase for the main temperatures predicted by the thermodynamic simulation. The growth of δ ferrite was notably suppressed after the γ phase reaction, thus indicating that the γ phase nucleation was principally responsible for expanding the solidification range, as shown in Figure 5-2.

Figure 5-2. Solidification simulation of the LAS steel.

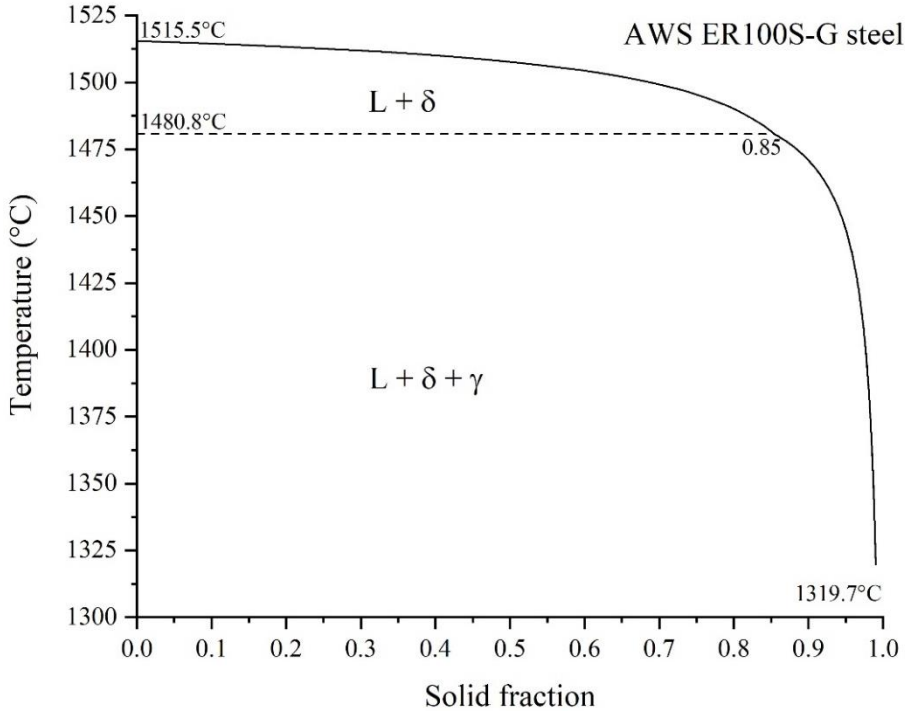

Source: Developed by the author.

Table 5-2. Solidification simulation of the LAS based on Scheil-Gulliver model.

Solidification simulation of AWS ER100S-G steel			
Temperature	Solid fraction	δ ferrite	γ phase
1515.5°C	0.04%	0.04%	0%
1480.8°C	85.4%	85.4%	0.12%
1319.7°C	99.0%	85.4%	13.6%

Source: Developed by the author.

Even with the increase in the solidification range, as a consequence of the γ phase nucleation, the simulation did not predicte any low melting point phases, which are notably known to cause solidification cracking. Moreover, the literature points out that when solidification begins with the δ ferrite, then normally, this alloy shows a low solidification cracking susceptibility[41,42]. In general, each crystalline structure has a different expansion coefficient and the configuration of the FCC atoms has an expansion coefficient greater than the BCC crystalline structure[43]. Naturally, at high temperatures the solid phases are in a state of high expansion, which promotes a tensile stress due contraction at final stage of the solidification process. This tensile stress is proportion to how much the phase expanded during the solidification process. For this reason and others, such as its high solubility of deleterious elements such as S and P, the BCC alloys show a lower susceptibility to solidification cracking in comparison with FCC alloys[44]. Brooks and Lambert evaluated austenitic stainless steels with different fractions of S and P and, the authors concluded that the conditions, in which a high fraction of δ ferrite were formed, presented a low susceptibility to solidification cracking even containing S and P in high concentrations[44].

5.4.2 Effect of dilution on the solidification simulation of the LAS

The previous topic discussed the solidification simulation of the LAS pass without considering any dilution, which represents in practice, the final passes to fill the joint. In this case the LAS pass will only mix with the API 5L X65 steel pipe. Now the study will focused on the evaluation of the effect of dilution of the LAS pass with the Ni-based alloy, which was deposited in the 1st and 2nd passes of the proposed joint. For this, it were predicted the chemical composition of fusion zone for several dilution levels for each Ni-based alloy diluted with AWS ER 100S-G steel. Tables 5-3 to 5-9 represent the mixture conditions of alloy 625, 686, C-276, 22, 59, 617 and 680, respectively.

Figure 5-3 shows the initial and final temperatures of solidification, as well as the solidification range for each dilution level for the deposition of AWS ER100S-G on alloy 625. In general, there was a tendency to increase the solidification range as the dilution level increased, except for the 5% dilution level. Two antagonistic phenomena promoted different effects on the solidification range in this case. The first is considered to be a decrease in the initial solidification temperature (T_{Si}) influenced by a reduction in the Fe content that is caused by the participation of Ni-based alloy in the fusion zone chemical composition, and which increases as the dilution level increases. The second phenomena and more effective is referred

to as the strong reduction of the final solidification temperature (T_{Sf}), which is probably a consequence of the nucleation reaction of low melting point phases. An increase of alloying elements from Ni-based alloy probably promotes a super saturation of the solute, which segregates to the liquid portion making the nucleation of secondary phases possible. In order to improve the discussion concerning the dilution effect on the solidification of these alloys, a Scheil-Gulliver diagram was constructed, as shown in Figure 5-4, for the dilution levels with the highest and lowest solidification ranges.

Table 5-3. Chemical composition for all dilution levels of the LAS with the Ni-based alloy 625.

Dilution of AWS ER100S-G steel filler metal with alloy 625								
Ele/Dil	0%	5%	10%	15%	20%	30%	40%	50%
Ni	0.823	4.047	7.271	10.495	13.719	20.167	26.615	33.063
Co	0.000	0.003	0.006	0.009	0.012	0.018	0.024	0.030
Cr	0.120	1.197	2.275	3.352	4.429	6.584	8.738	10.893
Cu	0.113	0.107	0.102	0.096	0.090	0.079	0.068	0.057
Fe	96.528	91.706	86.884	82.062	77.239	67.595	57.951	48.307
Hf	0.000	0.000	0.001	0.001	0.002	0.002	0.003	0.004
Mn	1.367	1.299	1.230	1.162	1.094	0.957	0.820	0.684
Mo	0.382	0.803	1.225	1.646	2.067	2.910	3.752	4.595
Nb	0.000	0.187	0.373	0.560	0.747	1.120	1.493	1.866
Si	0.623	0.591	0.560	0.529	0.498	0.436	0.374	0.311
Ta	0.000	0.001	0.002	0.003	0.004	0.007	0.009	0.011
Ti	0.000	0.008	0.017	0.025	0.034	0.051	0.068	0.085
V	0.000	0.002	0.005	0.007	0.009	0.014	0.019	0.024
C	0.044	0.047	0.050	0.053	0.056	0.061	0.067	0.072

Source: Developed by the author.

Table 5-4. Chemical composition for all dilution level of LAS with the Ni-based alloy 686.

Dilution of AWS ER100S-G steel filler metal with alloy 686								
Ele/Dil	0%	5%	10%	15%	20%	30%	40%	50%
Ni	0.823	3.685	6.547	9.409	12.272	17.996	23.720	29.445
Co	0.000	0.003	0.005	0.008	0.011	0.016	0.022	0.027
Cr	0.120	1.147	2.174	3.200	4.227	6.281	8.334	10.388
Cu	0.113	0.107	0.102	0.096	0.090	0.079	0.068	0.057
Fe	96.528	91.720	86.913	82.105	77.298	67.683	58.067	48.452
Mn	1.367	1.311	1.254	1.198	1.142	1.029	0.916	0.804
Mo	0.382	1.183	1.984	2.785	3.586	5.188	6.790	8.392
Re	0.000	0.003	0.005	0.008	0.011	0.016	0.022	0.027
Si	0.623	0.591	0.560	0.529	0.498	0.436	0.374	0.311
Ta	0.000	0.003	0.006	0.008	0.011	0.017	0.022	0.028
Ti	0.000	0.003	0.006	0.009	0.011	0.017	0.023	0.028
V	0.000	0.003	0.005	0.008	0.011	0.016	0.022	0.027
W	0.000	0.199	0.398	0.596	0.795	1.193	1.590	1.988
C	0.044	0.043	0.041	0.039	0.038	0.034	0.031	0.027

Source: Developed by the author.

Figure 5-4 shows that for the lowest dilution level, the simulation predicted a solidification path beginning with δ ferrite, while for the highest dilution level the solidification

began with the γ phase due the high fraction of Ni and other alloying elements from the dilution with the alloy 625[41,42]. This explains in part the reason for the low ΔT observed for the 5% dilution level, since the high fraction of the δ ferrite must solubilize a large amount of the alloying elements commonly segregated by the FCC structure[44]. A comparison with the LAS pass simulation discussed in Figure 5-2, shows that the 5% dilution level was the same for the nucleation reactions predicted for the LAS pass without any mixture with the Ni-based alloy, except by the nucleation of some carbides at the final stage of the solidification process. Thus, probably the addition of alloying elements such as Ni, Cr, Mo and Nb could promote changes in the micro chemical composition of the δ and γ phases leading to a reduction in the solidification range. Furthermore it is important to take in to account that the growth of the γ phase and carbides simultaneously may increase in the solidification rate.

Table 5-5. Chemical composition for all dilution levels of LAS with the Ni-based alloy C276.

Dilution of AWS ER100S-G steel filler metal with alloy C276								
Ele/Dil	0%	5%	10%	15%	20%	30%	40%	50%
Ni	0.823	3.692	6.561	9.430	12.298	18.036	23.774	29.512
Co	0.000	0.006	0.012	0.018	0.024	0.036	0.048	0.060
Cr	0.120	0.889	1.658	2.427	3.196	4.734	6.272	7.810
Cu	0.113	0.125	0.137	0.149	0.160	0.184	0.208	0.232
Fe	96.528	92.026	87.525	83.024	78.522	69.519	60.517	51.514
Mn	1.367	1.341	1.315	1.289	1.264	1.212	1.160	1.109
Mo	0.382	1.123	1.864	2.605	3.346	4.827	6.309	7.791
Si	0.623	0.594	0.565	0.537	0.508	0.451	0.394	0.336
V	0.000	0.007	0.013	0.020	0.026	0.039	0.052	0.065
W	0.000	0.155	0.310	0.465	0.620	0.930	1.240	1.550
C	0.044	0.043	0.042	0.041	0.040	0.037	0.035	0.032

Source: Developed by the author.

Table 5-6. Chemical composition for all dilution levels of LAS with the Ni-based alloy 22.

Dilution of AWS ER100S-G steel filler metal with alloy 22								
Ele/Dil	0%	5%	10%	15%	20%	30%	40%	50%
Ni	0.823	3.649	6.476	9.302	12.128	17.781	23.434	29.086
Co	0.000	0.012	0.025	0.037	0.050	0.075	0.100	0.125
Cr	0.120	1.166	2.213	3.259	4.306	6.398	8.491	10.584
Cu	0.113	0.107	0.102	0.096	0.090	0.079	0.068	0.057
Fe	96.528	91.949	87.371	82.792	78.213	69.056	59.899	50.741
Hf	0.000	0.000	0.001	0.001	0.001	0.002	0.003	0.004
Mn	1.367	1.305	1.242	1.180	1.117	0.993	0.868	0.743
Mo	0.382	1.020	1.658	2.296	2.935	4.211	5.487	6.764
Re	0.000	0.003	0.006	0.009	0.011	0.017	0.023	0.029
Si	0.623	0.591	0.560	0.529	0.498	0.436	0.374	0.311
Ta	0.000	0.003	0.006	0.009	0.012	0.018	0.024	0.031
V	0.000	0.001	0.003	0.004	0.006	0.009	0.012	0.015
W	0.000	0.148	0.297	0.445	0.593	0.890	1.186	1.483
C	0.044	0.043	0.042	0.040	0.039	0.036	0.033	0.030

Source: Developed by the author.

Table 5-7. Chemical composition for all dilution levels of LAS with the Ni-based alloy 59.

Dilution of AWS ER100S-G steel filler metal with alloy 59								
Ele/Dil	0%	5%	10%	15%	20%	30%	40%	50%
Ni	0.823	3.807	6.792	9.776	12.760	18.729	24.698	30.666
Co	0.000	0.002	0.003	0.005	0.006	0.009	0.012	0.015
Cr	0.120	1.253	2.386	3.518	4.651	6.917	9.182	11.448
Cu	0.113	0.110	0.107	0.104	0.101	0.095	0.088	0.082
Fe	96.528	91.740	86.952	82.164	77.375	67.799	58.223	48.647
Hf	0.000	0.000	0.000	0.001	0.001	0.001	0.002	0.002
Mn	1.367	1.310	1.253	1.197	1.140	1.026	0.912	0.799
Mo	0.382	1.133	1.884	2.635	3.386	4.887	6.389	7.891
Nb	0.000	0.003	0.006	0.010	0.013	0.019	0.026	0.032
Si	0.623	0.591	0.560	0.529	0.498	0.436	0.374	0.311
Ta	0.000	0.001	0.001	0.002	0.002	0.004	0.005	0.006
V	0.000	0.007	0.015	0.022	0.030	0.044	0.059	0.074
C	0.044	0.043	0.041	0.039	0.038	0.034	0.031	0.027

Source: Developed by the author.

Table 5-8. Chemical composition for all dilution levels of LAS with the Ni-based alloy 617.

Dilution of AWS ER100S-G steel filler metal with alloy 617								
Ele/Dil	0%	5%	10%	15%	20%	30%	40%	50%
Ni	0.823	3.496	6.169	8.842	11.514	16.860	22.206	27.552
Al	0.000	0.063	0.125	0.188	0.250	0.375	0.500	0.625
Co	0.000	0.623	1.245	1.868	2.490	3.735	4.980	6.225
Cr	0.120	1.204	2.288	3.372	4.456	6.624	8.792	10.960
Cu	0.113	0.107	0.102	0.096	0.090	0.079	0.068	0.057
Fe	96.528	91.739	86.950	82.161	77.372	67.794	58.217	48.639
Mn	1.367	1.299	1.230	1.162	1.094	0.957	0.820	0.684
Mo	0.382	0.815	1.249	1.682	2.116	2.982	3.849	4.716
Si	0.623	0.597	0.571	0.546	0.520	0.469	0.418	0.366
Ti	0.000	0.013	0.025	0.038	0.050	0.075	0.100	0.125
C	0.044	0.045	0.046	0.047	0.048	0.049	0.051	0.052

Source: Developed by the author.

Table 5-9. Chemical composition for all dilution levels of LAS with the Ni-based alloy 680.

Dilution of AWS ER100S-G steel filler metal with alloy 680								
Ele/Dil	0%	5%	10%	15%	20%	30%	40%	50%
Ni	0.823	3.842	6.861	9.880	12.899	18.937	24.976	31.014
Cr	0.120	1.111	2.102	3.092	4.083	6.065	8.046	10.028
Cu	0.113	0.107	0.102	0.096	0.090	0.079	0.068	0.057
Fe	96.528	91.729	86.930	82.131	77.332	67.734	58.136	48.538
Mn	1.367	1.299	1.230	1.162	1.094	0.957	0.820	0.684
Mo	0.382	0.679	0.976	1.273	1.570	2.163	2.757	3.351
Nb	0.000	0.179	0.358	0.537	0.716	1.074	1.432	1.790
Si	0.623	0.591	0.560	0.529	0.498	0.436	0.374	0.311
Ti	0.000	0.073	0.146	0.219	0.292	0.437	0.583	0.729
V	0.000	0.002	0.004	0.006	0.008	0.012	0.016	0.021
W	0.000	0.345	0.691	1.036	1.381	2.072	2.762	3.453
C	0.044	0.042	0.041	0.039	0.037	0.033	0.029	0.025

Source: Developed by the author.

The evolution of the solidification of the 5% and 30% levels indicates that in both cases the solidification rate was relatively high until 80% of the solid phases. After this point,

the solidification behavior changes by decreasing subtly with the reduction of temperature, even without a new nucleation reaction. This is probably associated with the enrichment of the liquid by solute, which changes the chemical composition of γ phase that will solidify. Moreover, with this high concentration of alloying elements in the liquid makes the nucleation of secondary phases such as carbides rich in Nb, Ti and Mo possible. These carbides were predicted for both these levels and this result was expect since carbon has a high diffusivity in the matrix and a great affinity with the alloying elements cited. The nucleation of carbides has a good effect, preventing solidification cracks. The high affinity of carbon with niobium reduces the fraction of Nb disponible to Laves phase nucleation.[25,45].

Figure 5-3. The solidification simulation results for all dilution levels of the LAS deposited on the Ni-based alloy 625.

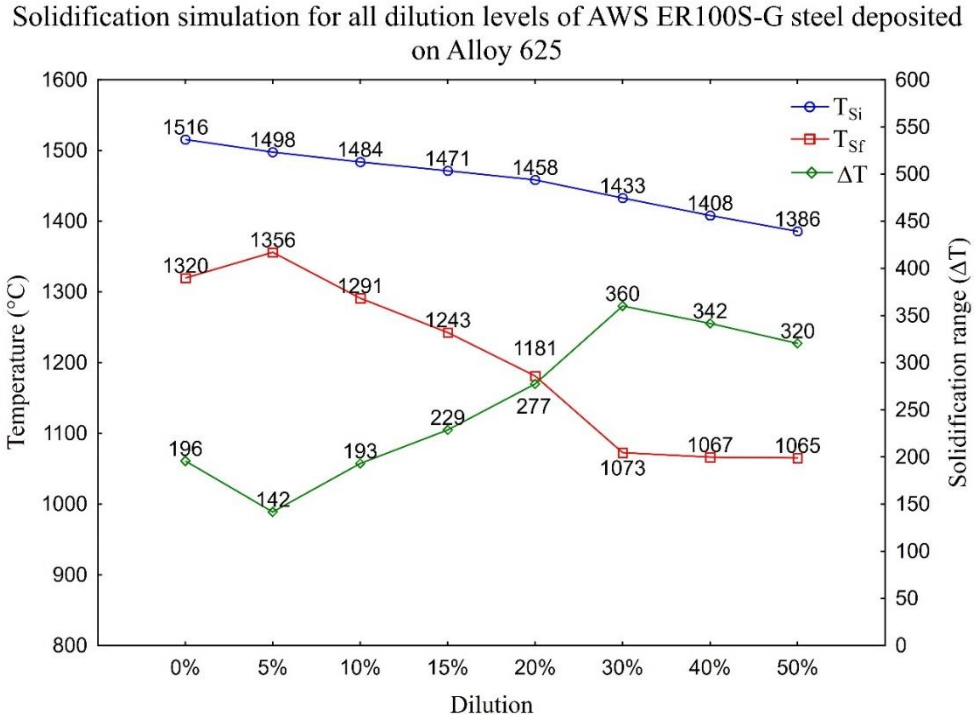

Source: Developed by the author.

The simulation predicted several secondary phase for the 30% dilution level at the end of the solidification process, such as Laves phase, and the M_6C, Ni_3Nb and μ phases. Certainly, these phases were determinant in the expansion of the solidification range for this dilution level. The enrichment of the alloying elements such as Nb, Cr, Mo, Ti and C makes the nucleation of these phases possible[11–13,25,29,46]. Among the predicted phases, the Laves is the most deleterious phase in terms of solidification cracking. The literature highlights that Laves phase nucleated at the end of the solidification process, located along the solidification grain

boundaries, reduces the mechanical resistance between them. Even though hot cracking is a complex phenomenon, the nucleation of Laves phase is an important factor, since the Laves phase is commonly associated to solidification cracking[47].

Figure 5-4. Solidification simulation diagrams of the deposition of LAS on the alloy 625 for the dilution levels of a) 5% and b) 30%.

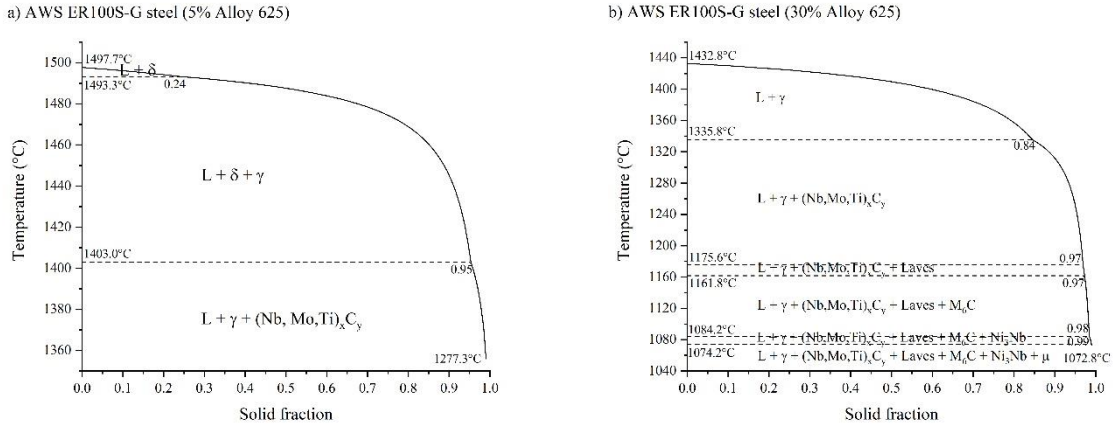

Source: Developed by the author.

Figure 5-5 shows the effect of dilution on the solidification simulation when the LAS pass is deposited on alloy 686. Differently from what was seen for the mixture with alloy 625, the increase of dilution promoted a decrease in the solidification range in most cases. The T_{Si} was reduced gradually with the increase of dilution, probably as an effect of a reduction of the Fe fraction. The T_{Sf} showed a more complex behavior, but without any drastic reduction, normally observed when there is a low melting point phase at the end of the solidification process. Figure 5-6 shows the 5% and 30% dilution levels, in which the simulation predicted the highest and lowest ΔT, respectively. The 5% dilution level started its solidification process as the δ ferrite until 52% of the solid phase fraction after this, the simulation predicted the nucleation reaction of γ phase. Naturally, the increase of Ni reduced the amount of δ ferrite, enlarging thus the solidification range of the alloy. Different from observed for the 5% dilution level of the mixture with the alloy 625, the absence of Nb, even in a small amount, may be the reason for these opposing results.

Figure 5-6 shows the 30% dilution level and in this case only the γ phase and M_6C carbide were predicted. The increase in dilution level caused an addition of alloying elements from the mixture with the alloy 686, exceeding the solubility of γ phase. Thus, there is a greater amount of alloying elements disponible to segregate and, consequently, to nucleate as carbides at the final stage of solidification. Beside this, the simultaneous solidification of γ phase and

M_6C carbide caused the increase of solidification rate. This phenomenon explains the tendency to reduction of ΔT with the increase in dilution level observed in Figure 5-5.

Figure 5-5. The solidification simulation results for all dilution levels of the LAS deposited on the Ni-based alloy 686.

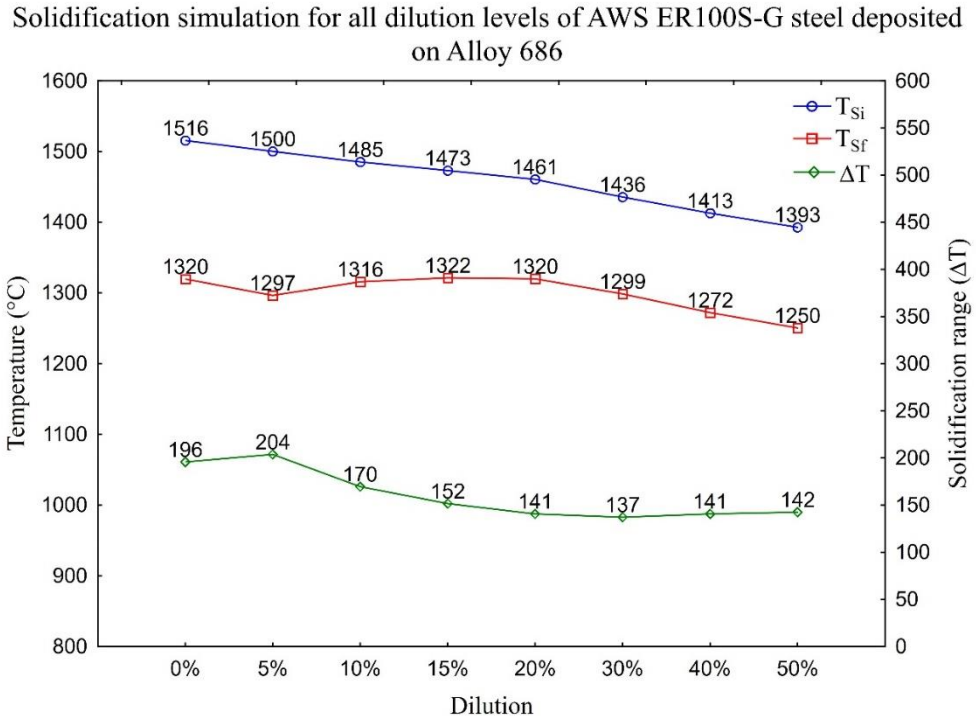

Source: Developed by the author.

Figure 5-6. Solidification simulation diagrams of the deposition of LAS on the alloy 686 for the dilution levels of a) 5% and b) 30%.

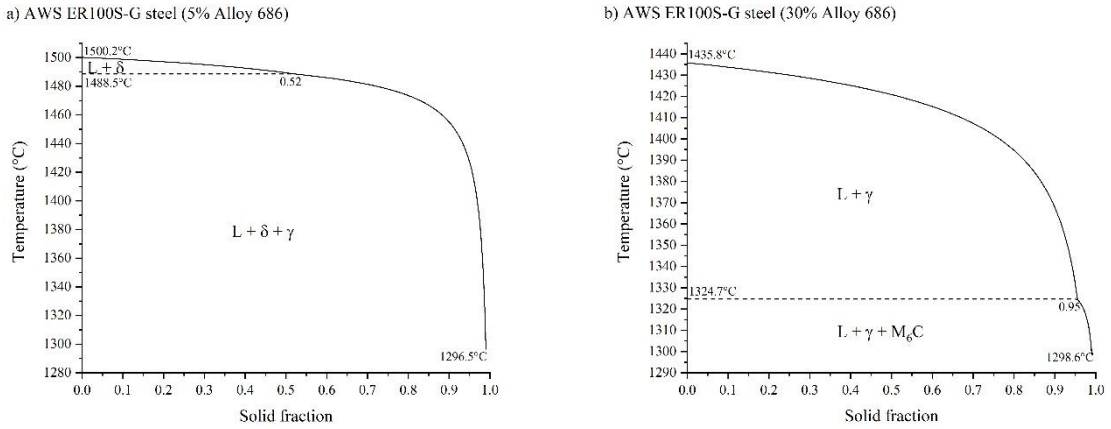

Source: Developed by the author.

Studies evaluating the mechanical behavior and the microstructure of alloy 686 in the as-welded condition point out that solidification cracks were not seen[11,28,29], even for dissimilar welding with high dilution levels[11,31,32]. According to the literature, different

secondary phases like the σ, P and μ phases were identified based on selected area electron diffraction in TEM analysis[29]. These phases depend on significant alloying elements, especially alloying elements like Mo and W, which segregate to make their nucleation possible. In terms of solidification cracking, different from Laves phase, these secondary phases do not reduce the solidification range drastically. Therefore, it is reasonable to assume that the conditions simulated considering the mixture of AWS ER100S-G steel with alloy 686 will probably show in practice a low susceptibility to solidification cracking.

Figure 5-7 highlights the simulation results for the solidification process referring to the dilution effect of the deposition of AWS ER100S-G steel with the alloy C276. In general, the results obtained were similar to the predicted ones for the mixture of the LAS pass with the alloy 686. This result was expected considering that the composition of these Ni-based alloys only has a few differences in terms of the Fe, Cr and Mo fractions. However, it is important to establish a comparison between them, since the Fe fraction present in alloy C276 elevated the T_{Si} in all cases when compared with the mixture of steel with alloy 686. The opposite behavior was observed in Figure 5-5, in which the Fe fraction decreased when the dilution levels was increased, reducing thus the T_{Si}. In all cases, the melting point of Fe, which is slightly higher than Ni, for example, caused the effect observed on simulations[48]. In addition, the lower contents of Cr and Mo in alloy C276 in comparison with alloy 686 plays an important effect, especially on the reduction of secondary phases, decreasing thus the solidification range. Figure 5-8 shows the evolution of the solid fraction as a function of temperature for the highest and lowest solidification ranges.

The simulation results for 5% dilution level with alloy C276 predicted a high fraction of δ phase nucleated at the begin of solidification, followed by nucleation of G phase. On the other hand, the simulation for 30% dilution level did not predict the δ phase, while the nucleation of M_6C was predicted at the final stage of solidification. These results were similar to simulated for mixture of LAS with alloy 686, in terms of predicted phases by simulation. The differences in terms of ΔT between the cases discussed here were related basically to the amount of Fe, Cr and Mo content in C276 and 686 alloys.

Figure 5-9 shows the dilution effect on the solidification simulation when the LAS pass is deposited on alloy 22. Again, there was a reduction in ΔT, when the dilution was increased. The dilution effect showed the same behavior as observed for the mixture of the LAS pass with the alloys 686 and C276. Figure 5-10 highlights the evolution of the solid fraction in function of the temperature for the highest and lowest solidification ranges. The simulation

predicted, for the low dilution level, only δ ferrite and the γ phase in equilibrium with the liquid, while for the high dilution level the thermodynamic simulation only predicted the formation of the γ phase and M_6C carbides.

Figure 5-7. The solidification simulation results for all dilution levels of the LAS deposited on the Ni-based alloy C276.

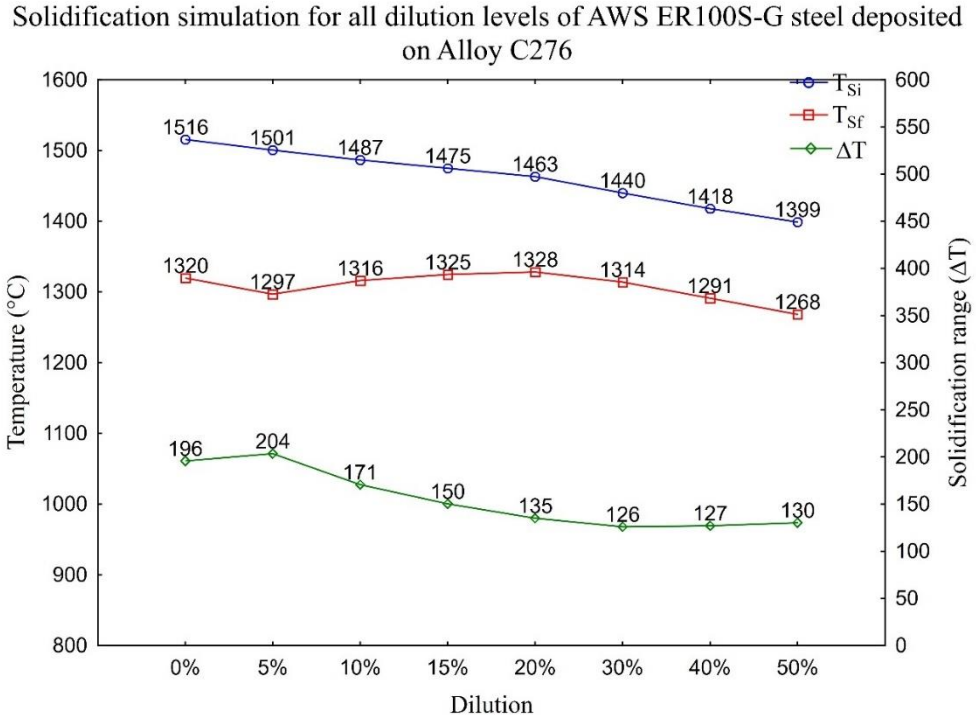

Source: Developed by the author.

Figure 5-8. Solidification simulation diagrams of the deposition of LAS on the alloy C276 for the dilution levels of a) 5% and b) 30%.

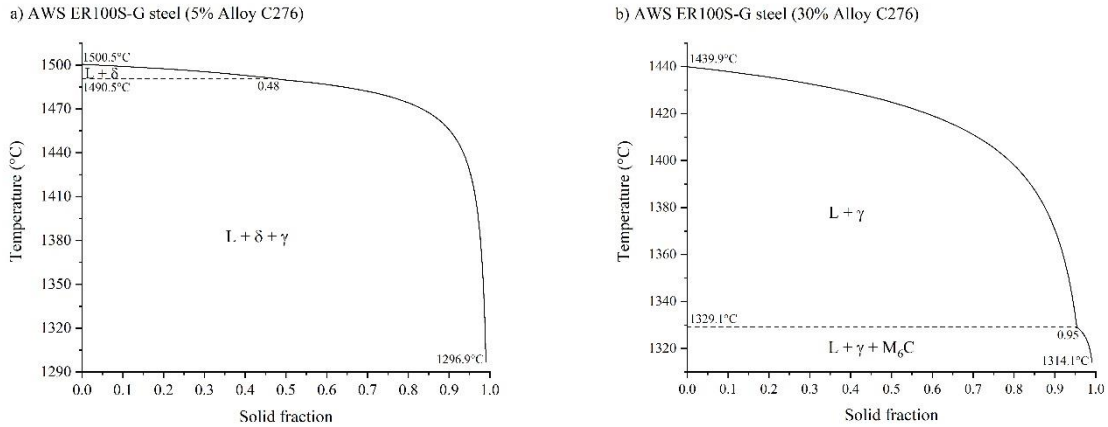

Source: Developed by the author.

Figure 5-11 highlights the solidification simulation results referring to the dilution effect of the deposition of LAS with the alloy 59. The results were similar to those observed for

the other Ni-based alloys from the Ni-Cr-Mo class, except for the alloy 625 that contains Nb in its chemical composition. Figure 5-12 shows the highest and lowest solidification range obtained for the simulated cases. As observed previously, the increase in the dilution level suppressed the nucleation reaction of δ ferrite, while allowing the nucleation of M_6C, as a consequence of the addition of the alloying elements from the Ni-based alloy.

Figure 5-9. The solidification simulation results for all dilution levels of the LAS deposited on the Ni-based alloy 22.

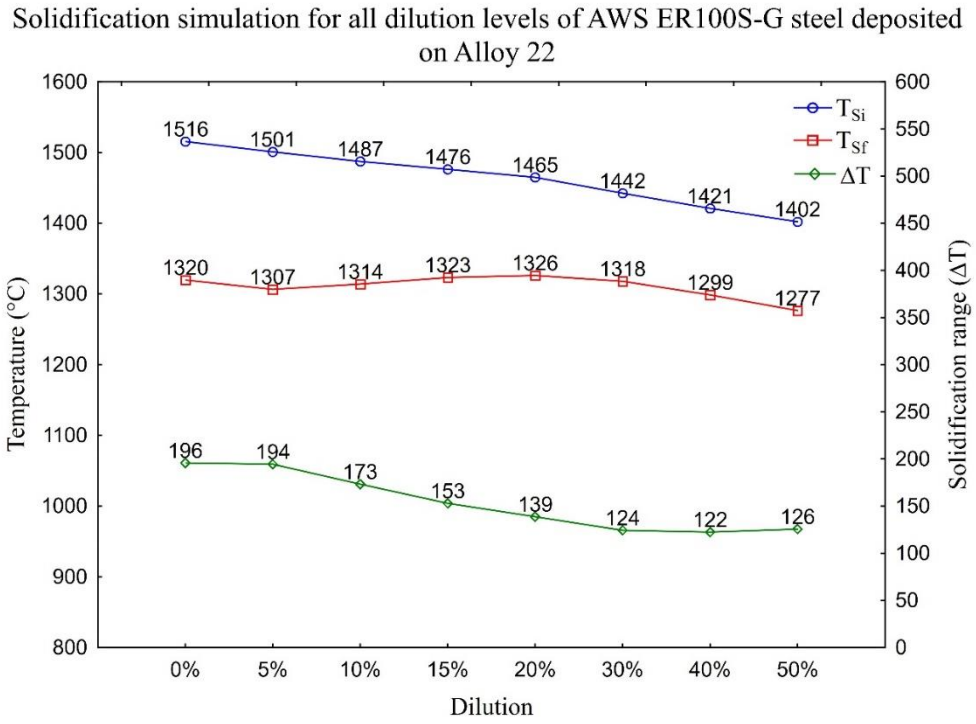

Source: Developed by the author.

Figure 5-10. Solidification simulation diagrams of the deposition of LAS on the alloy 22 for the dilution levels of a) 5% and b) 40%.

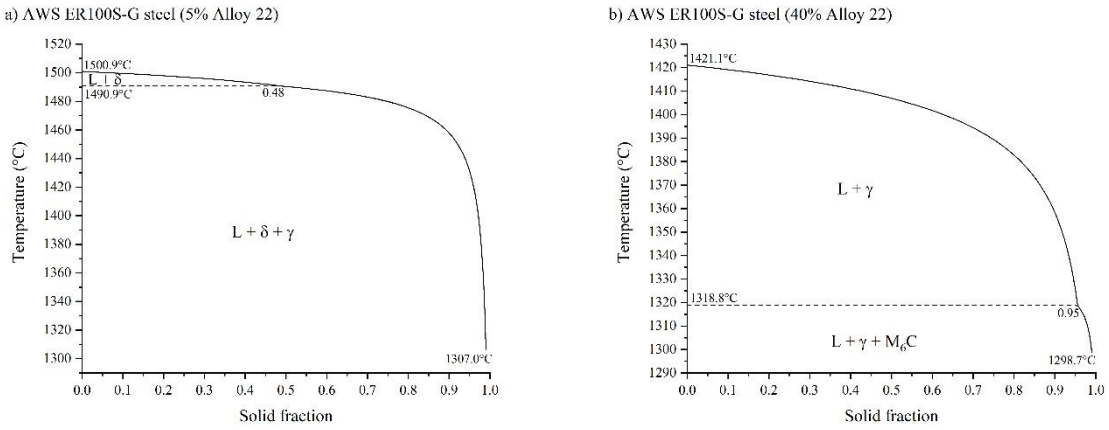

Source: Developed by the author.

Figure 5-11 The solidification simulation results for all dilution levels of the LAS deposited on the Ni-based alloy 59.

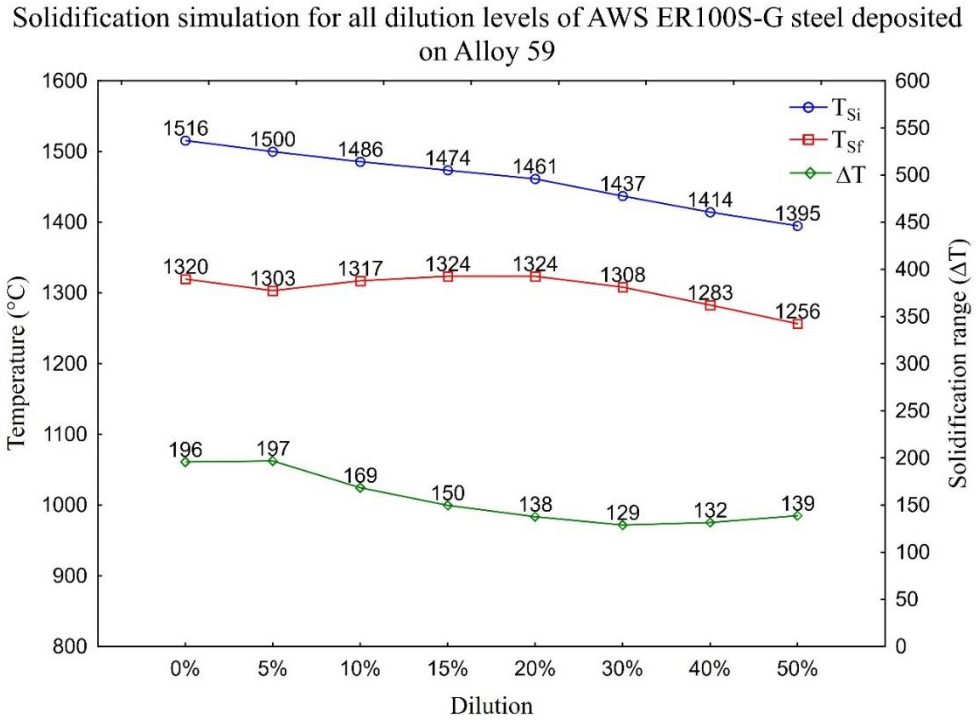

Source: Developed by the author.

Figure 5-12. Solidification simulation diagrams of deposition of LAS on the alloy 59 for the dilution levels of a) 5% and b) 30%.

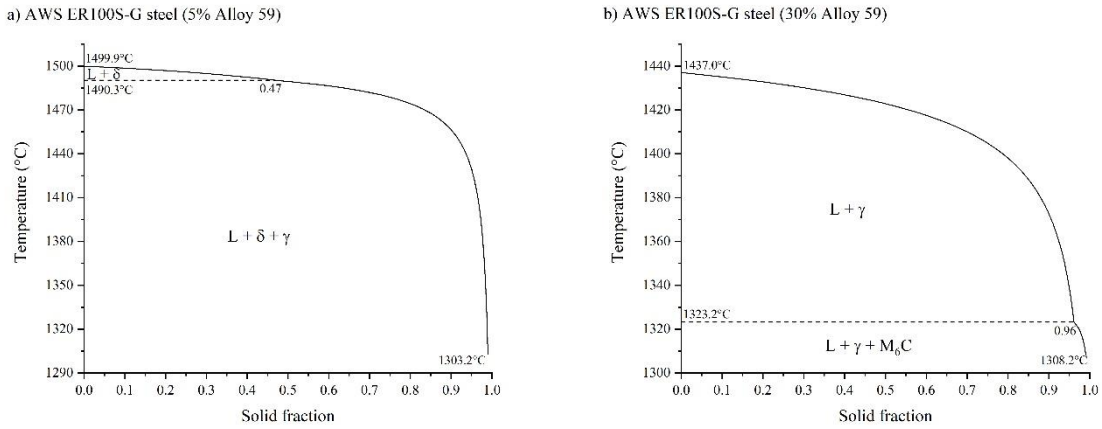

Source: Developed by the author.

Figure 5-13 shows all results for the evaluation of the effect of dilution for the mixture of LAS pass with the only alloy in the study from the Ni-Cr-Co-Mo family, the alloy 617. Even with a reduction tendency of the solidification range due to an increase of the dilution, the predicted values of ΔT were slightly larger than those predicted for the Ni-Cr-Mo alloys without Nb. This could be related to the T_{Si}, for which values superior than the one simulated for the mixture with Ni-based alloys containing Fe in solution were predicted. Co-

addition may leaded to this phenomenon. Figure 5-14 shows in details the solid evolution as a function of temperature for the 5% and 40% dilution levels. Carbides were predicted for the low dilution level, similar to that observed the for mixtures with alloy 625. This occurred due to the higher carbon content of this Ni-based alloy in comparison with the simulated chemical compositions referred to in alloys 22, C276, 686 and 59. Figure 5-14 shows the simulation predicted for the high dilution level in the nucleation reaction of the γ phase, the M_6C and complex $(Ti,Cr)_xC_y$ carbides, similar to that predicted for the Ni-Cr-Mo alloys without Nb.

Figure 5-13. The solidification simulation results for all dilution levels of the LAS deposited on the Ni-based alloy 617.

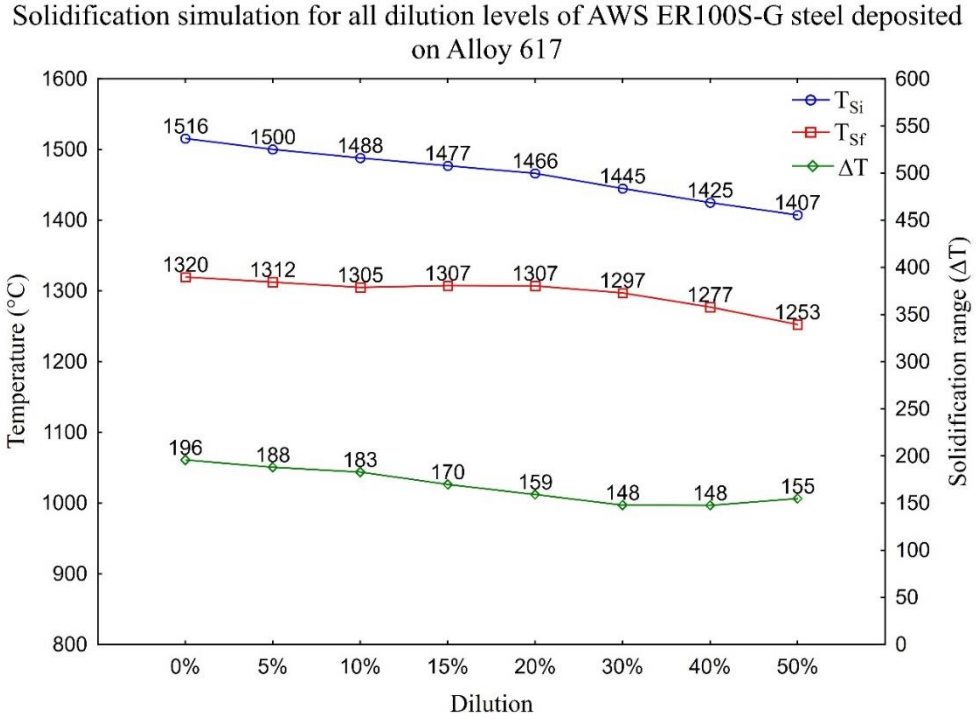

Source: Developed by the author.

The last Ni-based class evaluated was the Ni-Cr-Mo-W-Nb-Ti. The alloy 680 is the only alloy from this class. Recently patented, the alloy 680 was developed to solve new offshore challenge[49]. This alloy is considered a solid solution Ni-based alloy, and its mechanical properties in the as-welded state may show a yield strength superior to 600 MPa[49]. Nonetheless, the high addition of Nb and Ti could probably lead to a precipitation strengthened with adequate aging heat treatments. The simulation performed in Figure 5-15 shows the effect of dilution on the solidification behavior when deposited as the LAS pass on alloy 680. Similar to that observed for the mixture with alloy 625, the 5% dilution level promoted a reduction in the ΔT. This is probably a consequence of a small amount of Nb segregated by the δ ferrite to

the liquid portion, which may elevate the solidification rate of the subsequent nucleation reactions of γ phase. These Ni-based alloys were the only simulated alloys with a significant amount of Nb

Figure 5-14. Solidification simulation diagrams of deposition of LAS on the alloy 617 for the dilution levels of a) 5% and b) 40%.

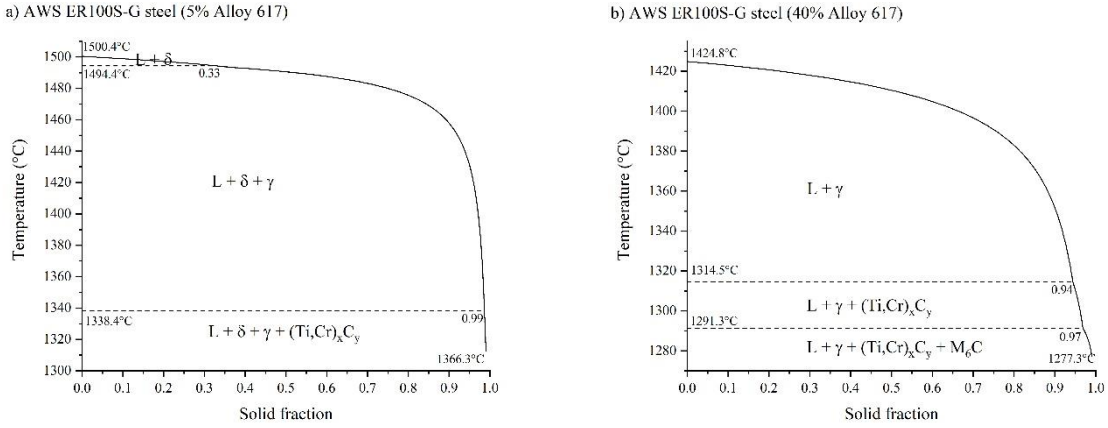

Source: Developed by the author.

Figure 5-15. The solidification simulation results for all dilution levels of the LAS deposited on the Ni-based alloy 680.

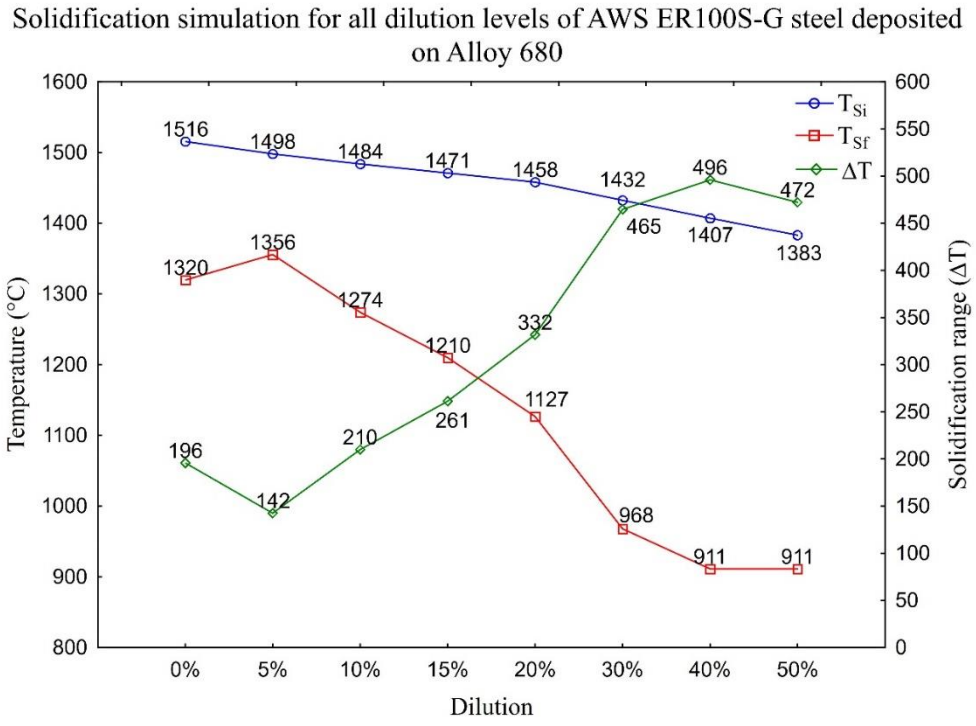

Source: Developed by the author.

Figure 5-16 shows in detail the evolution of the solidification process for the 5% and 40% dilution levels. A low ΔT was predicted for the low dilution level and the

thermodynamic simulation pointed out the nucleation reactions of δ ferrite, followed by the γ phase and carbides rich in Nb, Ti and Mo. The simulation predicted several secondary phases for the high dilution level: complex carbides, Laves, Ni_3Nb, G, σ and Ni_3Ti phases. These secondary phases were clearly responsible for enlarging the solidification range, especially the Laves phase. The Ni_3Nb and Ni_3Ti phases naturally predicted due to the high amount of Nb and Ti segregated to the liquid portion at the end of the solidification process. According to the literature Ni_3Ti has a significant effect on the mechanical properties, including introducing creep resistance as a consequence of the blocking dislocation movement[50]. The high amount of Nb, Ti and Si allowed the simulation to predict this G phase silicate[50,51].

Figure 5-16. Solidification simulation diagrams of deposition of LAS on the alloy 680 for the dilution levels of a) 5% and b) 40%.

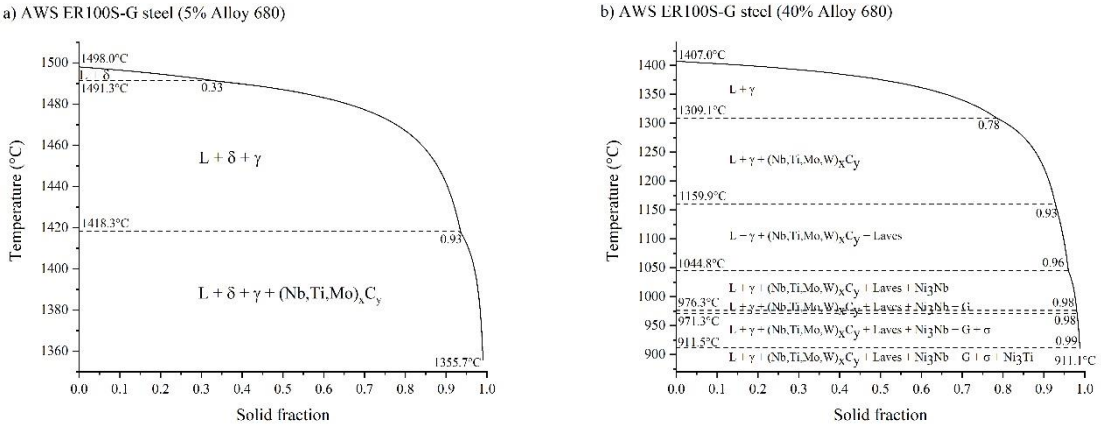

Source: Developed by the author.

The simulation results of the main alloys from the Ni-Cr-Mo class confirms that small chemical changes in important alloying elements such as Cr, Mo, W and Fe do not cause significant changes in the nucleation of secondary phases, except in their volume fraction. Moreover, most importantly, these chemical changes do not cause any significant increase in the solidification range and, consequently, no increase solidification cracking susceptibility. Nonetheless, the addition of Nb combined with Fe from the LAS pass made the prediction of the Laves phases during the final stage of the solidification process possible. The evaluation of alloys from other classes such as Ni-Cr-Co-Mo and Ni-Cr-Mo-W-Nb-Ti corroborate with this hypothesis, considering that alloy 680 showed a solidification behavior similar to that predicted for alloy 625, while alloy 617, on the other hand, showed solidification results similar to those observed for alloys Ni-Cr-Mo without Nb. These results may lead to an important assumption in terms of material selection of Ni-based alloys: for nickel alloys without Nb, the addition or

reduction of alloying elements, such as Co, Cr, Mo, W and Fe, has low effect on ΔT, while for Ni-based alloys with Nb, the addition of Fe, Si, Ti and C, has a great effect on enlargement of ΔT.

Considering the ΔT results for the deposition of the LAS pass on the Ni-based alloys evaluated, the 686, C276, 22, 59 and 617 alloys showed the best results, in terms of solidification cracking susceptibility. The alloys 625 and 680 that contained high amounts of Nb as an alloying element showed the highest tendency to solidification cracks in comparison with the other Ni-based alloys in this study. The mixture of Nb and Ti from the Ni-based alloy with the Fe, Si and C of steel makes the prediction of deleterious phases possible, based on thermodynamic simulation, especially Laves phase that enlarges the solidification range.

Nonetheless, the solidification cracking is a complex phenomenon, where the metallurgical analyses performed in the present study represents a strong factor to this complex equation, but is not the only effect to be considered[20]. Mechanicals factors, especially the stress distribution has strong effect on solidification cracking mechanism. The solidification shrinkage due liquid-to-solid transformation and thermal contraction represents some of main factor responsible to cause rupture between solidification grain[20]. Considering these factors, it is premature obtain a definitive conclusion about solidification crack for the system evaluated, but based on results shown, for the mixture of LAS with 625 and 680 alloys, is recommend the welding only for low dilution levels, up to 5%, while for welding with 686, C276, 22, 59 and 617 alloys a large field of dilution levels are allowable to weld.

5.5 Conclusion

Based on the simulated results produced and discussed in the present study entitle "Thermodynamic simulation of joint welding solidification of API 5L X65 steel pipe using low alloy steel and Ni-based alloys", it was possible to conclude that:

- The thermodynamic simulation of the solidification based on the classical model of Scheil-Gulliver demonstrated to be a powerful model to predict the solidification of weld metals. The analyses were able to identify the best alloys for the applications contemplated.
- In almost all simulated cases the γ-FCC was predict as the matrix phase, except for the 5% dilution level of the filling pass with the Ni-based alloys. The increase in dilution promoted, for all levels, a tendency for the nucleation of the M_6C phases and complex carbides to become stable. The simulation predicted secondary phases such as Laves, Ni_3Nb, Ni_3Ti, σ and G phase for the alloys containing Nb and Ti.
- The solidification simulation of the mixture of the LAS passes with alloys 625 and 680, which contained Nb, showed the highest solidification range among the alloys evaluated. This result was attributed to the prediction of Laves phase, which is pointed out in the literature as increasing the susceptibility to solidification cracking. In this context, to perform the joining proposed, using LAS as filler metal combined with nickel-based alloys for root and hot passes, a dilution level up to 5% is recommended.
- The dilution of LAS with 686, C276, 22 and 59 alloys showed the best results, in terms of ΔT. The ΔT of the alloy 617 was slightly higher than the Ni-Cr-Mo alloys without Nb, however, none low melting point phases was predicted. According to the results obtained for these nickel-based alloys, it must be possible to perform the joining proposed, depositing LAS for a large field of dilution levels, keeping low the solidification cracking susceptibility.

REFERENCES

1 SILVA, C. C. *et al*. Austenitic and ferritic stainless steel dissimilar weld metal evaluation for the applications as-coating in the petroleum processing equipment. **Materials & Design**, v. 47, p. 1-8, 2013.

2 SUN, Z.; ION, J. C. Laser welding of dissimilar metal combinations. **Journal of Materials Science**, v. 30, n. 17, p. 4205-4214, 1995.

3 BALDRIDGE, T. *et al*. Laser cladding of Inconel 690 on Inconel 600 superalloy for corrosion protection in nuclear applications. **Optics and Lasers in Engineering**, v. 51, n. 2, p. 180-184, 2013.

4 SILVA, C. C. *et al*. A study on the effect of the interpass temperatures in properties and microstructures of the Alloy 625 dissimilar fusion zone. **Materials Science Forum**, v. 783–786, p. 2816-2821, 2014.

5 SARAIVA, D. L. *et al*. Application of low Ms temperature consumable to dissimilar welded joint. **Materials Science and Technology**, v. 30, n. 9, p. 1057-1062, jul. 2014.

6 KOURDANI, A.; DERAKHSHANDEH-HAGHIGHI, R. Evaluating the properties of dissimilar metal welding between Inconel 625 and 316L stainless steel by applying different welding methods and consumables. **Metallurgical and Materials Transactions A**, v. 49, n. 4, p. 1231-1243, 2018.

7 SAEDI, A. H.; HAJJARI, E.; SADROSSADAT, S. M. Microstructural characterization and mechanical properties of TIG-welded API 5L X60 HSLA steel and AISI 310S stainless steel dissimilar joints. **Metallurgical and Materials Transactions A**, v. 49, n. 11, p. 5497-5508, 2018.

8 DUPONT, J. N.; BABU, S.; LIU, S. Welding of materials for energy applications. **Metallurgical and Materials Transactions A**, v. 44, n. 7, p. 3385-3410, 2013.

9 SILVA, C. C. *et al*. Evaluation of the corrosion resistant weld cladding deposited by the TIG cold wire feed process. **Materials Science Forum**, v. 783-786, p. 2822-2827, 2014.

10 MOHAMMADI ZAHRANI, E.; ALFANTAZI, A. M. Hot corrosion of Inconel 625 overlay weld cladding in smelting off-gas environment. **Metallurgical and Materials Transactions A**, v. 44, n. 10, p. 4671-4699, 2013.

11 MINÁ, É. M. *et al*. The effect of dilution on microsegregation in aws ER NiCrMo-14 alloy welding claddings. **Metallurgical and Materials Transactions A: Physical Metallurgy and Materials Science**, v. 47, n. 12, 2016.

12 DUPONT, J. N. Solidification of an alloy 625 weld overlay. **Metallurgical and Materials Transactions A**, v. 27, n. 11, p. 3612-3620, nov. 1996.

13 SILVA, C. C. *et al*. New insight on the solidification path of an alloy 625 weld overlay. **Journal of Materials Research and Technology**, v. 2, n. 3, p. 228-237, 2013.

14 DAI, T.; LIPPOLD, J. Characterization of the Interface of an Alloy 625 Overlay on Steels Using Nanoindentation. **Journal of Materials Engineering and Performance**, v. 27, n. 7, p. 3411-3418, 2018.

15 HODGE, F. G. The history of solid-solution-strengthened Ni alloys for aqueous corrosion service. **JOM**, v. 58, n. 9, p. 28-31, 2006.

16 JONES, R. L. *et al*. Reeled clad SCR weld fatigue qualification. *In*: OFFSHORE TECHNOLOGY CONFERENCE, 2011, Houston. **Proceedings**. Houston: Offshore Technology Conference, 2011. p 1-13.

17 SOUZA, R. F.; RUGGIERI, C. Fracture assessments of clad pipe girth welds incorporating improved crack driving force solutions. **Engineering Fracture Mechanics**, v. 148, p. 383-405, 2015.

18 CHONG, T.-V. S. *et al*. Effects of elevated temperatures on the mechanical properties of nickel-based alloy clad pipelines girth welds. **Engineering Fracture Mechanics**, v. 152, p. 174-192, 2016.

19 LIN, S. *et al*. Effect of cyclic plastic deformation on microstructure and mechanical properties of weld metals used for reel-lay pipeline steels. **Materials Science and Engineering: A**, v. 737, p. 77-84, 2018.

20 CROSS, C. E. On the origin of weld solidification cracking. *In*: BÖLLINGHAUS, T.; HEROLD, H. **Hot Cracking Phenomena in Welds**. Heidelberg: Springer Berlin Heidelberg, 2005. p. 3-18.

21 DNVGL. DNVGL ST F101: **Submarine Pipeline Systems**. Oslo. p. 520. 2017.

22 DNV. JIP: **Lined and Clad Pipeline Materials: Guidelines for Design and Construction of Clad and Lined Pipelines**. Oslo. 2007.

23 LIPPOLD, J. C. *et al*. Weld solidification cracking in solid-solution strengthened ni-base filler metals BT. *In*: BÖLLINGHAUS, T. *et al*. **Hot Cracking Phenomena in Welds II**. Heidelberg: Springer Berlin Heidelberg, 2008. p. 147-170.

24 CIESLAK, M. J.; HEADLEY, T. J.; FRANK, R. B. Welding metallurgy of custom age 625 PLUS alloy. **Welding Journal (Miami, Fla)**, v. 68, n. 12, p. 473s-482s, 1989.

25 CIESLAK, M. J. The welding and solidification metallurgy of Alloy 625. **Welding Journal**, v. 70, n. 2, p. 49-56, 1991.

26 AGARWAL, D. C.; HERDA, W. R. The "C" family of Ni-Cr-Mo alloys' partnership with the chemical process industry: The last 70 years. **Materials and Corrosion**, v. 48, n. 8, p. 542-548, ago. 1997.

27 ARULMURUGAN, B.; MANIKANDAN, M. Development of welding technology for improving the metallurgical and mechanical properties of 21st century nickel based superalloy 686. **Materials Science and Engineering: A**, v. 691, p. 126-140, 2017.

28 MALTIN, C. A.; GALLOWAY, A. M.; MWEEMBA, M. Microstructural evolution of Inconel 625 and Inconel 686CPT weld metal for clad carbon steel linepipe joints: A Comparator Study. **Metallurgical and Materials Transactions A**, v. 45, n. 8, p. 3519-3532, jul. 2014.

29 SILVA, C. C. *et al*. Assessment of microstructure of alloy Inconel 686 dissimilar weld claddings. **Journal of Alloys and Compounds**, v. 684, p. 628-642, 2016.

30 MINÁ, É. M. *et al*. Electron detection modes comparison for quantification of secondary phases of Inconel 686 weld metal. **Materials Characterization**, v. 133, p. 10-16, nov. 2017.

31 MINÁ, É. M. *et al*. Efeito da diluição sobre a microestrutura da liga AWS ERNiCrMo-14 na soldagem de revestimentos pelo processo TIG com alimentação de arame frio. **Soldagem & Inspeção**, v. 21, n. 3, p. 317-329, 2016.

32 MINÁ, E. M. *et al*. Effect of dilution on the microstructure of AWS ERNiCrMo-14 alloy in overlay welding by the TIG process with cold wire feed. **Welding International**, v. 32, n. 2, p. 130-138, 2018.

33 JAKUPI, P. *et al*. Corrosion product analysis on crevice corroded Alloy-22 specimens. **Corrosion Science**, v. 53, n. 5, p. 1670-1679, 2011.

34 LLOYD, A. C. *et al*. Cr, Mo and W alloying additions in Ni and their effect on passivity. **Electrochimica Acta**, v. 49, n. 17, p. 3015-3027, 2004.

35 SHAH HOSSEINI, H.; SHAMANIAN, M.; KERMANPUR, A. Characterization of microstructures and mechanical properties of Inconel 617/310 stainless steel dissimilar welds. **Materials Characterization**, v. 62, n. 4, p. 425-431, 2011.

36 KATTNER, U. R. The thermodynamic modeling of multicomponent phase equilibria. **JOM**, v. 49, n. 12, p. 14-19, 1997.

37 SZELIGA, D. *et al*. Investigation of casting-ceramic shell mold interface thermal resistance during solidification process of nickel based superalloy. **Experimental Thermal and Fluid Science**, v. 87, p. 149-160, 2017.

38 REN, W. *et al*. Effects of the long-time thermal exposure on the microstructure and mechanical properties of laser weldings of Inconel 617. **Journal of Materials Processing Technology**, v. 247, p. 296-305, 2017.

39 RAMKUMAR, K. D. *et al*. Characterization of weld strength and impact toughness in the multi-pass welding of super-duplex stainless steel UNS 32750. **Materials & Design**, v. 60, p. 125-135, 2014.

40 SCHEIL, E. No Title. **Z. Metallkd.**, v. 34, p. 70-72, 1942.

41 TAKALO, T.; SUUTALA, N.; MOISIO, T. Austenitic solidification mode in austenitic stainless steel welds. **Metallurgical Transactions A**, v. 10, n. 8, p. 1173-1181, 1979.

42 SUUTALA, N.; TAKALO, T.; MOISIO, T. Ferritic-austenitic solidification mode in austenitic stainless steel welds. **Metallurgical Transactions A**, v. 11, n. 5, p. 717-725, 1980.

43 LU, X.-G.; SELLEBY, M.; SUNDMAN, B. Assessments of molar volume and thermal expansion for selected BCC, FCC and HCP metallic elements. **Calphad**, v. 29, n. 1, p. 68-89, 2005.

44 BROOKS, J. A. AND LAMBERT, F. J. J. The effects of phosphorus, sulfur and ferrite content on weld cracking of type 309 stainless steel. **Welding Research Supplement**, p. 139s-143s, 1978.

45 DUPONT, J. N. *et al*. Solidification of Nb-bearing superalloys: part I. reaction sequences. **Metallurgical and Materials Transactions A**, v. 29, n. 11, p. 2785-2796, 1998.

46 CIESLAK, M. J.; HEADLEY, T. J.; ROMIG, A. D. The welding metallurgy of HASTELLOY alloys C-4, C-22, and C-276. **Metallurgical Transactions A**, v. 17, n. 11, p. 2035-2047, nov. 1986.

47 DUPONT, J. N.; ROBINO, C. V.; MARDER, A. R. Solidification and weldability of Nb-bearing superalloys. **Welding Journal (Miami, Fla)**, v. 77, n. 10, p. 417-431, 1998.

48 TURCHI, P. E. A.; KAUFMAN, L.; LIU, Z. K. Modeling of Ni-Cr-Mo based alloys: part I-phase stability. **Calphad**, v. 30, n. 1, p. 70-87, 2006.

49 IANNUZZI, M.; BARNOUSH, A.; JOHNSEN, R. Materials and corrosion trends in offshore and subsea oil and gas production. **npj Materials Degradation**, v. 1, n. 1, p. 2, 2017.

50 EVANS, N. D. *et al*. Microstructure and phase stability in INCONEL alloy 740 during creep. **Scripta Materialia**, v. 51, n. 6, p. 503-507, 2004.

51 MAZIASZ, P. J. Formation and stability of radiation-induced phases in neutron-irradiated austenitic and ferritic steels. **Journal of Nuclear Materials**, v. 169, p. 95-115, 1989.

Chapter 6

Assessment of the microstructure and cracks in dissimilar metal welds of AWS ER 100S-G steel deposited on different Ni-based alloys

6.1 Abstract

The present study evaluated the microstructure and cracks of mixtures of the AWS ER 100S-G steel with Ni-based alloy claddings to obtain information about their metallurgical compatibility. This study represents a continuation of an innovative project to manufacture dissimilar weld joints of the API 5L X65 steel cladded by Alloy 625. The AWS ER100S-G steel was deposited using three welding heat inputs (HI_w) on four claddings of the Alloys 625, 686, 22 and 59. A good wetting was observed for all the mixtures with the alloys. The solidification cracks were governed by two factors: stress contraction and microsegregation of the alloying elements. The mixtures with Alloys 686 and 22 showed cracks because of high stress contraction, especially for the lower HI_w. In contrast, the increase of the HI_w for the mixtures with Alloys 625 and 59 caused more and larger cracks because of microsegregation. In brief, the mixture with Alloy 59 showed a good potential for low weld energy, while the Alloys 686 and 22 showed a higher potential for a HI_w above 1.0kJ/mm. In contrast, the mixture with Alloy 625 showed a high tendency to exhibit solidification cracks independent of the weld heat input.

6.2 Introduction

Over the last decade, the discovery of huge oil reserves in the pre-salt layer located off the Brazilian coast increased the engineering challenges for oil exploration and production. Risers are an important component that have had to be adapted for this new reality, since the drilling wells are located at least 2000 meters of floating unit[1]. The first problems are the logistics of transportation and installation of these pipes. The oil & gas industry has adopted the reel lay process to transport and install the risers due to its advantages compared to the traditional S-lay and J-lay methods[2]. Nonetheless, the reel lay process requires a high overmatch of mechanical properties in the weld joint[3]. This requirement takes into account that the welding region commonly exhibits mechanical properties different from the base metal.

Moreover, it is important that the region of the welded joint has superior mechanical properties compared to the steel pipe, especially considering that defects are common in welds[4]. Therefore, from the metallurgical point of view, this requirement increases the challenge, especially for welding of high strength steel pipes with an internal corrosion resistant alloy (CRA) cladding[5].

CRA cladding in steel pipes represents important metallurgical factors that must be considered before executing any welding. The materials used for risers are responsible to maintain the integrity of the component under severe corrosion environments[6–8]. The good corrosion resistance of CRA is attributed to the addition of alloying elements such as Cr and Mo[9]. Alloy 625 is typically used as the CRA cladding of risers for offshore installations[10–12]. The most common welding procedure for girth welding of such components recommends the use of the same alloy as the CRA cladding as the filler metal for joint welding, in order to reduce any metallurgical problems due to mixing materials from different classes[5,13,14]. Thus, the mechanical properties of girth welding will be limited by the properties of the alloy used in CRA cladding. According to Jones *et al*.[5] Alloy 625 can only provide a mechanical overmatch of API 5L X65 steel after work hardening caused by the spooling and unspooling steps of the reel lay installation process. Clearly this is not the best solution for this problem, especially considering the joint welds of other steel pipes such as API 5L X70 and X80 steels are stronger.

A solution to this complex problem is the use of two different materials, one to provide a corrosion resistance similar to the CRA cladding and other to offer the mechanical overmatch required. The most economical and efficient materials that give good mechanical properties are the low alloy steels (LAS). The challenge is to define the mixture of LAS with a Ni-based alloy without causing solidification cracks. According to the literature, the mixture of Alloy 625 with steel causes solidification cracks at the final stage of solidification due to the incorporation of Fe, Si and C from dilution with the steel that combined with Nb content from the Alloy 625 and this may cause the nucleation of deleterious phases such as NbC and Laves phase[15,16]. This shows that despite appearing to be a simple solution to overcome this challenge, the use of LAS diluted with a Ni-based alloy makes the welding extremely complex from a metallurgical point of view.

In order to make this new approach viable for dissimilar girth welding of API 5L X65 steel pipe cladded with Alloy 625, a systematic study was carried out. Initially, a study to select the materials needed was realized based on thermodynamic simulations in order to obtain the most appropriate Ni-based alloy to mix with the API 5L X65 steel and the AWS ER 100S-G steel. The previous chapters pointed out the Alloys 686, 22 and 59 as the most appropriate as

they would maintain a very low solidification temperature range and consequently a low susceptibility to solidification cracks. Therefore, the present work continues this systematic by assessing the mixture of a single welding pass of the 100S-G steel deposited on four different Ni-based alloy.

6.3 Experimental procedure

The AWS ER100S-G steel was chosen as the LAS to be deposited on the Ni-based claddings in order to overmatch the yield strength of the API 5L X65 steel pipe and so attend the requirements to install the risers by the reel lay method. The Ni-based alloys chosen for the mixture with the 100S-G steel were defined considering the results from the thermodynamic studies of the solidification simulations presented in previously chapters. These studies assessed the mixture of some Ni-based alloys with the API 5L X65 and 100S-G steels by considering the solidification temperature range and phases predicted by the simulation. The studies pointed out the 686, 22 and 59 Ni-based alloys were the most appropriate to mix with these steels, taking into account the susceptibility to solidification cracks. Therefore, weld claddings were manufactured with these alloys in order to assess, experimentally, the dilution effect with the 100S-G steel and their metallurgical compatibility.

The Ni-based claddings were manufactured using a low weld heat input, approximately 0.8 kJ/mm, in order to minimize the dilution with the substrate composed of the ASTM A36 steel. In addition, two layers of the Ni-based alloy were deposited for each cladding. In sequence, single weld beads of LAS were deposited on the Ni-based alloy claddings using three different HI_w: 0.8, 1.1 and 1.6 kJ/mm. The chemical composition of the alloys and weld parameters are shown in Tables 6-1 and 6-2, respectively. Figure 6-1a shows the Alloy 22 cladding and Figure 6-1b shows the single weld bead pass of the 100S-G steel with 0.8 kJ/mm.

Three cross sections of each single weld bead were extracted and then subjected to conventional metallographic preparation and the samples were fully polished. The samples were examined without etching under a scanning electron microscope operating in the backscattered electron (BSE) mode, which detected the differences in the chemical compositions (Z-contrast) that enabled an investigation into the microsegregation phenomenon[17].

Table 6-1. Chemical composition of the alloys used in this study.

Chemical composition of alloys																				
Class	Alloy	Al	C	Co	Cr	Cu	Fe	Hf	Mn	Mo	Ni	Nb	P	Re	S	Si	Ta	Ti	W	Zn
NiCrMo	Alloy 625 ER NiCrMo-3		0.1	0.06	21.67		0.09	0.01		8.81	65.22	3.73	0.02		0.015		0.02	0.17		0.05
	Alloy 686 ER NiCrMo-14		0.01	0.05	20.66		0.38		0.24	16.40	58.07		0.02	0.05	0.02			0.06	3.98	0.06
	Alloy 22 ER NiCrMo-10		0.015	0.25	21.05		4.96	0.01	0.12	13.15	57.35		0.02	0.06	0.01		0.06		2.97	
	Alloy 59 ER NiCrMo-13		0.01	0.03	22.78	0.05	0.77		0.23	15.40	60.42	0.06	0.015		0.005		0.01			0.07
Steel	ASTM A36	0.04	0.11		0.12	0.18	97.51		1.17	0.14	0.34	0.03	0.012		0.004	0.28				
	AWS ER100S-G		0.04		0.12	0.11	96.47		1.37	0.38	0.82		0.055		0.014	0.62				

Source: Developed by the author.

Table 6-2. Welding parameters used to deposit the single weld beads of the AWS ER100S-G steel on the Ni-based claddings.

Single weld beads of the AWS ER100S-G steel									
Cladding	E_S (kJ/mm)	I_p (A)	t_p (ms)	I_b (A)	t_b (ms)	V_{alim} (m/min)	V_S (cm/min)	U_m (V)	I_m (A)
Alloy 625	0.8	320	2.2	100	3.5	5.6	40	28.3	182.1
	1.1	320	2.2	100	3.5	5.6	30	29.3	181.6
	1.6	320	2.2	100	3.5	5.6	20	30.3	180.9
Alloy 686	0.8	320	2.2	100	3.5	5.6	40	28.9	181.5
	1.1	320	2.2	100	3.5	5.6	30	29.9	181.3
	1.6	320	2.2	100	3.5	5.6	20	30.9	180.7
Alloy 22	0.8	320	2.2	100	3.5	5.6	40	27.9	182.3
	1.1	320	2.2	100	3.5	5.6	30	29.4	181.3
	1.6	320	2.2	100	3.5	5.6	20	29.6	181.3
Alloy 59	0.8	320	2.2	100	3.5	5.6	40	28.4	182.1
	1.1	320	2.2	100	3.5	5.6	30	29.3	181.2
	1.6	320	2.2	100	3.5	5.6	20	29.6	181.0

Source: Developed by the author.

The microstructure of each weld bead, including the heated affected zone (HAZ), was fully assessed for possible discontinuities or cracks using 500X magnification. Three cross sections of each weld condition were evaluated, in order to increase the statistically reliability. Moreover, microchemical composition analyses of energy-dispersive X-ray spectroscopy (EDS) was performed to provide support to explain the phenomena behind the formation of any discontinuities. The electron backscatter diffraction (EBSD) was also used in some cases to help understand the phenomena. Finally, further thermodynamic simulations were carried out to enrich the metallurgical discussion. All simulations were performed using ThermoCalc® software.

Figure 6-1. a) Alloy 22 cladding manufactured by two layers and b) the deposition of the first single weld bead pass of the AWS ER100S-G steel.

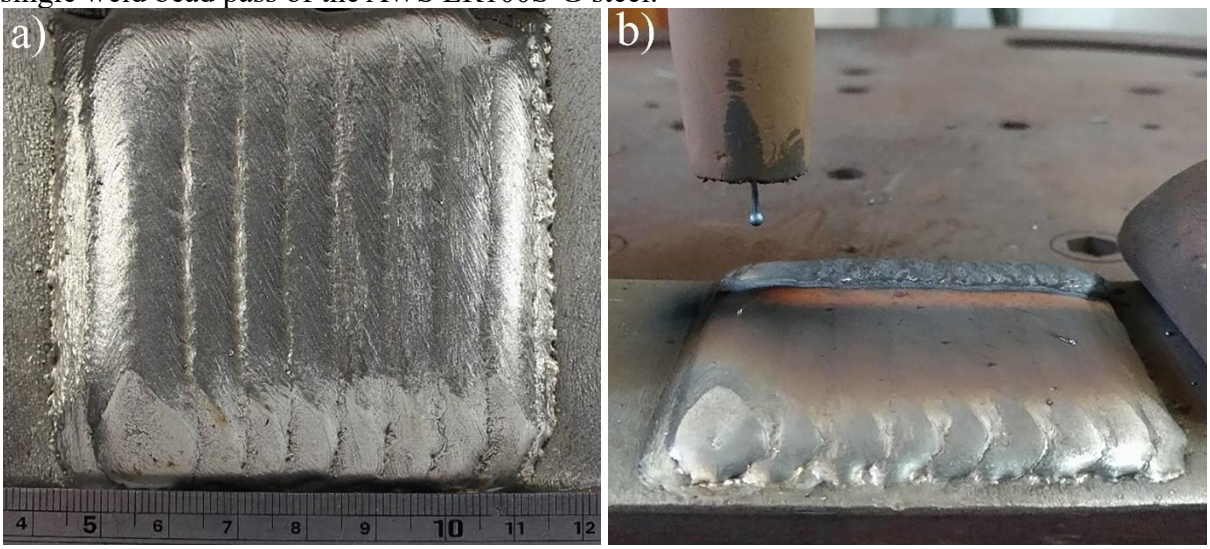

Source: Developed by the author.

6.4 Results and Discussion

6.4.1 Effect of welding heat input in microstructure

Independent of the HI_w applied, all single weld beads showed a good wetting with the Ni-based claddings. A good wetting is important when welding dissimilar materials, especially for joint welding with a narrow gap groove. Min *et al*.[18] highlighted the difficulty of manufacturing joints without a lack of fusion in the narrow gap joint due to low wetting experienced during welding.

All single weld beads exhibited a high dilution level with the Ni-based claddings, independent of the HI_w used to deposit the 100S-G steel. Table 6-3 highlights the dilution level of each single weld bead. The dilution was calculated considering the chemical composition of the fusion zone, filler and base metals (in this case, the chemical composition of second layer of the Ni-based alloy cladding[19,20].

The high dilution was attributed to the intrinsic physical properties of these classes of materials. In general, steels have a melting temperature slightly higher than Ni-based alloys. Thus, a large portion of the heating produced by arc welding will be consumed to melt a large part of the Ni-based alloy compared with the 100S-G steel. This hypothesis is supported by the thermodynamic results of the solidification simulations of these alloys performed by previous studies presented in early chapters. This phenomenon explains the good wetting and consequently the easy welding of these two materials. This is an important result considering

the notable differences in chemical composition, crystalline structures, thermal and electrical conductibility properties, and others. In practice, a good wetting allows a large field of welding parameters that can be used to avoid welding defects, especially the lack of fusion[18].

Table 6-3. Dilution of the single weld beads of the AWS ER100S-G steel for each weld heat input.

Dilution of each single weld beads of the AWS ER100S-G steel		
Cladding	Weld heat input (kJ/mm)	Dilution
Alloy 625	0.8	56.0%
	1.1	55.7%
	1.6	46.6%
Alloy 686	0.8	59.4%
	1.1	50.9%
	1.6	54.4%
Alloy 22	0.8	55.6%
	1.1	51.3%
	1.6	45.8%
Alloy 59	0.8	53.8%
	1.1	53.8%
	1.6	48.1%

Source: Developed by the author.

In general, the dilution level reduced with an increase of HI_w. Increasing the HI_w by reducing the welding travel speed, whilst keeping the wire fusion rate almost the same, caused an increase of filler metal deposited per unit length of the single weld bead. According to the literature an increase of the weld pool volume may act as a barrier between the arc welding and the base metal, preventing the arc welding to act on the base metal[18]. Independent of these effects, there was a very high dilution level of at least 45% in all conditions. Naturally, the dilution caused a significant incorporation of alloying elements such as Cr, Mo and Ni into the weld metal. The massive addition of Ni made the γ-FCC thermodynamically stable at room temperature, similar to the Ni-based alloys from the Fe-Ni family[21]. The chemical composition of all single weld beads is shown in Table 6-4. The high dilution transformed the LAS into a kind of high alloy steel or a Fe-Ni alloy.

A similar solidification behavior was seen for all conditions. The single weld beads showed an epitaxial growth of dendrites at the solidification interface[22], which corroborates with the fact that both weld metals and claddings have the same crystalline structure with minor changes in the lattice parameters, considering the small difference in atomic radius between the Fe and Ni elements. Thus, initially the first solids nucleated and grew as cells that posteriorly evolved to columnar dendritic morphology[22]. The solidification interface of the weld metal for the mixture of 100S-G steel with the Alloy 59 cladding is shown in Figure 6-2a. An epitaxial growth of cells and the transition of cellular solidification to columnar dendritic was apparent.

Interestingly the long extension of the cellular zone, exceeded 1000 μm in length. In this case, the tendency is an intense segregation between intercells, especially at the solidification grain interface, where the grain growth is interrupted by growth of another grain. Figures 6-2b and 6-2c show this phenomenon, in which some small discontinuities located in the intercellular zone and at the interface between solidification grains were observed.

Table 6-4. Chemical composition of the single weld beads of AWS ER100S-G steel for each weld heat input. [1]The percentage of carbon was estimated based on the dilution level.

Chemical composition of all single weld beads of AWS ER100S-G steel											
Cladding	Weld heat input (kJ/mm)	Fe	Ni	Cr	Mo	W	Ti	Nb	Si	Mn	C[1]
Alloy 625	0.8	43.1	35.8	12.5	5.4	-	-	2.1	0.4	0.8	0.074
	1.1	43.4	35.9	12.7	5.0	-	-	1.9	0.4	0.7	0.074
	1.6	52.1	30	10.6	4.4	-	-	1.7	0.4	0.8	0.069
Alloy 686	0.8	40.1	33.1	12.6	10.0	3.1	-	-	0.2	0.8	0.024
	1.1	48.1	28.7	10.8	8.6	2.8	-	-	0.2	0.9	0.026
	1.6	44.8	30.6	11.5	9.3	2.7	-	-	0.3	0.8	0.025
Alloy 22	0.8	46.1	30.4	12.0	7.6	2.7	-	-	0.3	0.8	0.027
	1.1	50.0	28.5	11.0	7.2	2.2	-	-	0.3	0.8	0.028
	1.6	55.0	25.5	9.9	6.4	2.0	-	-	0.3	0.9	0.030
Alloy 59	0.8	45.5	32.0	12.9	8.5	-	-	-	0.3	0.8	0.025
	1.1	45.5	31.9	12.7	8.7	-	-	-	0.4	0.9	0.025
	1.6	50.9	28.6	11.4	7.8	-		-	0.4	0.9	0.027

Source: Developed by the author.

Figure 6-2. a) The microstructure of the solidification interface highlighting the transition of the solidification modes and characterization of the discontinuities located at b) solidification interface and c) between solidification grains.

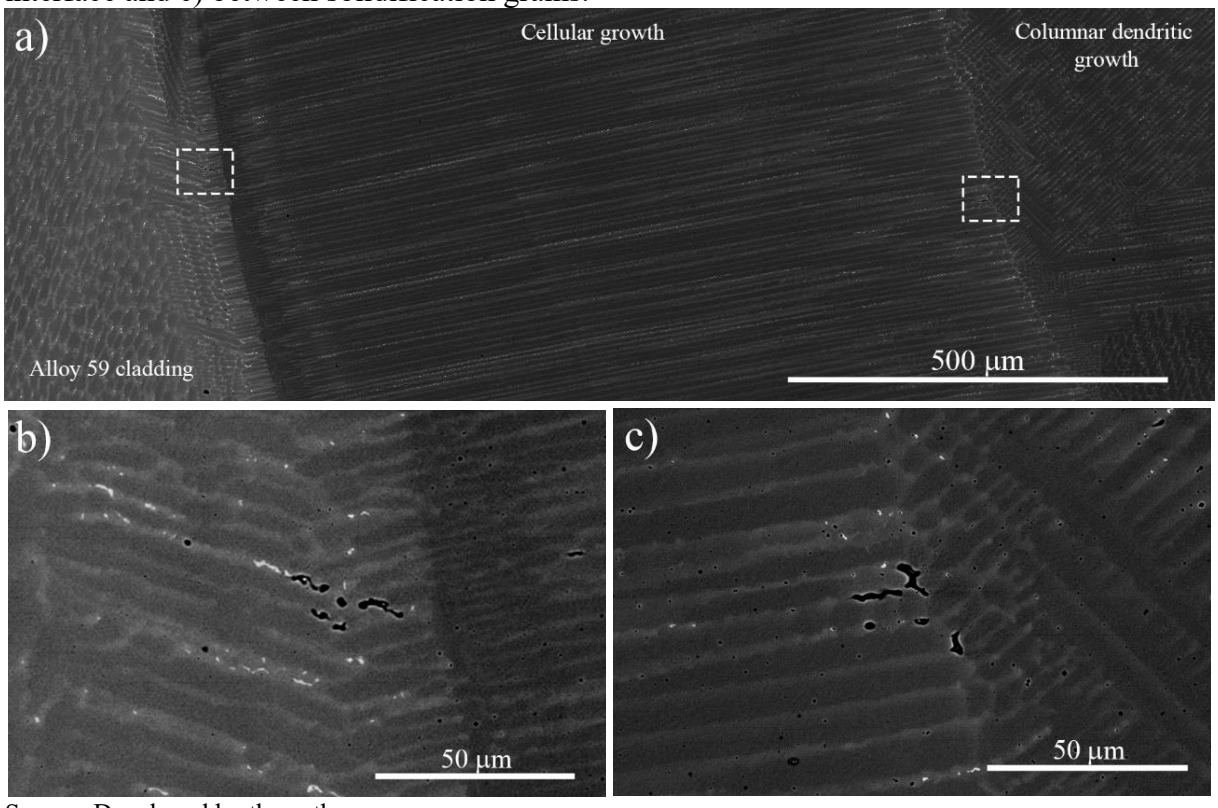

Source: Developed by the author.

Even with the strong similarity in the solidification mode, the microstructural characterization of the single weld beads revealed differences in terms of the secondary phase fractions present in the weld metal. Figure 6-3 compares the microstructures of the four claddings and their respective 100S-G steel deposited with the same $HI_{w.}$ The Figure shows the solidification pattern of the interface between the Ni-based cladding layers (items a, d, g and j), the solidification interfaces between the Ni-based cladding and the 100S-G steel deposits (items b, e, h and l) and the dissimilar fusion zones (items c, f, e and m).

On comparing the solidification interface between the cladding layers, the Alloy 686 cladding showed a larger secondary phase fraction than the other alloys. This was due to the high fraction of alloying elements such as Cr, Mo and W present in Alloy 686. The nucleation of secondary phases like σ, μ, P and Laves becomes possible when these elements are segregated to the liquid fraction during solidification. In terms of Ni-based alloys, theses phases are commonly known as topologically close-packed (TCP) phases due to the high atom density per cell unit. A recent study evaluated the weld microstructure of Alloy 686, and the authors identified the P, σ and μ phases using selected area electron diffraction[23].

In the case of the Alloy 625 cladding, the low nucleation of secondary phases was attribute to the low amount of Fe incorporated from the ASTM A36 steel substrate. Several studies, which have reported the effect of Fe in solution with other alloying elements such as Nb and Mo, pointed out that Fe increases the tendency of the nucleation of Laves, σ and μ phases[10,11,15,16]. Without the addition of Fe, the greater part of Cr, Mo and Nb are solubilized by the γ-FCC matrix. However, the low HI_w had a significant effect on this phenomenon, considering that low energy causes a fast solidification rate and consequently reduces the microsegregation of the alloying elements[24].

In the case of claddings based on Alloys 22 and 59 only a low fraction of secondary phases were observed, similar to what was observed for the Alloy 625 cladding. This result was expected as Alloy 22 was developed in order to prevent the nucleation of μ phases, which have detrimental effects on corrosion resistance[25,26]. Alloy 59 followed the same tendency, considering that it was designed as a pure Ni-Cr-Mo alloy without other elements such as Nb, Ti and W[25]. Thus, Alloy 59 has high thermal stability, i.e. the alloy solidifies as a γ-FCC with a very small fraction of secondary phases. Furthermore, it remains stable even in the face of high temperature service, where nucleation of the TCP phases in other Ni-based alloys of the same family commonly occurs [25].

Figure 6-3. Microstructure of the solidification interface between the 1st and 2nd layers of the Ni-based claddings, interface of single weld bead and cladding, and the fusion zone of dissimilar welding. The items a), b) and c) refer to combinations with Alloy 625; d), e) and f) Alloy 686; g), h) and i) Alloy 22; j), l) and m) Alloy 59.

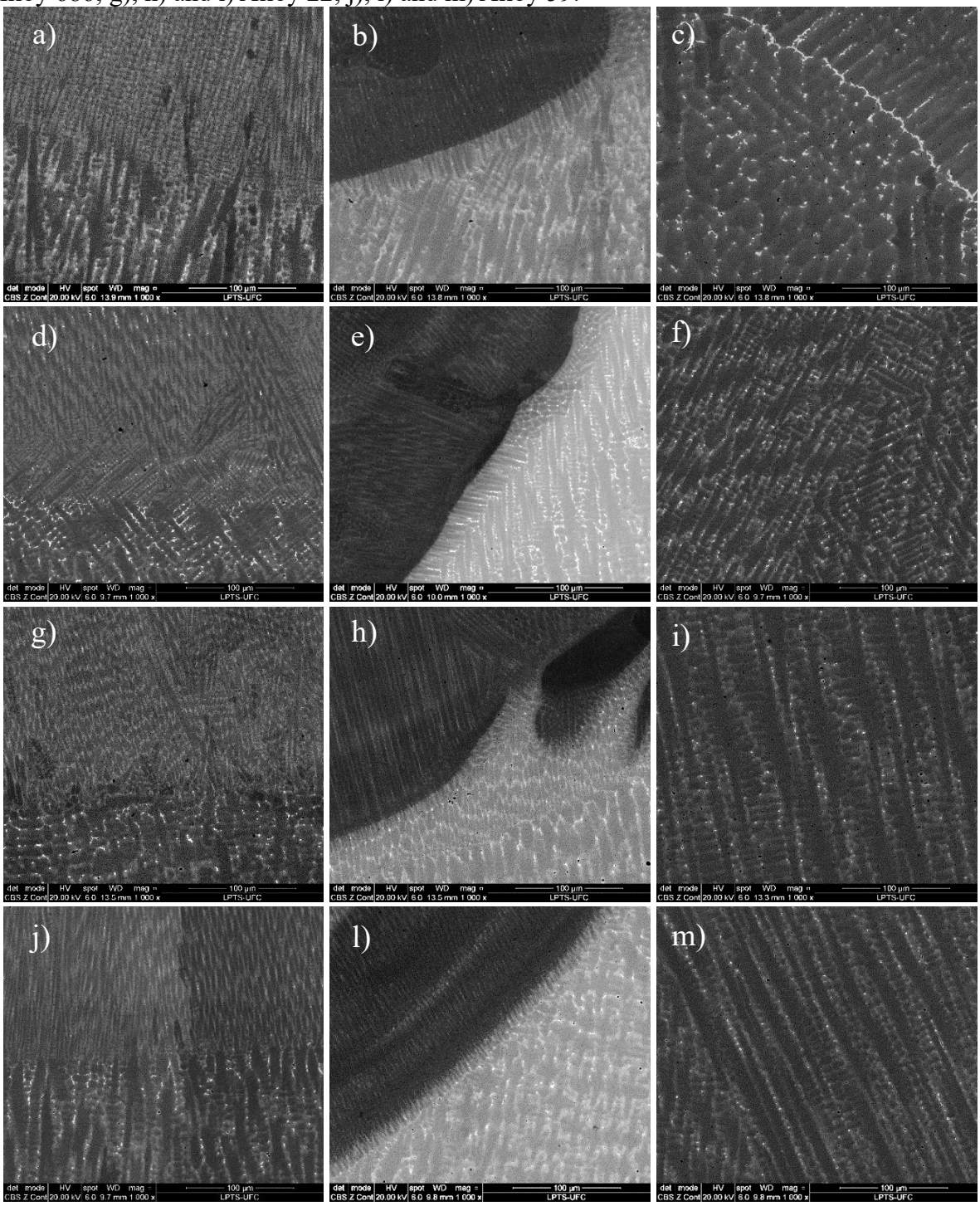

Source: Developed by the author.

The microstructure of the interface between 100S-G steel and Ni-based claddings demonstrated the same behavior discussed previously for the microstructure of the claddings. Alloy 686 showed a larger fraction of secondary phases close to the interface in comparison to

the other Ni-based alloys, due to the high fraction of alloying elements present in Alloy 686. As expected, the secondary phase fraction was slightly larger than that observed in the interface between the weld cladding layers. This was because the lower dilution of the second layer kept a large fraction of the alloying elements that were available to segregate and then accumulated them at the final stage of solidification.

The microstructures of the weld metal of the conditions showed a different behavior in terms of secondary phase fractions. The dissimilar weld metal of 100S-G steel that was diluted with the Alloy 625 cladding showed a higher fraction of precipitates in comparison with the other Ni-based claddings, even having less Cr, Mo and W than the other combinations (Table 6-4). The reason for this behavior is certainly related to the significant addition of Fe from 100S-G steel, which combined with Nb from Alloy 625 made the nucleation of Laves phase more favorable. Among the alloying elements, Nb is the most segregated element, especially in the presence of Fe. This behavior is more evident in Figure 6-3c, where a higher fraction of secondary phases concentrated between two solidification grains can be seen. The other mixture conditions showed a lower fraction of precipitates due to a significant reduction of Mo and W in the fusion zone.

Thermodynamic simulations of the solidifications were performed to support the discussion about the secondary phase fractions. Solidifications of the weld metal for all the single weld beads, based on the classical solidification model of Scheil-Gulliver, were simulated[27]. It is reasonable to adopted this model to estimate the secondary phase fractions, because most of the precipitates are the result of microsegregation experienced during solidification. Figure 6-4 shows the results predicted by the simulations. The mixtures with Alloy 625 showed the highest fraction of secondary phases, above 3%, followed by the mixtures with the 686, 59 and 22 Alloys. The massive addition of Fe caused the nucleation of Laves phases, which increased the secondary phase fraction. In the case of Alloy 686, the higher fraction of Cr, Mo and W doubled the number of σ phases predicted in comparison to the number predicted for the mixtures with the Alloys 22 and 59.

This qualitative and quantitative analysis of the secondary phase fractions is important in several aspects, and is not restricted to corrosion resistance but includes the mechanical behavior of the weld metal. Usually, these hard precipitates homogeneously distributed along the matrix have a blocking effect of dislocations, causing good mechanical effects. In the case of eutectic phases, which nucleate at the final stage of solidification, at solidification grains, they cause special mechanical effects. The exceptional location in the microstructure has an important effect preventing solidification grain migration at high

temperatures. Several studies have pointed out the harmful effect of the migration of solidification grain boundaries (SGB)[28–30], especially concerning the formation of ductility dip cracking (DDC). This kind of reheat cracking is a specific problem for austenitic alloys, due to grain growth at high temperatures, which causes loss of ductility. Lippold *et al.*[26] evaluated Alloy 22 weld metal through hot-ductility tests and highlighted the presence of ductility dip cracks. The authors attributed the formation of these cracks to migrations of SGB at high temperatures. In order to prove this hypothesis, the authors assessed the same weld metal after a heat treatment, which induced the formation of precipitates at the grain boundaries. The hot-ductility test indicated a significant increase in resistance to DDC. The P phase particles acted as pinning points that prevented grain growth and induced the dynamic recrystallization around particles before the initiation of cracks.

Figure 6-4. The thermodynamic simulation of the solidification of a single weld bead of the AWS ER100S-G for each weld heat input performed. The simulation highlights the secondary phase fraction of all combinations.

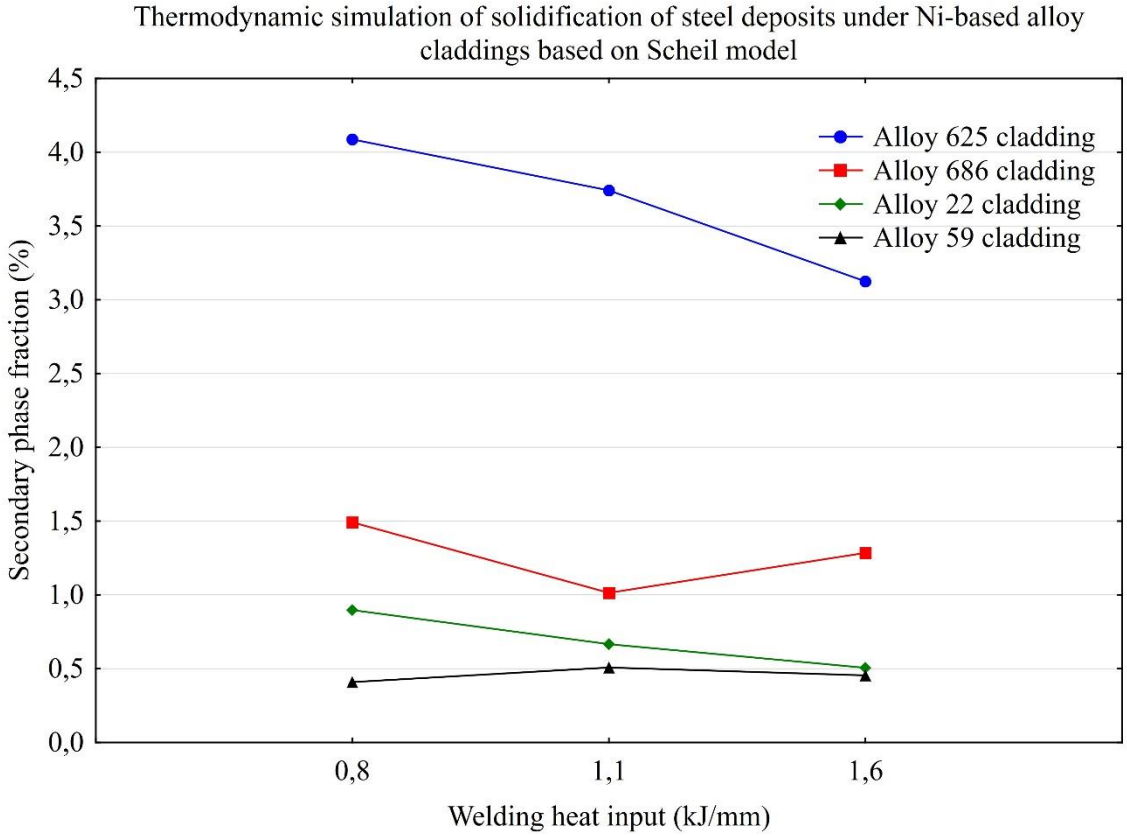

Source: Developed by the author.

Likewise, the Alloys 22 and 59 that showed a very small secondary phase fraction for mixtures with 100S-G steel, probably, these combinations have a higher susceptibility to ductility dip cracking than other mixtures with the Alloys 625 and 686. However, selection of

specific weld parameters may decrease the susceptibility to such cracking. The use of a high HI_w for example, induces a low solidification rate that increases the microsegregation of the alloying elements, which favor the formation of secondary phases at the final stage of solidification. As discussed previously, secondary phases at the SGB may reduce the susceptibility to DDC.

Although DDC represents a defect that may induce failure, especially for high temperature service, it is also important to considerer solidification cracking before defining the welding parameters. In general, microsegregation of alloying elements is induced by high HI_w, which in turn cause the formation of solidification cracks at the final stage of solidification. In some cases, microsegregation may lead to the crack backfilling phenomenon, in which the reminiscent liquid metal, rich in alloying elements, fills the volume between grains, avoiding the formation of solidification cracks[31]. In contrast, low HI_w causes an increase in the cooling rate, and therefore reducing the microsegregation of alloying elements. Thus, the alloy will solidify with a lower solidification cracking susceptibility, while the DDC is potentialized due to the reduction of precipitates at the solidification grain boundaries. On the other hand, the fast cooling rate reduces the time available for austenitic grains to grow and consequently minimizes the loss of ductility during reheating. Therefore, all these aspects must be considered before selecting the welding parameters, and before coming to any conclusion concerning these alloys, especially in terms of hot cracking susceptibility.

6.4.2 Solidification crack mechanisms

The experimental results show that almost all welding conditions, which include the different HI_w used, presented discontinuities up to 200 μm. Other numerous small discontinuities with dimensions of about 20 μm were also observed, especially in the partially mixed zones located at the fusion zone near the interface with the Ni-based cladding. Figure 6-5a shows a BSE macrograph of a mixture of 100S-G steel with Alloy 686 cladding with low HI_w. Several partially mixed zones were observed here. The light gray tone means that there is a high concentration of alloying elements with a chemical composition similar to the Ni-based cladding. Regions of macrosegregation with a long extension and far from the interface with the base metal were also seen. These regions appear to have been frozen by the solidification front, taking the shape of pool convection. Figures 6-5b and 6-5c highlight with details some discontinuities observed in the partially mixed zones. The morphology of the discontinuities confirms that the thin liquid metal film between the cells was not enough to completely filling

the volume, thus producing discontinuities. This liquid metal film was the result of the microsegregation of alloying elements. In some cases, secondary phases were seen to partially fill these discontinuities.

Figure 6-5. Macrograph of a single weld bead using backscattered electrons (a). Discontinuities along the regions richer in the base metal (b and c).

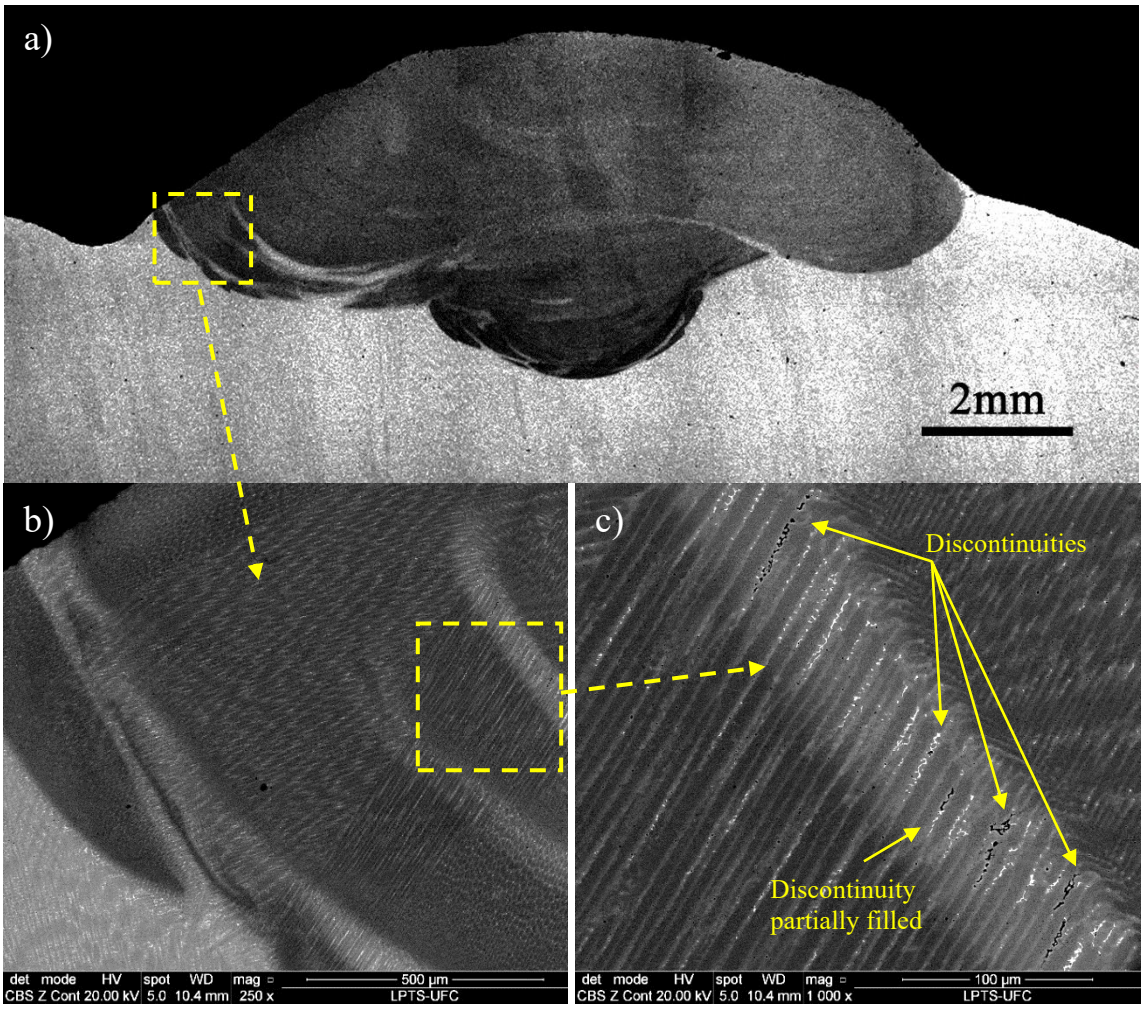

Source: Developed by the author.

Figure 6-6 shows an EDS mapping near the dissimilar fusion boundary for a mixture of the 100S-G steel with the Alloy 686 cladding. The turbulence during solidification caused the formation of the heterogeneous weld metal, in terms of chemical composition. The EDS maps of Fe and Ni revealed different regions rich in the LAS filler metal and Ni-based alloy base metal, respectively. Researchers at the University of Wisconsin–Madison have been studying the phenomena related to the solidification of the weld pool[32–35]. According to those studies, when the base metal has a lower melting point compared to the filler metal, the arc welding penetrates deeply into the base metal, which increase the turbulent effect in the weld

pool. Thus, some layers of the melted base metal are inserted into the fusion zone by pool convection and are quickly solidified without fully mixing with the filler metal. Moreover, the formation of a thin layer of base metal also occurs near the solidification interface, which melted during welding. This layer experienced a negligible mixture with the filler metal, since the speed of the liquid metal at the solid interface is almost zero, which impairs any mixing.

Figure 6-6. EDS mapping close to the solidification interface highlighting the different regions.

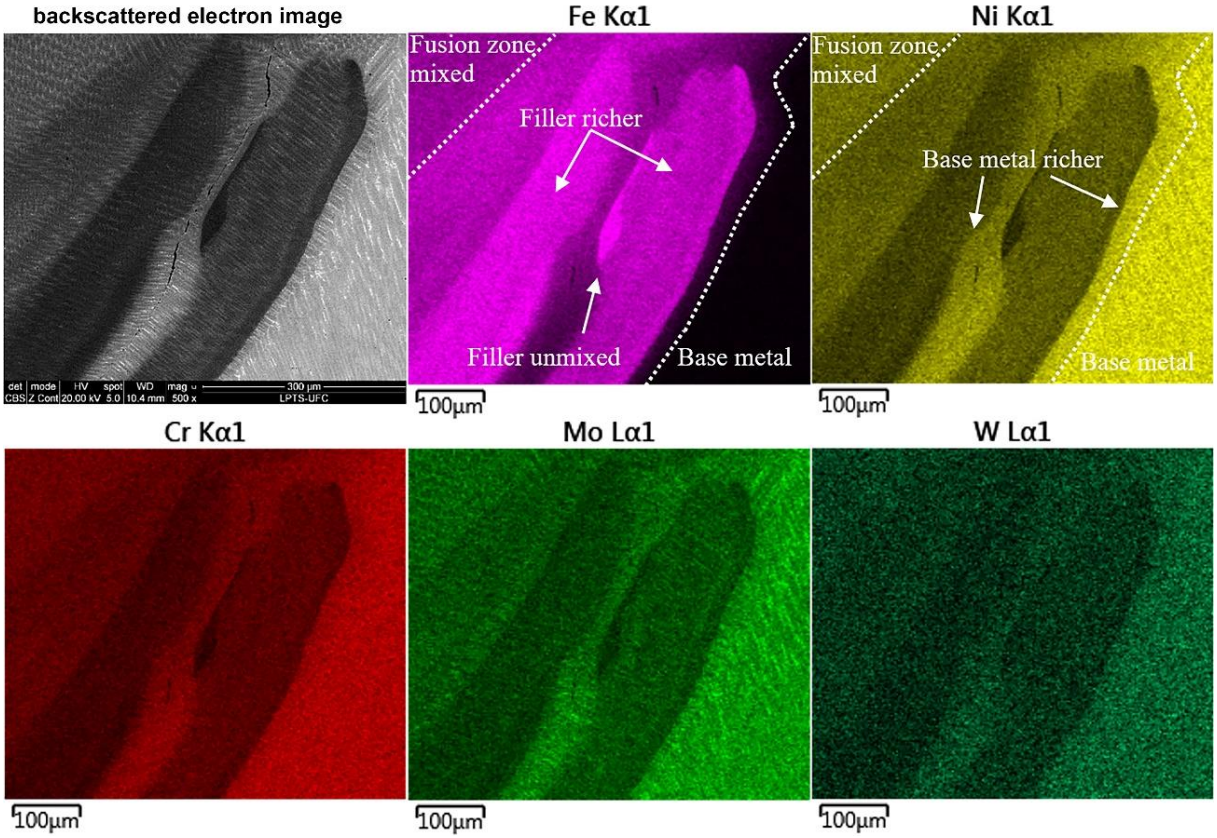

Source: Developed by the author.

All these macro regions with different chemical compositions have a different solidification behavior from the bulk weld metal, which may lead to the formation of cracks. The rich regions of the base metal exhibited a more intense microsegregation behavior due to the significant fraction of alloying elements, which caused the formation of discontinuities at the center of the macrosegregation zone. These discontinuities under high stress due to solid contraction may develop into large cracks. In the case of the Alloy 686, which presents a low eutectic volume in comparison to the mixture with Alloy 625, the stress due to solidification and solid contraction was probably more effective in forming cracks. Figure 6-7 shows the details of the phenomenon described, where cracking was initiated by microsegregation and increased due to solid contraction.

The other phenomenon behind the formation of these solidification cracks is related to the concentration of the liquid metal between the solidification grains and cells or dendrites of the same grain. This phenomenon is governed by the microsegregation of the alloying elements and, it has been extensively discussed in several studies about solidification cracks[10,11,23,26,36]. Normally, solidification cracks are more frequent in alloys that have a high fraction of liquid metal rejected, which favors the nucleation of low melting point phases. These cracks exhibit the same shape as the space between the cells or dendrites. Figure 6-8 shows EBSD and EDS maps of a discontinuity observed for a mixture of 100S-G steel with Alloy 625. The meeting of solidification grains caused the accumulation of alloying elements that made the nucleation of low melting point phases rich in Nb and Mo thermodynamically stable, and which solidified posteriorly causing the formation of a large solidification crack.

Figure 6-7. Solidification crack observed at the rich region of the base metal. The defect was started by microsegregation and a stress contributed to its growth.

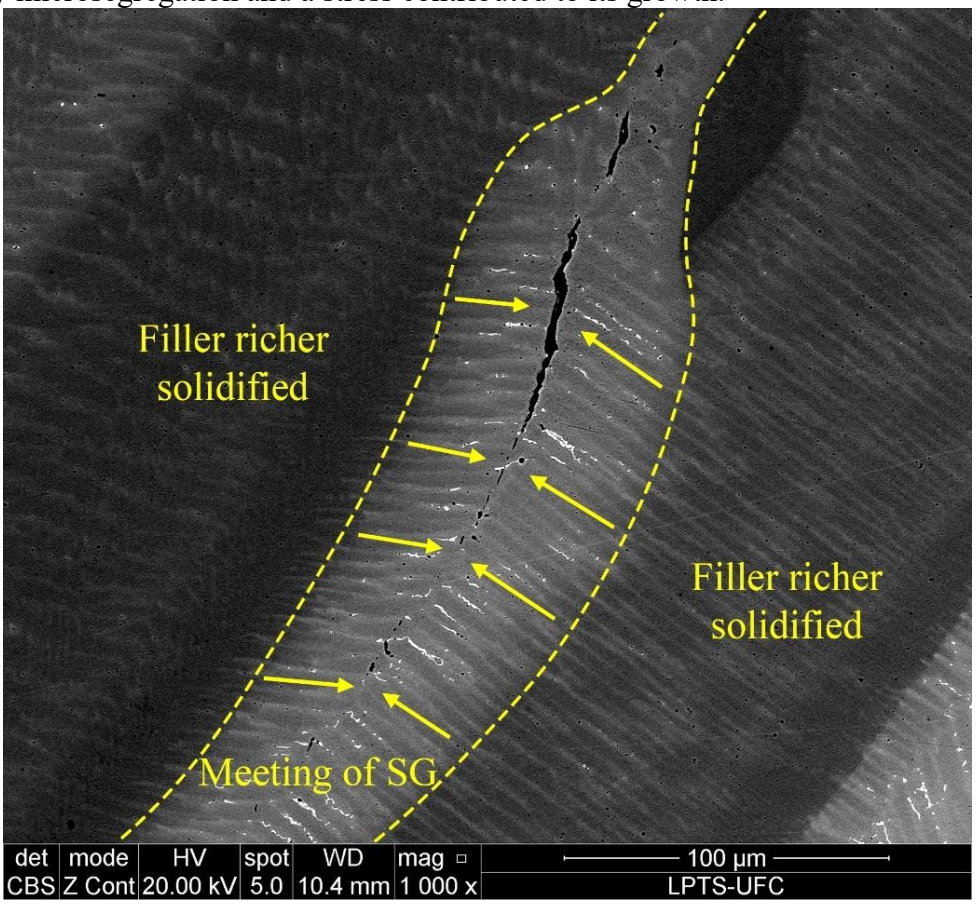

Source: Developed by the author.

This mechanism of solidification crack formation governed by microsegregation is not restricted to the meeting of solidification grains but it can also be observed at subgrain interfaces. Figure 6-9 shows EBSD mapping of solidification cracks that occurred in a

solidification grain, between its dendrites. The grain misorientation between grains around the crack was about 1º, evidencing that the crack occurred at the same solidification grain. Such defects occur when the weld metal experiences an intense microsegregation.

Figure 6-8. EBSD and EDS mapping of the fusion zone with the Alloy 625 cladding. a), b) and c) highlight the macrostructure of the grains solidified; d), e) and f) show, in details, a discontinuity between the solidification grains as a consequence of Nb and Mo microsegregation.

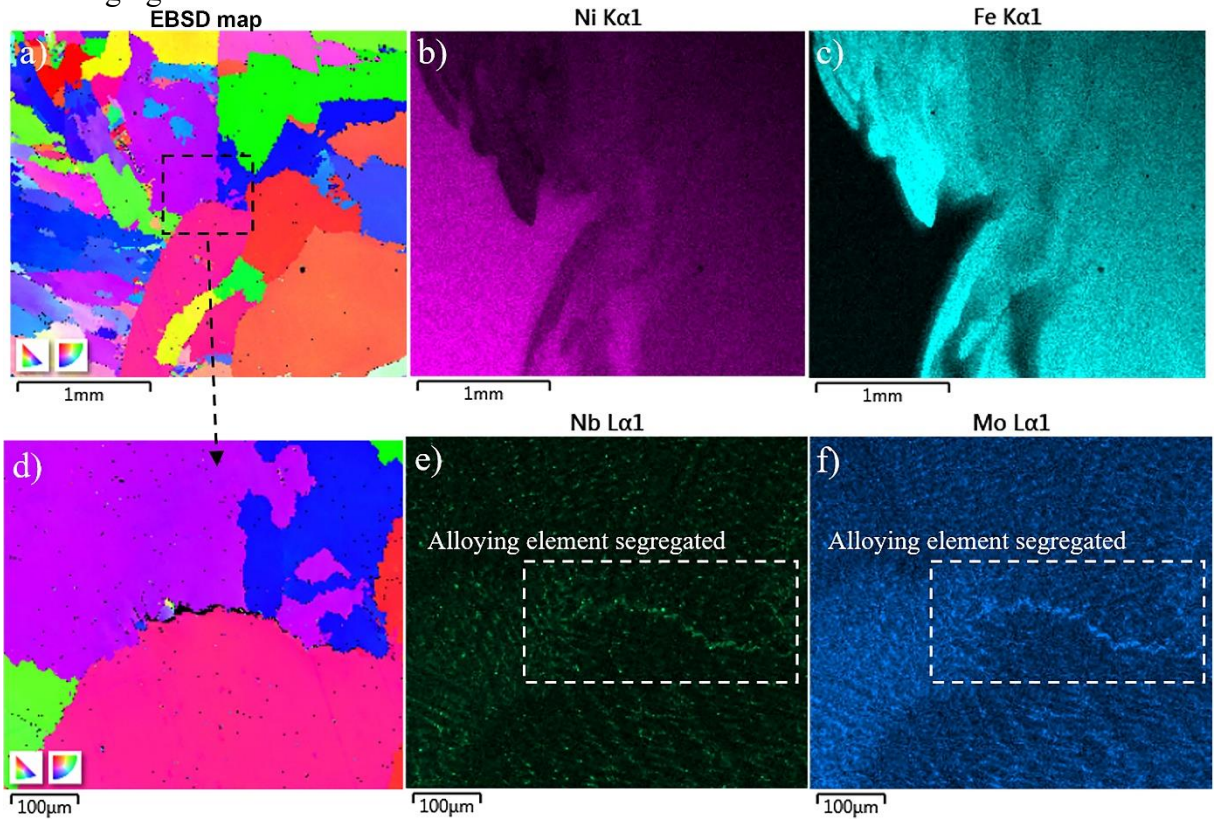

Source: Developed by the author.

Figure 6-9. Discontinuity characterized in the combination with the Alloy 625 cladding. a) EBSD mapping showing the defects in the subgrain boundary. b) and c) EDS mappings showing the microsegregation of Nb and Mo.

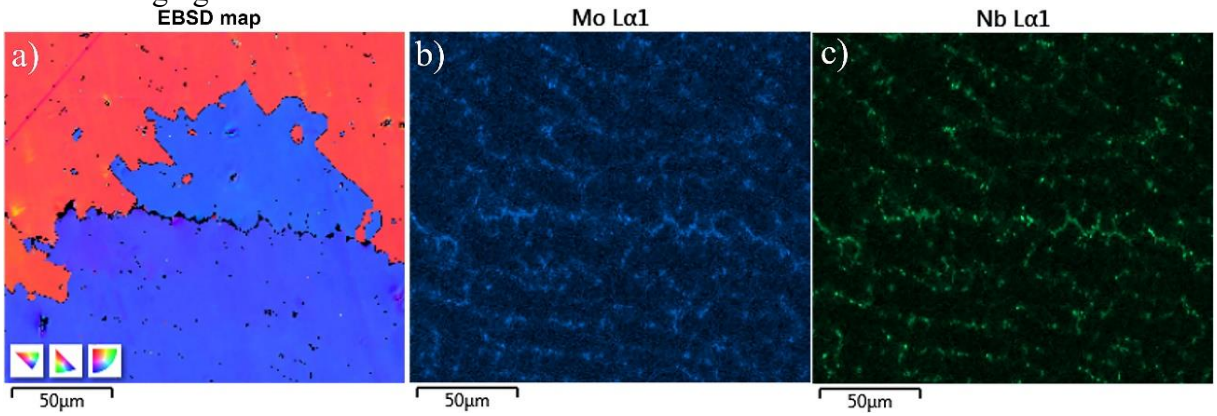

Source: Developed by the author.

The classical phenomenon of the formation of solidification cracks is governed by microsegregation and, therefore, it is strongly influenced by HI_w. As previously discussed, depending on how much energy was used for the welding, the microsegregation will have more or less time to take place. Thus, it is reasonable to expect that HI_w will effect a quantitative analysis of solidification cracks, especially if the crack backfilling effect is considered. Figure 6-10 shows an example of crack backfilling for the mixture of 100S-G steel with Alloy 625. However, in this case, the solidification crack could be larger if the discontinuity was not filled by the eutectic phases at the final stage of solidification.

Figure 6-10. EDS mapping of a solidification crack that was backfilled by eutectic phases at the final stage of solidification.

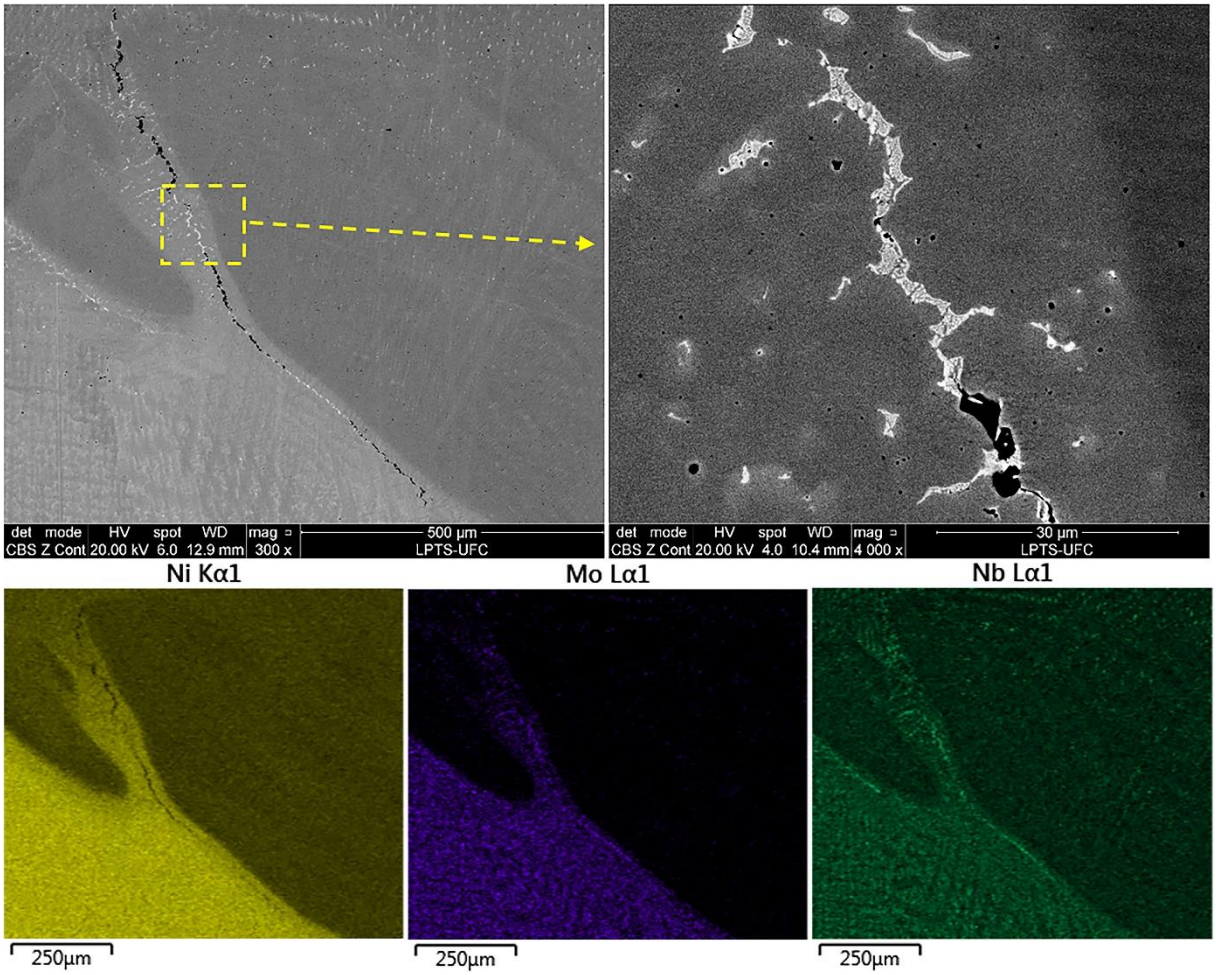

Source: Developed by the author.

6.4.3 Quantitative analysis of solidification cracks

The maximum crack size and total number of cracks are shown in Figure 6-11 and Figure 6-12, respectively. Only discontinuities with at least 100 µm were taken into account for

these analyses. Among all the combinations of the 100S-G steel with Ni-based claddings, a mixture with the Alloy 22 cladding had the largest defects in this study. In general, the largest cracks were observed under low HI_w. This phenomenon was probably a consequence of a higher solid contraction stress due to a higher thermal gradient temperature. Therefore, it is important to highlight that HI_w causes different phenomena under the dissimilar welding conditions investigated here.

Figure 6-11. Maximum crack size characterized in all single weld beads.

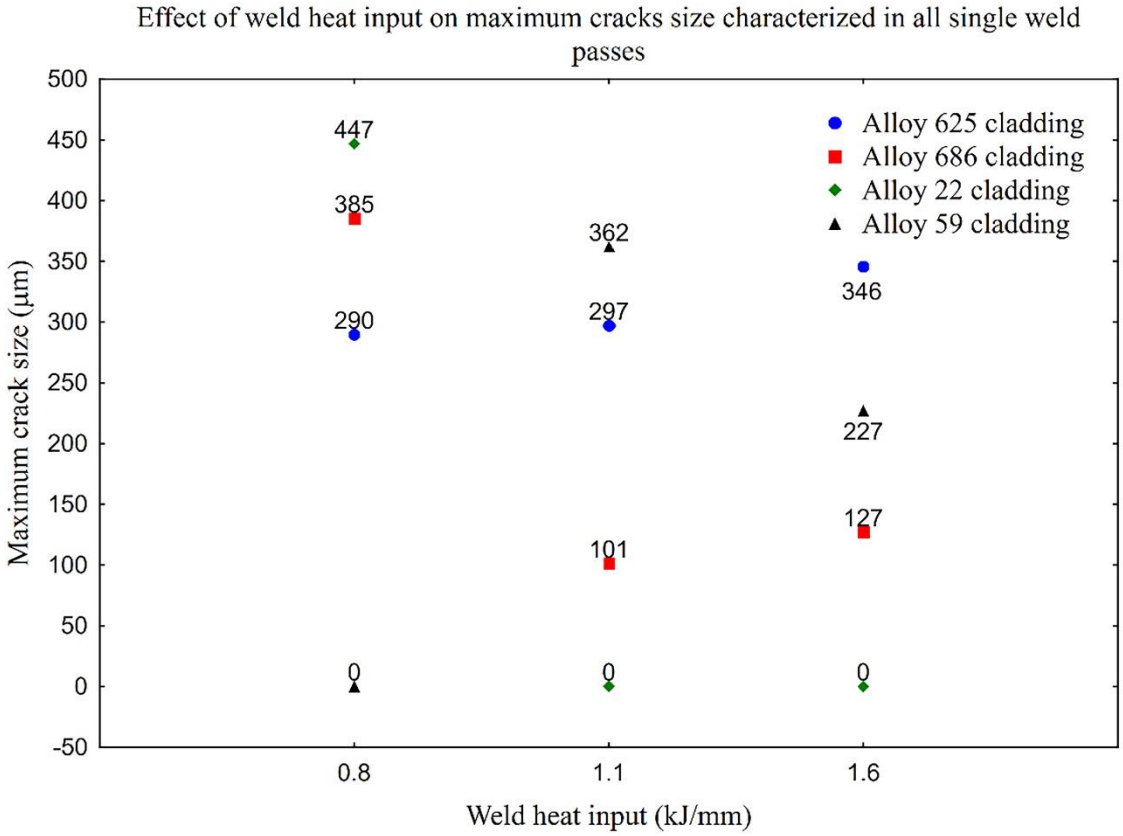

Source: Developed by the author.

In the case where the weld metal exhibited a high fraction of segregated alloying elements that is when mixed with the Alloy 625 cladding, the high HI_w potentialized the microsegregation causing an increase in the maximum crack size observed. On the other hand, the backfilling phenomenon is potentialized by increasing the microsegregation, causing a reduction of crack size. This may explain the decrease in the total number of cracks above 100 µm observed[31]. This intense microsegregation was induced by very low solubility of Nb in γ-FCC, especially in the presence of Fe, Si, Mo and C in solution[10,11].

The same phenomenon may explain the behavior observed for the mixture with the Alloy 59 cladding. An increase of HI_w potentialized the number of cracks. Considering that

Alloy 59 was developed to solidify with low number of secondary phases, and without any low melting point phases, an increase in the weld heat input caused the formation of weld shrinkage porosities due to the intensification of microsegregation. Normally, alloys with high Mo may show eutectic phases, especially when a microsegregation is potentialized.

Figure 6-12. Total number of cracks greater than 100 μm observed for all single weld beads evaluated.

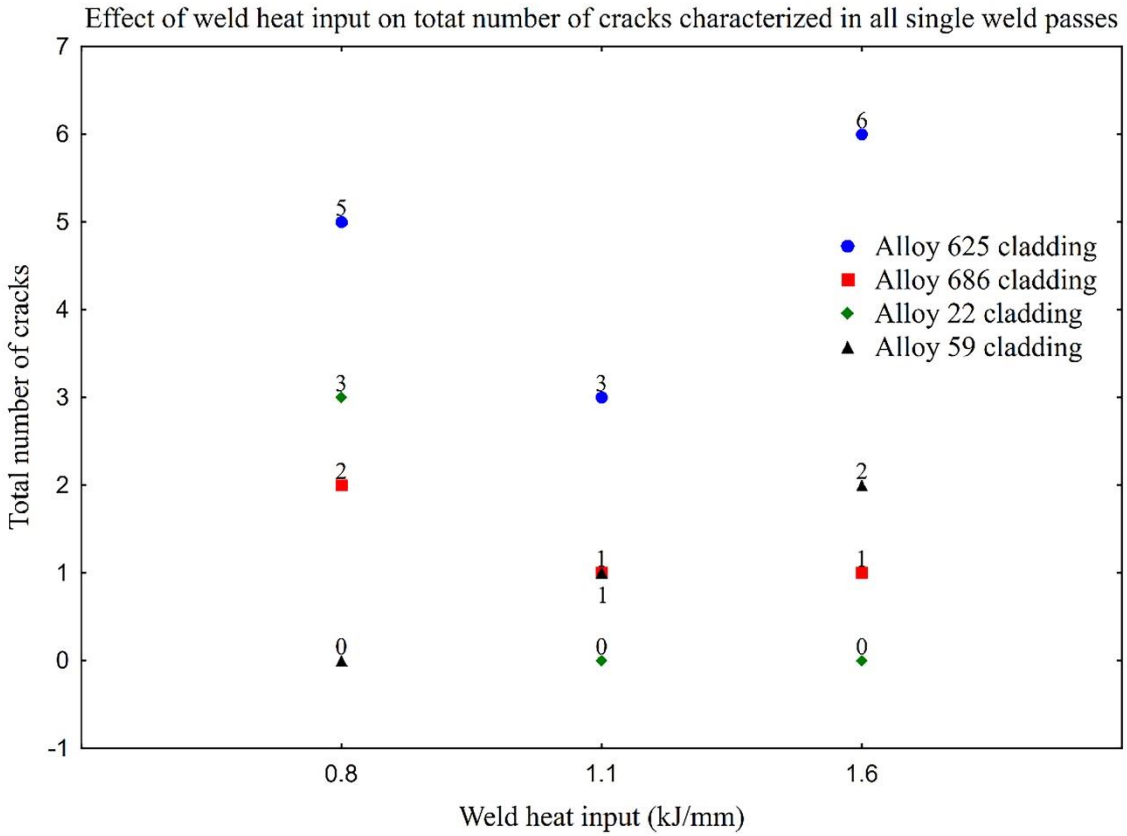

Source: Developed by the author.

The combinations of the 100S-G steel with Alloys 22 and 686 showed the same behavior in terms of solidification cracks. In both cases, a lower HI_w exhibited larger cracks. In these cases, few secondary phases were observed around the cracks presented with the Alloy 686, while negligible secondary phase fractions were observed with the Alloy 22. This behavior was expected, as with a low HI_w the microsegregation effect is slower; in contrast to a fast cooling rate which does not allow the full segregation of the alloying elements. Therefore, these cracks probably occurred as an effect of higher contraction stress induced by the higher thermal gradient. In the same way, the high HI_w caused a reduction of contraction stress, while microsegregation increased, and the result was the reduction of a maximum crack size and the total number of cracks observed. Therefore, a decrease in the cooling rate and consequently an

increase in the time to segregate the alloying elements was not more relevant than a reduction in contraction stress, in terms of solidification crack. This occurred due to the significant solubility of the alloying elements present in Alloys 22 and 686. Different from Nb and Ti, the Cr, Mo and W elements are more soluble in a Ni-γ-FCC matrix.

The heat-affected zone around the single weld bead was also investigated in order to observe any reheat cracking. The only discontinuity observed was characterized in a mixture with the Alloy 22 cladding for the lowest HI_w. The reheat crack was identified as a ductility dip crack. During reheating, a ductility drop probably occurred at high temperatures as a consequence of the austenitic grain growth. This phenomenon causes the formation of small defects that when accumulate at triple point grains or high angle grain boundaries facilitate crack nucleation. Figure 6-13 shows a crack close to the solidification interface. The EBSD mapping highlighted the position of the cracks between the solidification grain boundaries. As discussed previously, the literature has reports concerning the occurrence of ductility dip cracking in the Alloy 22[26]. Nonetheless, it is important to highlight that for other HI_w conditions this phenomenon was not observed. Probably the reduction of stress due to solid contraction was minimized for the high HI_w, preventing DDC.

Figure 6-13. Ductility dip cracking characterized in the Alloy 22 cladding, when submitted to thermal cycling of 0.8kJ/mm.

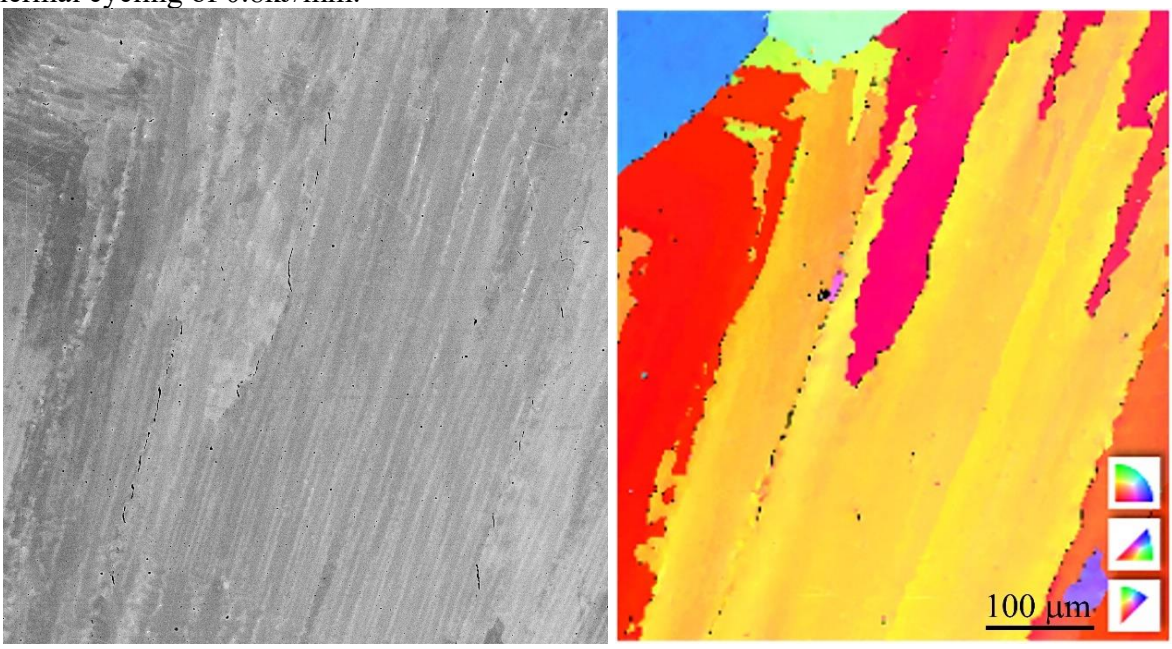

Source: Developed by the author.

6.5 Conclusion

Based on the results of the present study, which investigated the metallurgical compatibility between LAS and Ni-based alloys, we conclude that:

- The single weld bead deposition of 100S-G steel on different Ni-based alloy claddings created new alloys based on the Fe-Ni system with a γ-FCC matrix, and an excellent weldability was observed.
- Numerous partially mixed zones were observed as a consequence of melting point differences between the 100S-G steel and the Ni-based alloy claddings. Small discontinuities and secondary phases were observed mainly in these regions. The thermodynamic simulation predicted a high fraction of secondary phases for the 100S-G steel with the Alloy 625 cladding, followed by the combinations with the 686, 22 and 59 Alloy claddings. This result was confirmed by qualitative analysis of the microstructures.
- The solidification cracks for the mixture with the Alloy 625 cladding was strongly affected by the microsegregation, especially for a high HI_w. The combinations with the Alloys 686 and 22 exhibited larger cracks with low HI_w due to the high contraction stress, while high HI_w suppressed the large cracks, even potentializing the microsegregation. The combinations with the Alloy 59 cladding exhibited large shrink porosities due to the microsegregation, particularly with high HI_w.
- Ductility dip crack was observed only for low HI_w with the Alloy 22 cladding. The low secondary phase fraction was not enough to prevent the γ-FCC grain growth causing the formation of discontinuities.
- Based on the results assessed, the combinations with the Alloy 59 showed good potential applications for low HI_w, whereas the Alloys 686 and 22 showed a good potential for HI_w over 1.0kJ/mm. In contrast, the combinations with the Alloy 625 showed a high tendency for the formation of solidification cracks in all cases assessed.

REFERENCES

1 BELTRAO, R. L. C. *et al*. SS: Pre-salt Santos basin - challenges and new technologies for the development of the pre-salt cluster, Santos basin, Brazil. *In*: OFFSHORE TECHNOLOGY CONFERENCE, 2009, Houston. **Proceedings**. Houston: Offshore Technology Conference, 2009. p. 1-11.

2 LIU, Y.; KYRIAKIDES, S.; HALLAI, J. F. Reeling of pipe with Lüders bands. **International Journal of Solids and Structures**, v. 72, p. 11-25, 2015.

3 DNVGL. DNVGL ST F101: **Submarine Pipeline Systems**. Oslo. p. 520. 2017.

4 CROSS, C. E. On the origin of weld solidification cracking. *In*: BÖLLINGHAUS, T.; HEROLD, H. **Hot Cracking Phenomena in Welds**. Heidelberg: Springer Berlin Heidelberg, 2005. p. 3-18.

5 JONES, R. L. *et al*. Reeled clad SCR weld fatigue qualification. *In*: OFFSHORE TECHNOLOGY CONFERENCE, 2011, Houston. **Proceedings**. Houston: Offshore Technology Conference, 2011. p 1-13.

6 DUPONT, J. N.; BABU, S.; LIU, S. Welding of materials for energy applications. **Metallurgical and Materials Transactions A**, v. 44, n. 7, p. 3385-3410, 2013.

7 SILVA, C. C. *et al*. Evaluation of the corrosion resistant weld cladding deposited by the TIG cold wire feed process. **Materials Science Forum**, v. 783-786, p. 2822-2827, 2014.

8 MOHAMMADI ZAHRANI, E.; ALFANTAZI, A. M. Hot corrosion of Inconel 625 overlay weld cladding in smelting off-gas environment. **Metallurgical and Materials Transactions A**, v. 44, n. 10, p. 4671-4699, 2013.

9 LLOYD, A. C. *et al*. Cr, Mo and W alloying additions in Ni and their effect on passivity. **Electrochimica Acta**, v. 49, n. 17, p. 3015-3027, 2004.

10 DUPONT, J. N. Solidification of an alloy 625 weld overlay. **Metallurgical and Materials Transactions A**, v. 27, n. 11, p. 3612-3620, nov. 1996.

11 SILVA, C. C. *et al*. New insight on the solidification path of an alloy 625 weld overlay. **Journal of Materials Research and Technology**, v. 2, n. 3, p. 228-237, 2013.

12 DAI, T.; LIPPOLD, J. Characterization of the Interface of an Alloy 625 Overlay on Steels Using Nanoindentation. **Journal of Materials Engineering and Performance**, v. 27, n. 7, p. 3411-3418, 2018.

13 SOUZA, R. F.; RUGGIERI, C. Fracture assessments of clad pipe girth welds incorporating improved crack driving force solutions. **Engineering Fracture Mechanics**, v. 148, p. 383-405, 2015.

14 CHONG, T.-V. S. *et al*. Effects of elevated temperatures on the mechanical properties of nickel-based alloy clad pipelines girth welds. **Engineering Fracture Mechanics**, v. 152, p. 174-192, 2016.

15 CIESLAK, M. J. The welding and solidification metallurgy of Alloy 625. **Welding Journal**, v. 70, n. 2, p. 49-56, 1991.

16 CIESLAK, M. J.; HEADLEY, T. J.; FRANK, R. B. Welding metallurgy of custom age

625 PLUS alloy. **Welding Journal (Miami, Fla)**, v. 68, n. 12, p. 473s-482s, 1989.

17 MINÁ, É. M. *et al*. Electron detection modes comparison for quantification of secondary phases of Inconel 686 weld metal. **Materials Characterization**, v. 133, p. 10-16, nov. 2017.

18 MIN, D. *et al*. Welding of quenched and tempered steels with high-spin arc narrow gap MAG system. **The International Journal of Advanced Manufacturing Technology**, v. 55, n. 5, p. 527-533, 2011.

19 MINÁ, É. M. *et al*. Efeito da diluição sobre a microestrutura da liga AWS ER NiCrMo-14 na soldagem de revestimentos pelo processo TIG com alimentação de arame frio. **Soldagem & Inspeção**, v. 21, n. 3, p. 317-329, 2016.

20 MINÁ, E. M. *et al*. Effect of dilution on the microstructure of AWS ERNiCrMo-14 alloy in overlay welding by the TIG process with cold wire feed. **Welding International**, v. 32, n. 2, p. 130-138, 2018.

21 CHEN, S. *et al*. Effect of post-weld aging treatment on the precipitation and mechanical behavior of Fe-Ni based alloy weldment. **Materials Science and Engineering: A**, v. 718, p. 363-370, 2018.

22 KOU, S. **Welding Metallurgy**. 2 ed. Hoboken, New Jersey: John Wiley & Sons, Inc., 2003.

23 SILVA, C. C. *et al*. Assessment of microstructure of alloy Inconel 686 dissimilar weld claddings. **Journal of Alloys and Compounds**, v. 684, p. 628-642, 2016.

24 SILVA, C. C. *et al*. Mechanical properties and microstructural characterization of aged nickel-based Alloy 625 weld metal. **Metallurgical and Materials Transactions A: Physical Metallurgy and Materials Science**, v. 49, n. 5, p. 1653-1673, may. 2018.

25 AGARWAL, D. C.; HERDA, W. R. The “C” family of Ni-Cr-Mo alloys’ partnership with the chemical process industry: The last 70 years. **Materials and Corrosion**, v. 48, n. 8, p. 542-548, ago. 1997.

26 GALLAGHER, M. L.; LIPPOLD, J. Weld cracking susceptibility of alloy c-22 weld-metal. *In*: BÖLLINGHAUS, T.; LIPPOLD, J.; CROSS, C. E. **Hot Cracking Phenomena in Welds III**. Heidelberg: Springer, Berlin, Heidelberg, 2011. p. 367-391.

27 SCHEIL, E. No Title. **Z. Metallkd.**, v. 34, p. 70-72, 1942.

28 RAMIREZ, A. J.; LIPPOLD, J. C. High temperature behavior of Ni-base weld metal: Part II – Insight into the mechanism for ductility dip cracking. **Materials Science and Engineering: A**, v. 380, n. 1, p. 245-258, 2004.

29 RAMIREZ, A. J.; LIPPOLD, J. C. High temperature behavior of Ni-base weld metal: Part I. Ductility and microstructural characterization. **Materials Science and Engineering: A**, v. 380, n. 1, p. 259-271, 2004.

30 RAMIREZ, A. J.; LIPPOLD, J. C. New insight into the mechanism of ductility-dip cracking in Ni-base weld metals. In: BÖLLINGHAUS, T.; HEROLD, H. **Hot Cracking Phenomena in Welds**. Heidelberg: Springer Berlin Heidelberg, 2005. p. 19–41.

31 HU, Y. L. *et al*. Effect of Ti addition on cracking and microhardness of Inconel 625 during the laser solid forming processing. **Journal of Alloys and Compounds**, v. 711, p. 267-277, 2017.

32 YANG, Y. K.; KOU, S. Macrosegregation in Cu–30Ni welds made with dissimilar filler metals. **Science and Technology of Welding and Joining**, v. 13, n. 4, p. 318-326, maio 2008.

33 YANG, Y. K.; KOU, S. Macrosegregation mechanisms in arc welds made with dissimilar filler metals. **Science and Technology of Welding and Joining**, v. 15, n. 1, p. 15-30, jan. 2010.

34 KOU, S.; WANG, Y. H. Weld pool convection and its effect. **Welding Journal (Miami, Fla)**, v. 65, n. 3, p. 63s-70s, 1986.

35 SOYSAL, T. *et al*. Macrosegregation in dissimilar-metal fusion welding. **Acta Materialia**, v. 110, p. 149-160, 2016.

36 MINÁ, É. M. *et al*. The effect of dilution on microsegregation in AWS ER NiCrMo-14 alloy welding claddings. **Metallurgical and Materials Transactions A: Physical Metallurgy and Materials Science**, v. 47, n. 12, 2016.

Chapter 7

Dissimilar girth welding of nickel-based alloy cladded pipelines: a new approach combining Alloy 625 and low alloy steel as the filler metals for overmatch requirements

7.1 Abstract

The present study manufactured and evaluated a new approach to weld API 5L X65 steel pipe with an internal cladding of Alloy 625, using two different filler metals in the same joint to provide an overmatch of yield strength. The filler metals used were alloy 625 for the 1st and 2nd weld passes of the joint and AWS ER100S-G steel from the 3rd weld pass onwards. The microstructure and mechanical properties of the welded joint were evaluated. The results showed that the mixture of the steel weld pass and the previous Ni-based alloy weld pass caused the incorporation of Ni, Cr, Mo and Nb. This incorporation caused hardenability by quenching and solid solution and caused the formation of a microstructure based on martensite with retained austenite, MA particles and complex carbides rich in Ti and Nb. Moreover, the microsegregation of Nb and Mo caused the nucleation of low melting point phases, which favored the nucleation of numerous solidification cracks along the two first steel weld passes. These solidification cracks impaired the mechanical properties of the welded joint that did not pass the transverse tensile, bending and impact toughness tests.

7.2 Introduction

The welding of dissimilar materials is a powerful manufacturing technique that is widely used by industry in general[1–3]. The possibility to combine properties of interest from materials of different classes allows the manufacturing of complex equipment and/or components[4–10]. The oil & gas industry commonly uses dissimilar welding to manufacture risers based on steel pipes with an internal corrosion resistant alloy (CRA) cladding[11–14]. Normally, the CRA claddings are manufactured with a Ni-based alloy, especially Alloy 625[15–17]. The excellent corrosion resistance of Alloy 625 extends the life of the component and has a good cost-benefit[13].

The procedure to perform the dissimilar welding of steel pipe using a Ni-based alloy is well established. In general, the most common practice applies the same Ni-based alloy as

used for the CRA cladding. Sarzosa *et al*.[18] studied the CTOD fracture toughness of a dissimilar welded joint of an API 5L Grade X65 pipeline steel with inner cladding made from alloy 625, and where the joint groove was fully filled with alloy 625. Chong *et al*.[19] also evaluated the tensile and fracture toughness of API 5L Grade X65 pipelines cladded with Incoloy 825, which were fully welded using alloy 625.

Even though these procedures are well established, a certain amount of care is required to achieve a good result, especially when associated with the mixture of different chemical elements[19–21]. Therefore, a low dilution with the steel pipe is recommended, considering that dilution causes the incorporation of some elements such as Fe, Si, Mn and C and this may lead to the formation of solidification cracks[20]. The mechanical properties of a welded joint are based on the mechanical features of the Ni-based alloy used, in this case, the Alloy 625. This assumption reduces the field of application for such components, especially for welding high strength low alloy steel (HSLA) pipes such as API 5L X65, X70 and X80 steel[19,20].

Before defining the welding procedure to perform the girth joint welding of such a component, it is important to define the installation process that will be used for the pipeline. Nowadays, there are three methods in use: S-lay, J-lay and reel-lay. In the two first methods, the pipes are transported to an offshore unit and then the pipeline is manufactured by conventional welding processes[22,23]. In the case of the reel-lay process, the girth joint welding of the pipes and inspection of the weldments are carried out onshore; thus increasing the productivity and quality of the manufactured components[24]. Even with the advantages offered by the reel-lay process, this installation method submits the pipeline to a spooling step onto a large diameter drum and subsequently an unspooling step when installing and both steps introduce a plastic deformation of about 2%[25]. As welding processes commonly introduce some defects such as porosity, shrink porosity, solidification cracks and reheat cracks[26], the reel-lay process requires weldments with an excellent quality and good mechanical properties due to the inherent plastic deformation caused by the installation process. Therefore, the challenge is how to perform the joint welding of such risers to provide sufficient overmatch for application.

The DNVGL ST F101[27] defines some requirements for girth welding of pipelines that will be installed by the reel-lay process taking into account the plastic deformation of the spooling and unspooling steps. The minimum yield strength (YS) of the welded joint must be at least equal to the maximum established for the YS of the base metal minus 20 MPa. While for the other installation processes such as S-lay and J-lay, the standard defines that the YS of

the welded joint must overmatch the standard minimum yield strength (SMYS) of the base metal by at least 80 MPa[27]. In fact, common practice recommends a minimum overmatch of about 100 MPa, even for the reel-lay installation processes[22]. The Alloy 625 in the as-welded condition does not reach the minimum YS required by DNVGL ST F101. According to Jones *et al*.[20], the Alloy 625 does not offer the minimum YS to overmatch the mechanical properties of API 5L X65 steel pipe. In this case, the overmatch is only achieved after work hardening caused by the spooling and unspooling steps[20]. The authors pointed out that DNV classifies this kind of girth weld as 'partially overmatch' and recommends considering this assumption in all necessary calculations[28]. Naturally, this welding procedure is not the best way to perform the joint welding of this type of component.

One solution to this problem is to use low alloy steel (LAS) in order to provide overmatch for the YS required. Nonetheless, the corrosion resistance of CRA cladding must be kept to guarantee the integrity of the component. Thus, the 'simplest' solution must consider the use of a Ni-based alloy for the root weld pass, while the other weld passes use a low alloy steel. However, this solution is not so simple considering the metallurgical problems related to the mixture of a steel with a Ni-based alloy, especially for Alloy 625. According to the literature, Alloy 625 has a relatively high solidification crack susceptibility, which is increased when Fe, Si and C are incorporated by dilution with LAS steel[29]. These elements, combined with Nb, potentiate the nucleation of low melting point phases such as the Laves phase[15,16,29,30].

Notably, Alloy 625 is a Ni-based alloy with a good cost-benefit in relation to other alloys of the same class. Alloy 625 was developed in the 60's and since its development it has been widely used in a number of applications, which include dissimilar welding with LAS steel. Recently, Silva *et al*.[15] successfully welded an overlay on C-Mn steel using Alloy 625. No solidification cracks were mentioned, even with the presence of Laves phase. Thus, it is difficult to predict the metallurgical problems associated to the use of Alloy 625 for this new propose to girth weld rigid risers with an internal CRA cladding of Alloy 625.

The present study manufactured and evaluated a new approach for girth welding of API 5L X65 steel pipes with internal cladding of Alloy 625, for a pipeline to be installed by the reel-lay process. The complex dissimilar girth welding was manufactured using two-filler metals from different classes of materials: Alloy 625 and AWS ER100S-G steel. The Ni-based Alloy 625 was used for the root and hot weld passes in order to guarantee a corrosion resistance similar to the internal cladding of the pipe. The 100S-G steel was selected to fill the main part of the joint, in order to provide the minimal overmatch of YS required by DNVGL ST F101. After the welding the microstructure and mechanical properties of welded joint were evaluated.

7.3 Experimental procedure

An API 5L X65 steel pipe with internal cladding of Alloy 625 was used to make a joint weld. The welding procedure followed the new approach as described above. The first two weld passes of the welded joint used the Alloy 625, while the other weld passes used the AWS ER100S-G steel. According to the AWS A5.28/A5.28M standard[31], the minimum YS of 100S-G steel is enough to overmatch the YS of API 5L X65 steel. A schematic drawing of the proposed welded joint is shown in Figure 7-1. The chemical compositions of the materials used in the present study are given in Table 7-1. The chemical compositions were obtained by optical spectroscopy measurements and, in the case of the filler metals the results were obtained following recommendations of the AWS A5.28/A5.28M and API 5L standards[31,32].

Figure 7-1. Schematic drawing of the proposed welded joint.

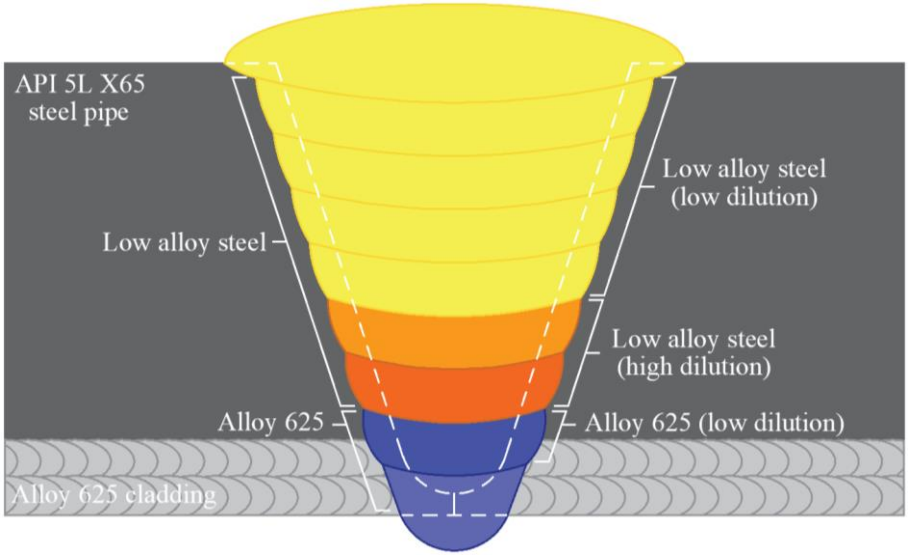

Source: Developed by the author.

Table 7-1. Chemical compositions of the materials used in the dissimilar joint welding.

Chemical composition of materials															
Alloy	Al	C	Co	Cr	Cu	Fe	Mn	Mo	Ni	Nb	P	S	Si	Ta	Ti
Alloy 625 (AWS ERNiCrMo-3)	-	0,1	0.06	21.67	-	0,09	-	8.81	65.22	3.73	0,002	0,015	-	0.02	0,17
API 5L X65 steel pipe	0,04	0,11		0,12	0,18	97,51	1,17	0,14	0,34	-	0,012	0,004	0,28		-
AWS ER100S-G steel	-	0,04		0,12	0,11	96,47	1,37	0,38	0,82	-	0,055	0,014	0,62		0.13

Source: Developed by the author.

The welded joint was manufactured using the pulsed gas metal arc welding process (GMAW-P). The weldments were realized on an industrial robotic workbench, which offered

accuracy in the movements, especially in the welding speed and weaving parameters adopted. The alloy AWS ERNiCrMo-3 and the AWS ER100S-G steel were used as filler metals with 1.1 mm and 1.2 mm of diameter, respectively. Pure argon gas was used as the protective gas to deposit the Alloy 625, while for the low alloy steel Ar + 4%CO_2 was used. Figure 7-2 shows the welding workbench used. The main welding parameters to manufacture the welded joint are given in Table 7-2.

Figure 7-2. Industrial robotic workbench with a) welding torch coupled. The welding torch position b) before and c) after a welding pass.

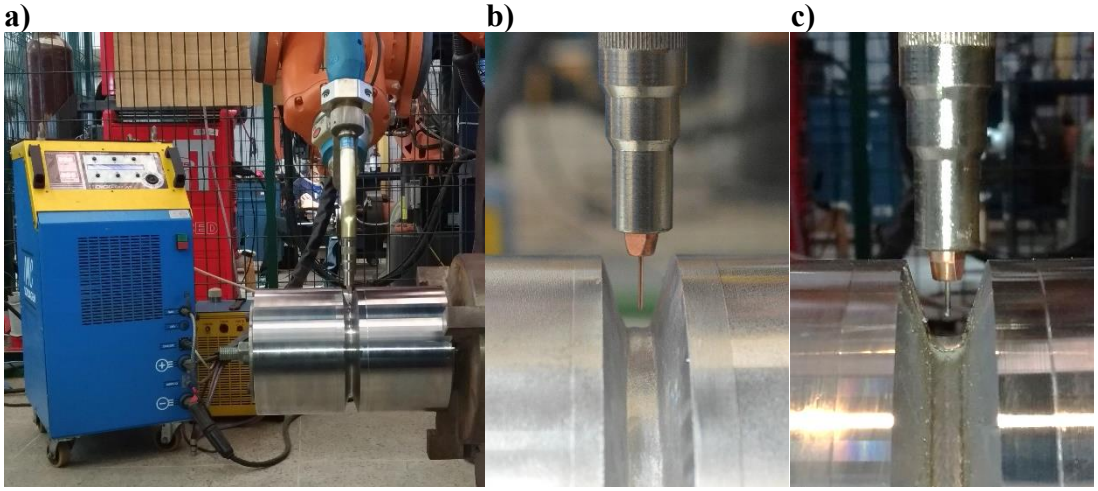

Source: Developed by the author.

Table 7-2. Main welding parameters used for each weld pass.

Welding parameters										
Passes	Alloy	I_p (A)	I_b (A)	t_p (s)	t_b (s)	S_w (cm/min)	U (V)	S_{wf} (m/min)	A_t (mm)	HI_w (kJ/mm)
1st pass	Alloy 625	300	90	2.2	4.4	45	20.9	7.2	0.6	0.50
2nd pass	Alloy 625	300	90	2.2	4.4	40	21.4	7.0	2.2	0.58
3rd pass	100S-G	300	90	2.2	4.4	35	21.6	5.5	3.7	0.65
4th pass	100S-G	300	90	2.2	4.4	35	20.1	5.5	4.7	0.62
5th pass	100S-G	300	90	2.2	4.4	25	20.2	5.5	5.5	0.88
6th pass	100S-G	300	90	2.2	4.4	18	20.2	5.5	6.0	1.23
7th pass	100S-G	320	100	2.2	4.4	15	21.7	5.8	6.5	1.75
8th pass	100S-G	320	100	2.2	4.4	14	21.9	5.8	7.0	1.75
9th pass	100S-G	320	100	2.2	4.4	13	22.2	5.8	7.5	1.89
10th pass	100S-G	320	100	2.2	4.4	12	22.6	5.8	8.4	2.11

Source: Developed by the author.

The welded joint was evaluated by macrograph and micrograph analyses. The basic metallographic steps that include cutting, gridding, polishing and etching were carried out on a cross-section of the welded joint. Etching was carried out using 2% nital and 10% chromic acid

solutions to reveal the microstructure of the steel and the Ni-based weld passes, respectively. The microstructure of the welded joint was evaluated using scanning electron microscopy (SEM) techniques.

The mechanical properties of the welded joint were assessed by bending, transverse tensile and Charpy-V tests. The samples were manufactured following the recommendation of DNVGL ST F101[27]. In total 4 bending, 2 transverse tensile and 5 Charpy-V samples were evaluated. Figure 7-3 shows a schematic image of the samples. The notch in the Charpy-V test was positioned at the 3rd weld pass of the welded joint, in other words, in the first 100S-G steel weld pass, which naturally showed a high dilution with the 2nd Alloy 625 weld pass.

Figure 7-3. Schematic image of a) bending, b) transverse tensile and c) Charpy-V tests with the notch in the 3rd weld pass.

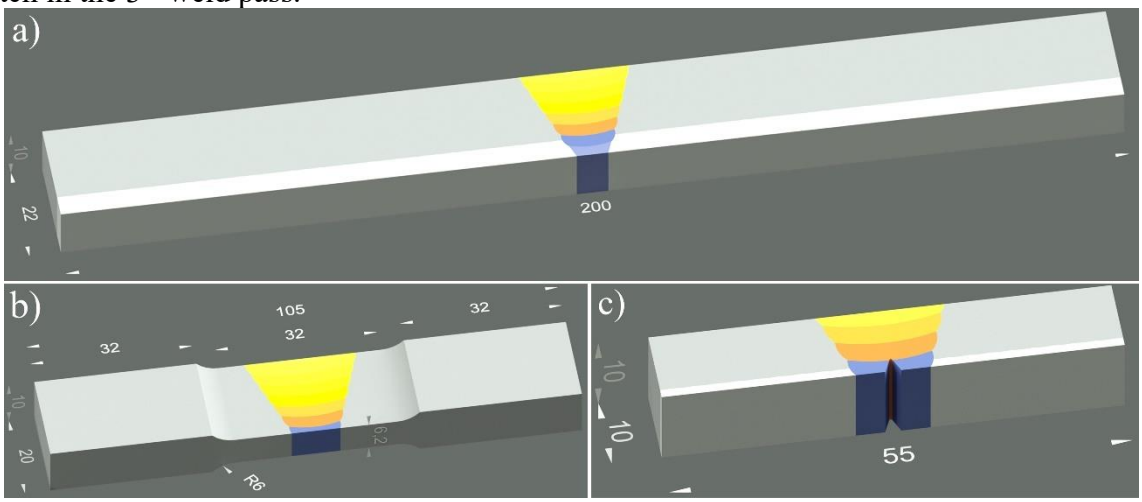

Source: Developed by the author.

The resistance to localized plastic deformation was investigated using two techniques: microhardness and hardness. A microhardness mapping was performed using 100 gf. The distance between the indentations of the microhardness map was 300 μm, over an area covering the first six weld passes of the welded joint. The hardness profile was made using a 10 kgf load. The test was made along the weld centerlines, for all weld passes, starting from the 1st weld pass (root), with 1 mm spacing between indentations.

7.4 Results and Discussion

7.4.1 Weldability of welded joint

The filler metals used were able to weld the pipes with ease. The deposition of the Alloy 625 for the root and hot passes showed a good wettability with the internal cladding of

the pipe, since they were the same Ni-based alloy. The same was also observed for the deposition of the low alloy steel weld passes. In general, Ni-based alloys have a lower melting point in comparison with steels in general. This physical feature favored the fusion of the Alloy 625 weld pass during deposition of the 100S-G steel, preventing a lack of fusion. On the other hand, the 3rd weld pass exhibited a large dilution with the 2nd weld pass due to the intrinsic physical feature mentioned, even for the use of low welding heat input (HI_w).

Although the wettability between the alloys showed good compatibility, the weldability was not satisfactory. The first two weld passes deposited using the 100S-G steel showed several solidification cracks. The cracks observed on the surface of these weld passes are shown in Figure 7-4. Large cracks were observed concentrated along the weld centerline of both weld passes, which suggest that the cracks occurred as a consequence of the segregation phenomenon[33]. During solidification, some alloying elements that have low affinity with solid phases are rejected into the liquid portion. Solidification grains (SG) grow from a solid-liquid interface following the heat gradient, so the elements that are segregated into the liquid zone (portion) concentrate along the weld centerline. A high concentration of Ni, Cr, Mo, Nb, Fe, Si and C may lead to the nucleation of secondary phases[15,16,34–36] that in some cases may have a low melting point. These phases may cause the expansion of the solidification temperature range which when associated with the shrinkage stresses due to solidification and cooling may cause the formation of solidification cracks[26]. More evidence of this will be discussed later in the text.

Except for solidification cracks observed along the 3rd and 4th weld passes, the welded joint did not exhibit any other cracks, porosity or lack of fusion. Figure 7-5 shows the macrograph of the welded joint, moreover, some microstructures were displayed, in order to give an idea of how dissimilar the welded joint is. Certain information can be extracted from this macrograph: the first two Ni-based weld passes fully filled the CRA cladding region, maintaining the corrosion resistance of the component intact; the 3rd weld pass of the welded joint was not revealed by chemical and electrochemical etching, due to the incorporation of a great amount of alloying elements from the dilution of the 100S-G steel weld pass with the 2nd Alloy 625 weld pass, which made the 3rd weld pass almost inert to nital and chromic acid solutions. For the same reason, the 4th weld pass was only lightly revealed if compared with the subsequent steel weld passes. Like the 3rd weld pass, the chemical composition of the 4th weld pass of the welded joint was significantly affected by dilution of the previous steel weld pass.

Figure 7-4. Solidification cracks observed at the surface of a) 3rd and b) 4th weld passes of the welded joint.

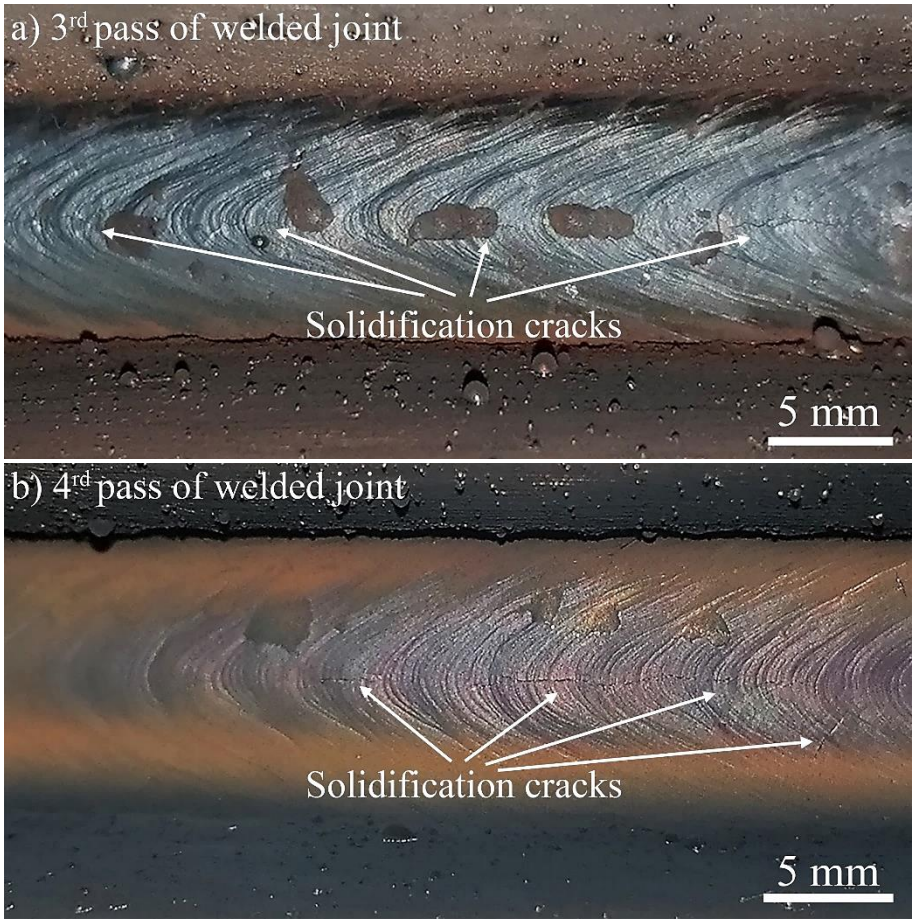

Source: Developed by the author.

Another important feature of the weld passes is related to the depth-to-width (D/W) ratio. All weld passes were deposited keeping a low D/W in order to avoid the concentration of alloying elements being segregated to the weld centerline. In this case, the weld pool shows an elliptical shape that prevents the growth of large SG and, consequently, their meeting at the weld centerline[33,37]. Thus, welding with weaving has at least two advantages. The first is related to the amplitude wave that increases the width of the weld pass. The second is that the arc waving promotes a constant motion of the heating source, which causes a deflection of grain growth during solidification, and prevents the SG meeting at the center of the weld bead. Even adopting good welding practices recommended by the literature[11,38], the 3rd and 4th weld passes exhibited solidification cracks. Thus, the mixture of the different materials used here introduced alloying elements with low affinity or solubility into the new matrix, and this had important role in nucleation of cracks. The microchemical and microstructure analyses of the weld passes and their respectively solidification cracks will be discussed with more details later in the text.

The chemical compositions of the first six weld passes of the welded joint are given in Figure 7-6. The two Alloy 625 weld passes exhibited a similar chemical composition. The main difference was due to the dilution of the 2nd Alloy 625 weld pass with the steel pipe that caused the increase of Fe and the reduction of Ni, Cr, Mo and Nb. In general, these weld passes will exhibit features quite similar to Alloy 625 for the as-welded condition, without dilution from another material.

Figure 7-5. Macrograph of a transverse cross-section of the welded joint and some of the microstructures of the main weld passes.

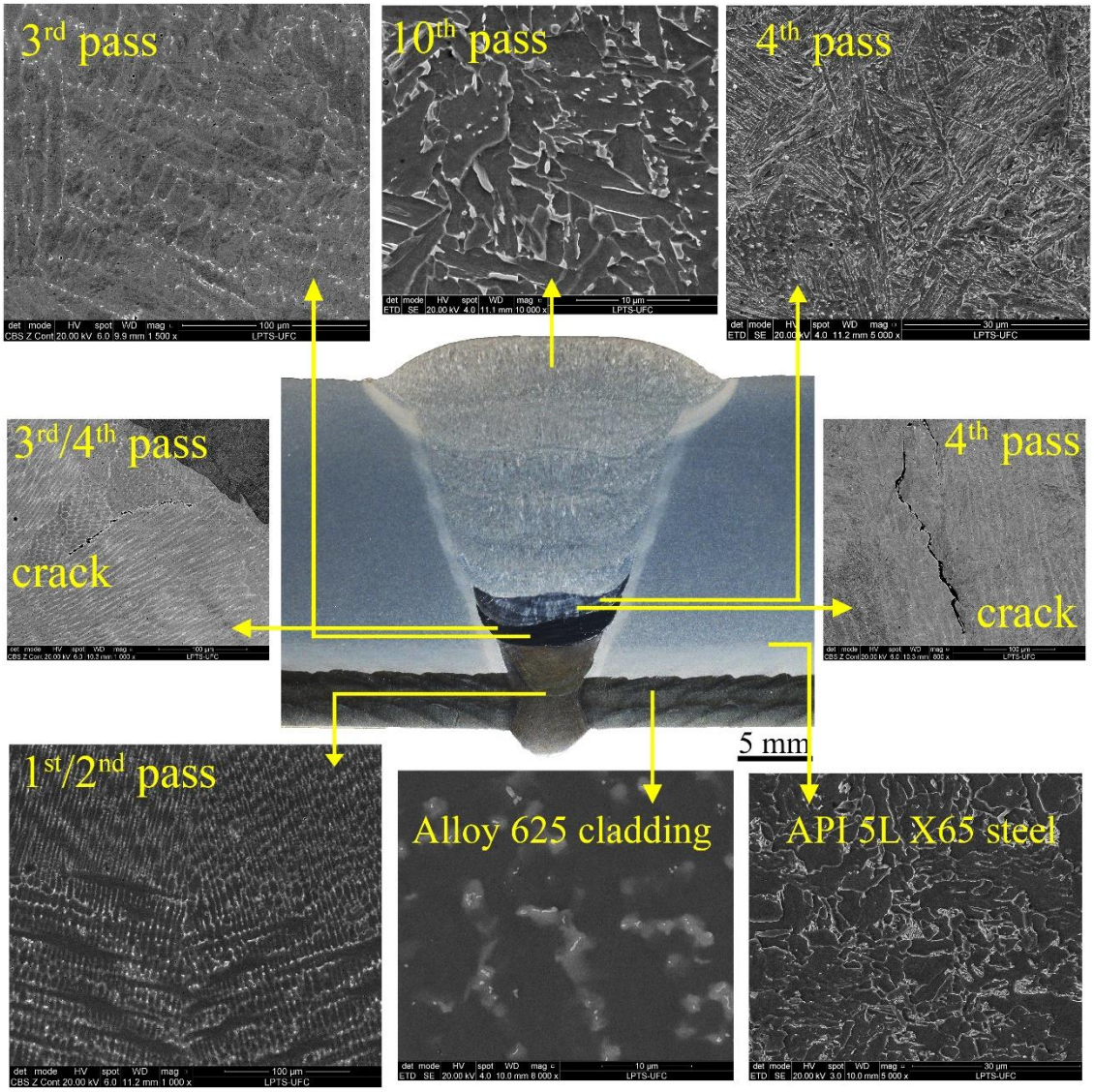

Source: Developed by the author.

In contrast, the 3rd weld pass of the welded joint exhibited greater dilution between 100S-G steel and Alloy 625, with a high incorporation of Ni, Cr, Mo, and Nb into the Fe matrix. The Ni and Nb fractions were about 15% and 1%, respectively, and the 3rd weld pass was diluted

by at least 30% with the 2nd weld pass. Certainly, the weld parameters influence the dilution. Nonetheless, the welding parameters used were in general those that give a low dilution level, that is: arc weaving of heat source and low HI_w. Therefore, it is reasonable to suggest that the differences in the melting points of Alloy 625 and 100S-G steel were the main reason for this medium-to-high dilution level obtained. Note that this inherent phenomenon to welding of these materials caused the addition of 1% of Nb in the 3rd weld pass and 0.2% of Nb in the 4th weld pass.

Figure 7-6. Chemical composition of the first six weld passes of the welded joint. The arrows indicate the scale bar side.

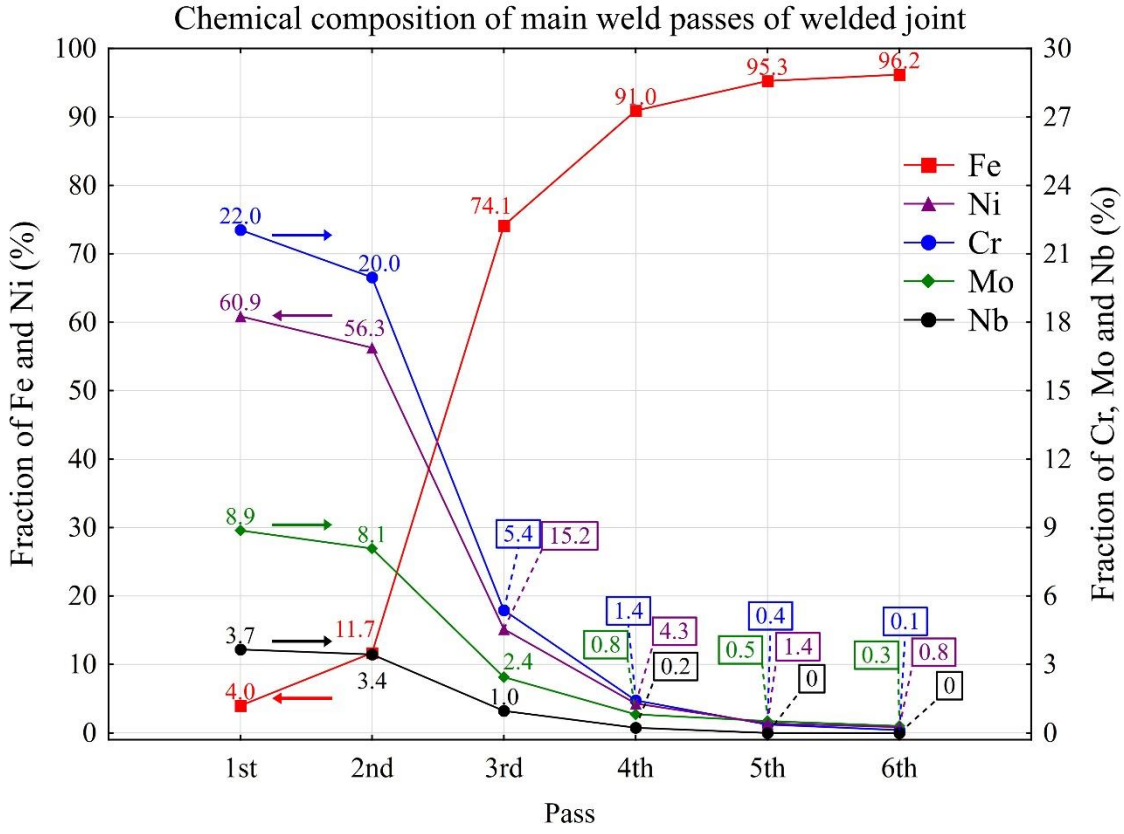

Source: Developed by the author.

Although the crystal lattice of pure Nb is a body centered cube (BCC) as well as general steels, these weld passes started the solidification as a γ face centered cubes (FCC), which have a lower affinity for Nb. Consequently, a fraction of Nb was segregated to remaining liquid and then solidified as a eutectic phase. This represents one reason among others that explains why BCC steels have a lower solidification crack susceptibility, because BCC crystal lattice has a stronger affinity for elements such as Nb, Si, S and P[39] when segregated to liquid turns thermodynamically stable the nucleation of low melting point phases at final stage of

solidification[29]. Probably the Nb fraction present in these weld passes when rejected to the liquid portion causes the formation of a liquid film between the solidified grains, thus reducing the mechanical resistance between them[40]. This phenomenon associated with stresses related to the liquid-to-solid state transformation and solid contraction cause the formation of solidification cracks.

The chemical composition of the 5th weld pass of the welded joint was also affect by dilution. This was due to a mixture of the first steel weld pass with the Alloy 625 weld pass. In this case, only a minor addition of Ni, Cr and Mo was achieved. From the 6th weld pass onwards the chemical composition was quite similar to the low alloy steel used.

7.4.2 Microstructural analysis

As previously discussed, the microstructures of the welded joint depicted in Figure 7-5 are quite complex and dissimilar. This is because different filler metals were used and these created several new materials at each weld pass. Figure 7-7 shows the microstructure of the 1st and 2nd weld passes of the welded joint. In general, the two Alloy 625 weld passes exhibited a very similar microstructure. Both showed a microstructure composed of a γ-FCC matrix with a dendritic morphology remaining from the solidification. Inside the interdendritic region (light gray tone), some small particles of secondary phases were observed; especially in the 1st weld pass. The final portion of the weld pass exhibited a greater concentration of segregated alloying elements and the reciprocal is also true. Moreover, the 2nd weld pass presented fewer alloying elements available for segregation (Figure 7-6) and subsequently to nucleate as secondary phases. No solidification cracks were observed in these weld passes, even along the weld centerline.

The bulk microstructure of the 3rd weld pass is shown in Figure 7-8. The microstructure exhibited a cellular feature due to solidification, which is typical for materials that kept the same matrix phase nucleated during solidification without any significant solid transformations. According to simulations of solidification based on the Scheil-Gulliver model, the 3rd weld pass started its solidification as γ-FCC; more details of this will be present later in the text. However, it is also important to highlight that the large addition of Cr, Mo and Nb from the Ni-based alloy associated with the fast cooling rate favored the martensitic transformation. Hence, the grains were seen to be aligned in the same direction, that is, at 45° in relationship to the solidification direction. Probably this microstructure was the result of a slip of the highest

atomic density plane, which is (111). Therefore, it is believed that a large part of the microstructure of the 3rd weld pass is martensite.

Figure 7-7. Microstructure of interface between the 1st and 2nd weld passes of the welded joint.

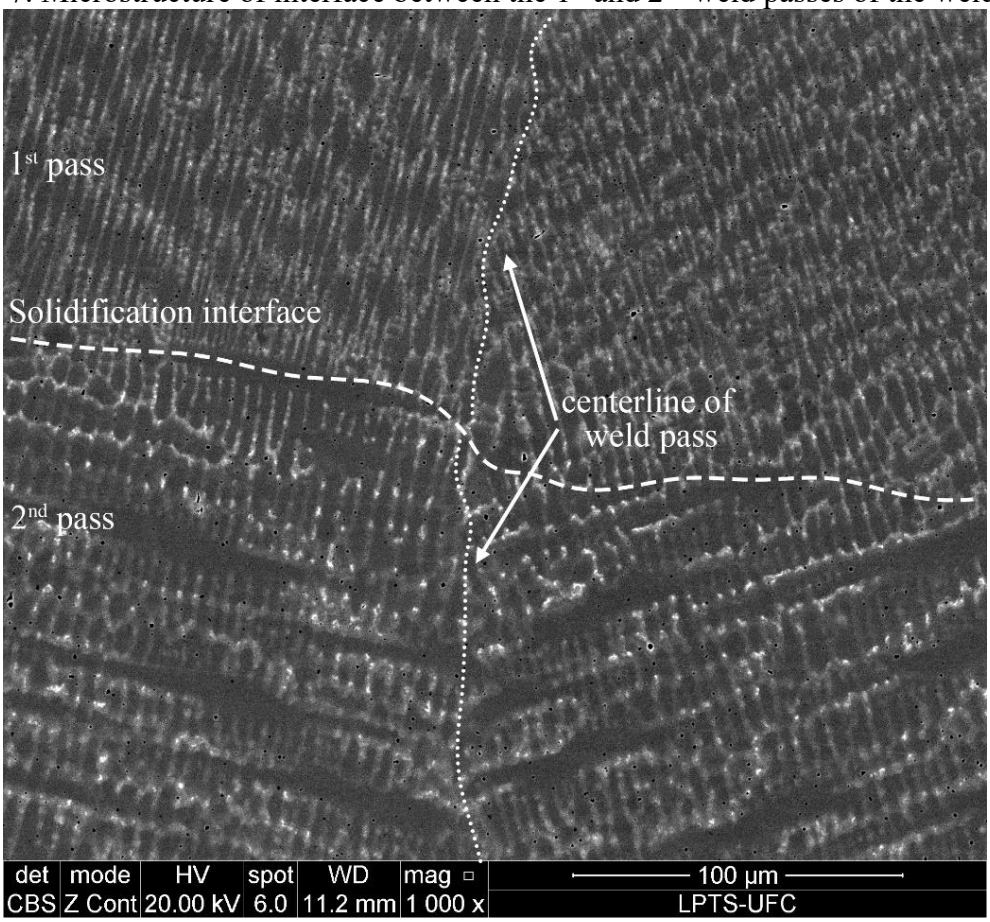

Source: Developed by the author.

Figure 7-8. Bulk microstructure of the 3rd weld pass of the welded joint, highlighting the presence of secondary phases and a shear microstructure.

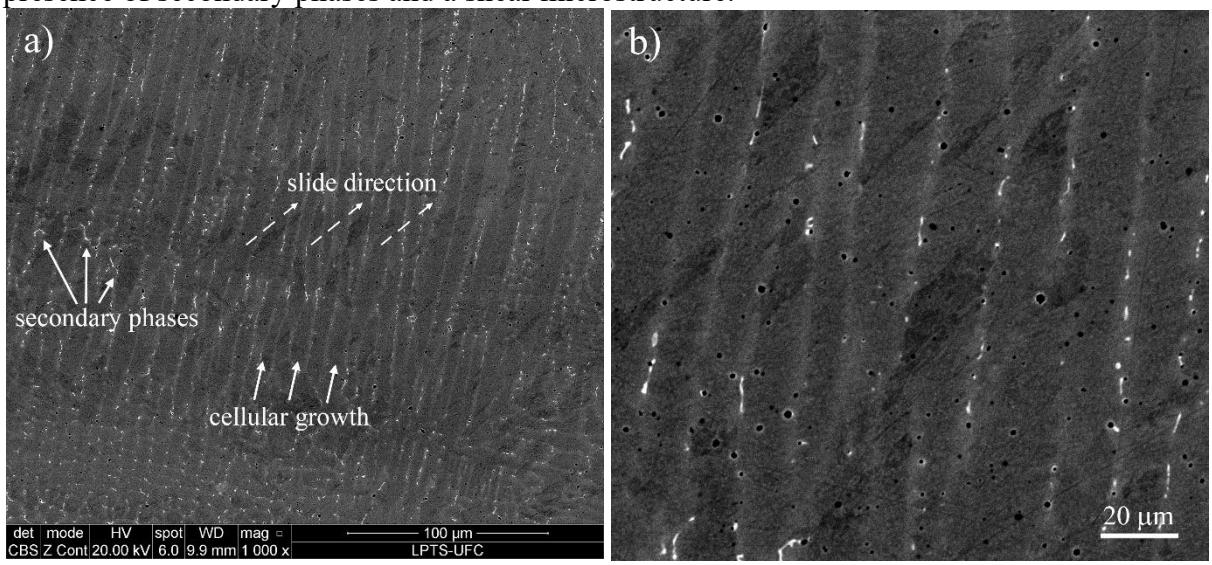

Source: Developed by the author.

It is important to highlight the presence of secondary phases in the intercellular regions. The fraction is not large, but these particles are present in almost all intercellular regions. Moreover, the misshapen and linear morphology suggest that these phases nucleated at the final stage of solidification taking the shape occupied by the remaining liquid. This elongated morphology indicates that reminiscent liquid has a low surface tension with solidified grains, which in other words means that the liquid has a great wetting with grain boundary[40]. This feature favors the formation of large solidification cracks at intercellular regions and or solidification grain boundaries.

An over etching using a higher concentration of HNO_3 was performed in order to assess with more details the microstructure of 3rd weld pass. The over etching revealed the presence of numerous macrosegregation regions. Figure 7-9 show these macrosegregation observed along of 3rd weld pass. Some factors contributed to formation of these macrosegregations that include, filler richer and base metal richer. In all cases happened a partially mixture between materials. The arc welding pressure caused a strong turbulence that impaired the full mixture of alloys. The weaving of arc welding also contributed to increase the turbulence during solidification, considering the continuous motion of heat source that melted different materials for each instant of time, since that when arc welding was positioned closed to wall groove there was a high participation of steel pipe in weld metal chemical composition, whereas when arc welding was in the center joint there was a higher participation of Alloy 625 weld pass in fusion zone. The fast cooling rate due to low HI_w adopted also contribute reducing the time able to mixture the melted materials. On the other hand, the differences about melting point of alloys was determinant to avoid the full mixture between them. The filler richer regions solidified early in comparison with base metal richer regions, since the great participation of Ni-based weld pass cause the reduction melting point.

Figure 7-9. Macrosegregation microstructure of the 3rd weld pass highlighting the filler richer regions and base metal richer regions as well.

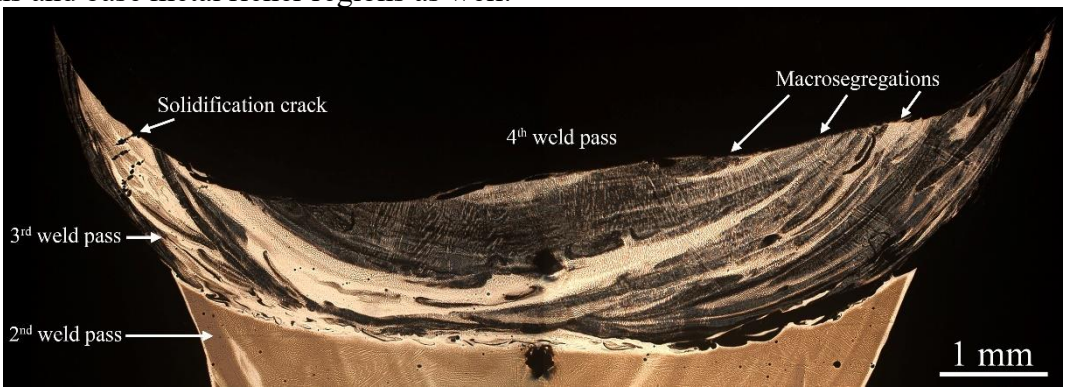

Source: Developed by the author.

The over etching also reveled the main feature of microstructure of the 3rd weld pass. Figure 7-10 exhibits the microstructure in low and high magnification. It was observed a martensite microstructure concentrated into dendrite region, but also troughing the interdendritic region. It is reasonable conclude that this weld pass is mainly composed by a α' martensite matrix. The great incorporation of Ni, Cr and Mo associated with C and Mn increased the quenching ability of the weld pass. Studies assessing the welding low alloy steel with massive addition of Ni and Mn had reported a microstructure composed by martensite[41,42], especially in high cooling similar to experienced in the present study, once that fast solidification introduce strain stress enough to provide the diffusionless transformation. Based in empirical relationship proposed by Andrews[43] to calculate the start temperature of martensite (M_s) considering substitutional and interstitial elements (Equation 1).

$$M_s(°C) = 539 - 423wt\%C - 30.4wt\%Mn - 17.7\ wt\%Ni - 12.1\ wt\%Cr - 7.5\ wt\%Mo \quad (1)$$

Figure 7-10. a) Microstructure of the 3rd weld pass after over etching highlighting NbC, TiC and eutetic film concentrated mainly at interdendritic region.

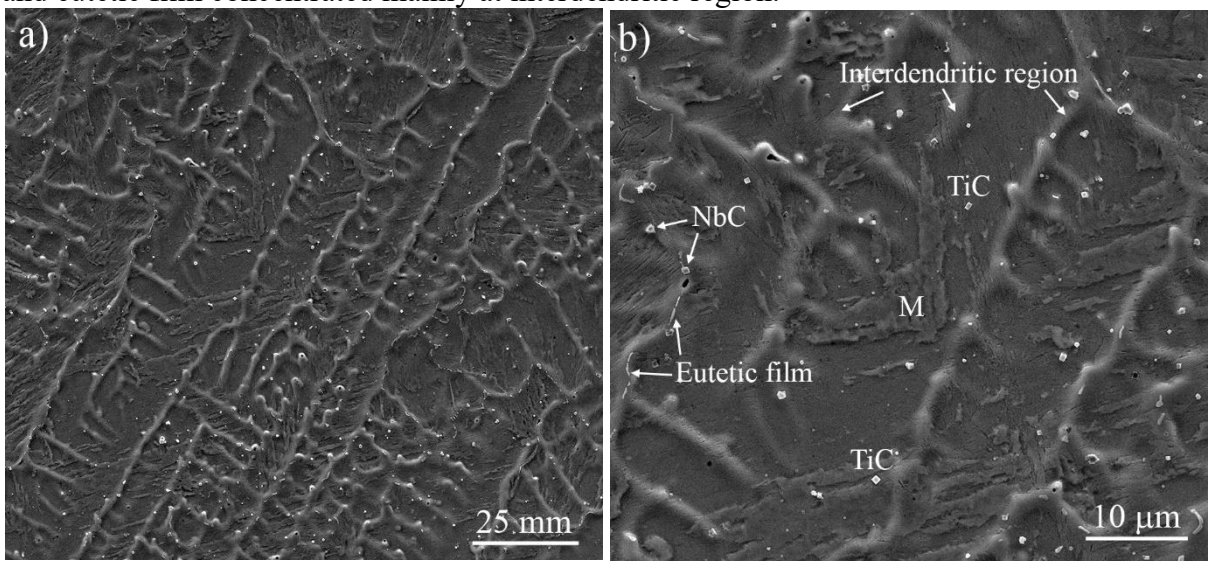

Source: Developed by the author.

In general, the addition of alloying elements reduces the M_s temperature, especially the elements that stabilize FCC crystal lattice such as C, N, Ni and Mn. The estimated M_s temperaturewas about 122°C, in turn, it is high enough to provide the martensite transformation. Kaufman and Cohen[44] assessed the martensitic transformation in Fe-Ni system by resistance-temperature curves. For alloy with 14.5wt% of Ni was obtained 350°C and 230°C for M_s and M_f, respectively. Comparing these results with M_s temperature calculated for 3rd weld pass is reasonable takes obtained value as good approximation, since Mn, Cr and Mo also were present

in solution. It is important mention that for this case the M_f temperature could be below to room temperature and consequently some retained γ-FCC is cannot be negligible, especially in interdendrite region rich in segregated elements like C, Mn, Ni and Mo. The austenite grain size before to experience the martensite transformation must be considered in this discussion. According to Yang and Bhadeshia[45] a large austenite grain size raises the M_s and M_f by consequence. Figure 7-8 provided an idea of how bigger was the grain size of austenite previous. Among of several factors, highlights the low D/W feature associated with fast cooling rate caused the grain growth from solid/liquid interface until surface of weld bead, providing large grains which its length were almost the same of weld bead depth.

Others phases were observed in Figure 7-10. Numerous complex carbonitrides rich in Ti and Nb were observed finely distributed along of microstructure. The chemical composition of such particles (Table 7-3) suggest the presence of oxides. Silva *et al.*[15] advanced in the characterization of such complex carbonitrides using selected area diffraction (SAD) and energy dispersive X-ray spectroscopy (EDS) in transmission electron microscope. The authors conclude core particle is composed by TiN act as an excellent nucleating agent for the formation of (NbTi)C shells surrounding the nitride particle (Figure 7-11).

Table 7-3. EDS chemical composition analysis performed in carbonitrides, dendrite, interdendrite and eutetic film.

Chemical composition of secondary phases of the 3rd weld pass											
Phase	Al	O	Mg	Si	Cr	Ti	Mn	Fe	Ni	Nb	Mo
α’	-	-	-	0.3	4.2	-	1.1	81.1	11.2	0.4	1.7
Ti(N,C)	12.8	9.0	0.3	0.3	3.6	8.0	0.9	51.0	7.2	5.4	1.6
(Nb,Ti)C	1.9	6.3	-	0.5	3.9	7.9	1.2	46.4	7.7	22.6	1.8
$Eutetic_{film}$	-	-	-	0.5	4.3	-	1.4	59	10.7	21.9	2.3

Source: Developed by the author.

As showed in Figure 7-5, the 3rd weld pass of the welded joint exhibited solidification cracks. Figure 7-12 gives a general view of the solidification cracks in the 3rd weld pass. Various cracks were observed not only along the weld centerline, but also well distributed along the weld pass itself, even considering that the weld pass had a low D/W ratio. This highlights the high susceptibility to solidification cracking. The mixture of 100S-G steel and Alloy 625 provided the segregation of alloying elements and consequently the formation of a liquid film at the intercellular and solidification grain boundaries. This caused the induction of defects, reducing the mechanical resistance between grains.

Figure 7-11. Morphology of complex carbonitrides and eutetic precipitates observed mainly in interdendritic regions.

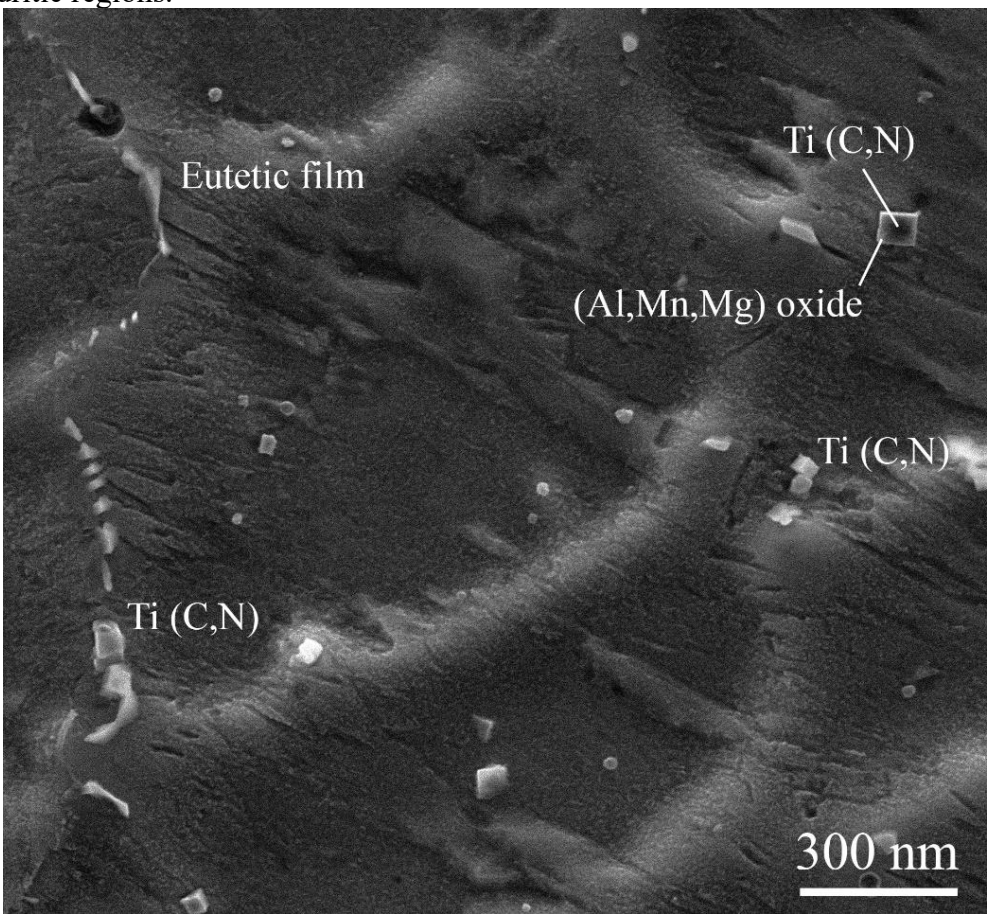

Source: Developed by the author.

Figure 7-12. Solidification cracks seen along the 3rd weld pass of the welded joint. The cracks were concentrated a) on the sides and b) along the centerline of the weld pass.

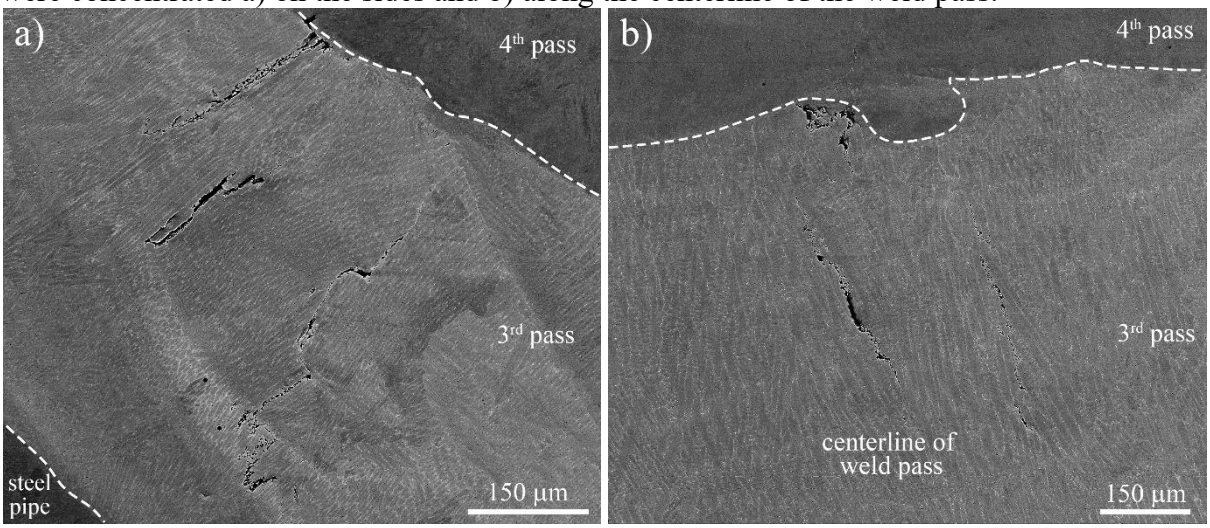

Source: Developed by the author.

Figure 7-13 shows the details of a solidification crack. On evaluating the morphology of the cells carefully, one can see that the solidification crack occurred at the SG

boundary, where the alloying elements are normally segregated and concentrated. Several secondary phases were also observed in the crack. These particles nucleated at the tip of the cells, therefore, after solidification of the γ matrix. Moreover, the chemical composition revealed that secondary phases nucleated due to the microsegregation of Nb and Mo. These elements normally compound the stoichiometry of Laves phase that are known as a eutectic phase with a very low melting point[46]. Others elements such as Ti, Cr and C were concentrated in some particles which are possibly carbides. With respect to back-filling phenomenon, the eutectic fraction was not enough to completely fill the empty volume. Moreover, the high restraint associated with contraction stresses also contributed to prevent the back-filling phenomenon by opening of discontinuities.

Figure 7-13. Details of the solidification cracking mechanism, highlighting solidification grains, secondary phases and chemical compositions.

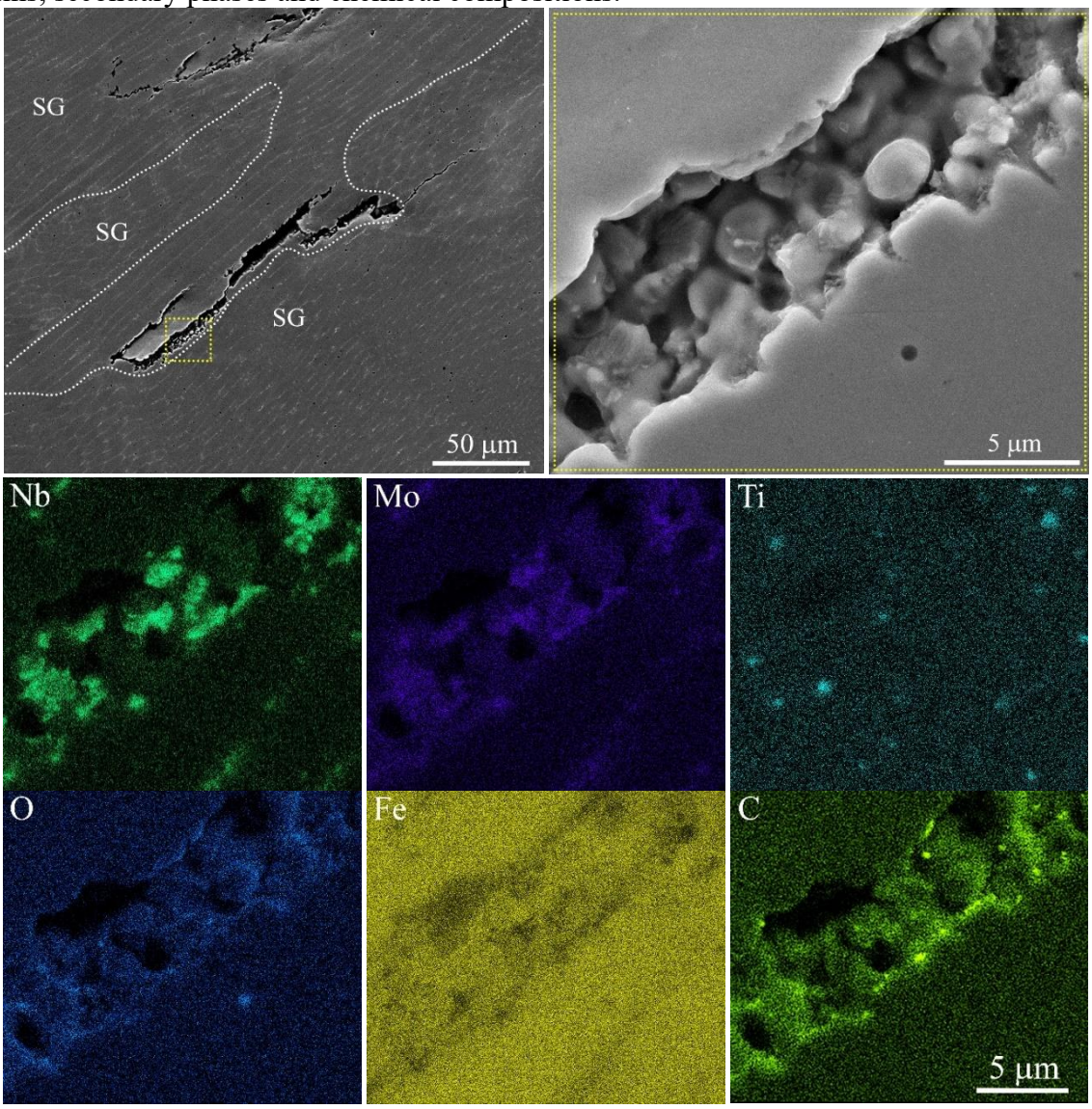

Source: Developed by the author.

The 4th weld pass of the welded joint showed a microstructure typical of martensitic materials. The incorporation of large amounts of Ni, Cr, Mo and Nb increased the hardenability by quenching and solid solution. Figure 7-14 shows the bulk microstructure of the 4th weld pass. The microstructure exhibited a martensitic matrix with several particles of austenite (γ). It is reasonable define the most part of these particles as retained γ-FCC, since the 4th weld pass have 4.3 wt% of Ni and its estimated M_S temperature is 372°C. In some regions, an intense microsegregation of C, Mn and Ni may avoid the martensite transformation, suppressing thus the formation of MA.

Figure 7-14. Bulk microstructure of the 4th weld pass of the welded joint showing a martensitic microstructure with A_{ret} particles.

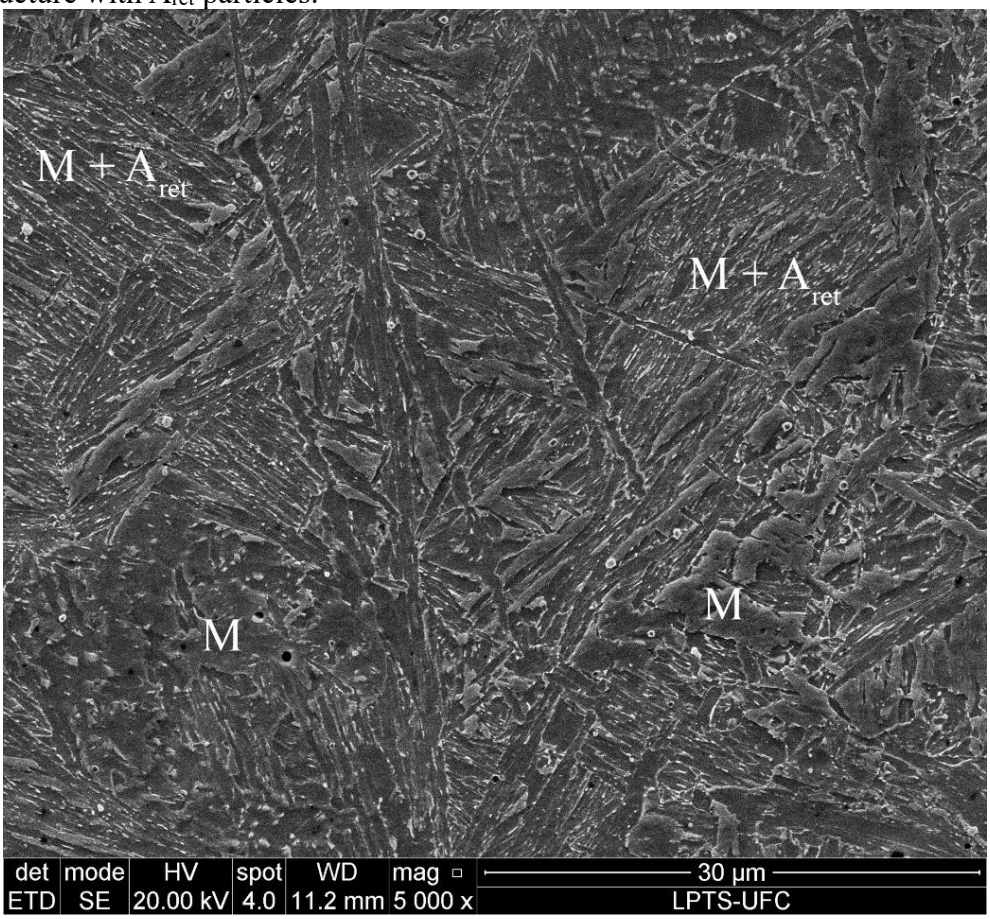

Source: Developed by the author.

The 4th weld pass of the welded joint shows (Figure 7-15) solidification cracks like the 3rd weld pass. Again, the crack was located at the solidification grain boundary. Therefore, this feature must have a relationship with microsegregation, even with low evidences of secondary phases, since only very small particles of secondary phase were observed using the

backscattered electron (BSE) technique. Thus, a thin liquid film at the SG boundaries probably started the nucleation of these cracks.

Figure 7-15. Solidification cracks in the 4th weld pass of the welded joint with highlights of a) primary austenite grain size and the location of cracks.

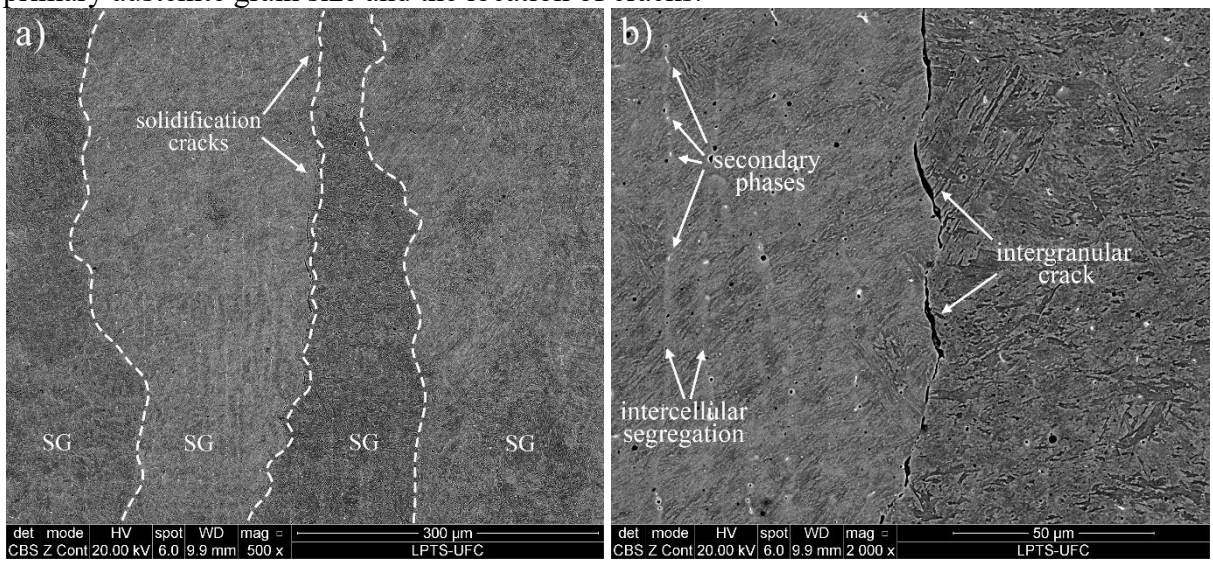

Source: Developed by the author.

The over etching corroded the dendrite highlighting the interdendrite region and the precipitation as well. Figure 7-16 shows a region of cellular growth which was observed an intense microsegregation of Nb and Mo to intercellular region. Certainly, these eutetic phases contributed to formation of solidification cracks observed into the 4th weld pass. Considering the high concentration of Nb and Mo must be Laves phase. A concentration of Ti carbides also were observed finely distributed along 4th weld pass which probably represent carbonitrides as observed in 3rd weld pass.

It is important to highlight that only the 3rd and 4th weld passes of the welded joint showed solidification cracks. In all cases, a Nb fraction present in these weld passes was detected. Even with a very low Nb content in the 4th weld pass of about 0.2%, and large cracks around the solidification grain boundaries were observed. This result suggest that the Alloy 625 is not the best Ni-based alloy for this new approach for this joint welding application. Previous chapters have assessed the dilution effect on thermodynamic simulation for the welding of Alloy 625 with API 5L X65 and AWS 100S-G. These studies highlighted evidences of the incompatibility of these materials for the present application. In terms of thermodynamic concepts, the Fe, Si and C which combined with Nb and Mo present in the Alloy 625, favored the prediction of low melting point phases such as Laves phase and NbC. Moreover, previous tests concerning the deposition of AWS ER100S-G steel on Alloy 625 claddings (Chapter 6)

highlighted the high susceptibility of solidification cracking, due to a large fraction of eutectic phases. The single weld beads showed several large cracks, even with evidence of the backfilling phenomenon, independent of HI_w. The important (and novel) results of the present study about solidification cracking susceptibility in this line of research suggests that a small fraction of Nb, even as lower as 0.2% and 1.0%, is enough to bring about the formation of solidification cracks in the two weld passes.

Figure 7-16. EDS map of 4th weld pass evidencing an intense microsegregation of Nb and Mo to intercellular region and particles richer in Ti.

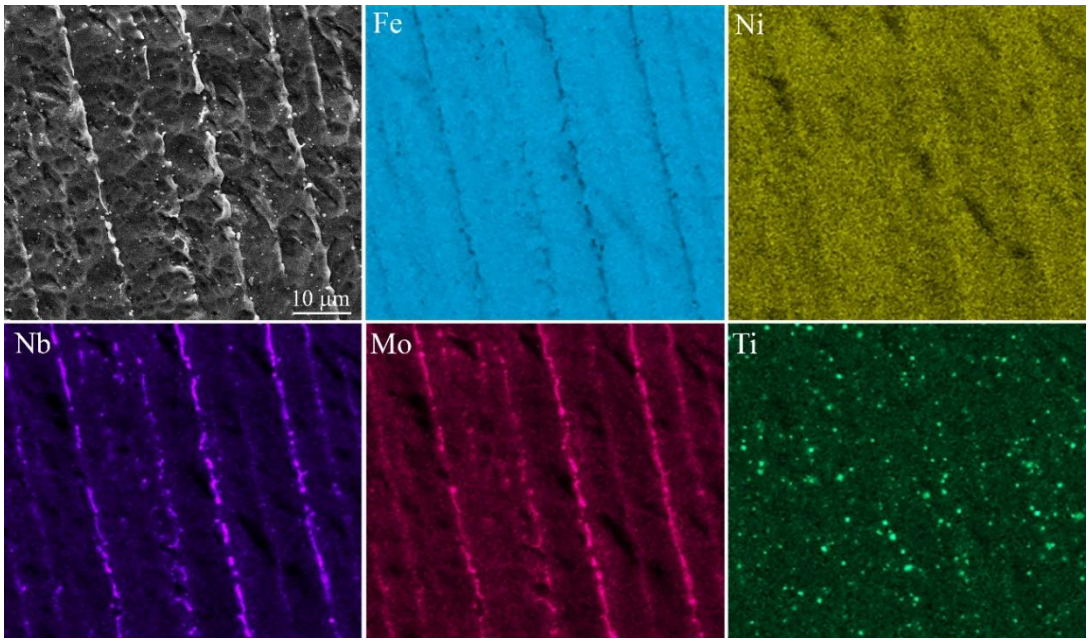

Source: Developed by the author.

The solidification of the 3rd and 4th weld passes were simulated, in order to support the cracking analysis. Figure 7-17 shows the Scheil-Gulliver solidification simulations of both weld passes. As expected, eutectic phases such as Laves, Ni_3Nb and Nb carbides were predicted. These phases expanded the solidification temperature range (ΔT) of the 3rd weld pass considerably, which according to the simulations is about 376°C. According to simulation, it is necessary 163°C to finish the solidification from the Laves reaction at 96% of solid phase nucleated. Even with a considerably lower ΔT of the 4th weld pass (183°C) in comparison with the 3rd weld pass, the Laves phase was also predicted, but in a low amount. This corroborates with the secondary phases fraction observed in the intercellular regions, which was almost negligible (Figure 7-15b). These results corroborated with the intergranular cracks observed in both weld passes. These predicted eutectic phases are usually close to the solidification cracks as reported in the literature[16,29,30,47].

Figure 7-17. Scheil-Gulliver solidification simulation of a) the 3rd and b) the 4th weld passes.

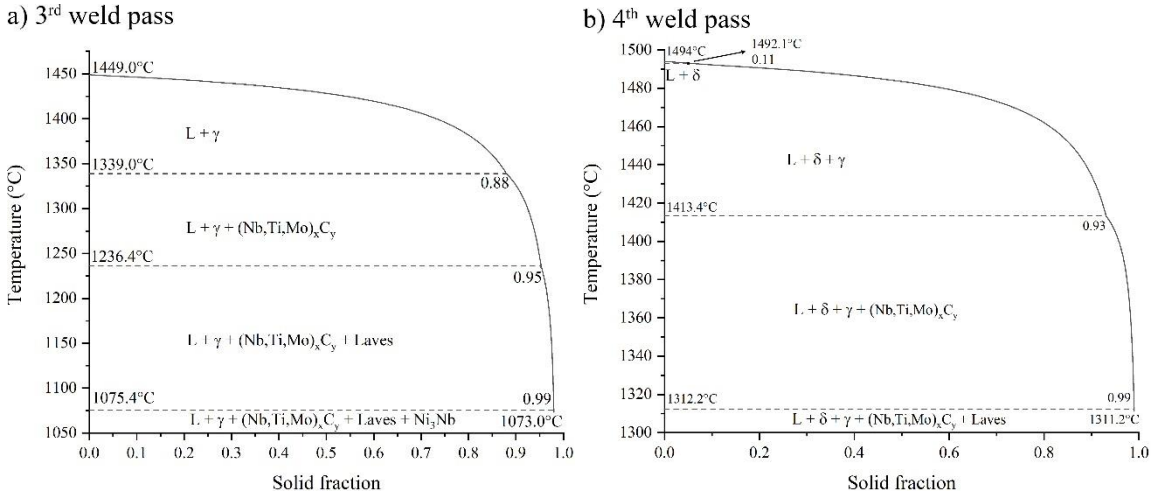

Source: Developed by the author.

The 5th pass of the welded joint did not exhibit any solidification cracks. The bulk microstructure is shown in Figure 7-18. This weld pass showed a microstructure coarser than the 4th weld pass (Figure 7-14). A bainitic matrix with some martensites with larger MA particles with stringer and block morphologies were observed. This time, there less alloying elements responsible to stabilize the austenite, thus, it is more ease obtain an MA microconstituent. According to the literature, martensite transformation occurs during the cooling of the austenitic grain, and rejects some elements such as Ni, Mn and C to the adjacent austenite grains[48]. These elements increase the stability of the austenite field in terms of thermodynamic concepts, thus preventing martensitic transformation and keeping the austenite retained at room temperature. In contrast, some bainite grains were also observed in the microstructure. Probably, the low incorporation of alloying elements from dilution with the previous weld passes reduced the hardenability, which favored the bainite transformation in some grains. Moreover, the HI_w used was a little bit greater than that used for to deposit the 4th weld pass. This difference caused a reduction of cooling rate and must be taken into account.

The microstructures of the 6th weld pass and onwards were quite similar to each other, as they has almost the same chemical composition. Figure 7-19 shows the microstructure of the 10th weld pass. As expected for the 100S-G steel, there was an acicular ferrite (AF) matrix. Moreover, several MA particles were observed as stringers and blocks distributed along the microstructure. No martensite phases were observed, even with the large primary austenite grains. On the other hand, the HI_w used for this weld pass was relatively higher than that used for the 3rd, 4th and 5th weld passes. This welding parameter had a significant contribution to

prevent martensitic transformations. The very low carbon present in the low alloy steel filler metal also must be considered, since the addition of carbon favors martensite transformations.

Figure 7-18. Bulk microstructure of the 5th weld pass of the welded joint showing martensite, stringer MA particles and bainite.

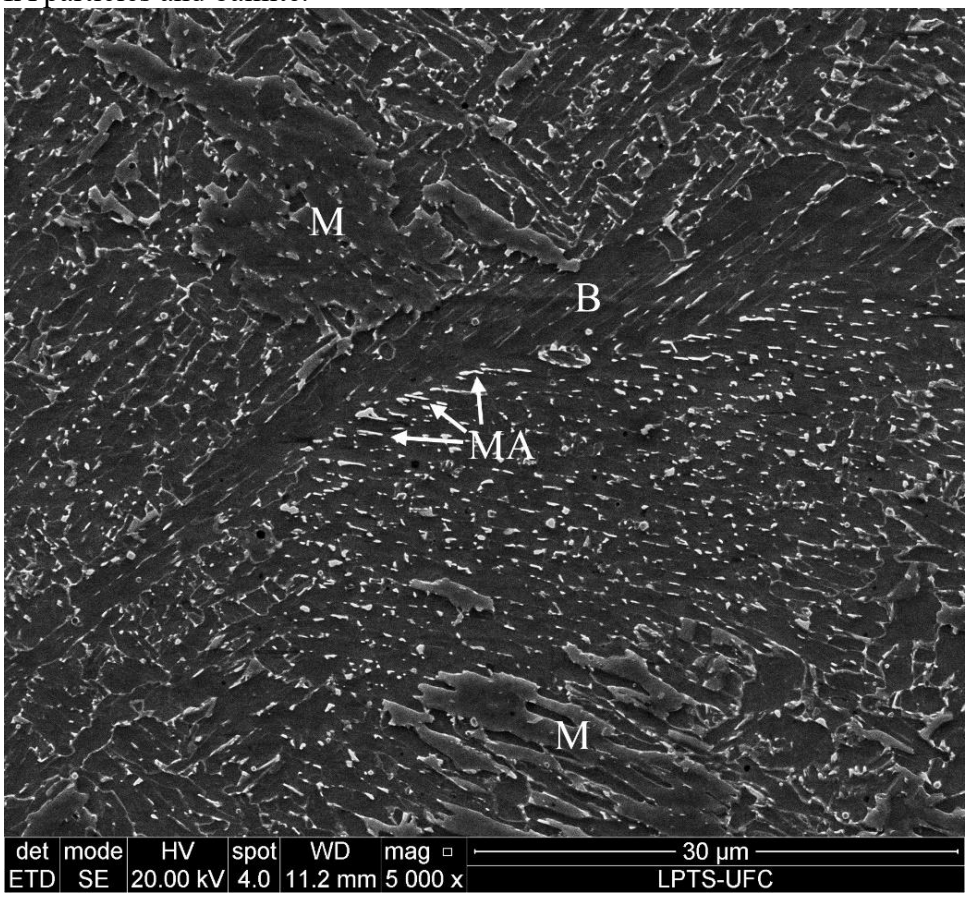

Source: Developed by the author.

Figure 7-19. Bulk microstructure of the 10th weld pass of the welded joint showing an acicular ferrite matrix with several MA particles.

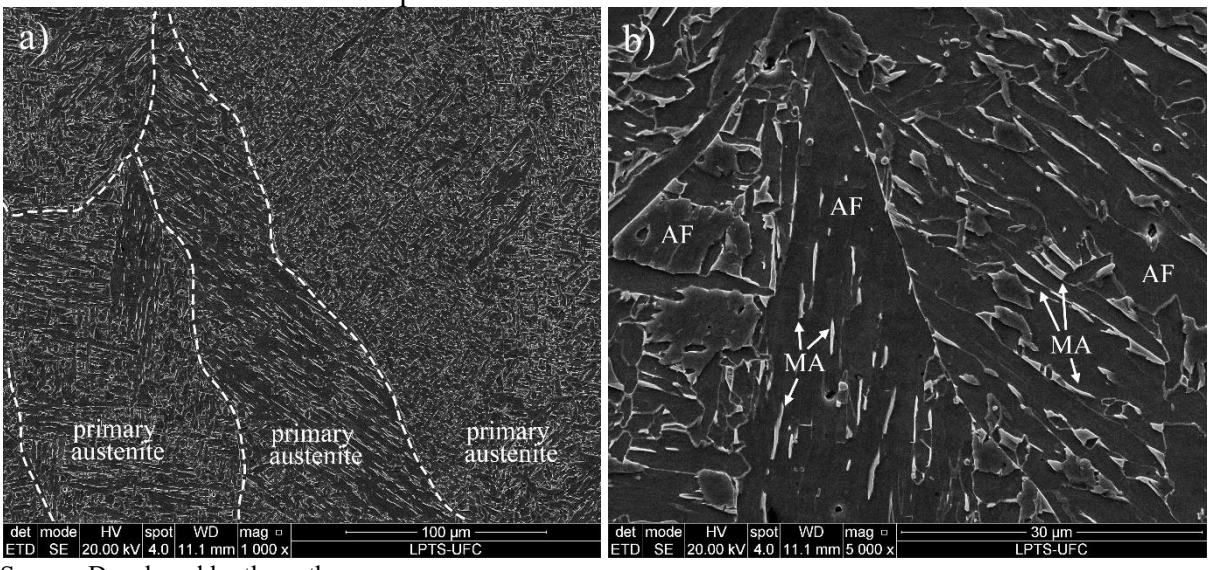

Source: Developed by the author.

7.4.3 Mechanical evaluation

7.4.3.1 Tensile testing

Transverse tensile tests were carried out on the welded joint in order to verify the strength of the weld and where a rupture could occur. Figure 7-20 shows the samples after testing and the average tensile strength was 737.7 MPa. This result is significantly superior to the minimum required for API 5L X65 steel, which is 535 MPa[32]. The samples exhibited a rupture at the base metal, far from the heat affected zone. On this point the welded joint was approved, considering that tensile strength of the welded joint was probably at least equal to the base metal[27], since the rupture happened on API 5L X65 steel pipe, even with several solidification cracks along the 3rd and 4th weld passes. Figure 7-21 shows the details of a sample after test using SEM images in the BSE detection mode.

Figure 7-20. Transverse tensile test samples after the tests. The fracture occurred at the base metal in all samples.

Source: Developed by the author.

Figure 7-21. BSE map of the transverse tensile test sample after the test. Several solidification cracks were observed at the 3rd and the 4th passes of the welded joint.

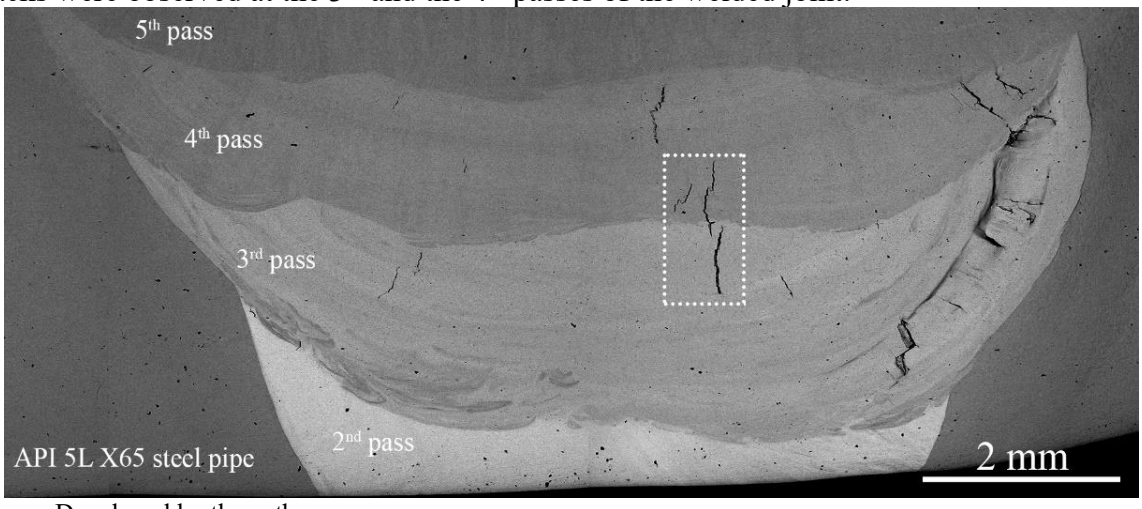

Source: Developed by the author.

In general, the solidification cracks did not demonstrate whether there was much growth during the tensile test. The cracks remained in their weld passes of origin. Only one centerline crack showed a growth towards the 3rd weld pass, advancing about 200 μm. These results highlight that yield strength of the welded joint was higher than the base metal. In this case a greater stress level is needed to cause the cracks to grow and cause the welded joint to rupture. A different base metal with a higher yield strength would be necessary to concentrate the stress on the welded joint.

Unfortunately, the presence of solidification cracks along the welded joint is an unacceptable condition for practical applications of this technique in the field. However, from the viewpoint of strength, it is clear that this result indicates the potential of this new approach for joint welding of high strength steel pipes with two different materials: one corrosion resistant alloy for welding the cladding region and, a second to fill the main portion of the groove to provide excellent mechanical properties. Therefore, low alloy steels can offer materials with different mechanical properties to be used in the joint welding of numerous components. This, therefore, opens up the perspective of welding high strength steel pipes such as API 5L X70, X80 and X90 steels. However, further investigations concerning the welding parameters and other minor adjustments must be carried out to avoid the formation of cracks and enhance the performance of the welded joint.

7.4.3.2 Bend testing

The bending test was was carried out on four samples taking into account the welded joint and the CRA cladding. All samples tested are shown in Figure 7-22. An otherwise behavior was observed for the bending test, in which only one sample did not exhibit a total rupture. This result evidenced the strong effect of cracks in components when they are subjected to bending stresses. The bending test causes a high stress on the surface of the sample that concentrates at the tip of cracks, causing crack growth. As the crack progresses, its size exceeded the maximum crack size admitted by the brittle martensite weld passes, causing an unstable crack propagation that leads to the total rupture of the sample.

Figure 7-22. Bending specimens after the test. Only one sample did not break.

Source: Developed by the author.

7.4.3.3 Microhardness and hardness tests

The microhardness mapping assessed the 2nd, 3rd, 4th, 5th, 6th weld passes of the welded joint, including the API 5L X65 steel pipe and Alloy 625 cladding. The distance between indentations was 300 μm, which provided a good spatial resolution. Figure 7-23 shows the microhardness map of the welded joint. The scale bar was defined from 250 HV to 400 HV.

Most of the base metal showed a microhardness below 250 HV. This result was expected as API 5L X65 steel has low alloying elements and low carbon content and its microstructure presented in Figure 7-5 consists of proeutectoid ferrite (α-BCC) with some fine perlites dispersed in the matrix. The good mechanical resistance of such materials is related to the thermomechanical processes that provide a grain refinement. In contrast, the Alloy 625 cladding and the 2nd weld pass showed a greater microhardness, about 330 HV. The large fraction of alloying elements present in Alloy 625 caused a hardening by solid solution, even in a γ-FCC matrix.

The 3rd and 4th weld passes showed the highest microhardness of the welded joint. A large portion of the 3rd weld pass exhibited a microhardness below 250 HV, while a few regions displayed results over 400 HV. This very low microhardness was due to the high incorporation of Ni from dilution with the 2nd Alloy 625 weld pass, while hard regions was related to macrosegregations rich in LAS filler metal. As showed previously, the 3rd weld pass exhibited an intense formation of macrosegregation regions due several factors such as

differences about melting point of alloys, fast cooling rate and turbulence created by arc welding pressure and waving of heating source as well. The regions rich in base metal (Alloy 625 weld pass) have a bigger concentration of Ni which according to literature cause the softening of steels, even in subzero temperatures[43,49]. On the other hand, the dilution with Alloy 625 also increase solid solution strengthening elements like Cr and Mo, which may cause the, hardening of martensite matrix reducing its toughness as well. The Ni content above to 15 wt% seems to overlapped the negative hardening effect of Cr and Mo for this weld pass.

Figure 7-23. Microhardness map of the welded joint, evaluating the 2nd, 3rd, 4th, 5th, 6th passes and the API 5L X65 steel pipe.

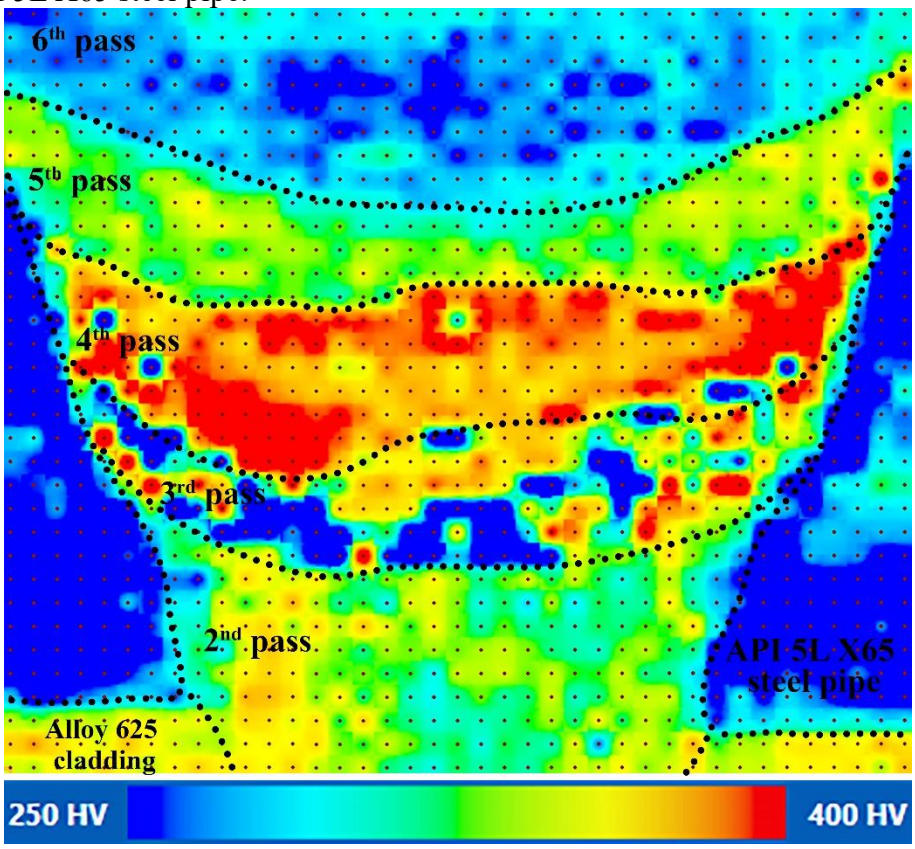

Source: Developed by the author.

In contrast, the 4th weld pass showed hard feature, above 400 HV in nearly the full length of the weld pass. The massive drop in Ni content reduced considerably its softening effect in martensite matrix. The solid solution strengthening of Cr and Mo was more relevant than positive effect of 4.3 wt% of Ni present in this weld pass. Moreover, the increase of carbon from dilution with steel pip wich have 0.11 wt% of C may caused the hardening of martensite matrix and A_{ret}. According to literature, the carbon have important role in mechanical properties of martensite. Normally, martensite with very low carbon content exhibits a lower strength and better toughness in comparison with high carbon martensite[50].

The 5th weld pass also exhibited the same tendency of hardening, but a reduction of alloying elements and a decrease in the cooling rate caused a slight softening that corroborates with the microstructure based on bainite matrix. The reduction of Ni, Cr and Mo present in martensite and MA particles caused the reduction of hardness in comparison with 4th weld pass. This tendency continued for 6th weld pass, in which showed in some regions a hardness quiet similar to obtained for steel pipe.

A hardness profile was also made along the weld centerline for all weld passes. A load of 10 kgf and spacing of 1 mm between indentations were employed. Figure 7-24 shows the results of the hardness profile. The first two weld passes exhibited a hardness with an average of approximately 265 HV. The 3rd weld pass showed the same tendency observed in the microhardness map, which had a hardness of around 300 HV. The increase of hardness occurred due to the addition of the alloying elements that caused hardening by quenching and solid solution. The 4th weld pass showed the same tendency, exhibiting a hardness varying from 348 HV to 391 HV. Probably, the lower Ni content caused the reduction of γ-FCC stabilization field in terms of thermodynamic concepts and, consequently, favored the martensitic transformation during the cooling of the weld pass. The 5th weld pass showed a reduction of hardness in comparison to the previous weld passes, varying from 264 HV to 317 HV. From the 6th weld pass onwards, the hardness of the welded joint reduced to an average of 244 HV.

Figure 7-24. Hardness profile of the welded joint covering all weld passes, starting from the root weld pass.

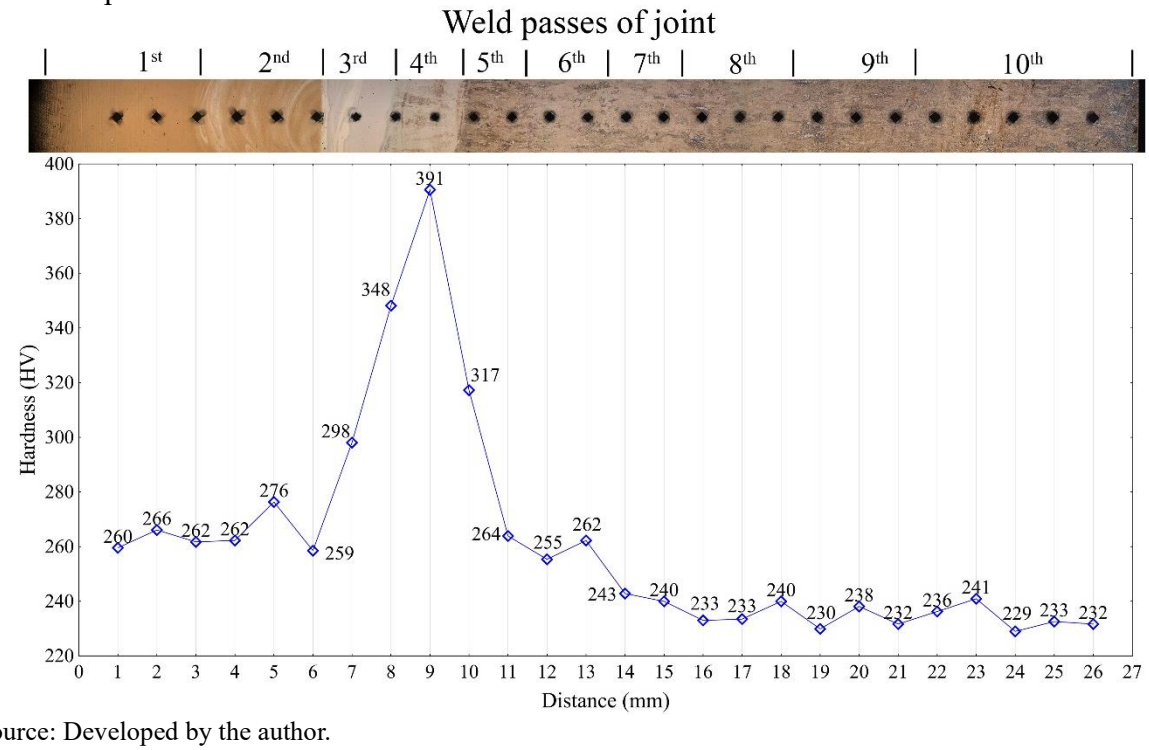

Source: Developed by the author.

7.4.3.4 Impact toughness

The impact toughness of the 3rd weld pass of the welded joint was evaluated in order to check the effect of dilution of the 3rd weld pass deposited with the 100S-G steel on the 2nd weld pass of Alloy 625. Obviously, the solidification cracks were taken into account. Figure 7-25 shows the fractography of a sample evaluated with details. Note: the Charpy-V samples have a square profile of 10 X 10 mm. The results obtained represent the impact toughness of some weld passes, from the 3rd to 6th weld passes.

The fractography obtained was composed of different regions due to the significant differences among the weld passes, considering their chemical compositions and microstructures. The 3rd weld pass showed a ductile fracture, whose feature is based in shallow dimples but without any evidence of fracture by cleavage. Probably, this result was due to the high fraction of Ni incorporated by dilution with the Alloy 625 weld pass. In contrast, the 4th, 5th and 6th weld passes of the welded joint exhibited a brittle fracture surface, and the predominant fracture was by cleavage. Several solidification cracks were observed, especially in the 3rd weld pass.

Figure 7-25. Fractography of a Charpy-V sample of notch in the 3rd weld pass of the welded joint highlighting a) an overview of the sample and b) fracture feature of the 3rd and the 4th weld passes.

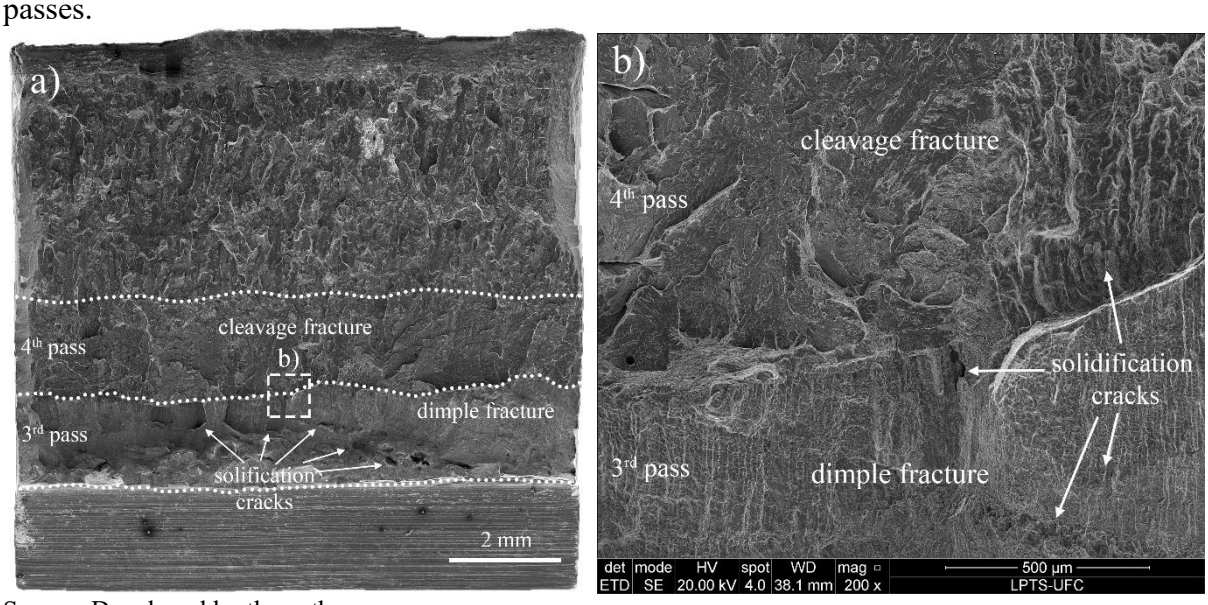

Source: Developed by the author.

Figure 7-26a shows one large solidification crack observed on the 3rd weld pass. In the case of a large solidification crack such as presented, one can see large γ-FCC dendrites (Figure 7-26b) that solidified in a large empty volume. This reinforces the susceptibility of

solidification cracks occurring with the deposition of low alloy steel on Alloy 625 weld metal. Moreover, secondary phases were also observed in the solidification cracks (Figure 7-26c), which evidence the strong effect of microsegregation in the formation of these cracks.

The welded joint did not demonstrate good toughness, in terms of absorbed energy in the Charpy-V impact test. The result on average was 11.3 J ± 1.1 J. The presence of several solidification cracks along the first two low alloy steel weld passes caused a drop in the absorbed energy. Nonetheless, the brittle features of the 4th, 5th and 6th weld passes of the welded joint should be pointed out. Probably, these weld passes contributed to this poor impact toughness.

Figure 7-26. Microstructure of a) a large solidification crack located at the 3rd weld pass of the welded joint, highlighting b) large dendrites and c) a secondary phase nucleated at the crack.

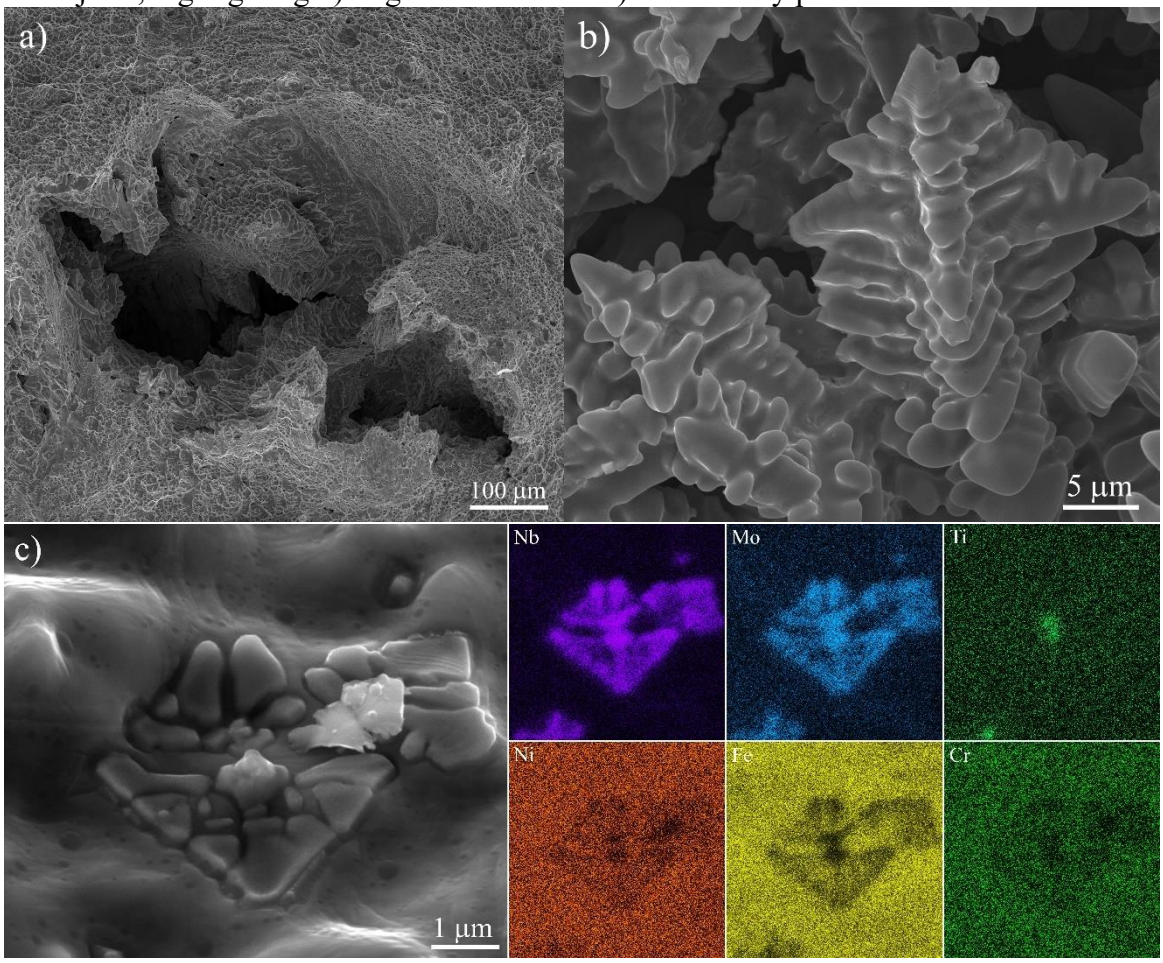

Source: Developed by the author.

7.5 Conclusion

Based on the experimental results in the present study that assessed a new approach to weld API 5L X65 steel pipe with an internal cladding of Alloy 625, using two different filler metals in the same joint to provide an overmatch of tensile strength, it was concluded that:

The new approach for joint welding of rigid riser with internal cladding of Alloy 625 using the two filler metals, Alloy 625 and 100S-G steel, reached the desired result from a tensile strength viewpoint.

- The low weldability evidenced by the presence of solidification cracks, observed on the dissimilar weld passes with a high mixture of the Alloy 625 and 100S-G steel, impaired the ductility and toughness of the welded joint.
- The incorporation of Nb and Mo into the 100S-G steel weld pass caused the nucleation of the low melting point phases that started the formation of solidification cracks.
- The dilution of the 100S-G steel weld pass with the Alloy 625 weld pass caused the incorporation of Ni, Cr, Mo and Nb, which increase the hardenability by quenching and solid solution.
- The welded joint exhibited a complex microstructure. The 1st and 2nd Alloy 625 weld passes showed a γ-FCC with some secondary phases distributed. The first LAS weld pass diluted with Alloy 625 created a martensite matrix with eutetic phase at interdendritic region and carbonitrides rich in Ti and Nb. The high Ni present in this weld pass cause a softening of martensite which provided a better toughness in comparison with two subsequent LAS weld passes. The second and third LAS weld passes exhibited a hard martensite matrix with MA microconstituents, eutetic phases which possibly is Laves phase and carbonitrides rich in Ti. Both weld passes showed a brittle fracture. The other weld passes exhibited a soft acicular ferrite matrix with MA particles.
- The toughness of the welded joint in region of mixture between 100S-G steel and Alloy 625 exhibited a very low absorbed energy due presence of solidification cracks in first two LAS weld passes.

REFERENCES

1 FARIAS, F. W. C. *et al*. Microstructural characterization of Ni-based superalloy 625 clad welded on a 9% Ni steel pipe by plasma powder transferred arc. **Surface and Coatings Technology**, v. 374, p. 1024-1037, 2019.

2 SHAMANIAN, M. *et al*. Microstructure and mechanical properties of Inconel 617/AISI 310 electron beam welds. **Metallurgical and Materials Transactions A**, v. 50, n. 7, p. 3164-3173, 2019.

3 KANGAZIAN, J.; SHAMANIAN, M.; ASHRAFI, A. Dissimilar welding between SAF 2507 stainless steel and Incoloy 825 Ni-based alloy: the role of microstructure on corrosion behavior of the weld metals. **Journal of Manufacturing Processes**, v. 29, p. 376-388, 2017.

4 SILVA, C. C. *et al*. Austenitic and ferritic stainless steel dissimilar weld metal evaluation for the applications as-coating in the petroleum processing equipment. **Materials & Design**, v. 47, p. 1-8, 2013.

5 SUN, Z.; ION, J. C. Laser welding of dissimilar metal combinations. **Journal of Materials Science**, v. 30, n. 17, p. 4205-4214, 1995.

6 BALDRIDGE, T. *et al*. Laser cladding of Inconel 690 on Inconel 600 superalloy for corrosion protection in nuclear applications. **Optics and Lasers in Engineering**, v. 51, n. 2, p. 180-184, 2013.

7 SILVA, C. C. *et al*. A study on the effect of the interpass temperatures in properties and microstructures of the Alloy 625 dissimilar fusion zone. **Materials Science Forum**, v. 783-786, p. 2816-2821, 2014.

8 SARAIVA, D. L. *et al*. Application of low Ms temperature consumable to dissimilar welded joint. **Materials Science and Technology**, v. 30, n. 9, p. 1057–1062, jul. 2014.

9 KOURDANI, A.; DERAKHSHANDEH-HAGHIGHI, R. Evaluating the properties of dissimilar metal welding between Inconel 625 and 316L stainless steel by applying different welding methods and consumables. **Metallurgical and Materials Transactions A**, v. 49, n. 4, p. 1231-1243, 2018.

10 SAEDI, A. H.; HAJJARI, E.; SADROSSADAT, S. M. Microstructural characterization and mechanical properties of TIG-welded API 5L X60 HSLA steel and AISI 310S stainless steel dissimilar joints. **Metallurgical and Materials Transactions A**, v. 49, n. 11, p. 5497-5508, 2018.

11 DUPONT, J. N.; BABU, S.; LIU, S. Welding of materials for energy applications. **Metallurgical and Materials Transactions A**, v. 44, n. 7, p. 3385-3410, 2013.

12 SILVA, C. C. *et al*. Evaluation of the corrosion resistant weld cladding deposited by the TIG cold wire feed process. **Materials Science Forum**, v. 783-786, p. 2822-2827, 2014.

13 MOHAMMADI ZAHRANI, E.; ALFANTAZI, A. M. Hot corrosion of Inconel 625 overlay weld cladding in smelting off-gas environment. **Metallurgical and Materials Transactions A**, v. 44, n. 10, p. 4671-4699, 2013.

14 MINÁ, É. M. *et al*. The effect of dilution on microsegregation in AWS ER NiCrMo-14 alloy welding claddings. **Metallurgical and Materials Transactions A: Physical Metallurgy and Materials Science**, v. 47, n. 12, 2016.

15 SILVA, C. C. *et al*. New insight on the solidification path of an alloy 625 weld overlay. **Journal of Materials Research and Technology**, v. 2, n. 3, p. 228-237, 2013.

16 DUPONT, J. N. Solidification of an alloy 625 weld overlay. **Metallurgical and Materials Transactions A**, v. 27, n. 11, p. 3612-3620, nov. 1996.

17 DAI, T.; LIPPOLD, J. Characterization of the interface of an Alloy 625 overlay on steels using nanoindentation. **Journal of Materials Engineering and Performance**, v. 27, n. 7, p. 3411-3418, 2018.

18 SARZOSA, D. F. B. *et al*. Fracture resistance testing of dissimilar nickel-chromium girth welds for clad line pipes. **International Journal of Fracture**, v. 205, n. 2, p. 169-188, 2017.

19 CHONG, T.-V. S. *et al*. Effects of elevated temperatures on the mechanical properties of nickel-based alloy clad pipelines girth welds. **Engineering Fracture Mechanics**, v. 152, p. 174-192, 2016.

20 JONES, R. L. *et al*. Reeled clad SCR weld fatigue qualification. *In*: OFFSHORE TECHNOLOGY CONFERENCE, 2011, Houston. **Proceedings**. Houston: Offshore Technology Conference, 2011. p 1-13.

21 SOUZA, R. F.; RUGGIERI, C. Fracture assessments of clad pipe girth welds incorporating improved crack driving force solutions. **Engineering Fracture Mechanics**, v. 148, p. 383-405, 2015.

22 SMITH, S. N.; CLOUGH, T. Deepwater Pipeline Installation by Reel-lay Method. *In*: OFFSHORE TECHNOLOGY CONFERENCE, 2010, Houston. **Proceedings**. Houston: Offshore Technology Conference, 2010. p 1-12.

23 BAI, Qiang; BAI, Yong. Installation Design. *In*: **Subsea Pipeline Design, Analysis, and Installation**. Boston: Gulf Professional Publishing, 2014. p. 707-751.

24 WANG, Y. *et al*. Advances in deepwater structure installation technologies. **Underwater Technology**, v. 34, n. 2, p. 83-91, 2017.

25 LIN, S. *et al*. Effect of cyclic plastic deformation on microstructure and mechanical properties of weld metals used for reel-lay pipeline steels. **Materials Science and Engineering: A**, v. 737, p. 77-84, 2018.

26 CROSS, C. E. On the origin of weld solidification cracking. *In*: BÖLLINGHAUS, T.; HEROLD, H. **Hot Cracking Phenomena in Welds**. Heidelberg: Springer Berlin Heidelberg, 2005. p. 3-18.

27 DNVGL. DNVGL ST F101: **Submarine Pipeline Systems**. Oslo. p. 520. 2017.

28 DNV. JIP: **Lined and Clad Pipeline Materials: Guidelines for Design and Construction of Clad and Lined Pipelines**. Oslo. 2007.

29 CIESLAK, M. J.; HEADLEY, T. J.; FRANK, R. B. Welding metallurgy of custom age 625 PLUS alloy. **Welding Journal (Miami, Fla)**, v. 68, n. 12, p. 473s-482s, 1989.

30 CIESLAK, M. J. The Welding and Solidification Metallurgy of Alloy 625. **Welding Journal**, v. 70, n. 2, p. 49-56, 1991.

31 AMERICAN WELDING SOCIETY. AWS A5.28/A5.28M: **Specification for Low-Alloy Steel Electrodes and Rods for Gas Shielded Arc Welding**. Miami. p. 40. 2015.

32 AMERICAN PETROLEUM INSTITUTE. API specification 5L: **Specification for Line Pipe**. Washington. p. 180. 2013.

33 LIPPOLD, J. C. Centerline cracking in deep penetration electron beam welds in type 304L stainless steel. **Welding Journal (Miami, Fla)**, v. 64, n. 5, p. 127s-136s, 1985.

34 SILVA, C. C. *et al*. Assessment of microstructure of alloy Inconel 686 dissimilar weld claddings. **Journal of Alloys and Compounds**, v. 684, p. 628-642, 2016.

35 CIESLAK, M. J.; HEADLEY, T. J.; ROMIG, A. D. The welding metallurgy of HASTELLOY alloys C-4, C-22, and C-276. **Metallurgical Transactions A**, v. 17, n. 11, p. 2035-2047, nov. 1986.

36 PERRICONE, M. J.; DUPONT, J. N. Effect of composition on the solidification behavior of several Ni-Cr-Mo and Fe-Ni-Cr-Mo alloys. **Metallurgical and Materials Transactions A**, v. 37, n. 4, p. 1267-1280, 2006.

37 SUN, Y. *et al*. Characterization and formation mechanism of periodic solidification defects in deep-penetration laser welding of NiCrMoV steel with heavy section. **The International Journal of Advanced Manufacturing Technology**, v. 100, n. 9, p. 2857-2866, 2019.

38 DAVID, S. A.; VITEK, J. M. Correlation between solidification parameters and weld microstructures. **International Materials Reviews**, v. 34, n. 1, p. 213-245, jan. 1989.

39 BROOKS, J. A. AND LAMBERT, F. J. J. The Effects of Phosphorus, Sulfur and Ferrite Content on Weld Cracking of Type 309 Stainless Steel. **Welding Research Supplement**, p. 139-s-143 s, 1978.

40 LIU, J.; KOU, S. Crack susceptibility of binary aluminum alloys during solidification. **Acta Materialia**, v. 110, p. 84-94, 2016.

41KANG, B. Y.; KIM, H. J.; HWANG, S. K. Effect of Mn and Ni on the variation of the microstructure and mechanical properties of low-carbon weld metals. **ISIJ International**, v. 40, n. 12, p. 1237-1245, 2000.

42 WANG, P.; KUMAR, K. S. Dynamic deformation response of a high-strength, high-toughness Fe-10Ni-0.1C steel. **Materials Science and Engineering: A**, v. 519, n. 1, p. 184-197, 2009.

43 ANDREWS, K. W. The calculation of transformation temperatures and austenite-ferrite equilibria. in steels. **Journal of the Iron and Steel Institute**, v. 184, p. 414-427, 1956.

44 KAUFMAN, L.; COHEN, M. The martensitic transformation in the iron-nickel system. **JOM**, v. 8, n. 10, p. 1393-1401, 1956.

45 YANG, H.-S.; BHADESHIA, H. K. D. H. Austenite grain size and the martensite-start temperature. **Scripta Materialia**, v. 60, n. 7, p. 493-495, 2009.

46 STEIN, F.; PALM, M.; SAUTHOFF, G. Structure and stability of Laves phases. Part I. critical assessment of factors controlling Laves phase stability. **Intermetallics**, v. 12, n. 7, p. 713-720, 2004.

47 CIESLAK, M. J. *et al*. A melting and solidification study of alloy 625. **Metallurgical Transactions A**, v. 19, n. 9, p. 2319-2331, 1988.

48 BISS, V.; CRYDERMAN, R. L. Martensite and retained austenite in hot-rolled, low-carbon bainitic steels. **Metallurgical and Materials Transactions B**, v. 2, n. 8, p. 2267-2276,

1971.

49 TANAKA, M. *et al*. Effects of Ni and Mn on brittle-to-ductile transition in ultralow-carbon steels. **Materials Science and Engineering: A**, v. 682, p. 370-375, 2017.

50 MORSDORF, L. *et al*. Multiple mechanisms of lath martensite plasticity. **Acta Materialia**, v. 121, p. 202-214, 2016.

Chapter 8

Novel proposal for dissimilar girth welding of API 5L X65 steel pipe with an internal Alloy 625 cladding using low alloy steel and Alloy 22 combined as the filler metals

8.1 Abstract

The present study manufactured and evaluated a novel proposal for dissimilar girth welding of API 5L X65 steel pipe internally cladded with Alloy 625 using Alloy 22 and AWS ER100S-G steel. The 1st and 2nd weld passes were deposited with Alloy 22 to provide strong corrosion resistance in the region of the Alloy 625 cladding. The other weld passes were deposited using 100S-G steel to provide high mechanical strength. The microstructure and mechanical properties of the welded joints were evaluated. The welded joints did not exhibit any serious solidification defects, and they passed all bending and transverse tensile tests under taken. The yield strength of the welded joints exhibited the overmatch necessary to perform joint welding of API 5L X65, X70 and X80 steels for posterior installation by the reel-lay process. The combination of two filler metals produced a complex microstructure, even thus, it was not observed solidification cracks along of weld passes of the welded joint. The first two weld passes, composed of Alloy 22, showed soft austenite matrix, while the first 100S-G steel weld passes showed a ductile martensite matrix rich in Ni, almost 12 wt%, with retained austenite (A_{ret}) and carbides. The second 100S-G steel weld pass exhibited a brittle martensite matrix with A_{ret} and carbides. The third 100S-G steel showed a banitic matrix with martensite, martensite-austenite (MA) and carbides. The largest regions of the welded joints showed a soft acicular ferritic (AF) matrix with MA particles. The impact toughness obtained for dissimilar region result of mixture of the 100S-G steel with previous Alloy 22 weld pass was 46 J, at -15°C, enough to attend the application requirement. In contrast, largest portion of the welded joint composed by AF absorbed only 14 J during impact test, typical of steels assessed in conditions below the ductile-to-brittle transition temperature (DBTT). The crack tip opening displacement (CTOD) specimens also experienced a brittle fracture, evidenced by abrupt failure during test, at -15°C.

8.2 Introduction

Crude oil and natural gas is transported by high strength steel pipes which are suitable for onshore and offshore applications[1]. In Brazil, the demand for energy resources and the discovery of large hydrocarbon reservoirs increased the investments in offshore exploration and production of oil and natural gas in ultra-deep water[2]. Subsea lines are needed to bring the hydrocarbons from the wellhead on the seabed to the oil platform. Due to their importance, the American Petroleum Society has specified the properties for these products in the API 5L standard[3]. Pipeline systems that extend for various kilometers require hundreds of pipes to be connected by welding. Various studies have been conducted to enhance the performance of these steels[4–7]. There are a lot of studies that are dedicated to evaluate the heat affected zone[8–10]. However, due to the characteristics of crude oil (petroleum and gas), its contaminants, and the subsea environment, the use of materials with high corrosion resistance becomes necessary.

Therefore, the oil & gas industry have great interest in dissimilar welding, especially for risers based on steel pipes internally cladded with a corrosion resistance alloy (CRA)[11–14], as well as having a good cost-benefit[13]. The Ni-based alloy 625 is commonly used as CRA cladding of such steel pipes due to its good oxidation and corrosion resistance[15–17]. Beltrão *et al*.[18] highlights that one option for pre-salt reservoir production is the use of rigid risers with an inner cladding of Inconel 625. Welding of dissimilar materials represents an important manufacturing technique, allows a combination of the best properties of each material selected in order to create complex compounds for specialized equipment[19–25]. The welding procedures to manufacture welding overlays have improved as demonstrated in recent studies[14,16,26]. However, the girth welding of such CRA cladded steel pipes still represents an engineering challenge.

The girth welding of steel pipes without internal CRA cladding is well established by offshore industries. Normally, low alloy steels (LAS) are used as the filler metal to manufacture the joint of the high strength low alloy (HSLA) steel pipes such as API 5L X65, X70 and X80[27]. Nonetheless, when the steel pipe is internally cladded with a Ni-based alloy, the filler metal selected to perform the girth welding must consider the metallurgical compatibility between the materials involved. Generally, the same Ni-based alloy of the cladding is used as the filling material to avoid metallurgical problems with a mixture of dissimilar materials[28–30]. Nevertheless, the mechanical properties of the Ni-based alloy used in both the cladding and the welding are the limiting factors for the mechanical properties of the girth weld.

Furthermore, the procedure used to install risers, in terms of mechanical properties, must be considered. Currently, the reel-lay process represents the most attractive process in comparison to the traditional methods such as S-lay and J-lay. In the reel-lay procedure the joint welding of pipe is performed onshore near the dock, increasing the quality of the welds, providing a gain of productivity and making the inspection of the weldments easy. Next, the pipeline is spooled onto a large diameter drum on a pipelaying vessel for transportation to an offshore unit, where it will be unspooled on installation. However, the bending and unbending steps cause about 2% plastic deformation on the pipe and on the weldment region[31]. Furthermore, the welding processes may introduce defects such as porosity, shrink porosity, solidification cracks and reheat cracks which must be taken into account[32]. Therefore, the use of the reel-lay process demands a high quality weldment with excellent mechanical properties, especially considering the plastic deformation introduced due to the installation process.

There are general recommendations for the overmatch of mechanical properties when installing pipelines by the reel-lay process. The recommendations are that girth welds exhibit a yield strength (YS) greater than the minimum standard yield strength of the base metal by at least 100 MPa[33]. According to the DNVGL-ST-F101 standard, a minimum YS for girth welding is defined as at least equal to the maximum YS of the base metal minus 20 MPa[34]. Thus, to perform the weld joint of API 5L X65 steel pipe, internally cladded by Alloy 625, to be installed by the reel-lay process a yield strength of at least 580 MPa is necessary. Jones *et al*.[28] made a study on welded joints of such cladded steel pipes using Alloy 625 as the filler metal. According to the authors, the Alloy 625 in the as-welded condition does not offer the minimal yield strength required, but during the reel-lay process the work hardening of Alloy 625 provided an overmatch[28]. According to the authors the DNV 'Guideline for design and construction of clad and lined pipe' classifies such girth welding as 'partially overmatch'[28]. Clearly, this procedure is not the best solution for welding rigid risers, especially for the welding of high strength steel pipes like API 5L X70 and X80 steels.

Probably the most intuitive dissimilar welding procedure to solve this challenge is to perform a root pass using the same Ni-based alloy used in the cladded pipes as the filler metal and then fill the weld groove using a LAS, compatible with the steel pipe. Possibly, this represents the best cost-benefit. Nonetheless, the dissimilar welding of steels and Ni-based alloys may lead to the formation of metallurgical defects. According to the literature, the dilution with steel causes the incorporation of Fe, Si and C that combined with Nb, Mo and Ti present in Alloy 625 may cause the nucleation of eutectic phases at the final stage of solidification[15,16,35–37]. The eutectic phases are frequently related to solidification cracking due

to their low melting points that widen the solidification range of alloys, and thus reduce the resistance of grain boundaries at the end of solidification[32]. These deleterious phases can be avoided by welding procedures that include an objective selection of materials.

There are Ni-based alloys from the same class as Alloy 625 with similar properties that may figure as an alternative to solve the challenge. Alloy 22 represents a good option to substitute Alloy 625 for the root pass. According to studies presented in previously chapters, Alloy 22 has demonstrated good metallurgical compatibility with LAS. Designed as a new insight of Alloy C-276 and Alloy C4, Alloy 22 combines the best features of them both[38]. The increase of Cr gives good resistance to oxidizing environments, while W improves the resistance to oxidizing chloride solutions[38]. Mo is reduced in comparison to Alloy C-276 which minimizes the sensitization caused by nucleation of intermetallic phases, especially the μ phase $(Ni, Fe, Co)_7 (W, Mo, Cr)_6$[39], which improves the corrosion resistance. Both Mo and W promote the increase in resistance to localized corrosion[40,41]. Lloyd *et al*.[41] evaluated the electrochemical behavior of Ni-Cr-Mo alloys including Alloy 22 and Alloy 625. The authors highlighted the strong and efficient action of the Cr passive layer present on the surfaces of these alloys[41]. Nonetheless, at high potential (500 mV) the oxidation of Cr(III) to Cr(IV) began, characterizing the dissolution of the passive layer, except for alloys containing Mo-W that kept low passive currents, suppressing the dissolution of the passive layer[41]. Therefore, Alloy 22 could be a good option for dissimilar girth welding of risers.

Considering the problems discussed above, the present study proposes a novel method to manufacture dissimilar girth weld joints for rigid riser with internal cladding of Alloy 625, for subsequent pipeline installation by the reel-lay process. The welding of this dissimilar girth joint was manufactured using two filler metals from different classes of materials: Alloy 22 and AWS ER100S-G steel. The Ni-based alloy was used for the root and hot passes in order to guarantee a corrosion resistance equal or superior to the CRA cladding of the riser. A LAS was selected to fill the greater part of the joint, in order to overmatch the mechanical properties of the riser required by DNVGL-ST-F101. The metallurgical features were assessed by microscopy and microanalysis and the mechanical properties were evaluated by tensile tests, bending tests, microhardness mapping, hardness profile, Charpy-V impact and CTOD tests.

8.3 Experimental procedure

The welding of the joint was performed on API 5L X65 steel pipe with an internal Alloy 625 cladding. The 1st and 2nd passes were deposited with the Ni-based Alloy 22 to provide

corrosion resistance equal or superior to the Alloy 625 cladding. The filler material for the weld joint was the AWS ER100S-G steel (LAS) and which was used from the 3rd to the 10th pass. This LAS was selected to give the welded joint an overmatch of mechanical properties in comparison to the API 5L X65 steel[3,42]. Figure 8-1 is a schematic drawing of the novel joint configuration proposed to weld the internally cladded riser. Table 8-1 gives the chemical composition of the materials used in the present study. The chemical composition was obtained from optical emission spectroscopy analysis.

Figure 8-1. Schematic drawing of the proposed welded joint.

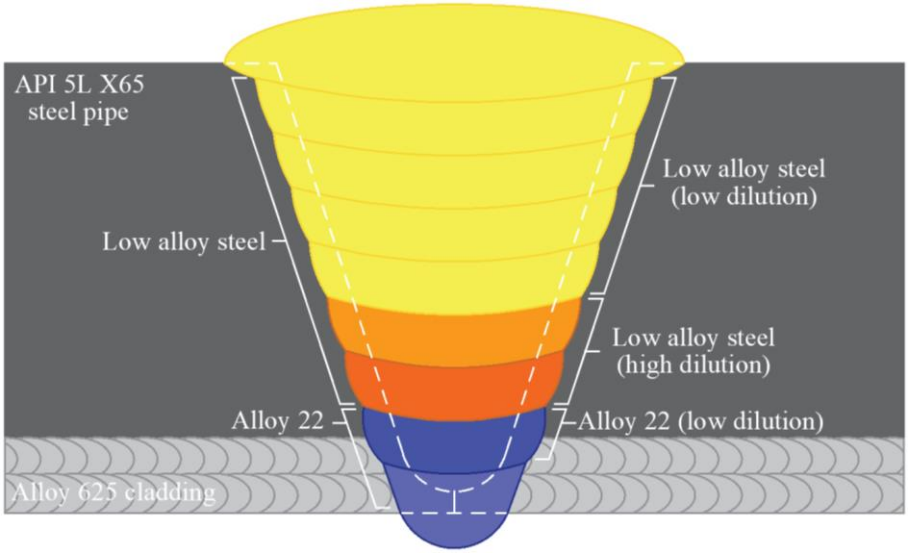

Source: Developed by the author.

Table 8-1. Chemical composition of the materials used in the dissimilar welded joint.

Chemical composition of materials														
Alloy	Al	C	Co	Cr	Cu	Fe	Mn	Mo	Ni	P	S	Si	Ti	W
Alloy 22 (AWS ER NiCrMo-10)		0,015	0,25	21,05		4,96	0,12	13,15	57,35	0,02	0,01		-	2,97
API 5L X65 steel pipe	0,04	0,11		0,12	0,18	97,51	1,17	0,14	0,34	0,012	0,004	0,28	-	
AWS ER100S-G steel		0,04		0,12	0,11	96,47	1,37	0,38	0,82	0,055	0,014	0,62	0.13	

Source: Developed by the author.

The pulsed gas metal arc welding process (GMAW-P) with a weld torch coupled to an industrial robotic workbench to provide high accuracy of movement was employed for the welds. The AWS ER NiCrMo-10 (Alloy 22) and the AWS ER 100S-G (LAS) were used as the filler metals, both with 1.2 mm of diameter under 100%Ar and 98%Ar – 2%CO_2 shielding gases, respectively. Figure 8-2 shows the welding workbench used to perform the joint welding. The main welding parameters of each pass used to perform the joint welding are given in Table 8-2. The welding speed was reduced from the 1st pass onward, in order to deposit more material

for fill each weld layers with only one weld pass. This led to a continuous increase of the heat input.

Figure 8-2. Industrial robotic workbench with a) welding torch coupled. The welding torch position b) before and c) after deposition of a welding pass.

a) **b)** **c)**

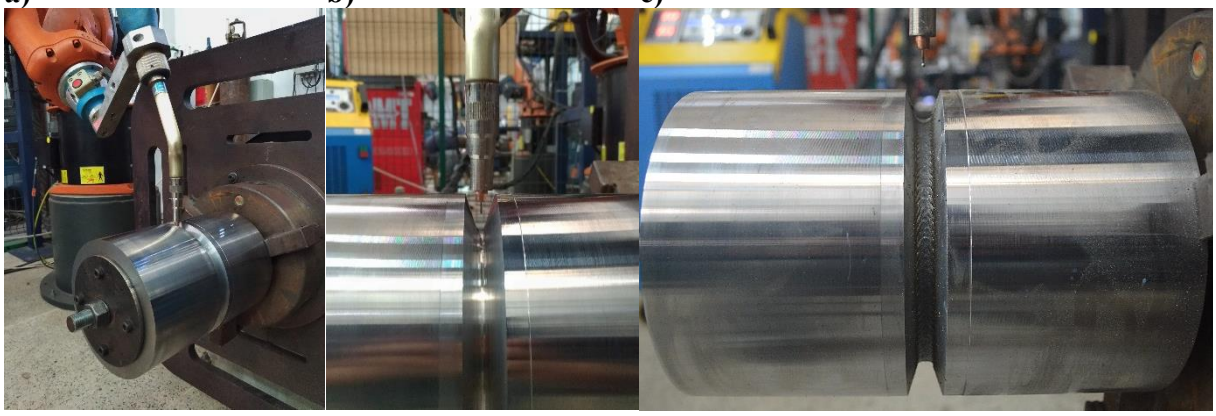

Source: Developed by the author.

Table 8-2. Main welding parameters used in each pass to fill the weld groove.

		Welding parameters								
Passes	Alloy	I_p (A)	I_b (A)	t_p (s)	t_b (s)	S_w (cm/min)	U (V)	S_{wf} (m/min)	A_t (mm)	HI_w (kJ/mm)
1st pass	Alloy 22	300	90	2.2	4.4	45	20.9	7.2	0.6	0.50
2nd pass	Alloy 22	300	90	2.2	4.4	40	21.4	7.0	2.2	0.58
3rd pass	LAS	300	90	2.2	4.4	35	21.6	5.5	3.7	0.65
4th pass	LAS	300	90	2.2	4.4	35	20.1	5.5	4.7	0.62
5th pass	LAS	300	90	2.2	4.4	25	20.2	5.5	5.5	0.88
6th pass	LAS	300	90	2.2	4.4	18	20.2	5.5	6.0	1.23
7th pass	LAS	320	100	2.2	4.4	15	21.7	5.8	6.5	1.75
8th pass	LAS	320	100	2.2	4.4	14	21.9	5.8	7.0	1.75
9th pass	LAS	320	100	2.2	4.4	13	22.2	5.8	7.5	1.89
10th pass	LAS	320	100	2.2	4.4	12	22.6	5.8	8.4	2.11

Source: Developed by the author.

Macrographs and micrographs were used to evaluate the physical metallurgy of the welded joint. A transverse cross-section of the welded joint was cut and the surface was prepared by conventional metallography for the macrographs. After which the surfaces were etched using 2% nital and 10% acid chromic solutions to revel the microstructure of the LAS and Alloy 22 passes, respectively. The microstructure was assessed using scanning electron microscopy techniques.

The mechanical behavior of the welded joint was evaluated following the recommendations of DNVGL-ST-F101[34]. Two transverse tensile and four bending tests were

made to verify the integrity of the welded joint and to verify if the welding procedure adopted was suitable. A collapse of the welding metal without evidence of defects may indicate that an unsuitable filler metal was used, while defects such as lack of fusion, porosity, shrink porosity and solidification cracks could be the result of incorrect welding parameters. Figures 8-3a and 8-3b show a schematic image of the transverse tensile and bending test samples.

Figure 8-3. Schematic image of a) bending, b) transverse tensile, c) transverse all weld tensile d) notch in the 3rd pass Charpy-V, e) notch in the 7th pass Charpy-V and f) CTOD tests.

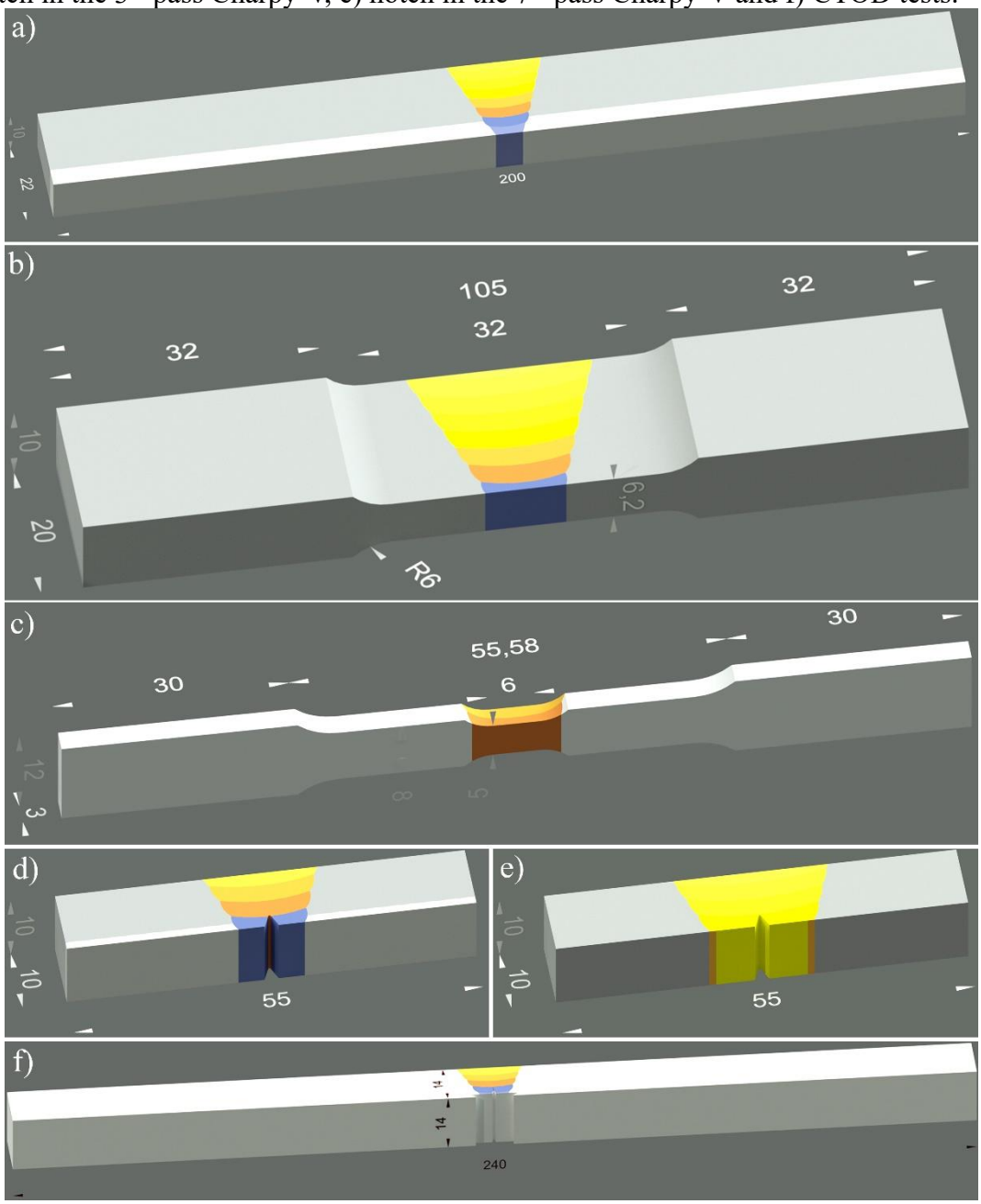

Source: Developed by the author.

The yield strength of the welded joints was assessed using the transverse all weld tensile test and they followed the recommendations of DNVGL RP F108[43]. Two samples of each of the four different regions of the welded joint were evaluated. The root and hot passes (1^{st} – 2^{nd}), high dilution LAS passes (3^{rd} – 4^{th}), low dilution LAS passes (5^{th} – 6^{th}) and filling region (7^{th} – 8^{th}) were all assessed. These tests are important to obtain the main mechanical properties of this complex dissimilar welded joint. Figure 8-3c shows a schematic drawing of the 3^{rd} and 4^{th} passes.

Microhardness mapping and hardness profiles were used to assess the resistance to penetration of the joint weld. The microhardness mapping applied a 100 gf load. The micro indentations were spaced 300 μm apart to provide a good spatial resolution. The hardness profile was performed from the 1^{st} weld pass to the last weld pass and a 10 kgf load with 1 mm of spacing between indentations was used.

The impact toughness (Charpy-V) test was performed on ten samples, 5 of which were on samples with the notch positioned at the begining of the 3^{rd} pass and the other 5 samples with the notch positioned at the 7^{th} pass. In all cases, the notch was positioned on the opposite face to the normal welding direction, and the tests were performed at -15°C. Figure 8-3d and 8-3e show the details of the Charpy-V impact test. Moreover, four CTOD samples (Figure 8-3f) were assessed with the pre-crack positioned at the beginning of the 3^{rd} pas. In this case, two samples were evaluated in the as-welded condition and the other two samples were assessed after a post weld heat treatment at 580°C for 1h.

8.4 Results and Discussion

8.4.1 Weldability of welded joint

Dissimilar welding is a versatile manufacturing process, but the mixture between materials from different classes represents a complex welding problem. Therefore, previous studies were performed in order to predict and avoid solidification defects (Chapters 4, 5 and 6). The first study evaluated the dilution effect for joint welding of API 5L X65 steel pipe using Ni-based alloys as the filler metals. Based on the classical solidification model, thermodynamic simulations for different dilution levels between the base metal and filler metals were made. Different from Ni-based alloys that contain Nb, Alloy 22 showed good weldability with X65 steel, considering the low solidification temperature range (ΔT) that was predicted by this study, even for high dilution with X65 steel. Using Alloy 22, the dilution with X65 steel caused a

reduction of Ni, Cr, Mo and W, while Fe, Mn, Si and C were incorporated into the weld metal, causing a reduction of the σ phase, as M_6C and MC were favored. No eutectic phases, usually related with the widening of the ΔT of the weld metal, were predicted in this case with Alloy 22.

The second thermodynamic simulation study assessed the solidification for dilution of the AWS ER 100S-G steel deposited on the Ni-based alloys. In this case, it was considered that two Ni-based alloys weld passes were previously deposited and, the study was interested in evaluated the dilution effect of 100S-G steel filler was evaluated. The simulation predicted that the 100S-G steel, when mixed with Alloy 22, would exhibit a δ ferrite in equilibrium with the γ-matrix. At a high dilution level, the δ ferrite is suppressed, and only M_6C was predicted in equilibrium with the γ-matrix. In the case of the mixture of 100S-G steel with Alloy 625, the simulation predicted eutectic phases rich in Nb, especially the Laves phase that showed a deleterious effect by increasing the ΔT of the alloy.

Both studies were important to indicate Alloy 22 as the filler metal for the root pass of this complex welding joint configuration, especially considering its good metallurgical compatibility with the X65 and 100S-G steels. Furthermore, knowing the deleterious effect of Nb when incorporated to the weld metal composed of steel and the Ni-based alloy was important to define the welding procedure. With this background, the 1st and 2nd passes were welded using Alloy 22 in order to provide good corrosion resistance in the root pass (1st) and for a reduction of Nb in weld pass (2nd) that will dilute with the first 100S-G pass. This procedure was indispensable to prevent solidification cracks in this very complex dissimilar welding. Figure 8-4 shows the macrograph of the transverse cross-section of the welded joint manufactured using Alloy 22 and 100S-G steel as the filler metals.

The macrographs reveled a welded joint with high quality, indicating that the welding procedure had been successfully executed on the joint, considering the absence of welding defects, especially lack of diffusion and solidification cracks on the centerline of the weld passes. The mixture of the 1st Alloy 22 pass with Alloy 625 cladding showed good metallurgical compatibility. The incorporation of Nb did not impair the weldability. The same behavior was observed for the 2nd Alloy 22 pass deposition, even with the addition of Fe, Mn, Si and C from the dilution with X65 steel. From the 3rd pass on 100S-G steel was used. As predicted by the thermodynamic simulation study, the mixture exhibited good metallurgical compatibility with no evidence of solidification cracks. This result followed the same tendency as the previous experimental study that evaluated the effect of welding heat input on the

formation of solidification cracks for single weld beads of 100S-G steel on Alloy 22 alloy cladding. The study observed only few discontinuities, even for a dilution level above 50%, when the size and number of these discontinuities were reduced for high welding heat input (HI_w) condition.

Figure 8-4. Macrograph of the transverse cross-section of the welded joint and the microstructure of the main passes.

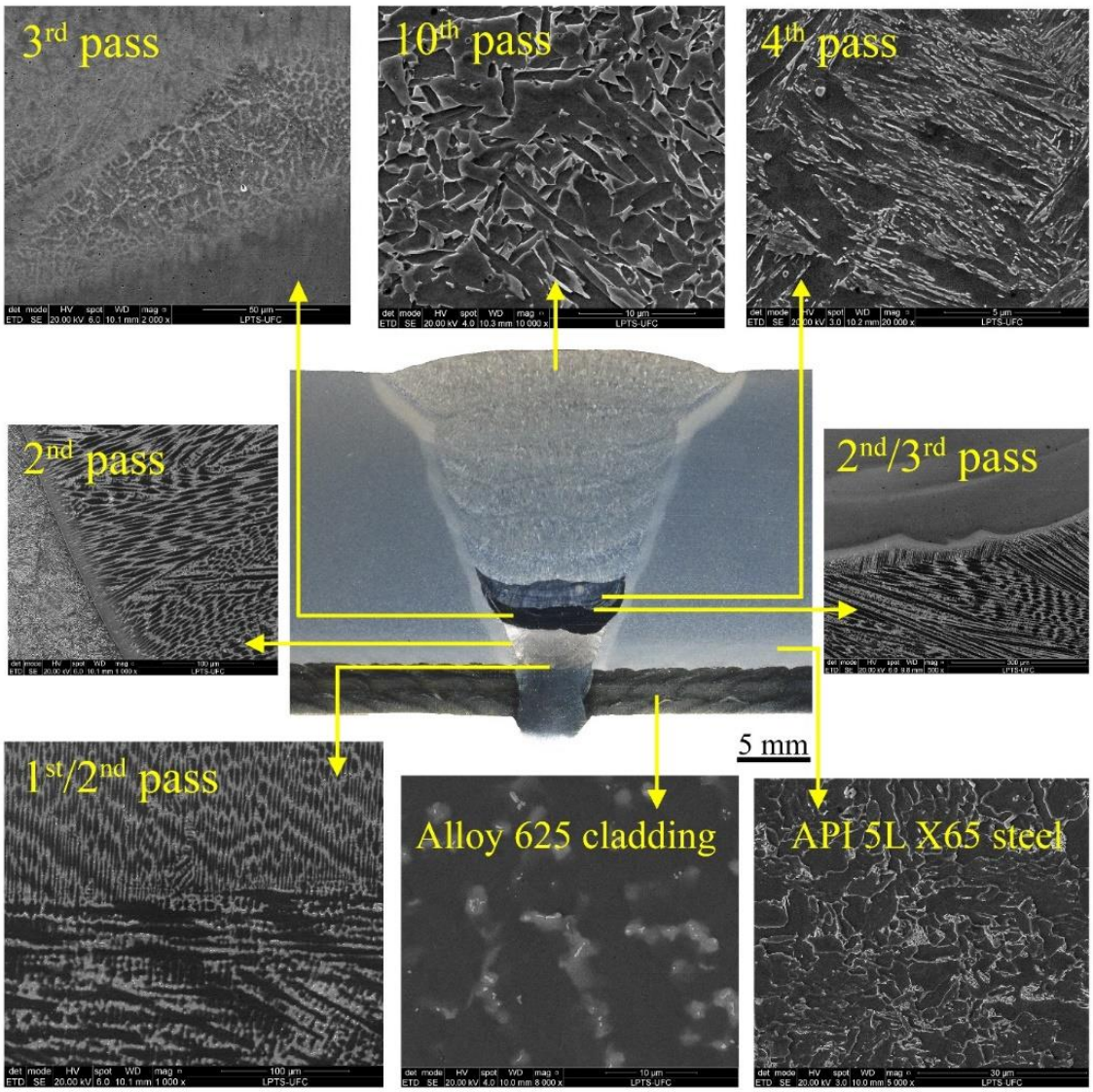

Source: Developed by the author.

Another important factor adopted was a low depth-to-width (D/W) ratio of the weld. Considering that solidification grains (SG) grow perpendicular to the solid/liquid interface, following the thermal gradient of the arc welding, a low D/W led to an elliptical weld pool causing a radial SG growth[44]. This prevented the meeting of SG on the weld centerline, and thus prevented the accumulation of alloying elements segregated during solidification[44]. This

is an important factor to inhibited solidification cracking, even when using welding materials with low solidification crack susceptibility. The opposite situation occurs for a high D/R ratio; the weld pool will show a teardrop shape[44] that allows the meeting of SG, and causes a high accumulation of alloying elements and impurities (S, P and O)[45], which cause centerline solidification cracking.

The etching of the transverse cross-section of the joint weld reveled further information in the macrographs. The 3rd pass, for example, did not react to the chromic acid nor nital. This was due to the high incorporation of alloying elements such as Ni, Cr, Mo and W from the dilution of LAS of the 2nd pass (Alloy 22). This made the pass almost inert to these reagents. The microstructure of this 3rd pass was only visualized (Figure 8-4) by backscattered electron (BSE) imaging, which obtained contrast by differences in atomic number (Z) contrast. Also, the 4th pass showed different contrast in comparison with the subsequent LAS passes due to the dilution effect with Alloy 22. From the 5th pass on the contrast exhibited was similar to a common steel. A detailed evaluation of the microstructure is presented later in the text.

The chemical compositions of the 1st, 2nd, 3rd, 4th, 5th and 6th passes of the welded joint are shown in Figure 8-5. The 1st pass shows the influence of the Alloy 625 cladding, considering the Nb fraction was about 1.2%. This represents about 35% dilution with the Alloy 625 cladding, considering that normally 3.5% of Nb is present in such Ni-based alloys. Possibly this significant amount of Nb could lead to solidification cracks when diluted directly with 100S-G steel. Therefore, one more Alloy 22 pass was deposited and this pass showed an almost zero Nb fraction. According to the literature, small fractions of Nb lead to the formation of low melting point phases that are normally related to the formation of solidification cracks[46]. The literature highlights the effects of small and large fractions of eutectic phases during the final stages of solidification[46]. Wheeling and Lippold[46] investigated the effect of Nb and Mo addition in amount of eutetic fraction formed during welding of Ni-30Cr alloy and, its effect on solidification crack susceptibility. The Nb addition increased the eutetic fraction predicted by simulation and measured by conventional metallographic analysis. According to authors, small eutectic fractions are considered more harmful in comparison to large eutectic volumes due to the absence of the backfilling phenomenon. This phenomenon considers that reminiscent eutectic liquid fills the volume between the dendrite arms, thus healing the cracks. For a moderate eutectic fraction, the dendrite arms confine the reminiscent eutectic liquid, impairing the backfilling effect. Even with such considerations, a very small or insignificant eutectic fraction is more interesting in terms of solidification cracks, because the SG will grow without

liquid metal between the grain boundaries that are notably reduce the resistance between solidification grains, which favored the formation of solidifications cracks.

Figure 8-5. Chemical composition of the main passes of the welded joint (Fe, Ni, Cr, Mo, Nb and W). The arrows indicate the scale side.

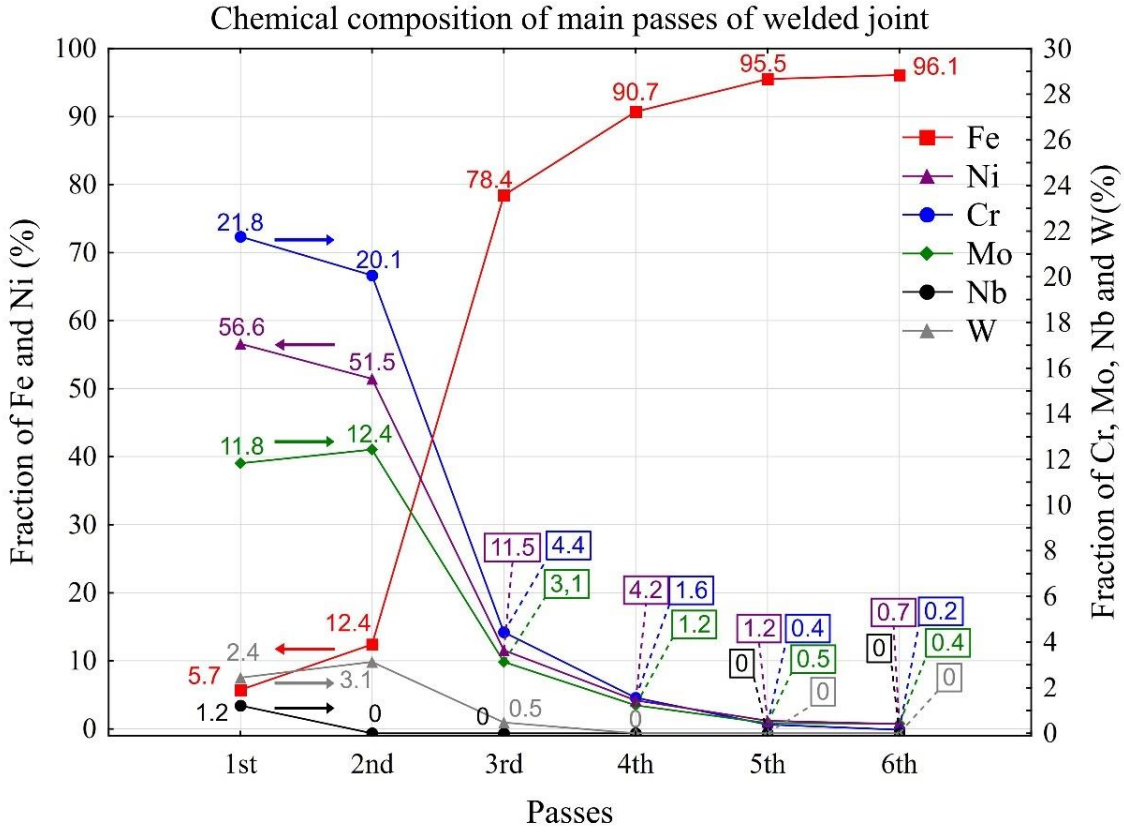

Source: Developed by the author.

As the 100S-G passes filled the joint by subsequent passes, the dilution effect of Alloy 22 was continuously reduced, decreasing the Ni, Cr, Mo and W fractions. From the 6th pass onward the chemical analysis revels a chemical composition virtually the same as LAS. While the 3rd and 4th passes showed approximately 11.5 wt.% and 4.2 wt.% of Ni, 4.4 wt.% and 1.6 wt.% of Cr, 0.5 wt.% and 0 wt.% of W, respectively. Note: a high fraction of alloying elements was incorporated in the 3rd, 4th and 5th passes, and provided an increase in the hardenability by solid solution and quenching.

8.4.2 Microstructural analysis

Figure 8-6 shows the as-solidified microstructure of the interface between the 1st and the 2nd passes of the welded joint. A γ-FCC matrix was observed as expected for a Ni-based alloy. The dendrite morphology with its respective interdendritic region was clearly observed

due to the etching effect on both passes. In addition, some secondary phases were observed within the interdendritic regions. These phases were nucleated during the final solidification stage as a result of the microsegregation of the alloying elements such as Cr, Mo and W. According to the literature, the Alloy 22 as welded followed the solidification path[47]:

$$L \rightarrow L + \gamma \rightarrow L + \gamma + \sigma \rightarrow \gamma + \sigma \rightarrow \gamma + \sigma + P + \mu$$

Figure 8-6. Microstructure of a) solidification interface between the 1st and the 2nd passes and b) details of the microstructure of the 2nd pass.

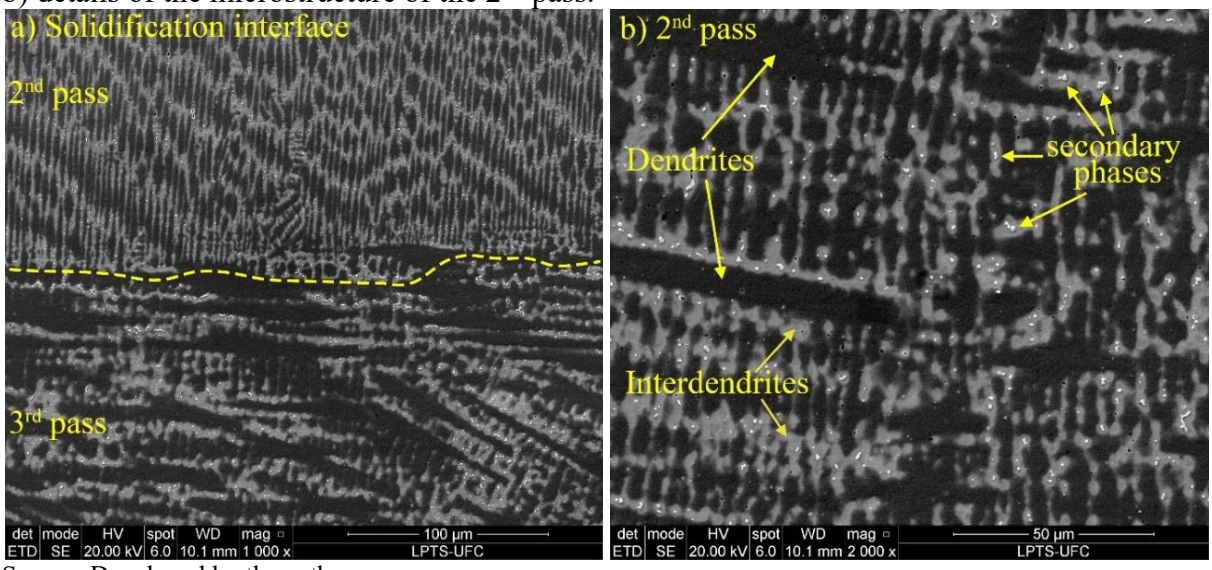

Source: Developed by the author.

Where the σ phase, nucleated during solidification, is decomposed by the P phase, which subsequently transforms into the μ phase[47]. Probably, all these phases are present on the weld metal, considering that fast cooling does not allow the diffusion of elements into equilibrium, in other words, there is not enough time to dissolve phases formed during solidification as a consequence of microsegregation of the alloying elements. The reheating due to subsequent passes may lead to some of these phase transformations.

Other important information is related to the amount and size of the secondary phases. Few small size particles were observed when compared with other studies[48–51]. As reported in the literature, Alloy 22 was developed in order to reduce the formation of μ phases, which impair corrosion resistance[38,39,52]. The fast cooling rate, as consequence of a low HI_w, of about 0.5 – 0.6 kJ/mm that was used to deposit the 1st and the 2nd passes, is directly related to this result.

Only a few discontinuities were observed at the last section of the solidified Alloy 22. Normally, alloys that present a low secondary phase fraction in the as-welded state have a

lower susceptibility to solidification cracking. On the other hand, the absence of these hard particles may decrease the resistance to formation of ductility dip cracks. According to Gallagher and Lippold[53], the presence of small secondary phases distributed along the Alloy 22 weld metal prevented ductility dip cracking[53]. In this case, these particles act as pinning points that block the motion of grain boundaries and consequently do not allow austenitic grain growth[53–56].

The microstructure of the 3rd pass of the welded joint is shown in Figure 8-7a. The solidification mode of this weld pass was mainly cellular, with the occurrence of small secondary dendrite arms in a few regions of the weld metal. The intercellular regions were characterized as rich in Ni, Mo and Mn, without evidence of any secondary phases. Moreover, it was observed macrosegregation into fusion zone. The aspect of the macrosegregation slightly more corroded than bulk of the microstructure suggest that represent a region rich in filler metal (100S-G steel). Figure 8-7b shows in more detail the morphology of the 100S-G steel rich region of the weld metal, while Figure 8-7c points out the differences in terms of chemical composition. The impoverishment of Ni, Cr and Mo, whereas there an enrichment of Fe, made evident that represent a filler metal rich region. Probably, this macrosegregation is composed by martensite, since reduction of Ni and others elements raise the martensite start (M_S) temperature.

A thermodynamic simulation based in chemical composition of the 3rd weld pass was performed (Figure 8-8), in order to give support for this analysis about martensite transformation. The simulation was performed based in equilibrium; therefore, it was assumed that elements had time enough diffuse along of matrix in direction for lower energy state. According to simulation the 3rd weld alloy started the solidification as γ-FCC, which become unstable as temperature decrease to formation of carbides, Laves phase and mainly the α-BCC. Nonetheless, the solidification and subsequent cooling of materials submitted to fusion welding processes occurs in non-equilibrium conditions, because cooling rate is too fast, which does not allow the diffusion of elements. Even thus, from 633°C onward the elements organize as α-BCC, nonetheless, the strain stress due to thermal contraction caused the difussionless transformation of γ-FCC in martensite. It is important highlight the prediction of Laves phase rich in Fe, Mo and W, at 759°C. Probably, the stabilization Laves phase field increased in intercellular regions, once that Mo is segregated to liquid during solidification.

Figure 8-7. Microstructure of the 3rd weld pass highlighting the a) cellular growth, b) the filler metal rich region and, c) the EDS microchemical maps of macrosegregation.

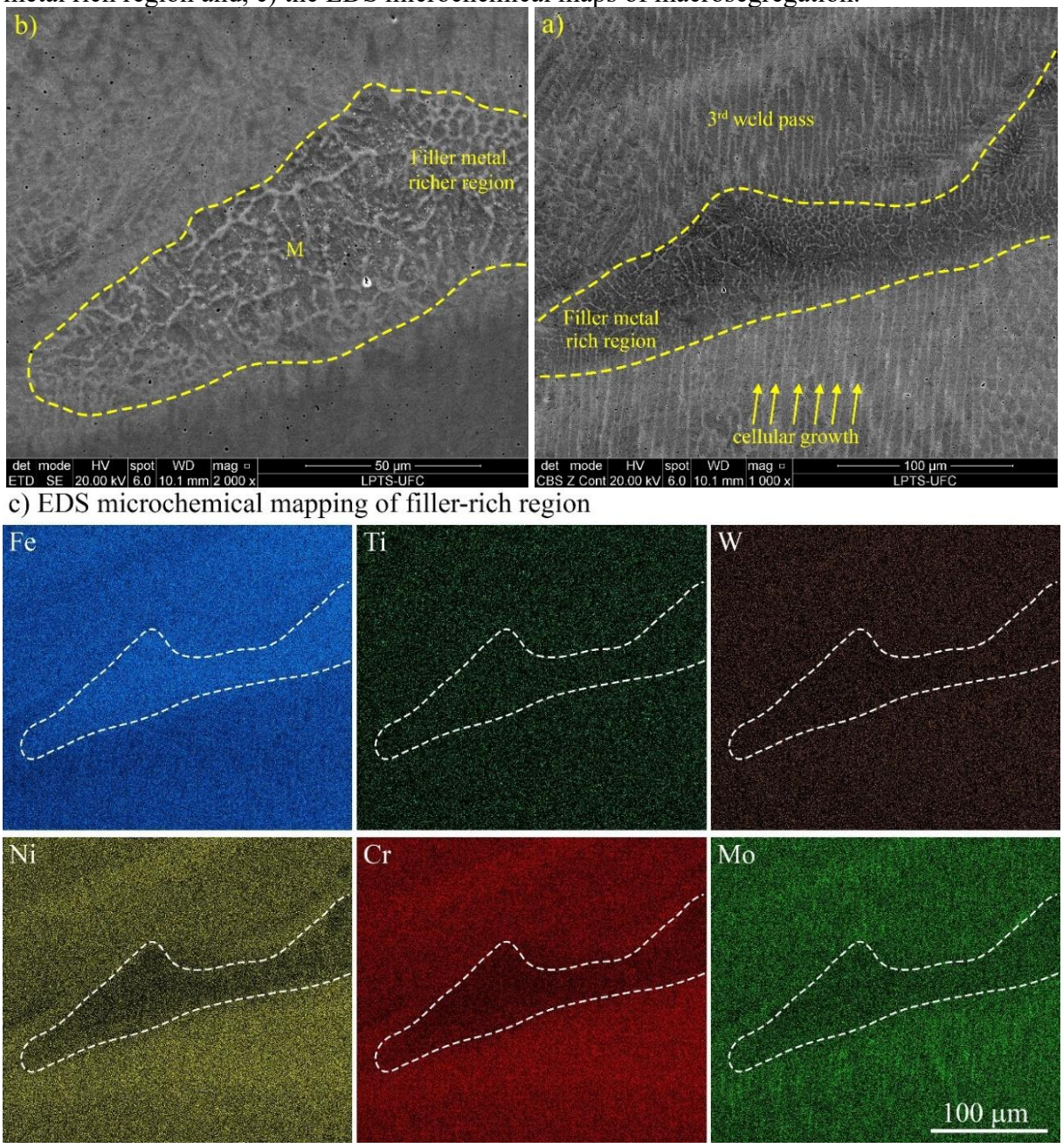

Source: Developed by the author.

A new chemical etching was performed using a high concentration HNO_3 with aim to provide a severe etching able to reveal the microstructure of the 3rd weld pass. The new etching procedure severely eroded the steel pipe and the weld passes of the welded joint from 4th weld pass onward. Moreover, the severe etching evidenced the presence numerous macrosegregation regions at all fusion zone. Figure 8-9 show an overview of 3rd weld pass after over etching using light microscopy images. The light gray regions were less corroded by acid

solution and consequently represent the base metal rich regions, while filler metal rich regions are highlighted in dark gray tons.

Figure 8-8. Thermodynamic simulation of 3rd weld pass based in equilibrium.

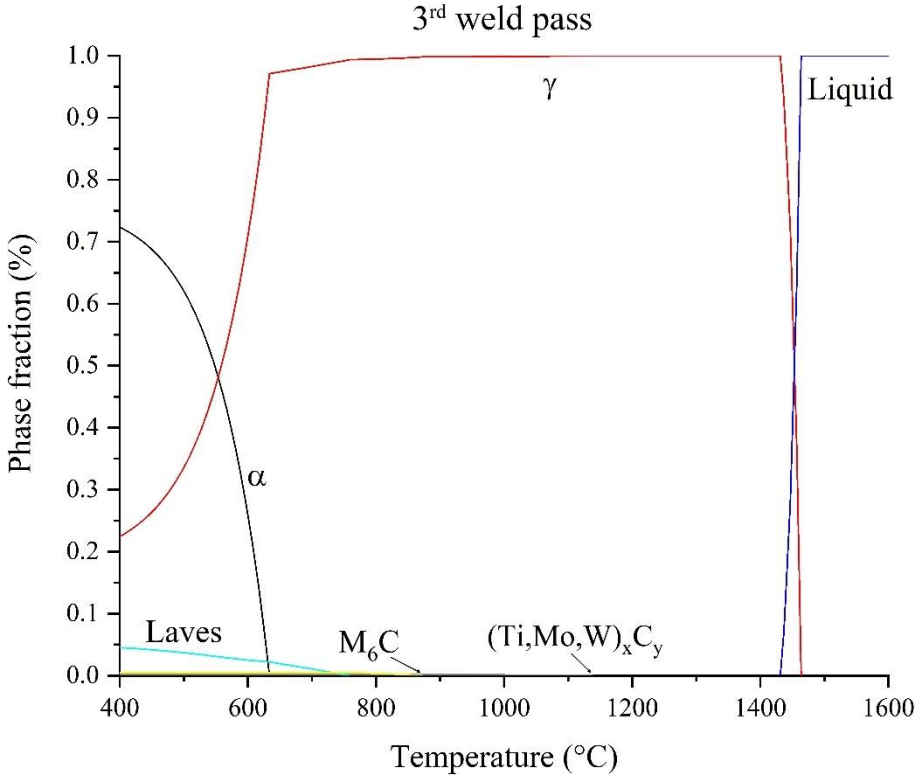

Source: Developed by the author.

Figure 8-9. Macrography of 3rd pass after severe etching, highlighting the macrosegregation regions along of weld pass.

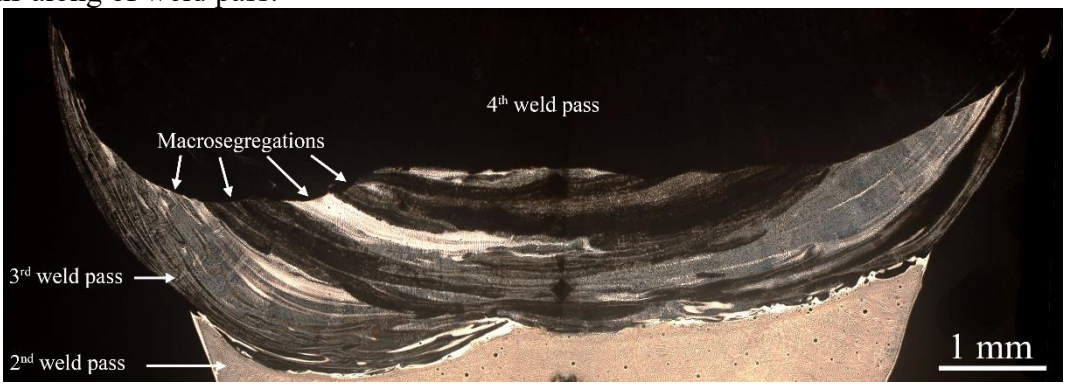

Source: Developed by the author.

The macrosegregations is phenomenon that occurs mainly in dissimilar welding. The physical and chemical differences between the filler metal (100S-G steel) and the base metal (2nd Alloy 22 weld pass) impair the mixture before solidification, especially when the materials have different melting points. Yang and Kou[57] investigated the macrosegregation in

Cu-30Ni alloys. The authors proposed macrosegregation mechanisms for different mixture condition, divided about liquidus temperature of filler metal, fusion zone and base metal. According to authors, when the liquids temperature of filler metal and fusion zone as well are bigger than experienced by base metal, the total mixture between alloys is impracticable. In this case, there a great melting and consequently penetration of base metal by arc welding. A portion of base metal melted is pushed up by pool convection which solidify quickly without complete the total mixture between alloys, since there is not time enough elements diffuse[57–61].

In fact, the 3rd weld passes have a martensitic matrix that cover all microstructure, even in regions rich in base metal and, therefore, Ni, Cr, Mo and W rich regions. Figure 8-10 show martensite matrix with details. The regions rich in filler metal and consequently poorest in Ni and others alloying elements, it was submitted to a super etching that evidenced clearly the martensite morphology, although, also been possible to observe the microstructural features into base metal rich region. Others phases were observed in bulk 3rd weld pass such as the A_{ret} and cubic carbides. The A_{ret} may form at intercellular and/or interdendrite regions, since there a great number of segregated elements, especially C, Ni and Mn, which enlarge the γ stabilization field, in terms of thermodynamic concepts. This phenomenon reduces the martensite start (M_S) temperature. It is possible calculate the M_S temperature based in classical Equation 1 proposed by Andrews[62]:

$$M_S(°C) = 539 - 423wt\%C - 30.4wt\%Mn - 17.7\ wt\%Ni - 12.1\ wt\%Cr - 7.5\ wt\%Mo \quad (1)$$

Figure 8-10. Microstructure of 3rd weld pass after a severe etching, highlighting the a) martensite present in both macrosegregation cases: filler and base metal rich regions. Others phases like b) A_{ret} and Ti carbonitrides also were observed.

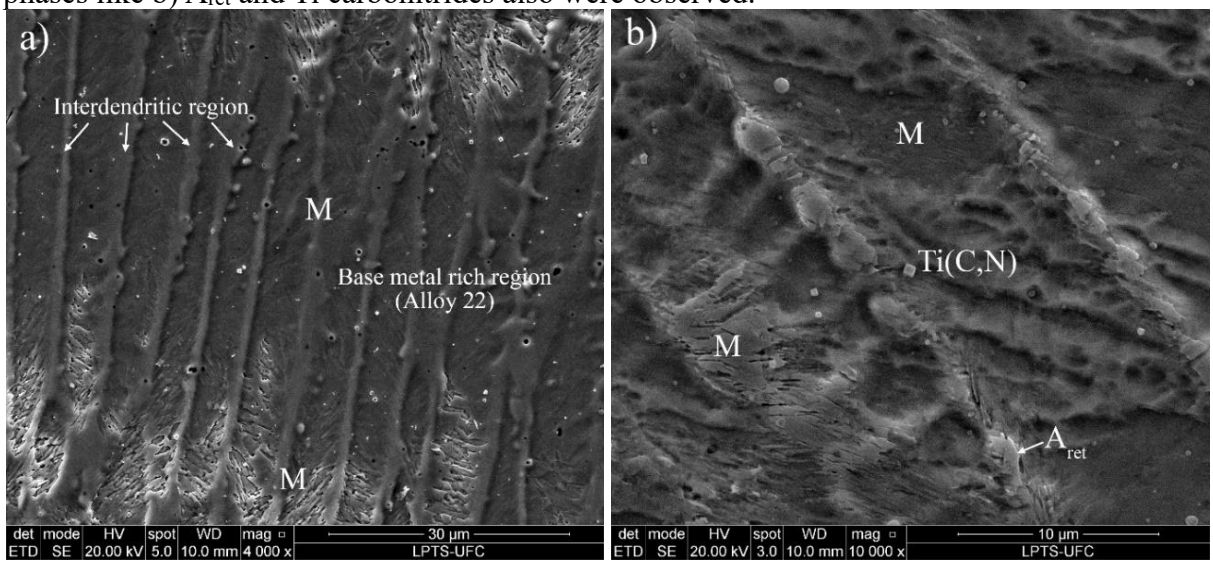

Source: Developed by the author.

The calculated M_S temperature for 3rd weld pass is approximately 203°C. This give support for assumption that 3rd weld pass is martensitic. Note that addition of alloying elements causes the reduction of M_S temperature, therefore, it is reasonable suppose that in intercellular and/interdendrite regions which presents a concentration of segregated elements may stabilize the A_{ret}. Not only microsegregation experienced during solidification contributes for A_{ret}. According to Krauss[63] during the martensite transformation, there is a short diffusion of C and others elements to lath martensite boundary that cause the stabilization of austenite. Shiue *et al*.[64] characterized this phenomenon for welding 9%Ni steels. Using selected area electron diffraction (SAED), the authors identified A_{ret} along of martensite interlath boundaries exhibiting the Kurdjumov–Sachs and Nishiyama–Wasserman orientation relationships with martensite.

On the other hand, the grain size of primary austenite also favors the martensitic transformation. This assumption was demonstrated in study of Yang and Bhadeshia[65], which the authors investigated the effect of grain size in M_S of Fe–0.13C–5Ni–2.27Mn steel. By dilatometric data, it was observed that M_S raised for samples who experienced long heat treatments that caused the increase of its primary austenite grain size.

Cubic carbides also were observed along of the 3rd weld pass. The EDS analysis revealed a high concentration of Ti, Al, Mg and O. Similar particle was investigated for weld overlay of carbon steel using Alloy 625. In to Silva *et al*.[16] study was demonstrated that these cubic carbides are cubic particles are Ti nitrides, may also be carbides or carbonitrides, since they have the same crystal structure with minor changes in lattice parameters. For this reason, they represent a great nucleating agent for Nb carbides observed by authors, but also is possible the nucleation of oxides rich in Al and Mg as observed in present study.

The severe etching also revealed a shrink porosity observed at interface between 3rd and 4th weld passes (Figure 8-11). The defect was concentrated at intercellular regions. This feature suggest that segregation of elements had a key role for the formation of this defect. The segregation occurs during all solidification, but at last portion of weld pass there a higher concentration of segregated elements, since represent the last liquid rejected by solid matrix to solidify. Probably this regions was melted by reheat experienced during the deposition of the 4th weld pass. This mechanism is the same of liquation cracks, where materials exhibits intergranular crack due fusion of low melting point phases located at grain boundaries. The Figure 8-11 also evidenced the formation of a precipitate that take the shape of previous $Eutetic_{film}$. The precipitate surrounded grains reducing the mechanical resistance among grains. Such defect under high stress and restraint condition provide the settings for raise cracks.

Figure 8-11. Shrink porosity located at interface between 3rd and 4th weld passes, evidencing a eutetic film contouring the SG boundaries and A_{ret}.

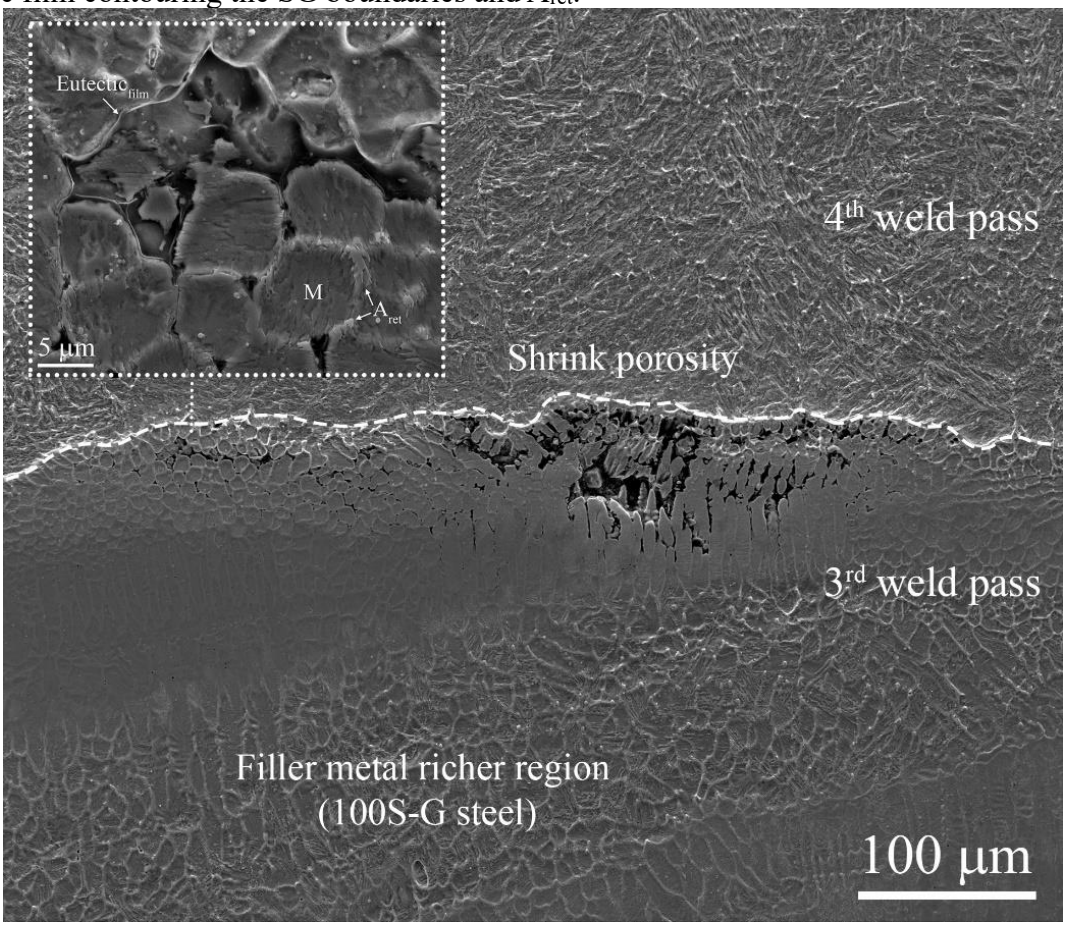

Source: Developed by the author.

Liu and Kou[66] investigated this phenomenon by phase diagram for γ-FCC binary Al alloy systems. The authors contributed for explains the relationship of grains morphologies in formation of such solidification defects. When cells growing with a 'virtually spherical' tip shape, the eutetic liquid wet the intercellular regions by capillarity[67] maintaining at least a thin eutetic film along of grain boundaries. Considering now cells growing with hexagonal tip shape, the early bridging among grains cause the concentration of eutetic liquid at dihedrals formed at triple point. This avoid the formation intergranular cracks and favor the nucleation precipitates like A_{ret} observed in Figure 8-11.

Figure 8-12 shows the microstructure of the 4th pass of the welded joint. This weld pass showed a microstructure based on a martensite matrix (Figure 8-12a). In this case, the dilution effect of the Alloy 22 pass was reduced, but was not enough to prevent the martensitic transformation. The Ni content was reduced from 11.5 wt.% to 4.2 wt.% which caused the reduction of austenitic field favoring the martensitic transformation. The M_s temperature calculated for this case was approximately 371°C. Considering that fast cooling rate

experienced by weld metal introduce high stress due contraction of solid, which associated with high restraint to strain, it is reasonable assume that sufficient shear stress for diffusionless transformations occurs. In addition, significant fractions of Cr, Mo and W were incorporated into the weld metal: approximately 1.6 wt.%, 1.2 wt.% and 0.5 wt.%, respectively. In general, these alloying elements cause the hardenability of steel by solid solution and quenching mechanisms, due to the fact that Cr, Mo and W are considered to be ferritizing elements[19,68]. At room temperature the atoms of these elements are arranged in a body-centered-cubic (BCC) structure, favoring martensite transformations.

Figure 8-12b reveals more details of the microstructure of the 4th pass. Here some stringer particles of A_{ret} and carbides into martensite in a matrix was observed. As discussed, the A_{ret} are favored by concentration of elements like C, Ni and Mn. During the cooling, part of the γ is transformed into martensite that is saturated in alloying elements, including carbon. During the martensite transformation, a fraction of Ni, Mn and C is segregated by martensite making the adjacent austenite grains rich in these elements, which causes the widening of the austenitic field, favoring the A_{ret}[63]. This phenomenon extends the γ-cfc equilibrium field, holding the γ retained at room temperature.

Figure 8-12. The bulk microstructure of the 4th pass highlighting the martensite and b) a high amount of MA distributed along the weld metal.

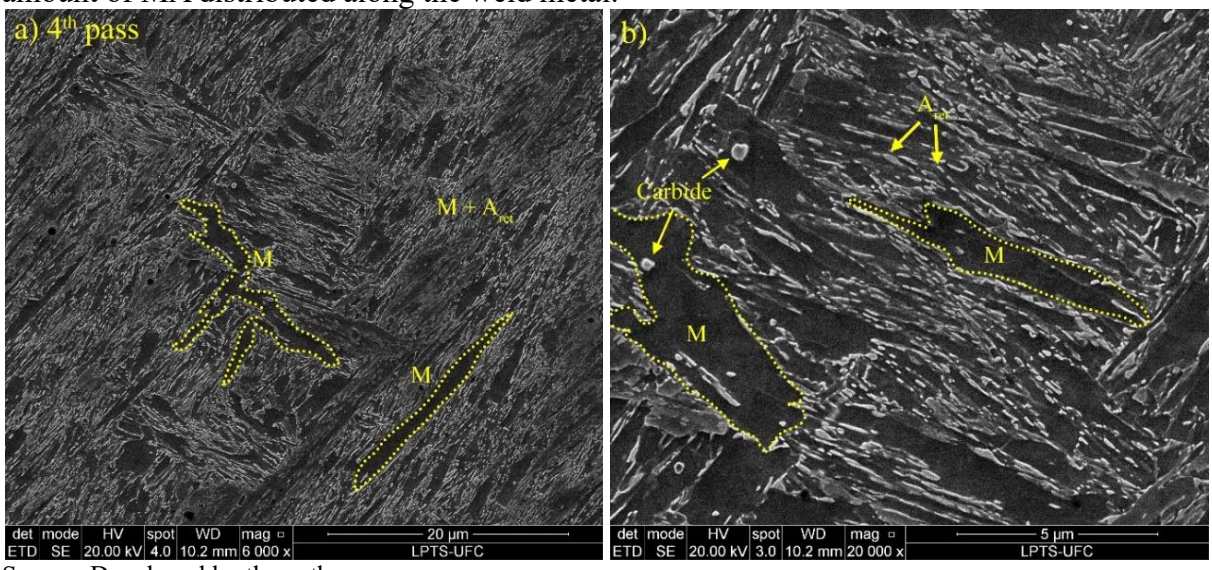

Source: Developed by the author.

The microstructure of the solidification interface between the 4th and the 5th weld passes and the bulk microstructure of the 5th weld pass are shown in Figure 8-13. The differences between the weld passes is evident. The 5th pass of the welded joint showed coarse

microstructures, while the 4th weld pass exhibited essentially thin blocks of martensite with fine A_{ret} well distributed along the matrix. The bulk microstructure of the 5th pass showed a matrix that is possibly formed by a bainitic microconstituents, with the presence of coarse martensite, MA paticles as stringer and carbides. The mechanism that origin the MA particles is quite similar to described for A_{ret}, since the concentration of Ni, C and Mn cause the stabilization of γ-FCC at interlath of martensite[64]. The martensitic structure was observed in this pass, even with the very low dilution effect of the Alloy 22 pass. Certainly, the low HI_w and consequently the fast cooling rate had a strong influence on the formation of the bainite and martensite observed here.

Figure 8-13. The microstructure of a) solidification interface between the 4th and 5th passes and, b) details of the bainite matrix with martensite, MA particles and carbides along the 5th weld pass.

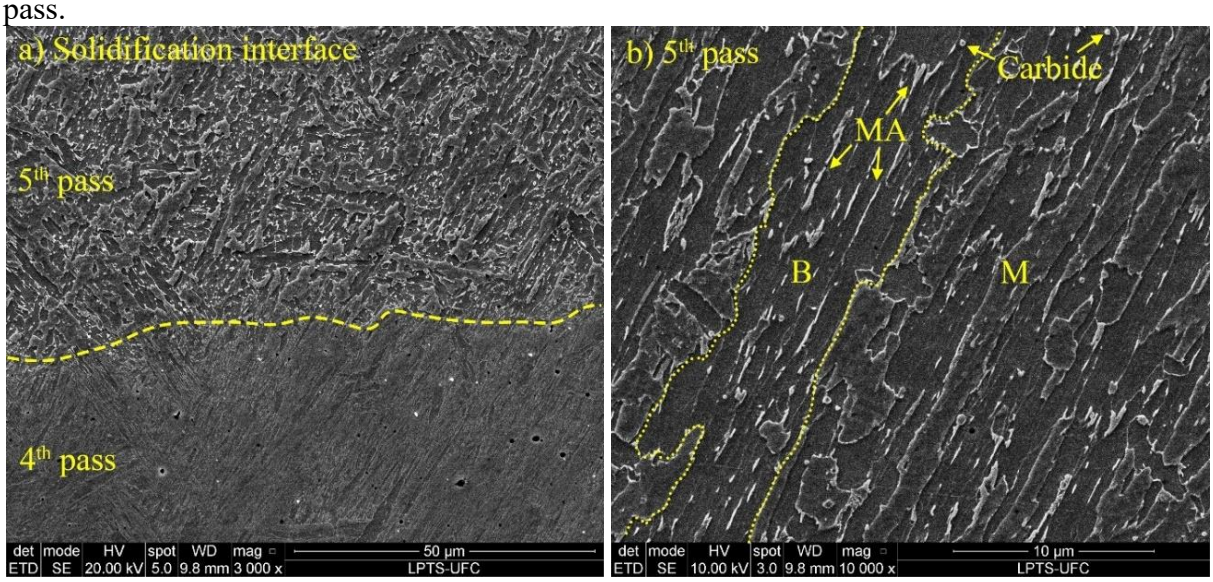

Source: Developed by the author.

From the 6th weld pass onward, the microstructure was essential similar to that observed on the top of the welded joint, following the microstructure of LAS due the similarity in terms of chemical composition. The last pass (10th) microstructure of the welded joint is shown in Figure 8-14. A fine microstructure constituted by acicular ferrite (AF) and MA. However, this time, the MA was observed as blocks, which in this case are characterized as stringer islands, and was different from the MA observed in the 4th and 5th passes.

Figure 8-14. The characterization of a) bulk microstructure of the 10th pass highlighting the b) acicular ferrite (AF) matrix and MA blocks.

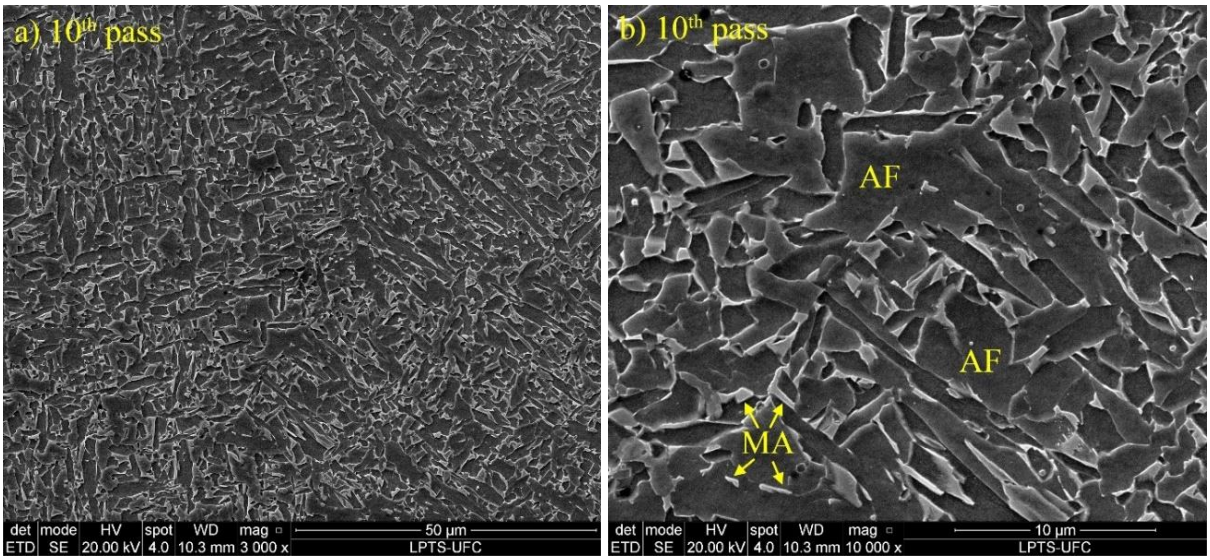

Source: Developed by the author.

8.4.3 Mechanical evaluation

8.4.3.1 Bend testing

Bend tests were done on four samples covering all weld passes of the welded joint, including the Alloy 625 cladding. The four samples after the tests are shown in Figure 8-15.

Figure 8-15. Bending specimens after the test. No samples showed any defects on the bending surface of the four samples of the welded joint.

Source: Developed by the author.

All four samples were approved. No defects were observed on the bended surfaces. This result reinforces the welding procedure, considering that the bending test submits the samples to high tension on the bending surface, thus favoring the growing of defects present on specimens, especially in the case of centerline weld cracks.

8.4.3.2 Tensile testing

The welded joint was assessed by uniaxial tensile tests for all weld passes of the joint in order to obtain the tensile strengths (TS) and verify where a collapse could occur: on the weld metal or on the base metal. Figure 8-16 shows two samples that had been tested. Both specimens exhibited a fracture located on the base metal, far from the weld metal, in other words, the welded joint was approved for all samples, demonstrating an overmatch of TS in comparison with the base metal. The average TS obtained was approximately 742 MPa. Moreover, no defects were observed on the welded joint after the tensile tests.

Figure 8-16. Transverse tensile specimens after the test. All specimens showed a collapse on the API 5L X 65 steel pipe.

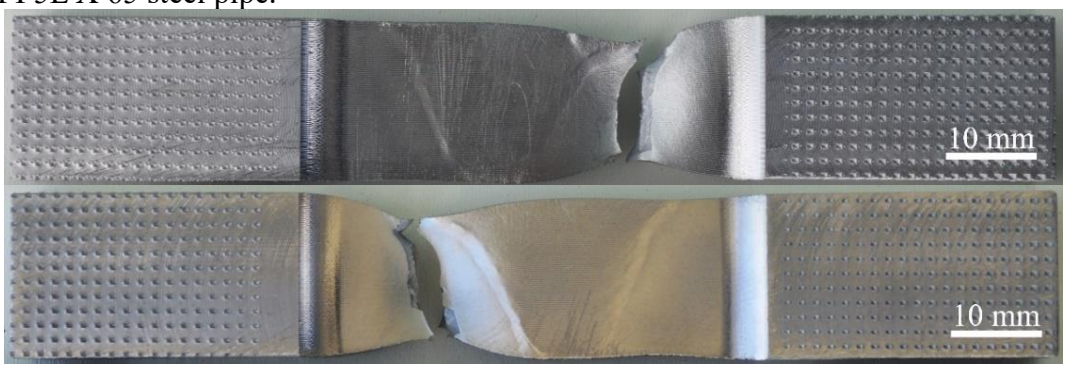

Source: Developed by the author.

This result again qualifies the welding procedure, since the filler metals selected for the welding provided the welded joint enough strength to overmatch the API 5L X65 steel pipe. The absence of defects, especially solidification cracks, is directly relate to the choice of the adequate weld parameters.

Several transverse all-weld tensile tests were performed to assess the mechanical properties of the welded joint. Four different conditions were tested; each condition represented different weld passes. The yield strength, tensile strength, elongation and location of rupture are given in Table 8-3. All the results obtained represent a good approximation of the main mechanical properties of the welded joint, but there was a mixture of materials in all the samples

that included, in general, two weld passes and a small portion of API 5L X65 steel at the fillet radius.

Table 8-3. Mechanical properties obtained from all transverse weld tensile tests. The letters W and R mean that rupture occurred at the weld metal and radius fillet, respectively.

Transverse all welding tensile test					
region (weld pass)	specimen	yield strength (MPa)	tensile strength (MPa)	elongation (%)	rupture
2nd	1	542.1	811.0	31.3	W
	2	498.6	812.0	32.1	W
3rd - 4th	1	963.3	1029.8	17.2	R
	2	980.1	1036.0	15.5	R
5th - 6th	1	-	-	-	-
	2	762.9	793.4	26.9	W
7th - 8th	1	710.5	759.6	26.6	W
	2	-	-	-	-

Source: Developed by the author.

The results revealed that a good overmatch of mechanical properties was achieved. Except for region of the 2nd weld pass that was not included in the overmatch of the YS criterion; however, the lower YS obtained for the other regions was enough to perform the joint welding of API 5L X65 steel for posterior installation by the reel-lay process. The good overmatch also attended the DNVGL-ST-F101 requirements for joint welding of API 5L X70 and X80 steels. For other installation processes, in which the component is not submitted to high strain, up to 0.4%, the YS of the welded joints attended the API 5L X90 steel as well.

This pioneer dissimilar girth-welding configuration for joining steel risers with an internal Alloy 625 cladding creates expectations for welding other high strength steels. This new design for dissimilar joint welds could possibly be a basis to weld high strength steel pipes such as API 5L X90 and X100 steels using an appropriated selection of other LAS like AWS ER 110S and 120S.

8.4.3.3 Microhardness and hardness tests

The resistance to penetration of the welded joints was assessed by microhardness mapping with the weld passes that were more affected by dilution of different materials present in these very complex dissimilar joint welds. The microhardness mapping was performed in an area of approximately 112 mm², evaluating the 2nd, 3rd, 4th, 5th, 6th passes, the API 5L X65 steel pipe and the Alloy 625 cladding. The indentations were made using a 100 gf load with spacing between indentations of 300 μm, to give a good spatial resolution. Figure 8-17 shows the

microhardness mapping of a welded joint. The scale bar adopted was restricted to 250 – 400 HV.

Figure 8-17. Microhardness map of the welded joint, evaluating the 2nd, 3rd, 4th, 5th, 6th passes and the API 5L X65 steel pipe.

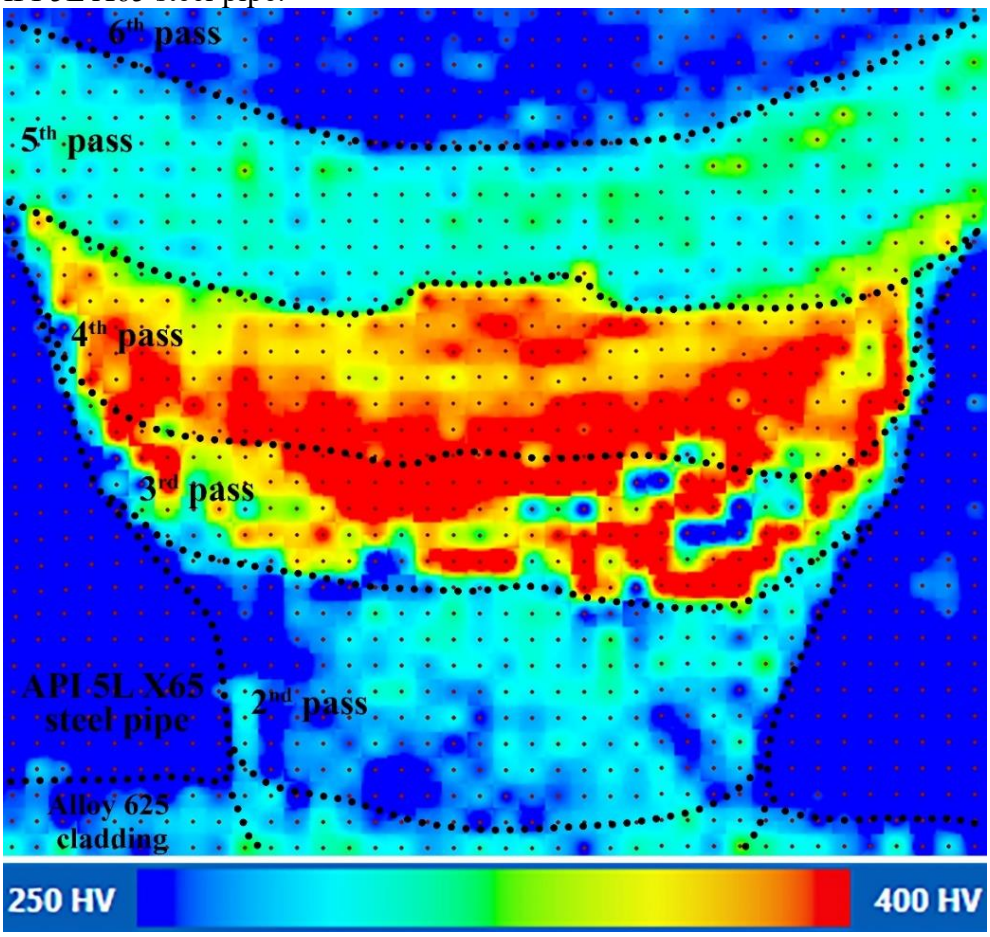

Source: Developed by the author.

The API 5L X65 steel pipe showed a microhardness below 250 HV. This result is expected for HSLA steels, which commonly achieve good mechanical properties by thermomechanical processes, and give a microstructure with low hardness. The Alloy 625 cladding showed a microhardness of approximately 285 HV and, a similar result was observed for 2nd pass of the welded joint.

The 3rd and 4th passes presented the highest hardness levels of the welded joints. Nonetheless, the 3rd pass had different regions with low and high hardness. In some regions of the 3rd pass a microhardness similar to that found in API 5L X65 steel pipe was obtained. Probably these regions a softer martensite due to the high concentration of Ni from the dilution with the 2nd pass, while the harder regions are rich in LAS filler metal. On the other hand, the 4th pass showed a microhardness varying from 350 to 400 HV. The reduction of Ni caused a

strong effect on hardenability by quenching and consequently in microhardness of the 4th pass, increasing the hardness considerably.

Usually, the Ni addition has a strong impact of microstructure and mechanical properties, as well. Zeng[69] investigated Ni effect in hardness of Fe-Ni alloys with different Ni contents: 1.8, 3.7, 5.5, 7.6 and 31 wt%. The huge addition of Ni not affected the microhardess, that kept stable in approximately 260 HV, even for Fe-31Ni, since carbon content in alloys was very low, smaller than 0.002 wt%. The author also highlight that compared to Fe-C system, the addition of approximately 0.1 wt% of C increase the hardness from 259.7 HV to 380 HV. A hypothesis to explain this behavior is about dislocations density into lath martensite. According to Morito[70], in some cases, the Fe-C system has dislocation density an order of magnitude bigger than Fe-Ni system. Theses discussion made evident that C has a bigger effect in hardness than solid solution strengthening caused by Ni.

The 5th pass of a welded joint was considerably affected by dilution with the previous passes diluted with the Alloy 22, in terms of hardness. The microhardness obtained for this weld pass was approximately 285 HV, the same hardness level presented by Alloy 22 on the 2nd pass of the welded joint. This reduction corroborates with bainitic matrix observed in Figure 8-13. The 6th pass also showed a reduction in microhardness. It was obtained a microhardness similar to that shown by the API 5L X65 steel pipe.

A hardness profile was made to obtain a general view of the hardness of each weld pass of the welded joint. Indentations were made using a 10 kgf load with a distance of 1 mm between them. The hardness profile started at the first weld pass and finished at the last weld pass of the welded joint. All results are displayed in Figure 8-18.

The 1st and 2nd weld passes showed an average hardness of approximately 264 HV. This result is compatible with austenitic Ni-based alloys. The 3rd and 4th passes exhibited the hardest weld passes of the welded joint, on average about 391 HV and 367 HV, respectively. These passes showed a microstructure of martensite with A_{ret} particles, especially for 4th weld pass. The high incorporation of the alloying elements from the dilution with the 2nd Alloy 22 pass caused a hardening by quenching, considering the microstructure was mainly formed by diffusionless solid transformation. Following the same tendency, the 5th weld pass exhibited a hardness of about 304 HV, which corroborates with bainitic microstructure. Again, the dilution effect of the previous weld passes caused a slight increase of alloying elements such as Ni, Cr and Mo in the 5th weld pass, which affected directly the microstructure and hardness as well. Nonetheless, the dilution effect of the 2nd Alloy 22 pass was drastically reduced from the 6th weld pass onward, which showed an average of approximately 247 HV. This result corroborates

with the 10th weld pass microstructure, which displayed an acicular ferrite matrix with MA microconstituent particles.

Figure 8-18. Hardness profile of the welded joint.

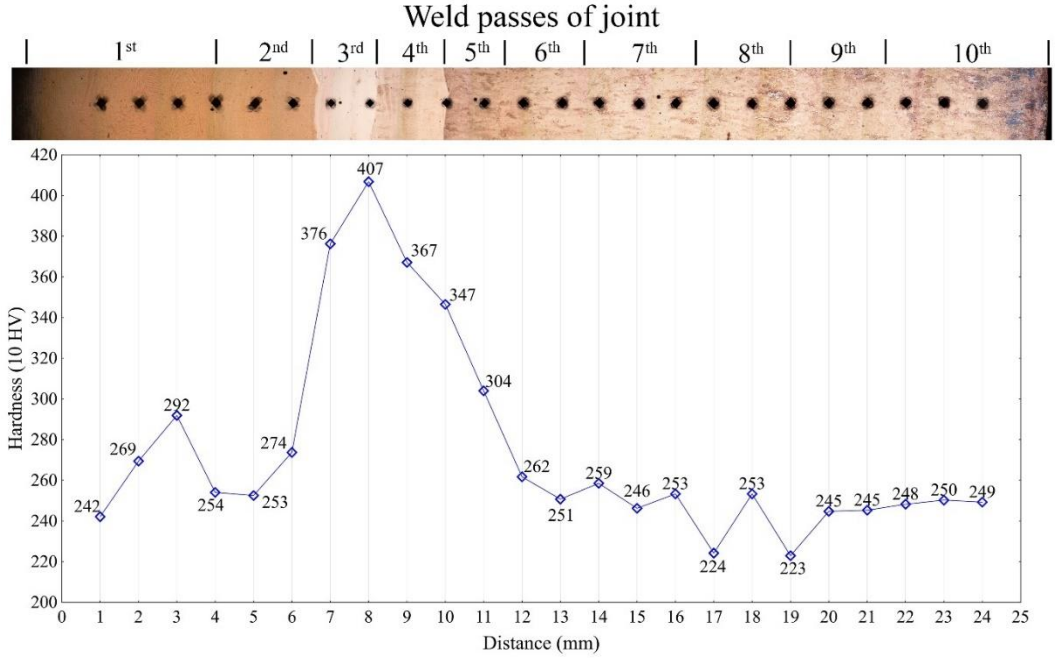

Source: Developed by the author.

The hardness profile highlighted how complex this dissimilar welded joint is. There are macro regions essentially different in terms of microstructure, hardness and certainly in other mechanical properties like yield strength, toughness, fatigue among others. Thus, care is necessary when evaluating specific regions or weld passes, without taking into account the general behavior of the welded joint. In the case of this hardness evaluation, the hardest passes represented approximately 13% of the wall thickness of the steel pipe, that were confined between soft weld passes.

8.4.3.4 Impact toughness

Another important mechanical property of welded joints that must be evaluated is the impact toughness. Therefore, the impact toughness of the most critical regions of the welded joint, the 100S-G steel passes of the highest dilution with the 2nd Alloy 22 weld pass were evaluated. In this case, the notch was positioned at the 3rd weld pass for Charpy-V specimen, assessing the impact toughness from the 3rd weld pass of the welded joint onward in the same direct as a normal weld vector. Moreover, another condition with the notch positioned at the 7th

weld pass was evaluated. This region represents the ferritic portion of the welded joint and is important to provide information to give a general conclusion about the toughness of the joint.

The fractography of the Charpy-V specimens after the tests are shown in Figures 8-19a and 8-19b. In all cases the samples showed a brittle fracture characteristic, except for condition which notch was postioned at 3rd pass, where a small matte surface region was observed. This suggest that a ductile fracture occurred on the 3rd pass. Figure 8-19c shows a microstructure overview of one specimen with assessed with notch at 3rd pass. More details are shown in Figures 8-19d and 8-19e. There was a difference between the 3rd and 4th passes. The high dilution pass showed a ductile fracture with shallow dimples, there were a few dispersed cleavage fracture regions and evidences of shrink porosity. While the 4th pass showed a cleavage fracture in full weld pass. From the 4th pass onward, all passes had a brittle fracture aspect.

Figure 8-19. The Charpy-V samples after the tests. Macrograph of a) notch in the 3rd pass and b) notch in the 7th pass samples. Micrography of c) 3rd pass samples highlighting fracture features.

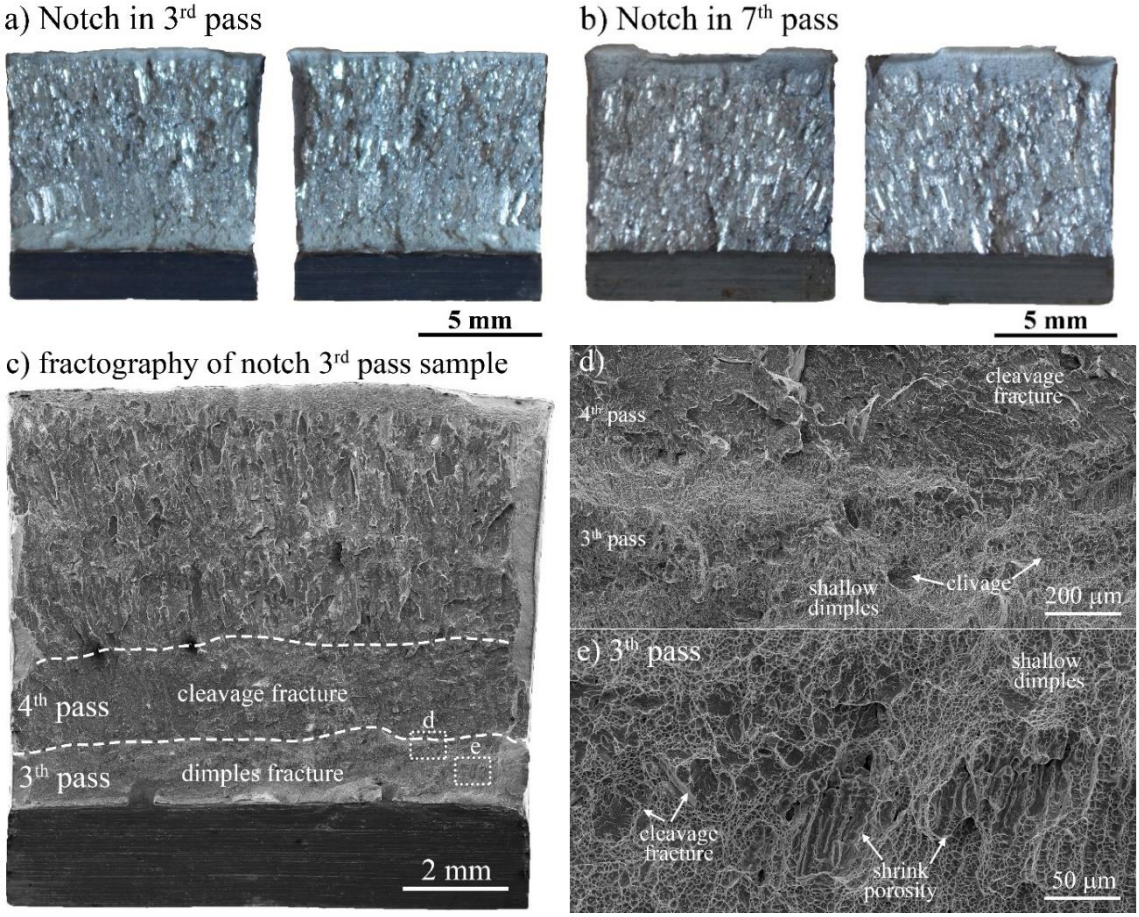

Source: Developed by the author.

Table 8-4 gives the average impact toughness of all specimens evaluated. All results were obtained at -15°C. A low toughness was observed in all cases, especially for the notch

conditions of the 7th pass, where the microstructure and chemical compositions of this region were basically constituted by the 100S-G steel. Probably the test, at -15°C, exceeded the DBTT for this weld metal. On the other hand, the 3rd weld pass condition showed an impact toughness relatively better, as it was strongly influenced by the high dilution with the Ni-based alloy. Probably, the high Ni incorporation from the dilution with Alloy 22 improved the local toughness, considering the soft regions observed on the microhardness map (Figure 8-17).

Table 8-4. The average impact toughness of the welded joint with the notch positioned on the 3rd and 7th passes.

Impact toughness of welded joint (J)	
Notch on 3rd pass	45.8 ± 1.3
Notch on 7th pass	14.3 ± 1.3

Source: Developed by the author.

Several studies have been performed in order to comprehend the Ni effect in mechanical properties of steels[69,71,72]. Kim *et al*.[72] evaluated the Ni addition effect on toughness of 9%Ni steel. The authors introduced pure Ni wires during welding 9%Ni steel plates, in order to increase the Ni content in fusion zone. It was observed a great improvement of impact toughness from 45 J for common 9%Ni steel to 118 J for 16.6 wt% of Ni experimental steel, at -196°C. The authors not considered the effect of Ni distributed into martensite, since probably has a bigger effect in toughness[70,73] than A_{ret}, that transformants in a hard martensite when submitted to stress.

Zeng[69] investigating Fe-Ni alloys with less than 0.002 wt% C and concluded that the Ni addition caused the refining of blocks and sub-blocks of hierarchy of martensite. A possible explanation for such phenomenon is related to competition of both martensite and austenite to strain accommodation may lead to refinement of block and, the Ni addition also cause the Ms decrease, in turns, cause the strengthening of martensite and austenite in different degrees, which cause the block refining.

In fact, the massive addition of Ni in 3rd weld pass as consequence of dilution with Alloy 22 provided this ductile aspect observed, increasing the energy absorbed. Probably, the toughness could be better, if carbon content in weld pass was lower than 0.002 wt%. The same can be attributed for behavior of 4th and 5th weld passes, since they exhibited a brittle feature. About very low impact toughness showed by LAS weld passes that virtually diluted only with steel pipe some aspect must be considered. The chemical composition of 100S-G steel has a great addition of Mn in comparison with Ni, 1.37 wt% and 0.82 wt%, respectively. The dilution with steel pipe causes the reduction of both Mn and Ni, but the Ni drop is higher, since there

1.17 wt% Mn and 0.38 wt% Ni in API 5L X65 steel used. According to Tanaka *et al*.[71], the addition of 2 wt.% of Ni in a low carbon steel causes a significant reduction of the DBTT, while the addition of 1 wt.% of Ni for the same low carbon steel showed a negligible effect when compared with a steel without the addition of Ni. Therefore, this may explain the unexpected result for impact toughness.

Another point to be considered is the presence of the MA microconstituents in the weld metal. According to the results from Akselsen *et al*.[74] an MA fraction greater than 6% results in serious degradation of toughness. The microsegregation processes of some elements under solidification, such as carbon, and the short-range diffusion during phase transformation have been shown to produce local chemical inhomogeneity, which leads to carbon-enriched grain boundary austenite and subsequently increases in hardenability. Zhu *et al*.[75] observed an increase in hardness in the intercritically reheated coarse-grained heat-affected zone for an API X70 steel pipe, which was attributed to the formation of blocky MA islands at the prior austenite grain boundaries. Since, the welded joint evaluated in this study was performed using a LAS filler metal by multiple passes, the reheating could also affect the MA precipitation in weld metal.

In addition, Zhu *et al*.[75] found that the steels they evaluated exhibited extremely low Charpy impact energies at −20 °C. The authors associated this result with the formation of the blocky grain boundary MA microconstituents along the prior austenite grain boundaries. Other studies performed by Moeinifar *et al*.[76] and Davis & King[77] have associated the presence of blocky M-A microconstituents along the prior austenite grain boundaries with cleavage fracture initiation and propagation of brittle fractures. Similarly, Avila and co-workers[78] associated the roles of MA particles, and bainite packets in the initiation and propagation of cleavage fractures in the hard zone at −40 °C.

8.4.3.5 Fracture toughness

Four single edge notched tension (SENT) tests was performed to evaluate the 3rd weld pass of the welded joint in terms of uniaxial quasi-static tensile load. Two samples were assessed as-welded, while the other two samples were evaluated after a heat treatment at 580°C for 1h.

The CTOD results in terms of force versus crack open displacements (COD) are shown in Figure 8-20. Similar to that observed for the impact toughness results, the samples showed a brittle feature, considering the abrupt collapse presented. A very small stable crack

propagation followed by a pop-in and subsequent collapse was observed for all tested samples. Probably a stable crack propagation occurred on the 3rd weld pass, considering the better impact toughness in comparison with the 100S-G steel passes (Table 8-4). In addition, probably the pop-ins were related to cleavage regions and eventually shrink porosities within the 3rd weld pass. A few shrink porosities were observed in this sample, especially at the solidification interface between the 2nd and the 3rd weld passes, located in the pre-crack region (Figure 8-21).

Figure 8-20. CTOD tests performed at -15°C with the pre-crack positioned in the 3rd weld pass. Conditions: a) as-welded and b) after heat treatment at 580°C for 1 h.

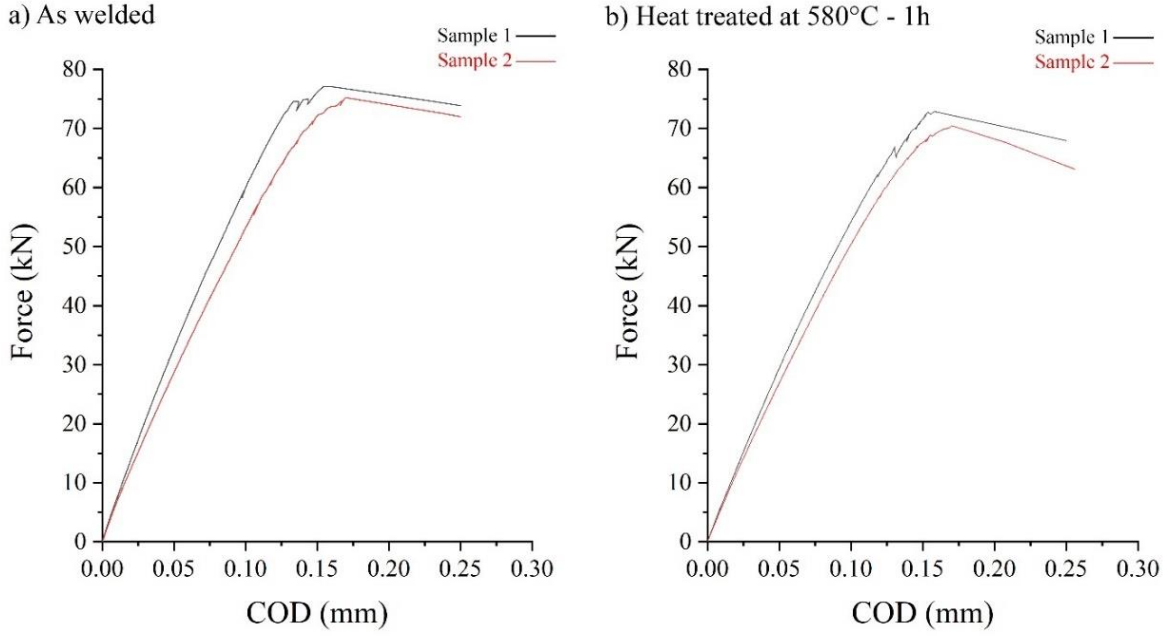

Source: Developed by the author.

The heat treatment at 580°C for 1h did not show any relevant effect on the fracture toughness. The same characteristic was observed in this case, since only a small region with stable crack propagation before catastrophic collapse was observed. The differences in comparison to the as-welded condition could be attributed to the 3rd weld pass area, reminiscent to crack propagation during the tests. Normally, the pre-crack grew more easily at the center of the sample than at the edges. This reduce the 3rd weld pass area able to provide a stable crack propagation during the tests. However, it is not possible to guarantee exactly the same conditions between samples. Figure 8-22 shows details of the fracture surface morphology of regions observed after the CTOD test, in which the pre-crack, the stable crack propagation region and the region where the brittle collapse started were observable.

Figure 8-21. CTOD microstructure highlighting a) pre-crack, 2nd, 3rd, 4th passes, stable crack propagation region and b) shrink porosity.

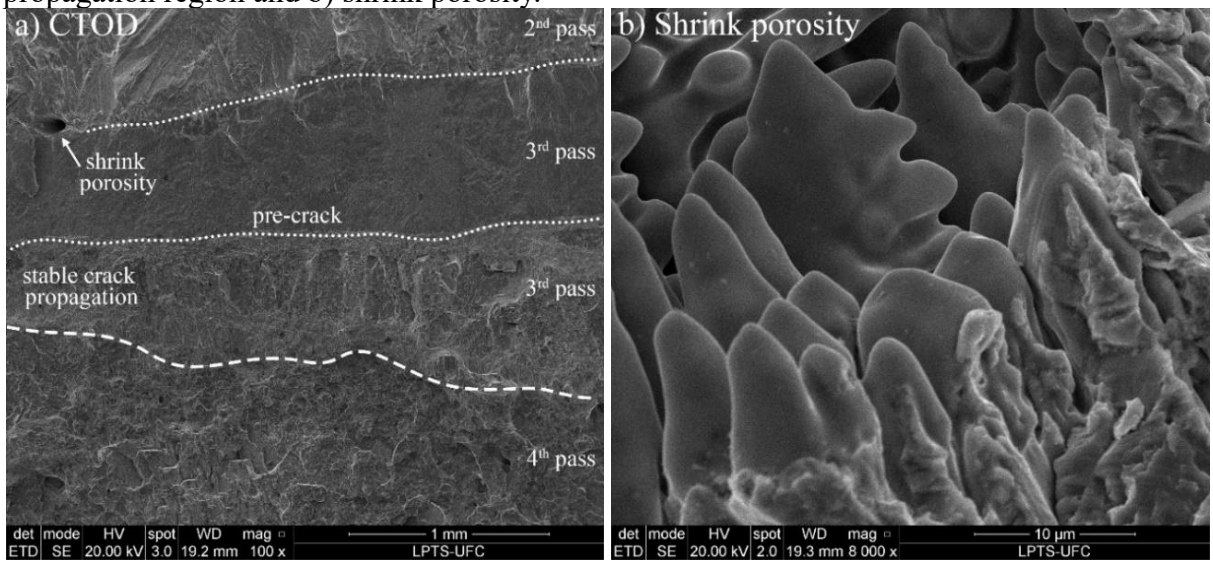

Source: Developed by the author.

Figure 8-22. Macrograph of CTOD samples tested after heat treatment at 580°C for 1h.

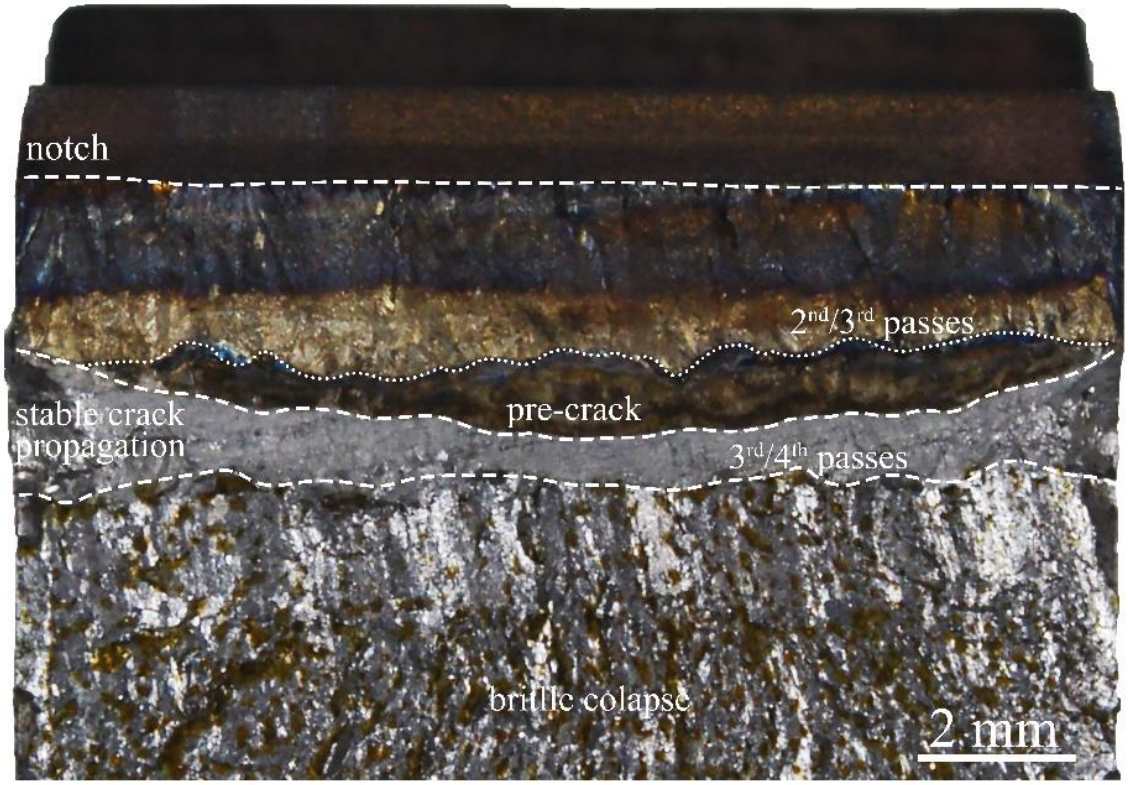

Source: Developed by the author.

8.5 Conclusion

Based on results discussed in the present study entitled “Novel approach for dissimilar girth welding of API 5L X65 steel pipe with an internal Alloy 625 cladding using Alloy 22 and low alloy steel as the filler metals”, it was concluded that:

- The novel approach for dissimilar girth welding of risers with internal Alloy 625 claddings using Alloy 22 for the root and hot passes and 100S-G steel to fill the joint successfully produced a welded joint without any solidification cracking.
- The YS of the welded joint attended the overmatched requirement for a weld joint with API 5L X65, X70 and X80 steels for a pipeline to be installed by the reel-lay process. For S-lay and J-lay, the welded joint also attend the minimum YS required for joints with API 5L X90.
- The dissimilar welding of API 5L X65 steel, Alloy 22 and 100S-G steels produced different materials in each weld pass of the welded joint. The Nickel-based alloy passes showed an γ-FCC matrix, while the first two 100S-G steel passes exhibited a martensitic matrix with Aret and carbides. A banitic matrix with martensite and MA was characterized for third 100S-G steel weld pass. The others LAS weld passes showed an acicular ferrite matrix with MA particles.
- The impact toughness at -15°C of the 100S-G steel pass that was diluted with Alloy 22 showed approximately 46 J of energy absorbed, while the 100S-G pass with a negligible dilution of the Alloy 22 pass showed a poor result, which was typical of a steel assessed at a temperature that exceeded its DBTT. The CTOD confirmed this phenomenon, considering the cleavage fracture from the 4^{th} weld pass onward, while the 3^{rd} weld pass exhibited a ductile fracture due to a greater concentration of Ni.

REFERENCES

1 SHARMA, S. K.; MAHESHWARI, S. A review on welding of high strength oil and gas pipeline steels. **Journal of Natural Gas Science and Engineering**, v. 38, p. 203-217, 2017.

2 SARZOSA, D. F. B. *et al*. Fracture resistance testing of dissimilar nickel–chromium girth welds for clad line pipes. **International Journal of Fracture**, v. 205, n. 2, p. 169-188, 2017.

3 AMERICAN PETROLEUM INSTITUTE. API specification 5L: **Specification for Line Pipe**. Washington. p. 180. 2013.

4 HASHEMI, S. H. Strength-hardness statistical correlation in API X65 steel. **Materials Science and Engineering: A**, v. 528, n. 3, p. 1648-1655, 2011.

5 SAMI, Z.; TAHAR, S.; MOHAMED, H. Microstructure and charpy impact properties of ferrite-martensite dual phase API X70 linepipe steel. **Materials Science and Engineering: A**, v. 598, p. 338-342, 2014.

6 BAEK, J. *et al*. Effects of pre-strain on the mechanical properties of API 5L X65 pipe. **Materials Science and Engineering: A**, v. 527, n. 6, p. 1473-1479, 2010.

7 MORALES, E. V *et al*. Strengthening mechanisms in a pipeline microalloyed steel with a complex microstructure. **Materials Science and Engineering: A**, v. 585, p. 253-260, 2013.

8 JU, J.-B.; KIM, W.; JANG, J. Variations in DBTT and CTOD within weld heat-affected zone of API X65 pipeline steel. **Materials Science and Engineering: A**, v. 546, p. 258-262, 2012.

9 ZHOU, P. *et al*. Effect of welding heat input on grain boundary evolution and toughness properties in CGHAZ of X90 pipeline steel. **Materials Science and Engineering: A**, v. 722, p. 112-121, 2018.

10 ZHU, Z. *et al*. Effect of inter-critically reheating temperature on microstructure and properties of simulated inter-critically reheated coarse grained heat affected zone in X70 steel. **Materials Science and Engineering: A**, v. 605, p. 8-13, 2014.

11 DUPONT, J. N.; BABU, S.; LIU, S. Welding of materials for energy applications. **Metallurgical and Materials Transactions A**, v. 44, n. 7, p. 3385-3410, 2013.

12 SILVA, C. C. *et al*. Evaluation of the Corrosion Resistant Weld Cladding Deposited by the TIG Cold Wire Feed Process. **Materials Science Forum**, v. 783-786, p. 2822–2827, 2014.

13 MOHAMMADI ZAHRANI, E.; ALFANTAZI, A. M. Hot Corrosion of Inconel 625 Overlay Weld Cladding in Smelting Off-Gas Environment. **Metallurgical and Materials Transactions A**, v. 44, n. 10, p. 4671-4699, 2013.

14 MINÁ, É. M. *et al*. The Effect of Dilution on Microsegregation in AWS ER NiCrMo-14 Alloy Welding Claddings. **Metallurgical and Materials Transactions A: Physical Metallurgy and Materials Science**, v. 47, n. 12, 2016.

15 DUPONT, J. N. Solidification of an alloy 625 weld overlay. **Metallurgical and Materials Transactions A**, v. 27, n. 11, p. 3612-3620, nov. 1996.

16 SILVA, C. C. *et al*. New insight on the solidification path of an alloy 625 weld overlay. **Journal of Materials Research and Technology**, v. 2, n. 3, p. 228-237, 2013.

17 DAI, T.; LIPPOLD, J. Characterization of the Interface of an Alloy 625 Overlay on Steels Using Nanoindentation. **Journal of Materials Engineering and Performance**, v. 27, n. 7, p. 3411-3418, 2018.

18 BELTRAO, R. L. C. *et al*. SS: Pre-salt Santos basin - challenges and new technologies for the development of the pre-salt cluster, Santos basin, Brazil. *In*: OFFSHORE TECHNOLOGY CONFERENCE, 2009, Houston. **Procedings**. Houston: Offshore Technology Conference, 2009. p. 1-11.

19 SILVA, C. C. *et al*. Austenitic and ferritic stainless steel dissimilar weld metal evaluation for the applications as-coating in the petroleum processing equipment. **Materials & Design**, v. 47, p. 18, 2013.

20 SUN, Z.; ION, J. C. Laser welding of dissimilar metal combinations. **Journal of Materials Science**, v. 30, n. 17, p. 4205-4214, 1995.

21 BALDRIDGE, T. *et al*. Laser cladding of Inconel 690 on Inconel 600 superalloy for corrosion protection in nuclear applications. **Optics and Lasers in Engineering**, v. 51, n. 2, p. 180-184, 2013.

22 SILVA, C. C. *et al*. A Study on the Effect of the Interpass Temperatures in Properties and Microstructures of the Alloy 625 Dissimilar Fusion Zone. **Materials Science Forum**, v. 783-786, p. 2816-2821, 2014.

23 SARAIVA, D. L. *et al*. Application of low Ms temperature consumable to dissimilar welded joint. **Materials Science and Technology**, v. 30, n. 9, p. 1057-1062, jul. 2014.

24 KOURDANI, A.; DERAKHSHANDEH-HAGHIGHI, R. Evaluating the properties of dissimilar metal welding between Inconel 625 and 316L stainless steel by applying different welding methods and consumables. **Metallurgical and Materials Transactions A**, v. 49, n. 4, p. 1231-1243, 2018.

25 SAEDI, A. H.; HAJJARI, E.; SADROSSADAT, S. M. Microstructural characterization and mechanical properties of TIG-welded API 5L X60 HSLA steel and AISI 310S stainless steel dissimilar joints. **Metallurgical and Materials Transactions A**, v. 49, n. 11, p. 5497-5508, 2018.

26 SILVA, C. C. *et al*. Assessment of microstructure of alloy Inconel 686 dissimilar weld claddings. **Journal of Alloys and Compounds**, v. 684, p. 628-642, 2016.

27 BASTOLA, A. *et al*. Investigation on the strain capacity of girth welds of X80 seamless pipes with defects. **Engineering Fracture Mechanics**, v. 180, p. 348-365, 2017.

28 JONES, R. L. *et al*. Reeled clad SCR weld fatigue qualification. *In*: OFFSHORE TECHNOLOGY CONFERENCE, 2011, Houston. **Proceedings**. Houston: Offshore Technology Conference, 2011. p 1-13.

29 SOUZA, R. F.; RUGGIERI, C. Fracture assessments of clad pipe girth welds incorporating improved crack driving force solutions. **Engineering Fracture Mechanics**, v. 148, p. 383-405, 2015.

30 CHONG, T.-V. S. *et al*. Effects of elevated temperatures on the mechanical properties of nickel-based alloy clad pipelines girth welds. **Engineering Fracture Mechanics**, v. 152, p. 174-192, 2016.

31 LIN, S. *et al*. Effect of cyclic plastic deformation on microstructure and mechanical

properties of weld metals used for reel-lay pipeline steels. **Materials Science and Engineering: A**, v. 737, p. 77-84, 2018.

32 CROSS, C. E. On the origin of weld solidification cracking. *In*: BÖLLINGHAUS, T.; HEROLD, H. **Hot Cracking Phenomena in Welds**. Heidelberg: Springer Berlin Heidelberg, 2005. p. 3-18.

33 SMITH, S. N.; CLOUGH, T. Deepwater Pipeline Installation by Reel-lay Method. *In*: OFFSHORE TECHNOLOGY CONFERENCE, 2010, Houston. **Proceedings**. Houston: Offshore Technology Conference, 2010. p 1-12.

34 DNVGL. DNVGL ST F101: **Submarine Pipeline Systems**. Oslo. p. 520. 2017.

35 LIPPOLD, J. C. *et al*. Weld solidification cracking in solid-solution strengthened ni-base filler metals BT. *In*: BÖLLINGHAUS, T. *et al*. **Hot Cracking Phenomena in Welds II**. Heidelberg: Springer Berlin Heidelberg, 2008. p. 147-170.

36 CIESLAK, M. J.; HEADLEY, T. J.; FRANK, R. B. Welding metallurgy of custom age 625 PLUS alloy. **Welding Journal (Miami, Fla)**, v. 68, n. 12, p. 473s-482s, 1989.

37 CIESLAK, M. J. The welding and solidification metallurgy of Alloy 625. **Welding Journal**, v. 70, n. 2, p. 49–56, 1991.

38 AGARWAL, D. C.; HERDA, W. R. The "C" family of Ni-Cr-Mo alloys' partnership with the chemical process industry: The last 70 years. **Materials and Corrosion**, v. 48, n. 8, p. 542-548, ago. 1997.

39 SRIDHAR, N.; WU, J. B. C.; MANNING, P. E. Corrosion Resistant Ni-Cr-Mo Alloys. **JOM**, v. 37, n. 11, p. 51-53, 1985.

40 JAKUPI, P. *et al*. Corrosion product analysis on crevice corroded Alloy-22 specimens. **Corrosion Science**, v. 53, n. 5, p. 1670-1679, 2011.

41 LLOYD, A. C. *et al*. Cr, Mo and W alloying additions in Ni and their effect on passivity. **Electrochimica Acta**, v. 49, n. 17, p. 3015-3027, 2004.

42 AMERICAN WELDING SOCIETY. AWS A5.28/A5.28M: **Specification for Low-Alloy Steel Electrodes and Rods for Gas Shielded Arc Welding**. Miami. p. 40. 2015.

43 DNVGL. DNVGL RP F108. **Assessment of flaws in pipeline and riser girth welds**. Oslo. p. 130. 2017.

44 LIPPOLD, J. C. Centerline cracking in deep penetration electron beam welds in type 304L stainless steel. **Welding Journal (Miami, Fla)**, v. 64, n. 5, p. 127s-136s, 1985.

45 SUN, Y. *et al*. Characterization and formation mechanism of periodic solidification defects in deep-penetration laser welding of NiCrMoV steel with heavy section. **The International Journal of Advanced Manufacturing Technology**, v. 100, n. 9, p. 2857-2866, 2019.

46 WHEELING, R. A.; LIPPOLD, J. C. Characterization of weld metal microstructure in a Ni-30Cr alloy with additions of niobium and molybdenum. **Materials Characterization**, v. 115, p. 97-103, 2016.

47 CIESLAK, M. J.; HEADLEY, T. J.; ROMIG, A. D. The welding metallurgy of HASTELLOY alloys C-4, C-22, and C-276. **Metallurgical Transactions A**, v. 17, n. 11, p. 2035–2047, nov. 1986.

48 DE ALBUQUERQUE, V. H. C. *et al*. Automatic evaluation of nickel alloy secondary phases from SEM images. **Microscopy Research and Technique**, v. 74, n. 1, p. 36-46, jan. 2011.

49 MINÁ, É. M. *et al*. Efeito da diluição sobre a microestrutura da liga AWS ERNiCrMo-14 na soldagem de revestimentos pelo processo TIG com alimentação de arame frio. **Soldagem & Inspeção**, v. 21, n. 3, p. 317-329, 2016.

50 MINÁ, É. M. *et al*. Electron detection modes comparison for quantification of secondary phases of Inconel 686 weld metal. **Materials Characterization**, v. 133, p. 10–16, nov. 2017.

51 MINÁ, E. M. *et al*. Effect of dilution on the microstructure of AWS ERNiCrMo-14 alloy in overlay welding by the TIG process with cold wire feed. **Welding International**, v. 32, n. 2, p. 130-138, 2018.

52 HODGE, F. G. The history of solid-solution-strengthened Ni alloys for aqueous corrosion service. **JOM**, v. 58, n. 9, p. 28-31, 2006.

53 GALLAGHER, M. L.; LIPPOLD, J. Weld cracking susceptibility of alloy c-22 weld-metal. In: BÖLLINGHAUS, T.; LIPPOLD, J.; CROSS, C. E. **Hot Cracking Phenomena in Welds III**. Heidelberg: Springer, Berlin, Heidelberg, 2011. p. 367-391.

54 RAMIREZ, A. J.; LIPPOLD, J. C. High temperature behavior of Ni-base weld metal: Part I. Ductility and microstructural characterization. **Materials Science and Engineering: A**, v. 380, n. 1, p. 259-271, 2004.

55 RAMIREZ, A. J.; LIPPOLD, J. C. High temperature behavior of Ni-base weld metal: Part II – Insight into the mechanism for ductility dip cracking. **Materials Science and Engineering: A**, v. 380, n. 1, p. 245-258, 2004.

56 RAMIREZ, A. J.; LIPPOLD, J. C. New insight into the mechanism of ductility-dip cracking in Ni-base weld metals. *In*: **Hot Cracking Phenomena in Welds**. Heidelberg: Springer Berlin Heidelberg, 2005. p. 19–41.

57 YANG, Y. K.; KOU, S. Macrosegregation in Cu–30Ni welds made with dissimilar filler metals. **Science and Technology of Welding and Joining**, v. 13, n. 4, p. 318-326, maio 2008.

58 YANG, Y. K.; KOU, S. Fusion-boundary macrosegregation in dissimilar-filler metal Al-Cu welds. **Welding Journal (Miami, Fla)**, v. 86, n. 11, p. 331s-339s, 2007.

59 KOU, S.; YANG, Y. K. Fusion-boundary macrosegregation in dissimilar-filler welds. **Welding Journal (Miami, Fla)**, v. 86, n. 10, p. 303-312, 2007.

60 YANG, Y. K.; KOU, S. Mechanisms of macrosegregation formation near fusion boundary in welds made with dissimilar filler metals. **Materials science and technology - association for iron and steel technology**, v. 5, p. 3201, 2007.

61 YANG, Y. K.; KOU, S. Macrosegregation mechanisms in arc welds made with dissimilar filler metals. **Science and Technology of Welding and Joining**, v. 15, n. 1, p. 1530, jan. 2010.

62 ANDREWS, K. W. The calculation of transformation temperatures and austenite-ferrite equilibria. in steels. **Journal of the Iron and Steel Institute**, v. 184, p. 414-427, 1956.

63 KRAUSS, G. Martensite in steel: strength and structure. **Materials Science and Engineering: A**, v. 273–275, p. 40–57, 1999.

64 SHIUE, R. K.; LAN, K. C.; CHEN, C. Toughness and austenite stability of modified 9Cr-1Mo welds after tempering. **Materials Science and Engineering: A**, v. 287, n. 1, p. 10-16, 2000.

65 YANG, H.-S.; BHADESHIA, H. K. D. H. Austenite grain size and the martensite-start temperature. **Scripta Materialia**, v. 60, n. 7, p. 493-495, 2009.

66 LIU, J.; KOU, S. Crack susceptibility of binary aluminum alloys during solidification. **Acta Materialia**, v. 110, p. 84-94, 2016.

67 LUNDIN, C.; QIAO, C.; LEE, C. Evaluation of backfilled solidification cracks in austenitic stainless welds in relationship to evaluation of hot cracking. **Welding Journal**, v. 72, p. 321–328, jan. 1993.

68 SILVA, C. C. *et al*. Microstructure, hardness and petroleum corrosion evaluation of 316L/AWS E309MoL-16 weld metal. **Materials Characterization**, v. 60, n. 4, p. 346-352, 2009.

69 ZENG, T. On the martensitic structure and hardness in as-quenched Fe-Ni alloys. **Journal of Alloys and Compounds**, 2017.

70 MORITO, S.; NISHIKAWA, J.; MAKI, T. Dislocation density within lath martensite in Fe-C and Fe-Ni alloys. **ISIJ International**, v. 43, n. 9, p. 1475-1477, 2003.

71 TANAKA, M. *et al*. Effects of Ni and Mn on brittle-to-ductile transition in ultralow-carbon steels. **Materials Science and Engineering: A**, v. 682, p. 370–375, 2017.

72 KIM, S.-H.; KANG, C.-Y.; BANG, K.-S. Weld metal impact toughness of electron beam welded 9% Ni steel. **Journal of Materials Science**, v. 36, n. 5, p. 1197-1200, 2001.

73 MORRIS J.W., J. *et al*. The Limits of Strength and Toughness in Steel. **ISIJ International**, v. 41, n. 6, p. 599-611, 2001.

74 AKSELSEN, O. M.; SOLBERG, J. K.; GRONG, O. Effects of martensite-austenite (M-A) islands on intercritical heat-affected zone toughness of low carbon microalloyed steels. **Scandinavian Journal of Metallurgy**, v. 17, n. 5, p. 194–200, 1988.

75 ZHU, Z. *et al*. The effect of chemical composition on microstructure and properties of intercritically reheated coarse-grained heat-affected zone in X70 steels. **Metallurgical and Materials Transactions B**, v. 45, n. 1, p. 229-235, 2014.

76 MOEINIFAR, S.; KOKABI, A. H.; HOSSEINI, H. R. M. Effect of tandem submerged arc welding process and parameters of Gleeble simulator thermal cycles on properties of the intercritically reheated heat affected zone. **Materials & Design**, v. 32, n. 2, p. 869-876, 2011.

77 DAVIS, C. L.; KING, J. E. Cleavage initiation in the intercritically reheated coarse-grained heat-affected zone: Part I. Fractographic evidence. **Metallurgical and Materials Transactions A**, v. 25, n. 3, p. 563-573, 1994.

78 AVILA, J. A. *et al*. Microstructure and fracture toughness of multipass friction stir welded joints of API-5L-X80 steel plates. **Materials Science and Engineering: A**, v. 673, p. 257-265, 2016.

Chapter 9

Advanced dissimilar welding procedure for HSLA steel pipes internally cladded with Alloy 625 with overmatch requirements: An approach combining the Alloy 686 and low alloy steel as filler metals

9.1 Abstract

The dissimilar welding of steel pipelines with inner claddings of Ni-based alloys is a common practice. However, these welded joints do not assure the strength needed for advanced applications with overmatch requirements. In the present study a dissimilar welding procedure combining the Alloy 686 and AWS ER100S-G steel as the filler metals was developed in order to enhance the mechanical strength of the welded joint for an API 5L X65 steel pipe with internal cladding of Alloy 625. This methodology required the 1st and 2nd weld passes to be made with the 686 Ni-based alloy, and the other weld passes with the low alloy steel. The welded joint did not exhibit any solidification cracks. Furthermore, a greater part of the welded joint exhibited a yield strength that was sufficient to attend the overmatch required to join the API 5L X65, X70 and X80 steels for posterior installation by the reel lay process. The dissimilar welding caused a significant incorporation of Ni in the first 100S-G steel weld pass and thus created a martensitic matrix with retained austenite and TiC. The second and third 100S-G steel passes showed hard martensite and bainite matrixes, with retained austenite (A_{ret}) and martensite-austenite (MA) microconstituents, respectively. Carbides also were observed in both 100S-G steel weld passes. The subsequent weld passes exhibited a soft acicular ferrite (AF) matrix with MA particles. The impact toughness obtained for the dissimilar region of the welded joint with a mixture of 100S-G steel and Alloy 686 was on average 38J, at -15°C, even with the presence of numerous shrink porosities observed at the dissimilar solidification interface.

9.2 Introduction

Weld cladding is a resource used to confer specific characteristics on a base metal[1–5], in order to improve certain desirable properties that are not inherent to the base metal, such as corrosion resistance[6]. This manufacturing process is widely used as a cheaper alternative to enhance the durability of such materials without having to make the whole component with a

corrosion resistant alloy (CRA)[7–10]. In the oil & gas industries, for example, rigid risers for offshore applications are manufactured using steel pipes with internal cladding of a CRA[11]. This combination of materials provides the mechanical resistance necessary to support the forces required and the corrosion resistance needed to maintain the integrity of the component[12–16]. Specifically for risers, the Alloy 625 is frequently used as the CRA cladding, as it can offer significant resistance to corrosion in harsh environments[17–20], whilst maintaining a good cost-benefit[14].

A common practice in joint welding of steel pipes with internal cladding of Alloy 625 is to use the same CRA cladding alloy as a filler metal, in order to avoid metallurgical problems, especially solidification cracks[21–23]. Xu *et al*.[24] developed a welding procedure for cladded pipes with Inconel 625, using AWS ERNiCrMo-3 (Inconel 625) as the filler metal by the GTAW process. The authors described the microstructure and hardness of the cladded layer and the weld metal, as well as their corrosion resistance. However, no data was presented concerning the tensile strength. In another study, the intergranular corrosion behaviors of the welded joints of the X65-Inconel 625 cladded pipe were evaluated[25].

The mixture of different materials may introduce some alloying elements that may or may not be well solubilized by the new solid matrix. This may lead to the segregation of alloying elements that remained liquid and in some cases may reduce the melting of point of remaining liquid, thus starting the formation of solidification cracks. In the case of dissimilar welding between steel and Ni-based alloys, the mixture of alloying elements such as Fe, Si, C, Nb and Mo favor nucleation of low melting point phases like Laves and NbC[26], which are commonly related to the formation of solidification cracks[21]. This procedure solves the weldability problem, on the other hand it reduces the applicability, as it will exhibit properties similar to the CRA alloy.

The method used to install pipelines and risers defines requirements that must be considered in joint welding procedure. The most usual methods for installation are: S-lay, J-lay and reel lay. The S-lay technology is mainly indicated for steel catenary riser installations in shallow to deep waters, while the J-lay technology was developed for deep and ultra-deep water. In addition, J-lay is less susceptible to weather conditions resulting in a better production rate[27]. According to Bruschi *et al*.[28], the limiting factor for S-lay installation in deep waters is the capacity to hold the weight of the long lay span and the ability to bend the pipeline along the stinger. In both S-lay and J-lay methods, the pipelines are assembled and launched by specialized pipelaying vessels (PLV) such as mono-hulls or laybarges, where the joint welding

and the inspection of the welded joints occur. Naturally, the execution of welding procedure on offshore units impairs the productivity and may introduce welding defects.

A lower cost and more productive solution for many enterprises has been the reel-lay method, in which the joint welding of the pipes occurs at an onshore unit; thus increasing the productivity and quality of the manufactured component[29]. Reel-lay installing is recommended for small to medium diameter rigid offshore pipelines in deep and ultra-deep water[30]. The pipeline manufactured is spooled onto a large drum and then transported to the offshore unit, where it is installed during the unspooling step. Nonetheless, the spooling and unspooling steps cause a plastic deformation of about 2% in the component[31]. The technical project to manufacture the pipeline must consider this deformation. Various oil companies are searching for pipeline installation solutions using the reel-lay method[32,33]. In the previous chapter was performed a joint welding of an X65 steel pipe with internal cladding of Alloy 625 using Alloy 625 for the root pass and low alloy steel for the other weld passes to provide the mechanical overmatch. The low alloy steel provided sufficient strength but the combination with Alloy 625 caused the formation of solidification cracks that impaired its performance in impact toughness and in the bending test.

The DNVGL-ST-F101 standard[34] establishes specific criterion for girth welding of pipelines that will be installed by the reel lay process. The standard requires a minimum overmatch of yield strength. The yield strength (YS) of a welded joint must be at least equal to the maximum YS defined for the base metal minus 20 MPa. For example, the welded joint of API 5L X65 steel must be at least 580 MPa. The criterion imposes a technical barrier for the use of other HSLA steels such as API 5L X70, X80 and X90 steels, where a minimum YS of 615 MPa, 685 MPa and 755 MPa, respectively is required. According to Jones *et al.*[21] the joint welding of an API 5L X65 steel using Alloy 625 as the filler metal cannot reach the minimum YS required by DNVGL-ST-F101 standard[34]. The authors highlighted that the YS required is only achieved after the inherent plastic deformation provided by the spooling and unspooling steps, that cause work hardening of the Alloy 625. The DNV classifies this joint welding as ‘partially overmatched’ and, recommends that this assumption is taken into account in the calculations[35]. Clearly, this welding procedure must be improved, especially for welding other HSLA steels.

The ‘simplest’ solution for welding of such components supposes the use of two materials to perform the joint welding. A Ni-based alloy only to weld the CRA cladding region, keeping the corrosion resistance of the component and, a low alloy steel (LAS) to weld the major portion of joint, providing the high strength required. Obviously, this welding procedure

is not so simple, considering the metallurgical problems related to deposition and mixture of LAS with a Ni-based alloy. In the case of Alloy 625, the combination of Fe, Si, C and Nb causes the nucleation of Laves that is known as an important factor in the formation of solidification cracks[17,18,26,36]. So, it is necessary to select another Ni-based alloy to mix with the LAS that has good weldability.

Alloy 686 is a good alternative for Alloy 625 as the filler metal with this new approach for welding a joint of API 5L X65 steel with an internal cladding of Alloy 625. According to previous chapters, no low melting point phases were predicted by the thermodynamic simulation of solidification for the dilution of Alloy 686 with API 5L X65 and AWS ER100S-G steels. Furthermore, Alloy 686 was designed for aggressive corrosive environments, specifically for wet scrubbing of flue gases from coal-fired power stations, where the traditional Ni-based alloys such as 625, C-276, and C-22 were not able to provide the performance necessary[37]. Alloy 686 is considered an alloy from the third generation of solid solution strengthened alloys[37,38], and is a high corrosion resistant alloy due to the massive addition of Cr, Mo and W. Mishra and Shoesmith[39] carried out an electrochemical study, assessing the effect of Cr, Mo and W on crevice corrosion of 625, C-276, C-22, 59 and 686 alloys. In general, Alloy 686 showed the best results, since the high Cr content provided a significant passive layer, while the high Mo content improved the repassivation after crevice propagation and, the combination of Mo + W helped to prevent the initiation of crevice corrosion. The authors ranked the crevice resistance of materials assessed from a generic point of view as: High Cr-Low Mo < Low Cr-High Mo<High Cr-High Mo < High Cr-High Mo+W.

Considering the context and concepts introduced, the present study aimed propose a new approach to perform dissimilar girth welds to manufacture steel catenary risers with internal CRA cladding. The complex dissimilar joint, proposed here, constituted of an API 5L X65 steel pipe with internal cladding of Alloy 625, and the two filler metals that were used to fill the joint were Alloy 686 for the first two weld passes and AWS ER100S-G steel for the other weld passes. The microstructure of each weld bead was evaluated by light and electron microscopy and the mechanical properties of the welded joint were assessed by a uniaxial tensile test, macro and microhardness tests, a bending test and Charpy-V.

9.3 Experimental procedure

A welded joint of an API 5L X65 steel pipe with internal cladding of Alloy 625 was produced. The 1st and 2nd weld passes of the joint were deposited using Alloy 686, in order to

keep the corrosion resistance of the root region at least the same as the CRA cladding. However, from the 3rd weld pass on the low alloy steel AWS ER100S-G was used in order to provide the overmatch of YS required for the reel lay installation process. Figure 9-1 shows a schematic drawing of the proposed welded joint. Table 9-1 gives the chemical composition of the materials used that had been obtained by optical spectroscopy measurements. In the case of the filler metal, weld metal pads were produced following the recommendations of AWS A5.28/A5.28M and A5.11/A5.11M standards[40,41].

Figure 9-1. Schematic drawing of the proposed welded joint.

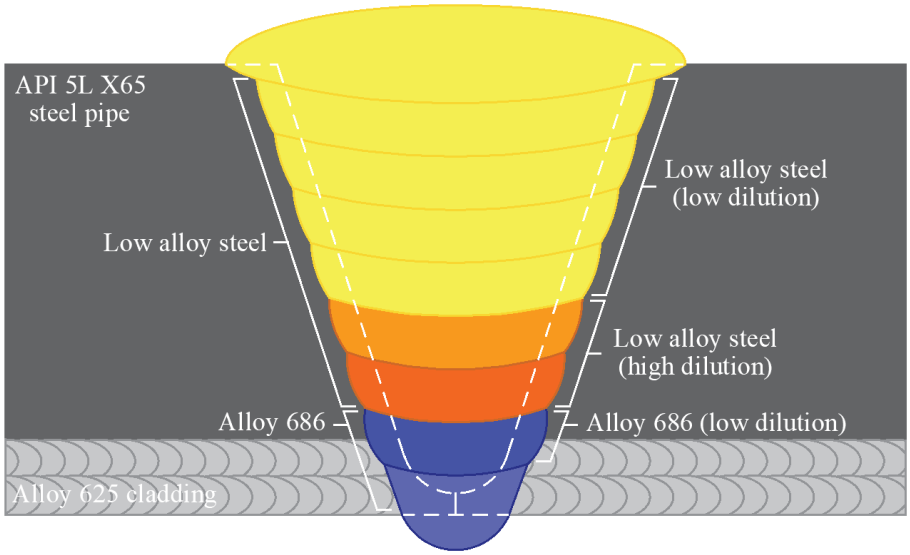

Source: Developed by the author.

Table 9-1. Chemical composition of the materials used in the dissimilar joint welding.

Chemical composition of materials														
Alloy	Al	C	Co	Cr	Cu	Fe	Mn	Mo	Ni	P	S	Si	Ti	W
Alloy 686 (AWS ERNiCrMo-14)	-	0.01	0.05	20.66	-	0.38	0.24	16.40	58.07	0.02	0.015	-	0.06	3.98
API 5L X65 steel pipe	0.04	0.11		0.12	0.18	97.51	1.17	0.14	0.34	0.012	0.004	0.28	-	-
AWS ER100S-G steel	-	0.04		0.12	0.11	96.47	1.37	0.38	0.82	0.055	0.014	0.62	0.13	-

Source: Developed by the author.

The welded joint was manufactured on an industrial robotic workbench with a welding torch. The weldments were performed using the pulsed gas metal arc welding process (GMAW-P). Figure 9-2 shows the workbench used to execute the joint welding. The main weld parameters are shown in Table 9-2. The filler metals used were the AWS ERNiCrMo-14 (Alloy 686) and AWS ER100S-G with 1.1 mm and 1.2 mm of diameter, respectively. Alloy 686 was deposited using pure argon (Ar) as the shield gas, while for the 100S-G steel Ar + 4% CO_2 was used.

Figure 9-2. Industrial robotic workbench with a) a welding torch. The welding torch position b) before and c) after deposition of a welding pass.

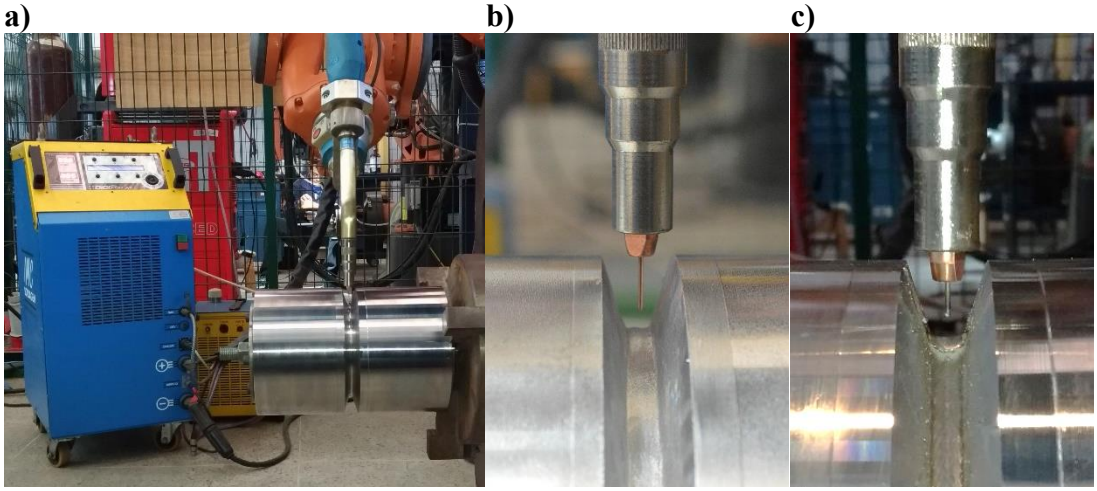

Source: Developed by the author.

Table 9-2. Main welding parameters used for each weld pass.

		Welding parameters								
Passes	Alloy	I_p (A)	I_b (A)	t_p (s)	t_b (s)	S_w (cm/min)	U (V)	S_{wf} (m/min)	A_t (mm)	HI_w (kJ/mm)
1st pass	Alloy 686	300	90	2.2	4.4	45	20.9	7.4	0.6	0.50
2nd pass	Alloy 686	300	90	2.2	4.4	40	21.4	7.2	2.2	0.58
3rd pass	100S-G	300	90	2.2	4.4	35	21.6	5.5	3.7	0.65
4th pass	100S-G	300	90	2.2	4.4	35	20.1	5.5	4.7	0.62
5th pass	100S-G	300	90	2.2	4.4	25	20.2	5.5	5.5	0.88
6th pass	100S-G	300	90	2.2	4.4	18	20.2	5.5	6.0	1.23
7th pass	100S-G	320	100	2.2	4.4	15	21.7	5.8	6.5	1.75
8th pass	100S-G	320	100	2.2	4.4	14	21.9	5.8	7.0	1.75
9th pass	100S-G	320	100	2.2	4.4	13	22.2	5.8	7.5	1.89
10th pass	100S-G	320	100	2.2	4.4	12	22.6	5.8	8.4	2.11

Source: Developed by the author.

Initially, the macrostructure and microstructure of a cross-section of the welded joint were assessed. The sample was prepared following the conventional metallographic steps: cutting, gridding, polishing and etching. In order to reveal the microstructure of the Ni-based weld passes a 10% of chromic acid solution was used, while for the steel weld passes nital 2% was used. The microstructure was investigated using scanning electron microscopy techniques.

The mechanical properties of the welded joint were assessed by the bending, transverse tensile, all-weld tensile, Charpy-V, microhardness and hardness tests. The samples were manufactured following the recommendation of DNVGL-ST-F101 standard[34]. A total of 4 bending, 2 transverse tensile and 5 Charpy-V samples were evaluated. Figure 9-3 shows a schematic drawing of the specimens. The bending sample assessed a full cross-section, including the CRA cladding. The CRA cladding was removed for manufacturing of the

transverse tensile samples. The tip of notch in the Charpy-V samples was positioned in the 3rd weld pass of the welded joint, in other words, from the first weld pass deposited using 100S-G steel.

Figure 9-3. Schematic drawing of specimens: a) bending, b) transverse all-weld tensile, c) transverse tensile and d) Charpy-V with notch at the 3rd weld pass.

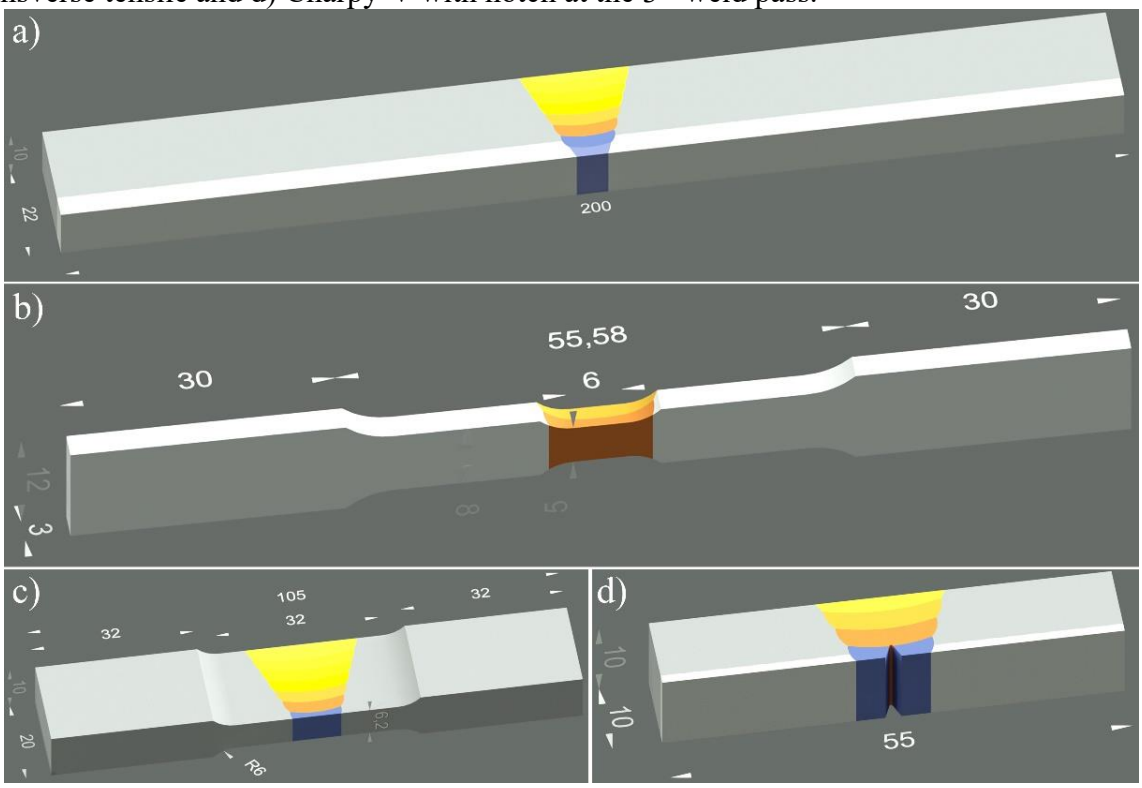

Source: Developed by the author.

The transverse all-weld tensile test evaluated four different regions of the welded joint covering two weld passes each: 1st + 2nd weld passes, 3rd + 4th weld passes, 5th + 6th weld passes and 7th +8th weld passes. Two samples for each condition were assessed. This specific evaluation is proposed by DNVGL-ST-F101 standard[34] in order to obtain the yield strength, tensile strength and elongation of the weld metal.

The microhardness map and hardness profile were performed using 100gf and 10kgf, respectively. The microhardness map was performed for the 2nd to 6th weld passes of the joint, including the API 5L X65 steel pipe and Alloy 625 cladding. A spacing of 300 μm was established between the microindentations. The hardness profile assessed all weld passes of welded joint with 1 mm spacings between indentations.

9.4 Results and Discussion

9.4.1 Weldability of welded joint

In a dissimilar welding, the fusion zone will be a mixture of the two or more materials involved in the manufacturing process. This results in a new material with its specific chemical composition. The microstructure and features of this material, such as corrosion resistance, mechanical properties and weldability will depend on the chemical composition and weld parameters adopted during the welding. Weldability in dissimilar welding is different from similar welding, and does not depend only on the weldability of base and filler metals but on the whole system defined by the welding procedure. In other words, the dissimilar welding of two materials with good weldability does not necessarily lead to the development of a new material with good weldability and the reciprocal is also true.

Beginning our discussion on weldability, Figure 9-4 shows a macrograph of the welded joint manufactured in this work and some micrographs showing the representative structures of the weld passes. These images show that there were no large solidification cracks in the welded joint. In general, the welded joint exhibited good weldability. The deposition and consequent mixture of the Alloy 686 filler metal with the Alloy 625 cladding and steel pipe showed good weldability, because no defects such as large shrink porosities, solidification cracks or lack of fusion were observed. This result was expected, since Alloy 686 and Alloy 625 are of the same Ni-Cr-Mo family and their chemical compositions are similar. The low fraction of steel pipe that melted and mixed to compose the 2nd weld pass did not impair the weldability. In this case, the addition of Fe, Mn, Si, C and other elements present in the X65 steel were well solubilized by the solid matrix phase of this weld pass.

The 3rd weld pass also showed good weldability. The deposition of 100S-G steel on the 2nd Alloy 686 weld pass and steel pipe wall exhibited good wettability. In part, this good wettability was the result of similar welding of 100S-G steel with the groove sidewalls that is composed by steel pipe. The other side of wettability is related to the fusion of the Ni-based weld pass. In general, the Ni-based alloys have a lower melting point in comparison to common steels. Considering the intrinsic physical features of these materials, the arc welding easily melted the Alloy 686 weld pass during deposition of the 100S-G steel, thus preventing weld defects such as a lack of fusion. In fact, the subsequent 100S-G weld passes exhibited good weldability too, since it was deposited on the previous steel weld pass.

Figure 9-4. Macrograph of a transverse cross-section of the welded joint and some microstructures of main weld passes.

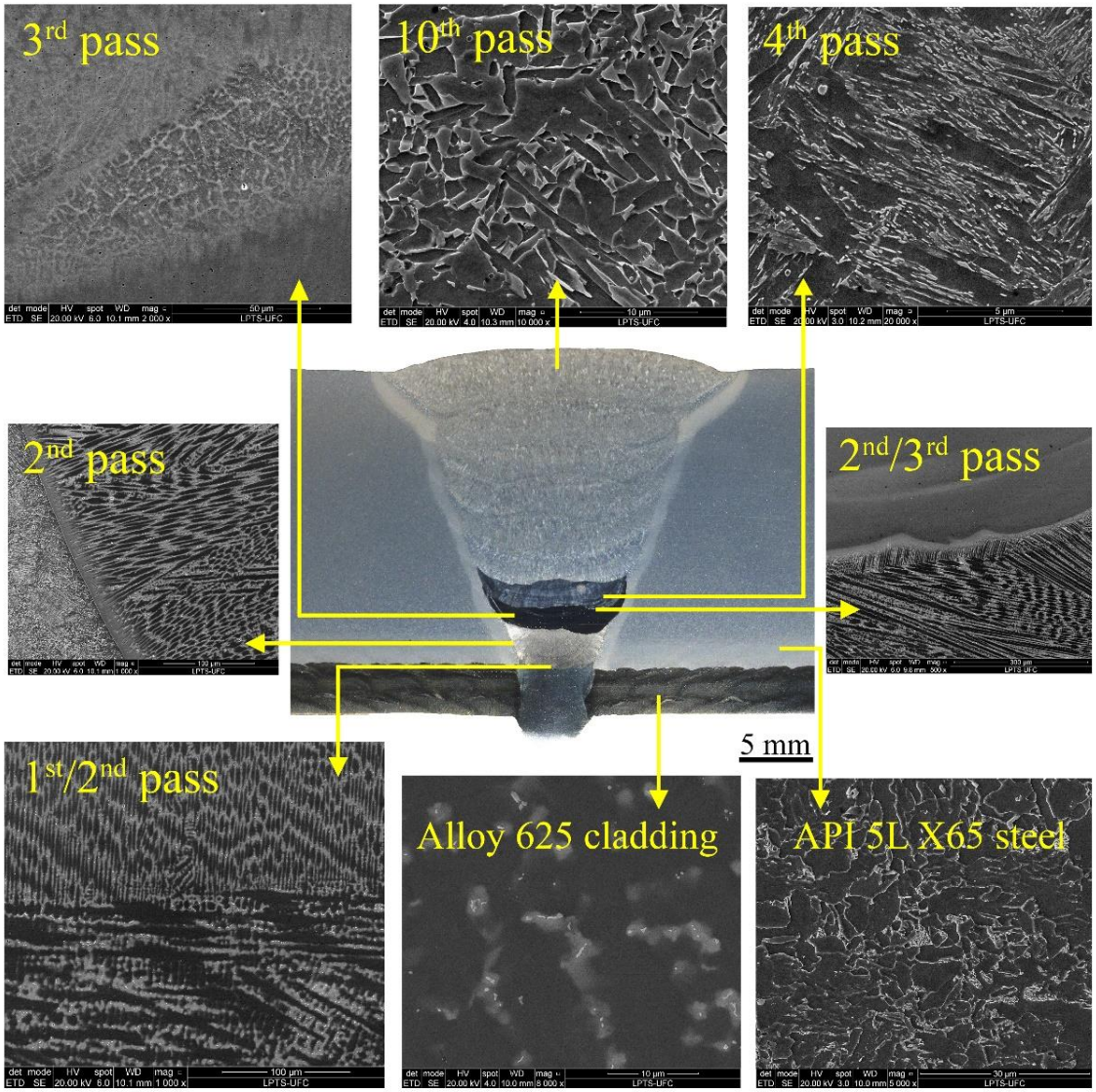

Source: Developed by the author.

Certainly, the metallurgical compatibility of the materials involved was crucial to avoid solidification cracks, especially for the deposition of the first 100S-G steel weld pass. The alloying elements present in Alloy 686 that were incorporated into the 3rd weld pass were well solubilized by the Fe matrix. In other words, the intrinsic segregation of alloying elements during solidification did not cause the nucleation of low melting point phases that, in turn, are directly related to the formation of solidification cracks. Therefore, the selection of Alloy 686 for two first weld passes and consequently to the mixture directly with the first steel pass had an important role to avoid any solidification defects.

Previous chapters that assessed the mixture among Alloy 686, API 5L X65 steel and AWS ER100S-G steel by gave support for the good weldability observed. The thermodynamic

simulation of solidification studies assessed the effect of dilution in two cases. The first study evaluated the deposition of Alloy 686 on API 5L X65 steel, while the second study investigated the deposition of AWS ER100S-G steel on a cladding of Alloy 686. Neither study predicted secondary phases with low melting points, even for the high dilution levels. Only P phase, σ phase and M_6C carbide were predicted by the thermodynamic simulation, which, however, did not induce a significant enlargement of the solidification temperature range.

Moreover, the previous chapter that assessed the effect of mixture of the 100S-G steel with Alloy 686 gave support for this good weldability observed. In this analysis, a single weld bead of 100S-G was deposited on Alloy 686 cladding, in order to verify the susceptibility to solidification cracking. Even with high dilution and consequently a significant incorporation of Ni, Cr, Mo and W into the 100S-G steel weld bead, only a few discontinuities were observed. In most cases, the discontinuities were concentrated in the macrosegregation regions, which were rich in the base metal (Alloy 686). These macrosegregations regions only solidified at the final stage of solidification, surrounded by the solidified weld metal. This phenomenon caused a concentration of segregated alloying elements during the solidification of the macrosegregation regions, and consequently the formation of small shrink porosities.

Furthermore, the welding parameters also help prevent the occurance of solidification cracks. The welding heat input (HI_w), dilution, weaving of the heating source and geometry of the weld pass represent some of the welding parameters that have a significant influence on solidification cracks. For the 3rd weld pass a low HI_w was used. In general, low HI_w have a low dilution with the base metal and a high cooling rate. Both factors minimize microsegregation effects that are directly related to solidification cracks. The weaving of the heat source also affects the microsegregation in a similar way to low HI_w, since it reduces the dilution and prevents the concentration of segregated alloying elements only in few solidification grain boundaries. Furthermore, weaving causes a continuous deflection of the heat source and consequently changes the direction of the grain growth. The geometry of a weld pass is also important to prevent centerline cracking. Keeping a low depth-to-width (D/W) ratio is fundamental to prevent the concentration of segregated alloying elements at the center of the weld pass[42,43].

Macrographs have further information concerning the welded joint features. The first two weld passes deposited using Alloy 686 completely filled the region composed by CRA cladding, guaranteeing the corrosion resistance of the component. The 3rd weld pass was not revealed by nital or the chromic acid solutions. Due to the dilution, which stimulates the incorporation of high amounts of alloying elements, such as Ni, Cr, Mo and W, the 3rd weld

pass became almost inert to attack by the acid etching solutions used. The dilution also affected the etching of 4th weld pass for the same reason. The chemical composition of the joint was obtained, in order to give support to the discussion about the etching of weld passes. Figure 9-5 shows the chemical composition of the first six weld passes of the welded joint.

Figure 9-5. Chemical composition of the first six weld passes of the welded joint. The arrows indicate the scale bar side.

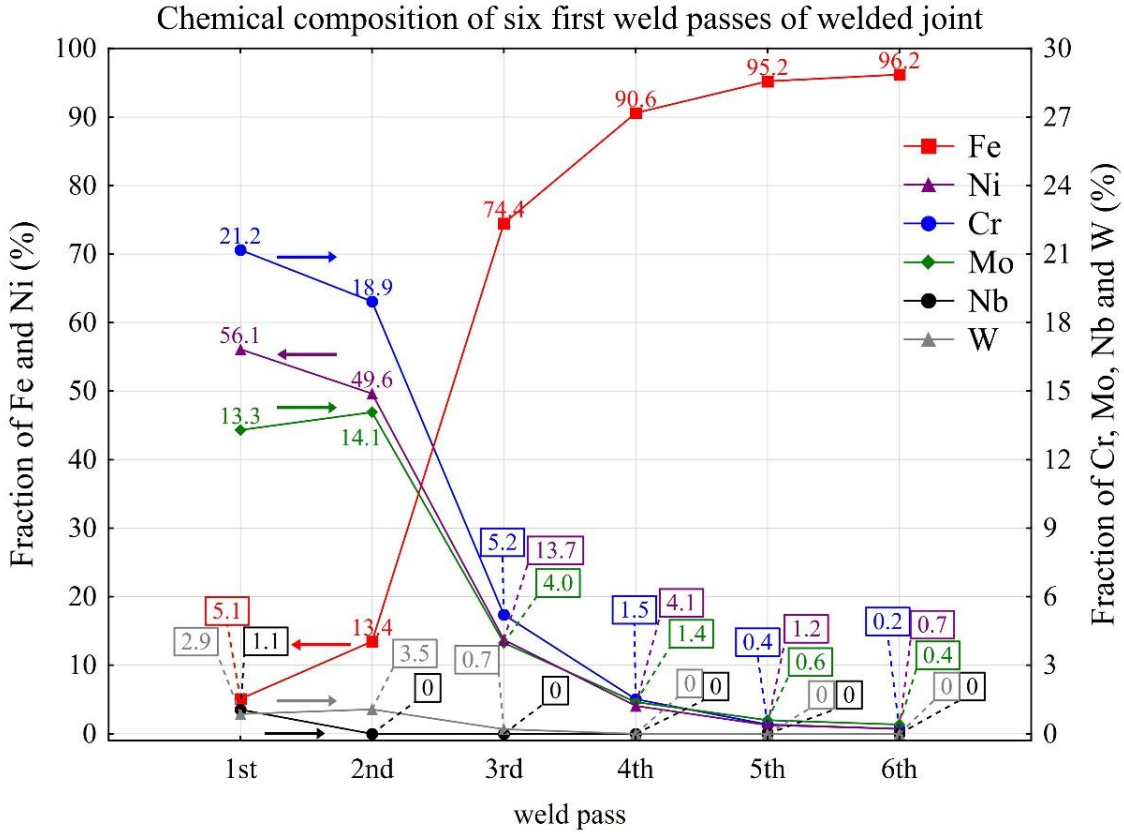

Source: Developed by the author.

The 1st weld pass shows a chemical composition similar to Alloy 686. The dilution with the Alloy 625 cladding decreased the content of Cr, Mo and W, while Fe, Ni and Nb increased. The Fe present in the Alloy 625 cladding came from the dilution with the steel pipe. In contrast, Mo and W increased in 2nd weld pass due to the dilution with the previous Alloy 686 weld pass. From the 3rd weld pass onward, the chemical composition changed drastically. The first 100S-G steel weld pass exhibited a new material in terms of chemical composition, as result of the mixture with the filler metal, the Alloy 686 and the steel pipe. Almost 14 wt% of Ni was incorporated into the Fe matrix. Considering the Ni content in 2nd weld pass, the 3rd pass diluted at least 27% of the previous weld pass. This reinforced the influence of the melting point of Alloy 686 on the dilution obtained for the deposition of 100S-G steel. A lower dilution level could not be obtained even using a low HI_w and weaving the heating source. The 4th and 5th

weld passes also exhibited an increase of alloying elements due to the dilution with previous weld passes. The chemical composition of the 6th weld pass observed is quite similar to the 100S-G steel. The remaining weld passes, the 7th to 10th, followed the same tendency as the 6th weld pass, as the 100S-G steel filler metal was only diluted with the API 5L X65 steel pipe.

9.4.2 Microstructural analysis

The microstructures and the chemical composition of the welded joint are shown in Figures 9-4 and 9-5, respectively. These images gave an idea of the complexity of the microstructures of the welded joint. The main microstructural features of each weld pass are discussed below. Figure 9-6a shows the microstructure interface between the 1st and 2nd weld passes. Both weld passes show a γ-FCC microstructure with secondary phases located at the interdendritic regions. These secondary particles were observed in almost all the interdentritic regions, which were nucleated due to the microsegregation of Cr, Mo and W.

Figure 9-6. Microstructure of a) interface between the 1st and 2nd weld passes of the welded joint and b) a shrink porosity.

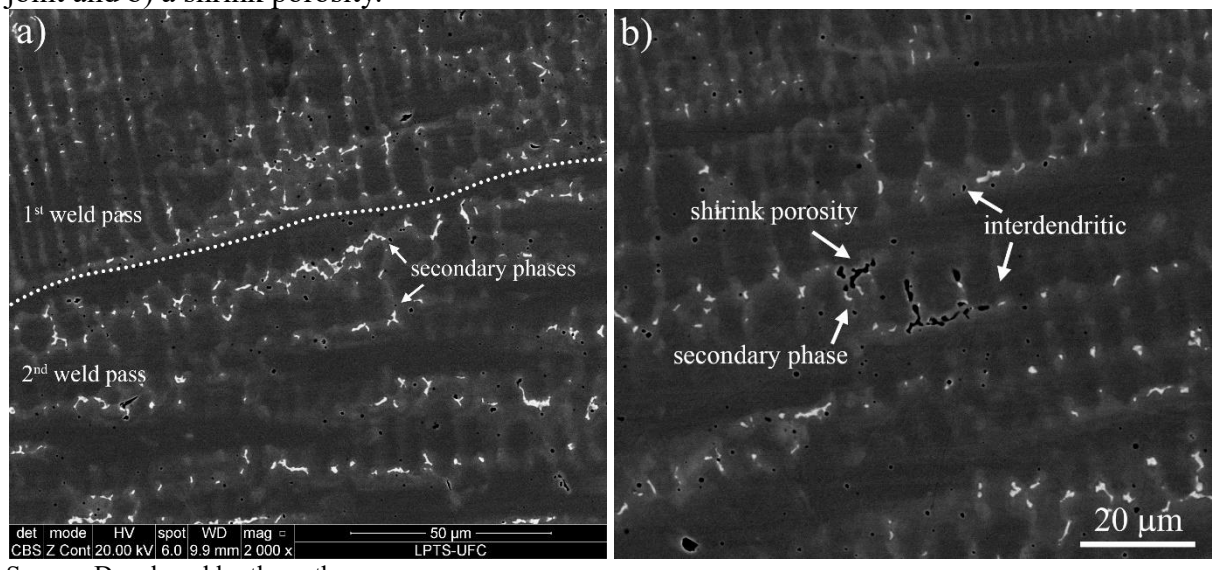

Source: Developed by the author.

Silva *et al.*[44] assessed the microstructure of the Alloy 686 as welded.. The microstructure of the mixture of Alloy 686 with ASTM A516 Gr60 steel exhibited several Mo-rich secondary phases located at the intercellular and interdendritic regions. The authors characterized these topologically closely packed phases using electron diffraction patterns and concluded that they were σ, μ and P phases. Initially, the alloying elements rejected to remaining liquid solidify as σ and P phases and next undergone a solid transformation of σ in P phase and

finally of P in μ phase. These phases concentrate the alloying elements responsible for the corrosion resistance of the alloy. Gorhe *et al*.[45] assessed the Alloy 22 from the family Ni-Cr-Mo-W and highlighted the deleterious effect of the μ phase and another phase rich in Cr on intergranular corrosion.

The microsegregation and then the nucleation of the aforementioned phases does not only affect the corrosion resistance but may also affect the mechanical properties of the joint. Figure 9-6b exhibited a shrink porosity seen at the top of 1st weld pass. These discontinuities observed have a few microns, but the phenomenon is similar to the origins of solidification cracks. This highlights that even with a significant fraction of secondary phases, this was not the key factor to increase cracking susceptibility during solidification. Possibly, this behavior is associated with the nucleation of the secondary phases that are Mo-rich and do not have a low melting point, as the deleterious phases like Nb-rich Laves phase do.

The microstructure of the 3rd weld pass was assessed using backscattered electron (BSE) microscopy as the microstructure could not been revealed by the chemical solutions used. Figure 9-7 shows the microstructure of the interface between the 2nd and 3rd weld passes. A predominant cellular solidification with evidence of microsegregation at the intercellular regions could be seen as the BSE technique highlights differences in chemical compositions. A large macrosegregation was also observed near the interface. These macrosegregations occurred due to several physical reasons. The lower melting of the base metal in comparison with the filler metal caused a high fusion of the base metal as well as deep penetration. According to Yang and Kou[46] it is not possible obtain a total mixture between alloys when the base metal has a lower liquidus temperature in comparison to the liquidus temperatures of the filler metal and fusion zone. This is because there is not enough time to solute diffuse along of macrosegregation regions, as the solidification in the welding process occurs rapidly, especially for low $HI_{w,}$ which is the case of the 3rd weld pass.

According to study of a previous chapter, the macrosegregation regions rich in the Ni-based alloy have a tendency to show shrink porosities. The cross section assessed did not exhibit any relevant defects, but on investigating the fracture surface of the Charpy-V impact test specimens, shrink porosities at the interface between 2nd and 3rd weld passes were observed. Figure 9-8 shows one of the defects, where a large shrink porosity exhibited several cells and dendrites with its tip growing in the direction opposite to the thermal gradient direction. Probably, this defect occurred in the macrosegregation rich in the Alloy 686, which solidified surrounded by the major portion of solidified weld metal. This explains the cellular growing

opposite to the thermal gradient direction. Thus, the cells grew perpendicular to the solid/liquid interface, in the direction to the center of the macrosegregation.

Figure 9-7. Bulk microstructure of a solidification interface between the 2nd and 3rd weld passes.

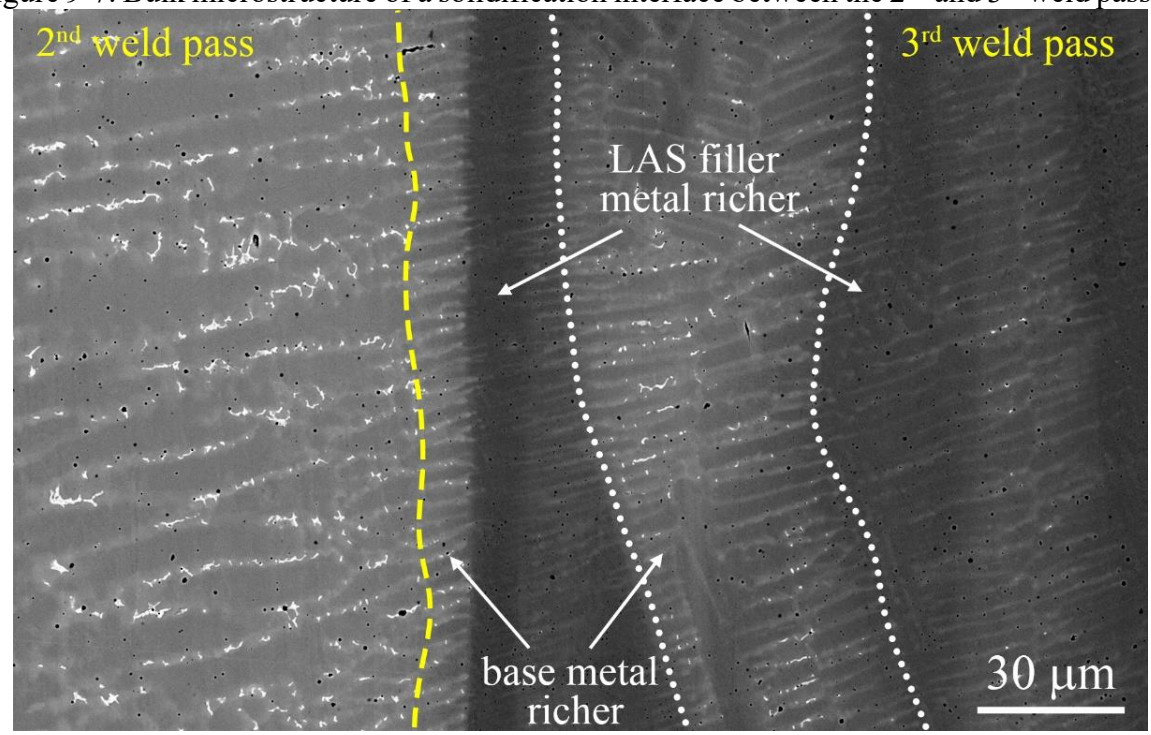

Source: Developed by the author.

With respect to the bulk microstructure of the 3rd weld pass, a new chemical etching using a solution with a higher concentration of HNO_3 over an extended period of time was done in order to reveal the weld pass. The severe etching corroded the 3rd weld pass and severely eroded the steel pipe and the welded joint from the 4th weld pass onward. Figure 9-9 shows, in low magnification, a macrograph of a light microscopy image. Numerous macrosegregations can be seen along the weld. Even with the presence of macrosegregations, a similar microstructure was observed in both regions: a martensitic matrix with an interdendritic region rich in Ni and other elements (Figure 9-10a), which provided a higher resistance to the corrosive action of acid etching. Retained austenite (A_{ret}) and some cubic particles (Figure 9-10b) also were observed. Table 9-3 show the EDS analysis of these microstructures. The cubic particles are carbides rich in Ti. According to Silva *et al.*[18] such carbides can also be a Ti nitride and are an excellent nucleation agent for Nb carbides that surround the TiC. Oxides rich in Al and Mg can be nucleated by the same mechanism, since they have the same cubic crystal structure (NaCl) with minor changes in their lattice parameters.

Figure 9-8. A large shrink porosity observed in a fracture surface of a Charpy-V specimen. The defect was observed at the interface between the 2nd and 3rd weld passes. The shrink porosity raised into macrosegregation rich in Alloy 686 and, its cells and dendrites grew in the opposite direction to the thermal gradient direction, showing that solidified after solidification of the bulk weld pass.

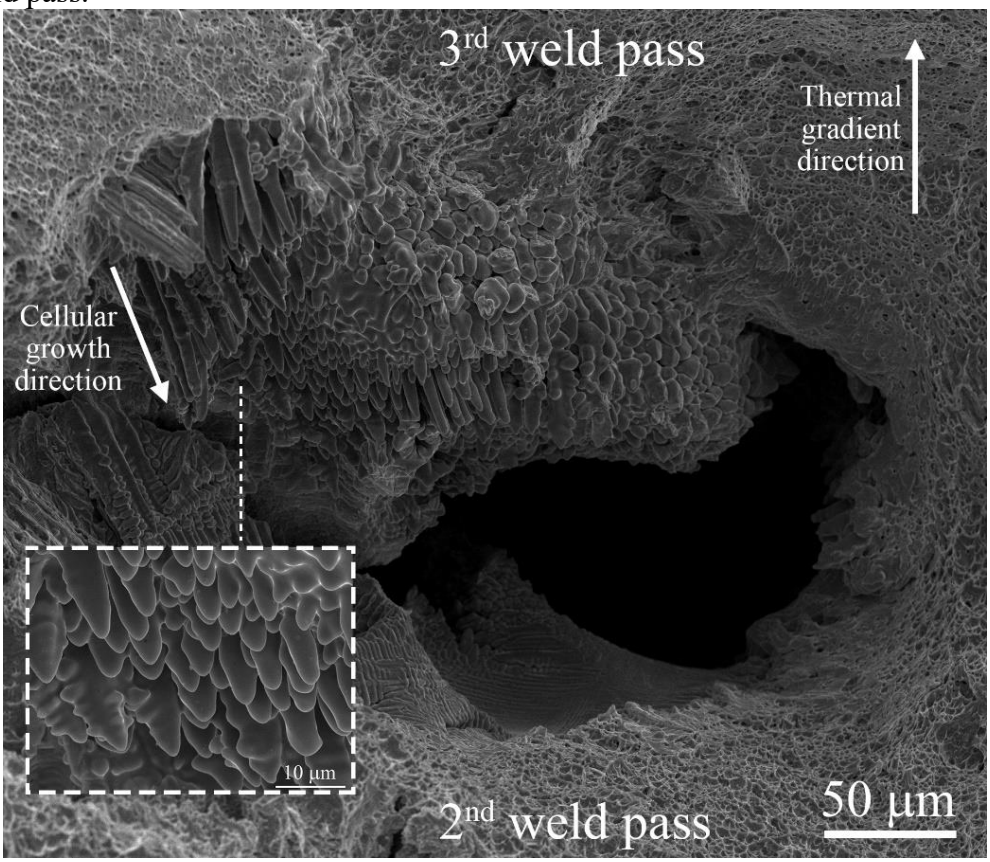

Source: Developed by the author.

Figure 9-9. Macrosegregation regions observed in the 3rd weld pass by light microscopy.

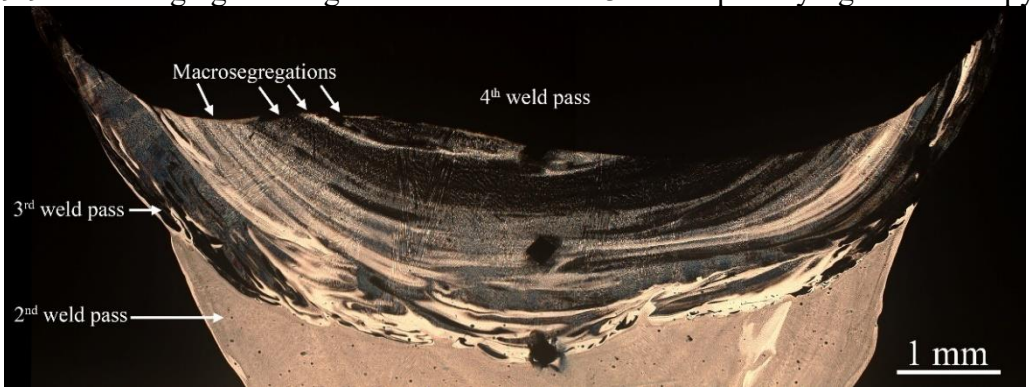

Source: Developed by the author.

Table 9-3. EDS chemical composition analysis performed on Aret, martensite and cubic carbide.

Chemical composition of secondary phases of the 3rd weld pass											
Phase	Al	O	Mg	Si	Cr	Ti	Mn	Fe	Ni	W	Mo
A_{ret}	0.3	0.8	-	0.6	4.9	0.8	1.5	72.4	12.8	0.8	5.2
Martensite	-	0.7	-	0.4	4.5	-	1.1	78.6	11.5	0.5	2.6
TiC	12.2	17.2	2.1	0.2	3.5	13.0	0.8	42.9	5.8	0.5	2.0

Source: Developed by the author.

Figure 9-10. The microstructure of the 4th weld pass highlighting a) martensite morphology observed in the richer regions of the filler and base metals and b) other phases such as A_{ret} and TiC.

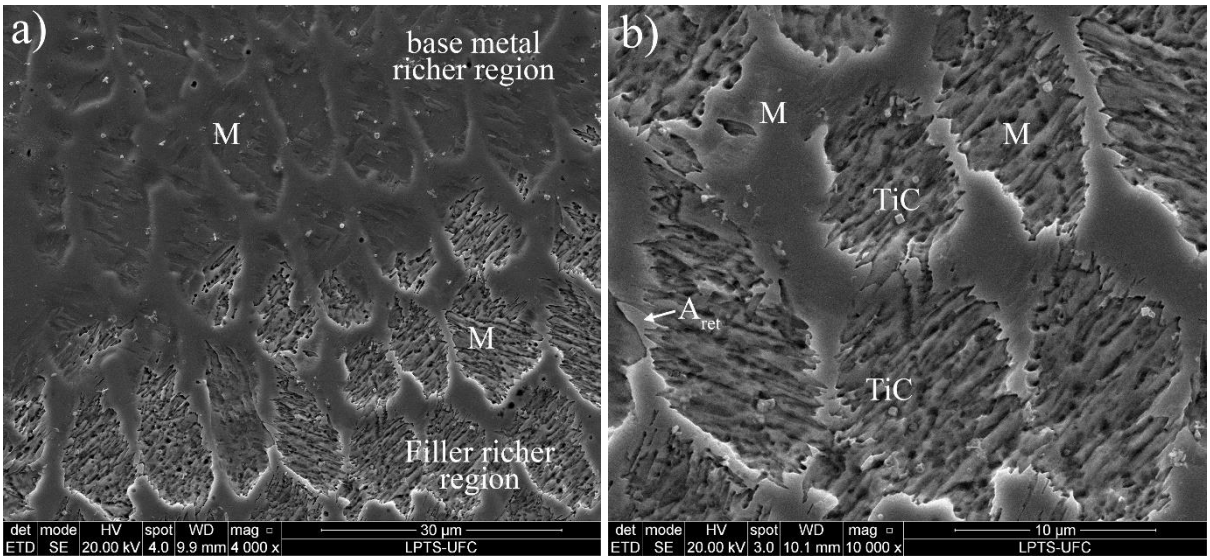

Source: Developed by the author.

The thermodynamic calculations performed for the chemical composition of the 3rd weld pass indicate that austenite becomes unstable below 608ºC, indicating the occurrence of a phase transformation (Figure 9-11). Additionally, the calculation for the starting martensite transformation temperature (M_s) was base on Equation 1[47]. The estimated temperature was 151ºC, which is high enough to enable martensitic transformation. Associated with this assumption, it is necessary to consider that the cooling rate experienced by the weld metal will be fast enough to provide shear stress for the diffusionless transformation to occur. Other studies assessing low alloy steels with similar concentrations of Ni have presented a martensitic matrix when subjected to fast cooling[48,49]. Kaufman and Cohen[50] investigated the martensitic transformation in Fe-Ni steels and found that for an alloy with 14.5 wt% of Ni, the M_s and M_f temperatures were 350ºC and 230ºC, respectively. Other factors may affect the hardenability and temperature transformations. Yang and Bhadeshia[51] confirmed that the austenite grain size depended on the martensite-start temperature (M_s). For the same chemical composition, higher grains sizes promote an increase in the M_s temperature. As the solidification grains are very large compared to other processing conditions, the M_s temperature is expected to rise.

$$M_S(°C) = 539 - 423wt\%C - 30.4wt\%Mn - 17.7\ wt\%Ni - 12.1\ wt\%Cr - 7.5\ wt\%Mo \quad (1)$$

The fracture surface of the Charpy-V impact test specimens also revealed the presence of defects in the interface between the 3rd and 4th weld passes. Figure 9-12 shows the

microstructure of small shrink porosities. Probably these defects appeared during reheating and consequently fusion of the top of the 3rd weld pass. Normally, the final portion of the weld metal to solidify has a greater concentration of segregated elements. In this case, the concentration of Ni, Cr and Mo, reduced the liquidus temperature of this region retarding its solidification, which caused the formation of a shrink defect.

Figure 9-11. Simulation of phase fraction of the 3rd weld pass in equilibrium.

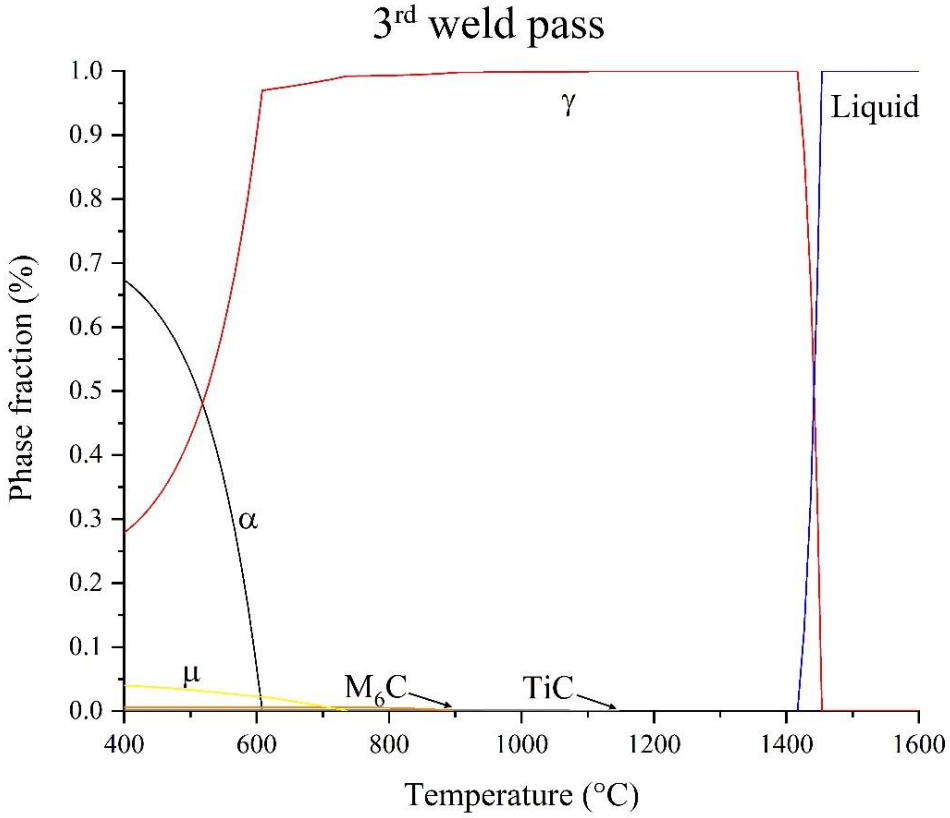

Source: Developed by the author.

The fracture surface also revealed the differences concerning the fracture mode of each weld pass. Shallow dimples were observed for the 3rd weld pass, while a transgranular cleavage fracture was predominant for the 4th weld pass. These features have a relationship with the chemical composition, microstructure, crystallography and absorbed energy experienced by the specimen during the impact test. More details will be presented later.

Similar to the 3rd weld pass, the 4th weld pass showed a well-defined martensitic microstructure. Figure 9-13 shows the bulk microstructure of the 4th weld pass. The microstructure showed a martensitic matrix with several stringer particles of a retained austenite phase and some carbides. According to the literature, this microconstituent occurs during martensite transformation due to short-range diffusion, which rejects Ni, Mn and C. Thus, the austenite grain adjacent to the lath martensite becomes richer in these alloying elements that

increase the thermodynamic stabilization field of the γ-FCC[52]. This phenomenon causes the retention of the A_{ret} phase. According to Krauss[53] austenite is retained between the laths of martensite due to C and the diffusion of other alloying elements during the transformation.

Figure 9-12. Small shrink porosities observed on the fracture surface of Charpy-V specimens. The defects are located at the interface between the 3rd and 4th weld passes.

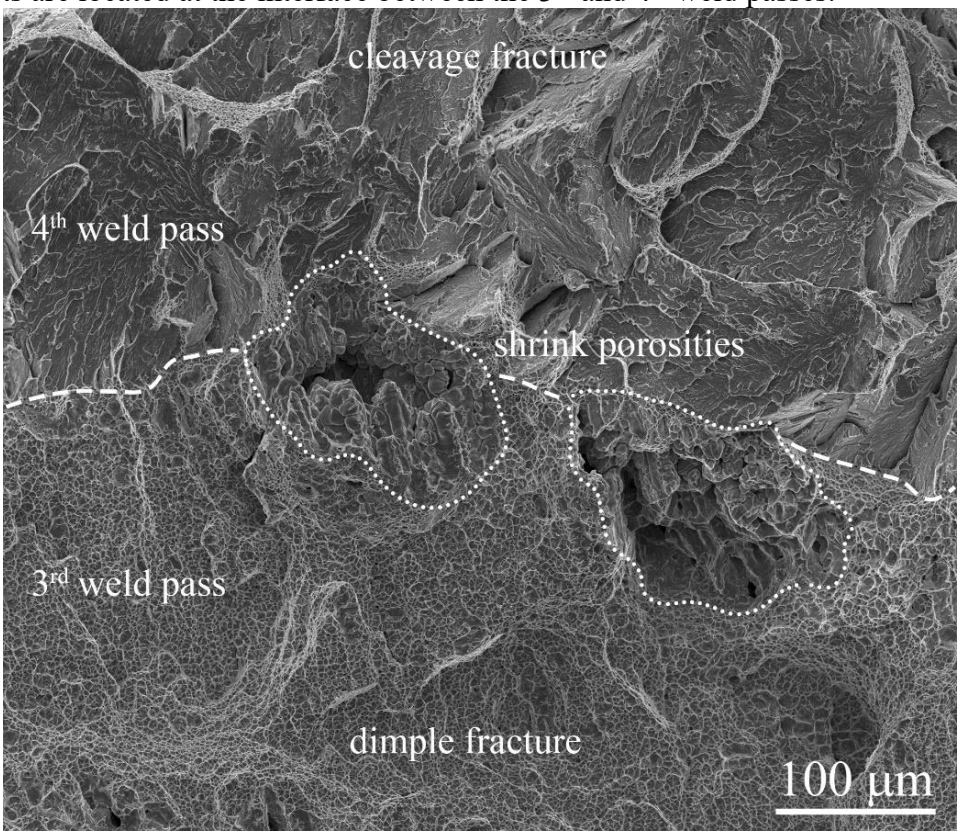

Source: Developed by the author.

Figure 9-13. a) the bulk microstructure of the 4th weld pass, highlighting b) the martensite matrix with several stringer A_{ret} particles.

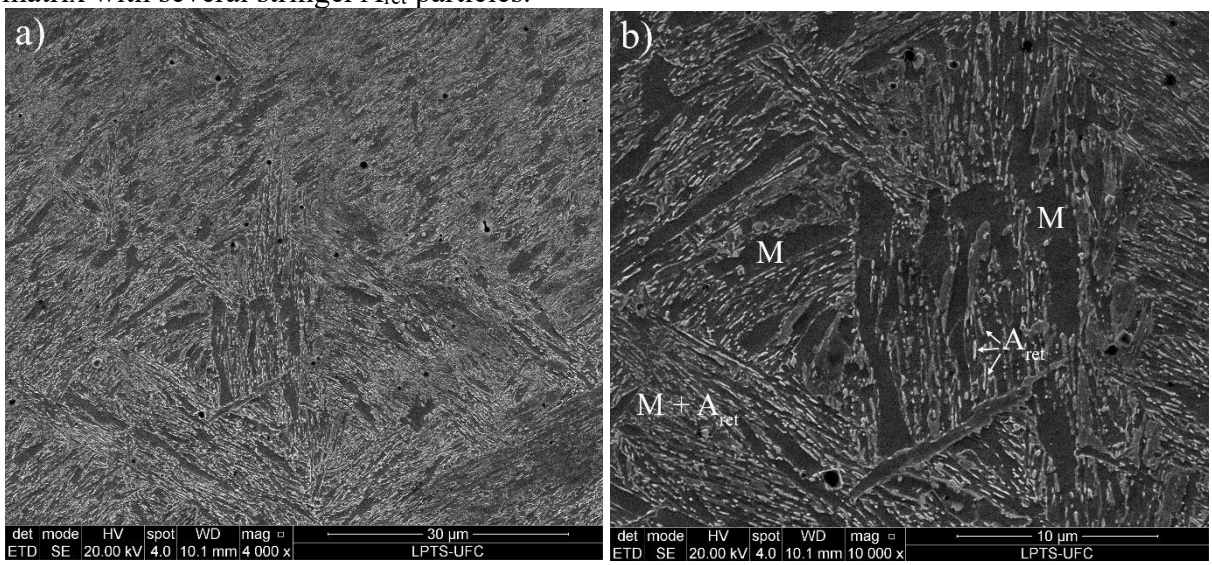

Source: Developed by the author.

The bulk microstructure for the 5th weld pass in Figure 9-14 shows a bainitic matrix with some martensites associated with the presence of carbides and MA particles with stringer and/or block morphologies. The increase of HI_w favored the bainite transformation instead of martensite. However, it is believed that more than the cooling rate, the reduction of alloying elements like Ni, Cr and Mo in this weld pass favored the bainite formation. Moreover, the low Ni content in this weld pass, approximately 1 wt%, favored the MA microconstituent and then the formation of large MA particles due to the microsegregation of Ni and Mn and the short diffusion of C that stabilized the γ-FCC into MA particles.

Figure 9-14. Bulk microstructure of the 5th weld pass highlighting the matrix based on martensite and bainite with several MA particles as long stringers and blocks.

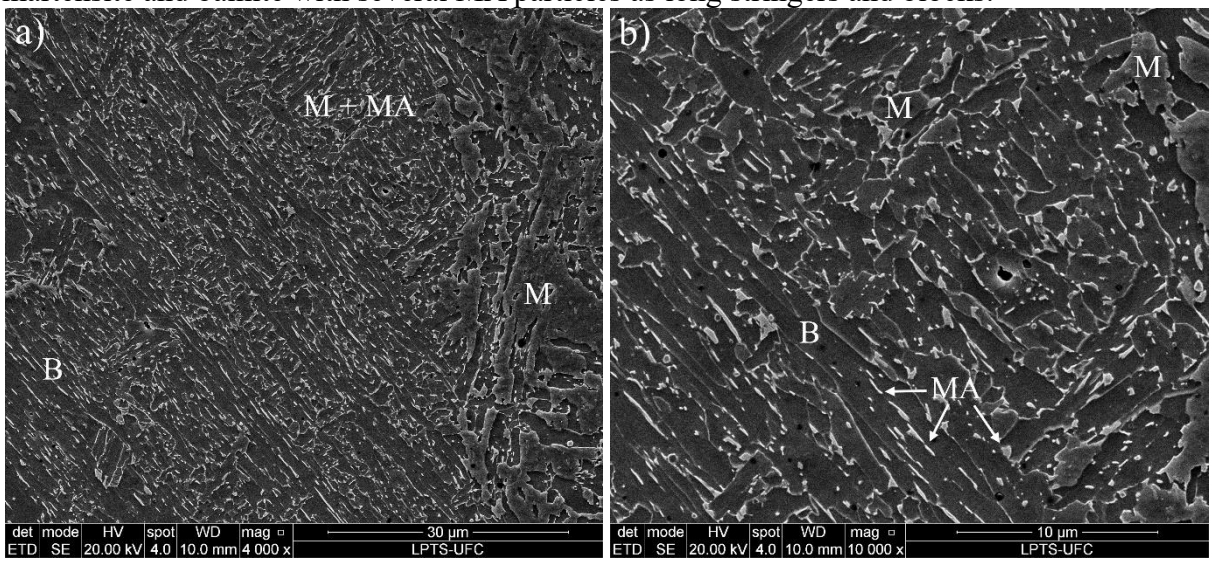

Source: Developed by the author.

As previously discussed, the chemical composition of the 6th to 10th weld passes are quite similar. The differences among them are related to the HI_w used. Thus, the 10th weld pass was assessed, and it gave an idea of the microstructure of these weld passes. Figure 9-15 shows that the bulk microstructure of the 10th weld pass has an acicular ferrite matrix with several MA particles. The MA microconstituents showed a morphology similar to that shown by the 5th weld pass, and the difference between them is mainly relate to the amount of Ni and other alloying elements.

Figure 9-15. Bulk microstructure of the 10th weld pass highlighting the acicular ferrite matrix with several MA particles as long stringers and blocks.

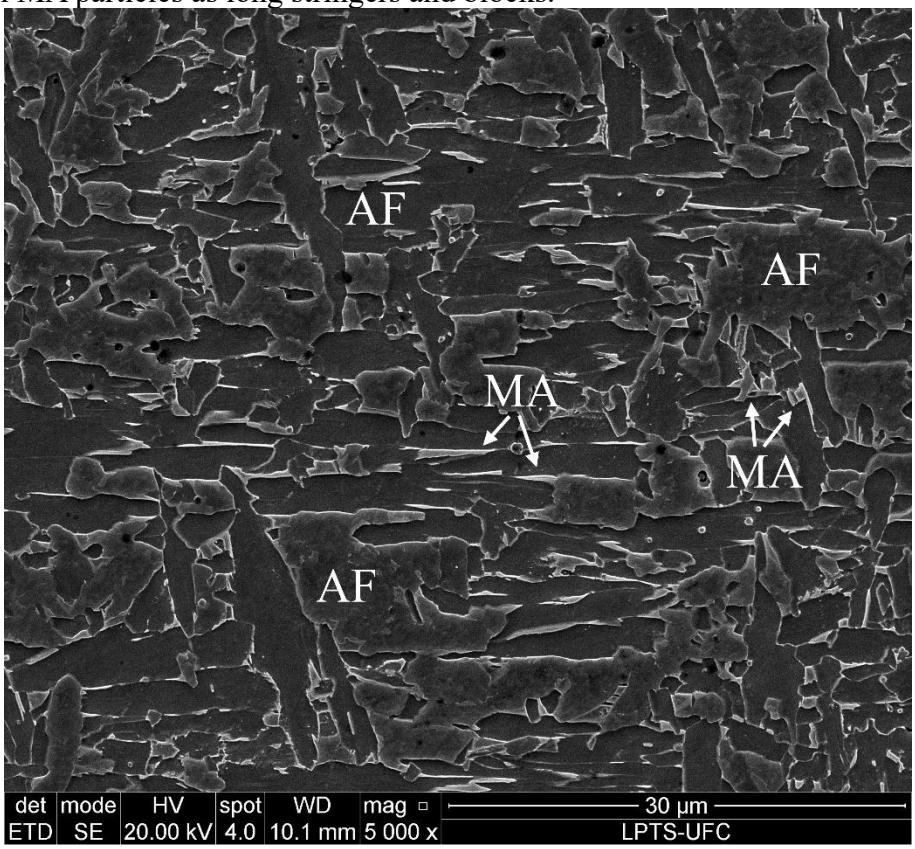

Source: Developed by the author.

9.4.3 Mechanical evaluation

9.4.3.1 Bend testing

The bending test represents one of the most important mechanical tests that is able to assess the integrity of welded components. Defects in a welded joint may grow (and cause failure) during the bend test because the surface that is bent is subjected to a high tensile stress, while the opposite face is submitted to a high compressive stress. Therefore, big solidification defects such as porosities, solidification cracks and lack of fusion may lead to failure of the welded joint. A weld metal failure indicates a weldability problem, which suggests that a wrong filler metal and/or welding procedures were adopted.

The four bending samples tested are shown in Figure 9-16. All samples were approved in the bending test, as no defects were observed on the bent surface. This positive result reinforces the welding procedures adopted, as no discontinuity introduced during welding was big enough to grow during the bending test.

Figure 9-16. Bending specimens after test. All samples were approved without exhibiting any defects on their bending surfaces.

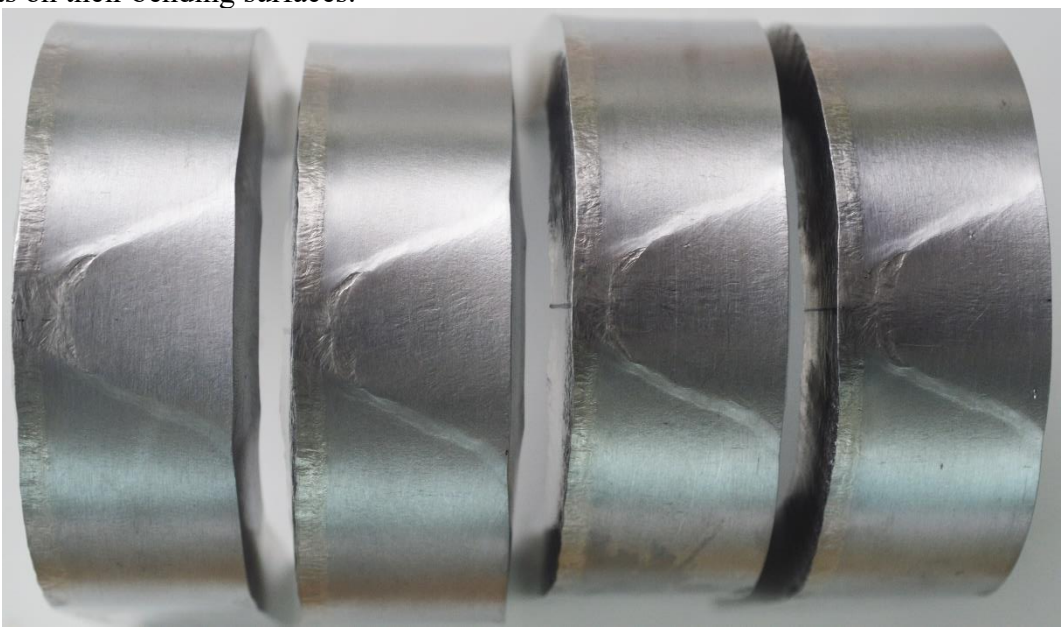

Source: Developed by the author.

9.4.3.2 Tensile testing

The transverse tensile test, which is a severe destructive mechanical test, was also performed to check the integrity of the welded joint. Figure 9-17 shows two samples that were evaluated. The rupture occurred, for both specimens, at the steel pipe, far from the heat affected zone. An average of 638.1 MPa of ultimate strength was applied to these specimens. As with the bending test results, the absence of defects on the surface of the welded joint reinforces that the correct welding parameters had been adopted. This also includes the filler metals selected to perform the dissimilar welding. The good metallurgical compatibility between Alloy 686 and 100S-G steel provided a satisfactory weldability, considering the microstructure and the mechanical properties evaluated.

The mechanical overmatch requirement, the yield strength, tensile strength and elongation of the welded joint were assessed by the transverse all-weld tensile tests. Four different positions of the welded joint were tested, because the dissimilar welding created new materials, especially in the first three 100S-G steel weld passes. Thus, the mechanical properties of 2nd weld passes, 3rd to 4th weld passes, 5th to 6th weld passes and 7th to 8th weld passes were all evaluated. Table 9-4 shows the main mechanical properties of the regions assessed.

Some important details about the samples should be mentioned before a final evaluation of the results. Even when using the smaller specimens as suggested by DNVGL-ST-F101 standard[34], a larger portion of the fillet radius for the samples manufactured to assess the

2nd weld pass and 3rd to 4th weld passes were composed of the steel pipe. Therefore, in these cases the mechanical properties obtained are only a good approximation, especially when the rupture of the sample occurred at the fillet radius.

Figure 9-17. Transverse tensile test samples after the test. The fracture occurred in the base metal in all samples.

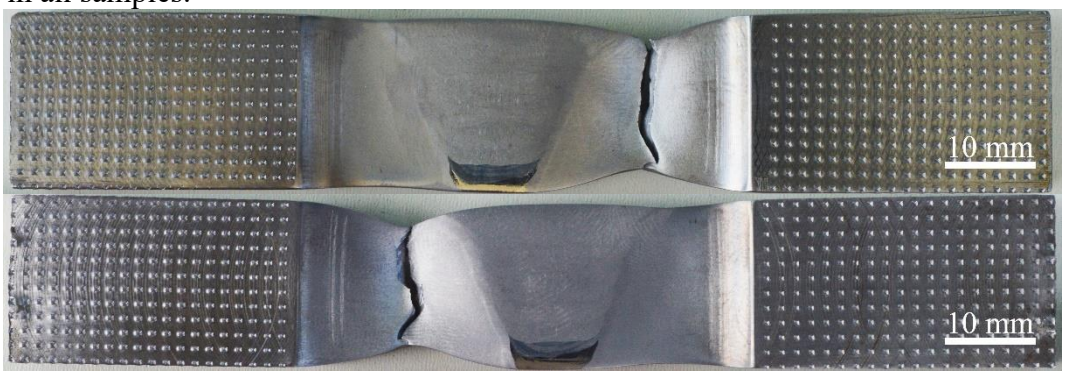

Source: Developed by the author.

The welded joint exhibited good mechanical properties that satisfied the overmatch requirements for several HSLA steels. Except for 2nd weld pass or hot pass that DNVGL-ST-F101 standard[34] does not take into account for overmatch criterion, the welded joint easily overmatched the yield strength of the API 5L X65 steel. Based on the lowest yield strength obtained for a major region of the welded joint, which exhibited a YS of approximately 692 MPa, the joint met the overmatch criterion to perform joint welding with API 5L X65, X70 and X80 steels for subsequent installation by the reel lay process. During the installation process the component will be submitted to a low strain stress, $\varepsilon < 0.4\%$. Moreover, the welded joint also met the requirements to perform the joint welding of API 5L X90 steel.

These results highlighted the potential of this new approach for joint welding of such components. The use of a low alloy steel provided the welded joint the mechanical properties necessary to perform the joint welding of HSLA steels with internal cladding of Alloy 625 that until now had been impracticable. Currently, the overmatch criterion is achieved only for joint welding of API 5L X65 steel using Alloy 625 as the filler metal, but the minimum YS required is only achieved the after work hardening provided by the bending steps of the reel lay installation process. Moreover, it is important to highlight that this new approach for joint welding opens up the possibility for joining other HSLA steels like API 5L X90 and X100 steels, by only selecting another low alloy steel as the filler metal.

Table 9-4. Mechanical properties of the welded joint obtained from the transverse all-weld tensile tests. The letters W and R mean that rupture occurred in the weld metal and radius fillet, respectively.

Transverse all welding tensile test					
region (weld pass)	specimen	yield strength (MPa)	tensile strength (MPa)	elongation (%)	rupture
2nd	1	500.6	826.9	36.6	W
	2	532.3	765.4	27.2	R
3rd - 4th	1	729.1	836.0	25.4	R
	2	-	-	-	-
5th - 6th	1	780.6	838.9	26.9	W
	2	753.0	792.8	22.3	W
7th - 8th	1	696.2	743.2	25.4	W
	2	691.8	744.5	23.3	W

Source: Developed by the author.

9.4.3.3 Microhardness and hardness tests

The resistance to localized plastic deformation of the welded joint was also assessed. Initially, a microhardness map was made by assessing the 2nd to 6th weld passes of the joint. The spacing between the microindentations was established at 300 μm. All microindentations were performed using 100 gf. Figure 9-18 shows the microhardness map obtained. Furthermore, a color scale bar from 250 HV to 400 HV was adopted.

The API 5L X65 steel showed the lowest microhardness with values below 250 HV. This result is in agreement with low carbon ferritic steels, considering their high strength is achieved by thermo-mechanical processes that provide grain refinement. The 2nd weld pass exhibited an average microhardness of approximately 300 HV. The high fraction of alloying elements present in Alloy 686 caused the hardening of the γ-FCC matrix.

In contrast, the 3rd weld pass showed a very low microhardness, of about 250 HV. This weld pass consists of the first pass deposited using LAS. As shown before, the chemical composition has at least 13.7 wt% Ni, 5.2 wt% Cr and 4.0 wt% Mo. However, the carbon content is a consequence of the contribution of each alloy involved. Both Alloy 686 and low alloy steel (100S-G) filler metals have a carbon content of 0.04 wt%. The API 5L X65 steel pipe used presented a carbon concentration of 0.11 wt%. Based on dilution of the LAS with Alloy 686 and API 5L X65 steel, the estimated carbon content for this weld pass was 0.04 wt%. Morsdorf *et al*.[54] pointed out that most critical analyses of alloying elements in martensite are related to carbon, since interstitial C plays one of the major roles in martensite properties, including hardness, strength and toughness. Despite being a martensitic microstructure, the incorporation of a significant amount of Ni, due to the dilution with Alloy 686, may contribute

to confer a softening effect on this martensite. According to the literature, the addition of approximately 5 wt% of Ni enhances the ductility and plasticity of the martensite[54]. Unfortunately, the dilution with Alloy 686 also promotes the addition of other solid solution strengthening elements like Cr and Mo, which would negatively affect the plasticity, hardness and toughness. However, this effect was not observed in this study. Therefore, the low dilution with API X65 steel pipe and low carbon content of this weld pass, associated with the high Ni content (almost 14 wt% of Ni) may have contributed to the low hardness measured in this weld pass.

Figure 9-18. Microhardness map of the welded joint, evaluating the 2nd, 3rd, 4th, 5th, 6th passes and the API 5L X65 steel pipe.

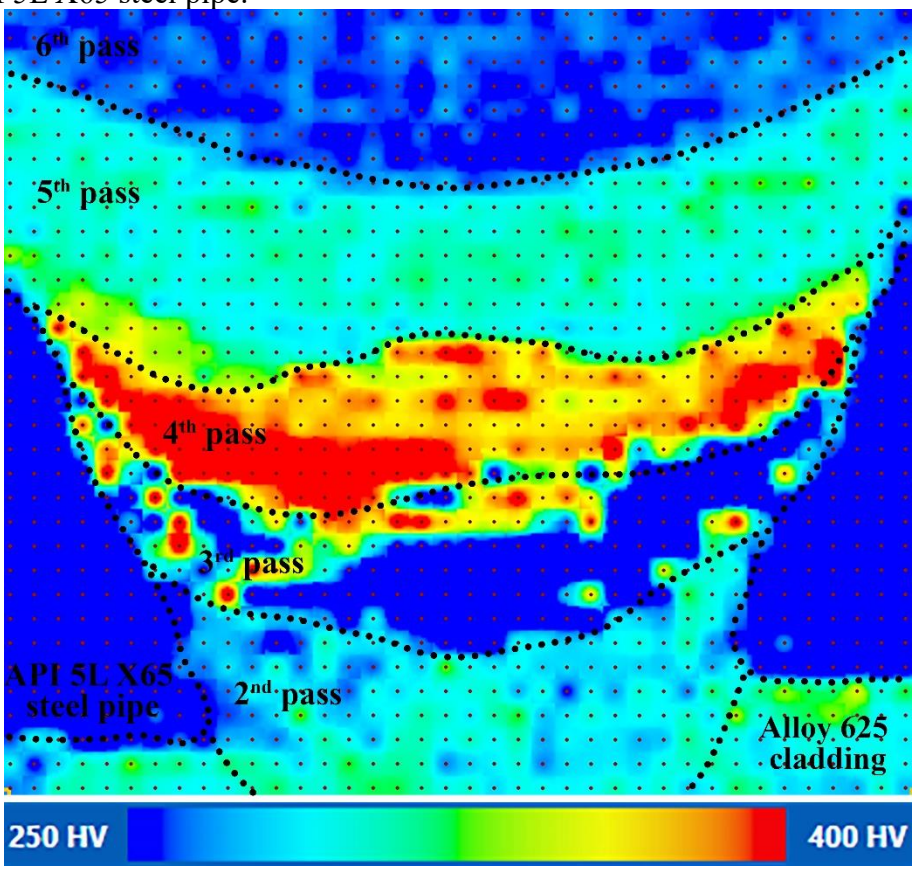

Source: Developed by the author.

The 4th weld pass showed the highest microhardness of the welded joint, of above 400 HV in the greater part of the weld pass. The incorporation of Ni, Cr and Mo caused a hardening by quenching and solid solution. Different from the 3rd weld pass, the Ni content in the 4th weld pass was not enough to confer ductility to the martensite microstructure. In addition, the increased attack on the sidewall of the pipe steel enhanced the dilution and, as a consequence, probably increased the carbon content of this weld. Since the carbon content plays

an important role on martensite hardening, the higher hardness levels found in this weld pass are most probably associated to an increased carbon content. The 5th weld pass also followed the same tendency of chemical composition and microstructure as the 4th weld pass, with a reduction of Ni, Cr and Mo and, a microstructure composed by martensite, bainite and MA. The average microhardness was around 300 HV, very similar to the microhardness of the 2nd weld pass. The 6th weld pass, in turn, exhibited a microhardness similar to API 5L X65 steel pipe, of about 250 HV. This corroborates with the chemical composition of the weld pass that is close to the 100S-G steel.

The hardness profile along the center of welded joint was also investigated. In this case 24 indentations using 10 kgf with a spacing of 1 mm between indentations were made. Figure 9-19 shows the hardness profile. The 1st weld pass exhibited an average of 293 HV, while the 2nd weld pass showed a hardness of approximately 248 HV. In contrast, the 3rd weld pass showed a hardness of about 211 HV. The 4th and 5th weld passes showed approximately 378 HV and 292 HV. Naturally, these results were very similar to those shown on the microhardness map.

Figure 9-19. Hardness profile of the welded joint covering all weld passes, starting from the root weld pass.

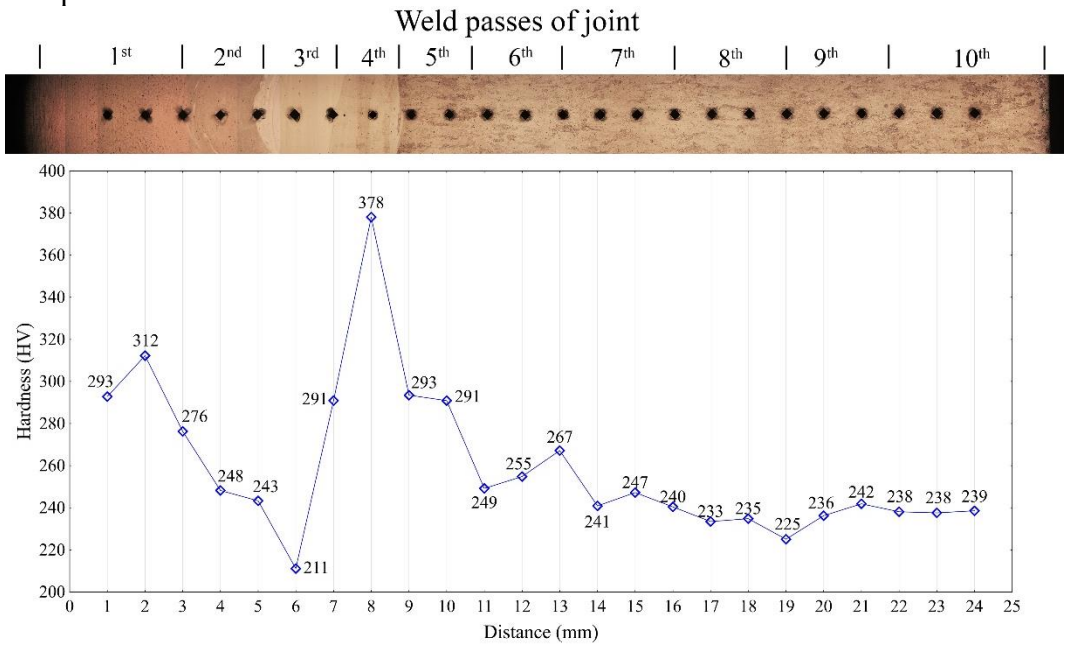

Source: Developed by the author.

Notably however, the hardness of the 6th to 10th weld passes were similar and on average were approximately 242 HV. The dilution effect of the 100S-G steel and Alloy 686

mixture was reduced, and therefore, a hardness typically for acicular ferrite steels like 100S-G steel was observed.

Note that the dissimilar joint welding of API 5L X65 steel pipe with internal cladding of Alloy 625 created an extremely complex joint from the metallurgical point of view. The first three weld passes that correspond to approximately 30% of the height of the welded joint show a soft microstructure composed of Ni γ-FCC matrix (1st and 2nd weld passes) and high Ni martensite, retained austenite and TiC carbides (3rd weld pass). The 4th and 5th weld passes, that represent 20% of the height showed a hard microstructure based on a low Ni martensitic matrix plus A_{ret} and TiC carbides in the 4th weld pass, and a bainitic matrix, some martensites, MA microconstituents and TiC carbides in the 5th weld pass. In contrast, the other half of the welded joint exhibited a soft acicular ferrite microstructure with MA microconstituents and TiC carbides. Obliviously, it is not so simple to assess the mechanical properties of such a joint.

9.4.3.4 Impact toughness

The impact toughness is one of the most important mechanical properties necessary to design such a component, especially in this case, where several weld passes with a strong chemical gradient along the welded joint will be produced, as well as exhibiting a complexity in terms of microstructure and hardness. Therefore, the energy absorbed by the impact toughness was assessed, firstly for specimens with a notch positioned at the 3rd weld pass, which represents the first weld pass that is a mix of 100S-G steel and Alloy 686.

The energy absorbed by the main region of the welded joint that is the 6th to 10th weld passes, must also be assessed since these weld passes were not affected by dilution with the Alloy 686 and, therefore, they represent the mixture between the 100S-G steel and the X65 steel pipe. A similar result was obtained in a previous study that manufactured a welded joint of the same components using Alloy 22 for first two weld passes, while 100S-G steel was used for the other weld passes of the joint[55]. This study assessed the impact toughness with the notch positioned at the 7th weld pass and, therefore, evaluated the absorbed energy of the mixture between the 100S-G steel and the X65 steel pipe only. Therefore, this result should be taken into discussion in the present study. The energy absorbed for each condition is shown in Table 9-5.

The condition with the notch positioned at the 3rd weld pass absorbed more energy in comparison to when the notch was positioned at the 7th weld pass. This result was not

expected, considering that from the 3rd to the 5th weld pass a microstructure based on a martensitic matrix exhibiting high hardness was found, while the weld passes from the 6th to 10th weld passes showed an acicular ferrite microstructure. According to a study showed in previous chapter, these 100S-G steel weld passes that were diluted only with X65 steel pipe were assessed below their ductile-to-brittle transition temperature and, for this reason showed a poor absorption of energy. Based on this, only the impact toughness of the dissimilar welding region complied with the requirements established by DNVGL-ST-F101 standard[34], which defines an absorbed energy of at least 38J at -15°C for the welding of base metals with a YS of above 450 MPa.

Table 9-5. The average absorbed energy of the welded joint with the notch positioned on the 3rd and 7th weld passes.

Impact toughness of welded joint (J)	
Notch in 3rd pass	38.5 ± 3.3
Notch in 7th pass	14.3 ± 1.3 [55]

Source: Developed by the author.

The fractographs of the samples tested for both conditions are shown in Figure 9-20a and 9-20b and clearly show the differences between the fractures presented. In the sample that evaluated the 3rd weld pass, a frosted-looking region near the edge of the notch can be seen. This feature is typical of materials that exhibit ductile fractures. Most of the fracture surface, however, exhibited a shiny appearance that indicates a brittle fracture. This ductile feature observed for the 3rd weld pass was attributed to the high Ni content incorporated due to the dilution with Alloy 686. In contrast, the sample with the notch positioned at the 7th weld pass showed a fully brittle feature. All these features corroborate with the absorbed energy obtained for each condition.

Continuing the fractographic analysis, Figure 9-20c shows details of the impact toughness samples that assessed the 3rd weld pass of the joint. The fractography of Figure 9-20a revealed that a small portion of the 2nd weld pass, composed of Alloy 686, was also included in the sample. Different from the martensitic weld passes, the 2nd weld pass which has a γ-FCC matrix, contributed to increase the toughness of the specimen. Both the 2nd and 3rd weld passes showed a fractography based on dimples, typically for ductile materials. The high amount of Ni in the 3rd weld pass, approximately 14 wt%, caused a softening of the martensitic matrix. This hypothesis corroborates not only with the fracture feature, but with the microhardness and hardness results too.

Despite this ductile feature in the 3rd weld pass, the specimens absorbed low energy during the impact test. Figure 9-20c presented numerous shrink porosities that were discussed previously. These shrink porosities were found at the solidification interface between the 2nd/3rd and the 3rd/4th weld passes. Certainly, these solidification defects strongly affected the absorbed energy of this region of the welded joint thereby reducing the toughness.

Figure 9-20. Fractography of a Charpy-V sample with the notch positioned at a) the 3rd weld pass and b) the 7th weld pass of a similar welded joint[55] and c) A macrograph of a Charpy-V specimen with the notch positioned at the 3rd weld pass by scanning electron microscopy.

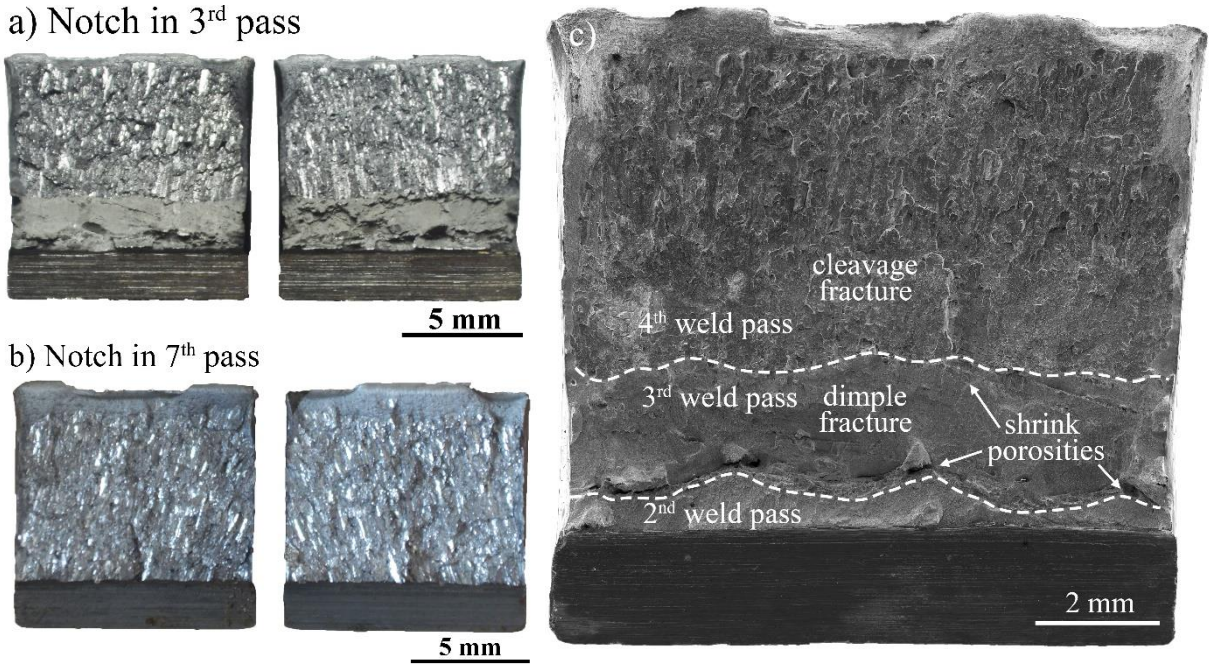

Source: Developed by the author.

In contrast, from the 4th weld pass onward cleavage was the predominant fracture mode. This fracture mode occurs in brittle materials. The 4 wt% of Ni in the 4th weld pass helped to soften the matrix, but the 1.5 wt% and 1.4 wt% addition of Cr and Mo, respectively, increased the hardening of the matrix by quenching and solid solution. In addition, the increase of dilution with the sidewall of the steel pipe also contributed to increase the carbon content. As discussed previously, carbon causes a hardening in both martensite and MA particles[54]. Thus, the hard martensite matrix with A_{ret} rich in C, Ni, Mn, Cr and Mo showed a low ability to absorb the energy during impact test. Moreover, the numerous hard Ti carbonitrides dispersed along the 4th weld pass also impaired the toughness, since they blocked the dislocation motion reducing thus the strain ability of material.

Some aspects of the impact toughness of the 3rd and 4th weld passes must be taken into consideration to comprehend their ductile and brittle fracture features, respectively. Morris Jr.[55] explained that when a stress is applied in a material failure, the peak stress at the crack tip will reach one of two levels: the effective yield stress (σ_γ) or the brittle fracture stress (σ_B). When the material experiences a load in which the σ_γ is reached, a significant plastic deformation occurs, while when the σ_B is reached, the crack propagates in a brittle mode. In steels with BCC or BCT crystal structures, the σ_γ rises as the temperature drops, and therefore, a ductile-brittle transition temperature is observed, where σ_γ rises above σ_B.

Many factors may affect the σ_γ and the plasticity and toughness of phases like martensite. Ni additions in steels are known to enlarge the austenite phase stability region and decreases the ductile–brittle transition temperature[56]. When Yao *et al*.[57] evaluated the effect of small additions of Ni (1.5 wt%) and the combined effect of Ni plus Cr (1.5 wt% and 1.63 wt%, respectively) they reported that the addition of Ni showed an enhancement in cryogenic impact toughness and, the addition of both Ni and Cr caused a decrease in toughness and an increase in hardness. In another study You *et al*.[58] studied the effect of Ni on toughness and microstructural evolution in the coarse grain heat affected zone and verified that impact toughness improved with Ni addition. Besides, these authors also found that prior austenite grain size was increased by Ni addition. Another change observed was the microstructure which changed from acicular ferrite plus lower bainite for a steel with 0.81 wt% Ni to pure lower bainite with 3.74 wt% Ni.

Morris Jr. *et al*.[59] reported that the addition of Ni enhances the formation of dislocated martensitic structures, combining good ductility with a fine effective grain size. Another interesting point is that Ni and Mn increase the resistance to cleavage fracture, improving ductility and lowering the DBTT. This dislocated martensite is associated to the dislocation density in the lath martensite. Morito *et al*.[60] evaluated the influence of C (ranging from 0.0026 wt% to 0.78 wt%) and Ni (ranging from 11 wt% to 31 wt%) on dislocation density within lath martensites. The results showed that on increasing the nickel content the dislocation density in the lath martensite increases very slightly. This behavior was associated with reducing the martensite temperature, which has a low effect on the volume change. Carbon strongly affected the density of dislocation, as a function of a large change in volume due to the phase transformation, which impairs the ductility and toughness as well. A significant difference in terms of Ni content in the 4th weld pass was found compared to the 3rd weld pass, and this

may increase the martensite DBTT, as well as the dislocation density within martensite, which impairs the ductility and the response of the steel under impact stress.

Another point to be considered is the effect of retained austenite. In high alloy steels the presence of A_{ret} is common, since a massive addition of alloying elements, especially elements like C, Ni and Mn, lower the M_s temperature. Shiue *et al*.[61] investigated the 9Ni-1Mo steel as welded and after tempering. The authors observed the formation of A_{ret} at the martensite interlath boundaries, where both Kurdjumov–Sachs and Nishiyama–Wasserman orientation relationships with martensite were seen.

Kim *et al*.[62] investigated the addition of Ni on the toughness of 9%Ni steel welded by the electron beam process. The Ni was added by introducing pure Ni wires during welding. It was evident the positive affect of adding of Ni in the toughness results. The conventional Charpy-V specimens with 16.6 wt% Ni showed 118 J at -196°C, while common 9% Ni steel exhibited only 45 J of absorbed energy. The Mössbauer spectroscopy detected and quantified a bigger fraction of A_{ret} for higher Ni steel, approximately 4.8 wt%, whereas conventional 9% Ni steel exhibited only 2.7 wt%. The authors did not mention, however, that the improvement in toughness is not only related to the contribution given by A_{ret}, but probably also due to the large amount of Ni distributed along the martensite and its grain boundaries which would have caused a higher contribution to toughness as reported earlier by other studies[59,60].

It is also important to consider the crystallography of martensite and the primary austenite grain size. The literature has provided important information concerning the effect of martensite crystallography on failure mechanisms. It is well known that martensite transformation results in a hierarchic pattern composed by laths, sub-blocks or blocks, packet and prior austenite grain[63,64]. According to Morito *et al*.[64] laths with the same orientation will originate a block. A group of blocks in which the laths have the same habit plane will form a packet and a set of packets will form a prior austenite grain, as shown in Figure 9-13.

In the past, toughness has been usually associated with grain size[65–67]. However, some results have shown that for martensite microstructures the toughness is not directly influenced by grain size of the previous austenite but is strongly affected by sub-structures like packets and blocks[68]. Morris Jr. *et al*.[59] have shown that the strength of martensite increases as packet size decreases. The pack size also affects the toughness of martensite as reported in the literature[69]. According to Krauss[53], the block and packet structures in lath martensite steels become the effective grain structures which also control deformation and toughness.

Inoue *et al*.[70] investigated the fracture in a low-carbon steel containing minor additions of Ni (2.4 wt%), Cr (0.95 wt%) and (0.41 wt%). According to these authors, the reason

for fractures with large cleavage facets comes from the fact that almost all martensite plates or laths within a packet present crystallographic features with the same orientation, and having the $\{100\}_{\alpha'}$ cleavage plane quasi-continuous throughout the packet. Recent results produced by Morris Jr. *et al*.[71] concerning the relationship between microstructure and cleavage fractures in 9 wt% Ni martensitic steel indicated that the effective grain size in these steels is the block size. In addition, they found that the cracks are deflected at the block boundaries, which change the crack path. The authors concluded that to control the block size is the best way to control the ductile–brittle transition in lath martensitic steels.

As the as-welded microstructure is originated from the solidification process the solidification grain size will be extremely large, and therefore, the package and blocks would also be expected to be large. Thus, in both martensitic passes (3^{rd} and 4^{th}) the coarse microstructure tends to be very harmful to toughness from a crystallographic point of view. However, despite displaying a coarse microstructure, the 3^{rd} weld pass was favored by the positive effect of Ni addition, which may act in reducing the DBTT.

9.5 Conclusion

Based on results shown in the present study, it was concluded that:

- The new approach for joint welding of API 5L X65 steel pipe with internal cladding of Alloy 625 using Alloy 686 and 100S-G steel as filler metals has great potential.
- The yield strength of the welded joint with API 5L X65, X70 and X80 steels was sufficient to attended the requirement for posterior installation by the reel lay process.
- The incorporation of large amounts of Ni into the dissimilar LAS weld pass with the Alloy 686 weld pass produced a soft martensitic matrix with A_{ret} particles located in some intercellular and interdendritic regions. For the second LAS weld pass, the reduction of dilution caused the formation of a hard martensite matrix with MA particles. Complex Ti carbonitrides were observed in both weld passes. The third LAS weld pass showed a bainitic matrix with some martensite and MA particles.
- The presence of several shrink porosities at macrosegregations located at dissimilar solidification interfaces impaired the impact toughness of the first two 100S-G steel weld passes. Moreover, the carbon incorporated by dilution from the steel pipe impaired the toughness, especially for the third LAS weld pass, since it caused the hardening of the martensite matrix and MA particles. Despite this, the impact toughness of this region attended the minimum required for an offshore pipeline to be installed by the reel lay process, 38J at -15°C.

REFERENCES

1 SILVA, C. C. *et al*. Austenitic and ferritic stainless steel dissimilar weld metal evaluation for the applications as-coating in the petroleum processing equipment. **Materials & Design**, v. 47, p. 1-8, 2013.

2 SUN, Z.; ION, J. C. Laser welding of dissimilar metal combinations. **Journal of Materials Science**, v. 30, n. 17, p. 4205–4214, 1995.

3 BALDRIDGE, T. *et al*. Laser cladding of Inconel 690 on Inconel 600 superalloy for corrosion protection in nuclear applications. **Optics and Lasers in Engineering**, v. 51, n. 2, p. 180-184, 2013.

4 SILVA, C. C. *et al*. A Study on the Effect of the Interpass Temperatures in Properties and Microstructures of the Alloy 625 Dissimilar Fusion Zone. **Materials Science Forum**, v. 783–786, p. 2816–2821, 2014.

5 KOURDANI, A.; DERAKHSHANDEH-HAGHIGHI, R. Evaluating the properties of dissimilar metal welding between Inconel 625 and 316L stainless steel by applying different welding methods and consumables. **Metallurgical and Materials Transactions A**, v. 49, n. 4, p. 1231-1243, 2018.

6 SILVA, C. C. Weld overlay. *In*: WANG, Q. J.; CHUNG, Y.-W. **Encyclopedia of Tribology**. 1 ed. New York: Springer, 2013. p. 4094-4101.

7 XU, X. *et al*. Research on microstructures and properties of Inconel 625 coatings obtained by laser cladding with wire. **Journal of Alloys and Compounds**, v. 715, p. 362-373, 2017.

8 SAROJ, S.; SAHOO, C. K.; MASANTA, M. Microstructure and mechanical performance of TiC-Inconel825 composite coating deposited on AISI 304 steel by TIG cladding process. **Journal of Materials Processing Technology**, v. 249, p. 490-501, 2017.

9 WANG, Q.-Y. *et al*. Microstructures, mechanical properties and corrosion resistance of Hastelloy C22 coating produced by laser cladding. **Journal of Alloys and Compounds**, v. 553, p. 253-258, 2013.

10 EVANGELINE, A.; SATHIYA, P. Dissimilar Cladding of Ni–Cr–Mo Superalloy over 316L Austenitic Stainless Steel: Morphologies and Mechanical Properties. **Metals and Materials International**, 2019.

11 BUNAZIV, I.; OLDEN, V.; AKSELSEN, O. M. Metallurgical aspects in the welding of clad pipelines-A global outlook. **Applied Sciences (Switzerland)**, v. 9, n. 15, 2019.

12 DUPONT, J. N. Solidification of an alloy 625 weld overlay. **Metallurgical and Materials Transactions A**, v. 27, n. 11, p. 3612–3620, nov. 1996.

13 SILVA, C. C. *et al*. Evaluation of the Corrosion Resistant Weld Cladding Deposited by the TIG Cold Wire Feed Process. **Materials Science Forum**, v. 783-786, p. 2822-2827, 2014.

14 MOHAMMADI ZAHRANI, E.; ALFANTAZI, A. M. Hot Corrosion of Inconel 625 Overlay Weld Cladding in Smelting Off-Gas Environment. **Metallurgical and Materials Transactions A**, v. 44, n. 10, p. 4671-4699, 2013.

15 MINÁ, É. M. *et al*. The effect of dilution on microsegregation in AWS ER NiCrMo-14 alloy welding claddings. **Metallurgical and Materials Transactions A: Physical Metallurgy and Materials Science**, v. 47, n. 12, 2016.

16 ROZMUS-GÓRNIKOWSKA, M.; BLICHARSKI, M.; KUSIŃSKI, J. Influence of weld overlaying methods on microstructure and chemical composition of Inconel 625 boiler pipe coatings. **Metallic Materials**, v. 52, n. 3, p. 141-147, 2014.

17 DUPONT, J. N.; BABU, S.; LIU, S. Welding of Materials for Energy Applications. **Metallurgical and Materials Transactions A**, v. 44, n. 7, p. 3385-3410, 2013.

18 SILVA, C. C. *et al*. New insight on the solidification path of an alloy 625 weld overlay. **Journal of Materials Research and Technology**, v. 2, n. 3, p. 228-237, 2013.

19 DAI, T.; LIPPOLD, J. Characterization of the Interface of an Alloy 625 Overlay on Steels Using Nanoindentation. **Journal of Materials Engineering and Performance**, v. 27, n. 7, p. 3411-3418, 2018.

20 ABIOYE, T. E.; MCCARTNEY, D. G.; CLARE, A. T. Laser cladding of Inconel 625 wire for corrosion protection. **Journal of Materials Processing Technology**, v. 217, p. 232-240, 2015.

21 JONES, R. L. *et al*. Reeled clad SCR weld fatigue qualification. *In*: OFFSHORE TECHNOLOGY CONFERENCE, 2011, Houston. **Proceedings**. Houston: Offshore Technology Conference, 2011. p 1-13.

22 SOUZA, R. F.; RUGGIERI, C. Fracture assessments of clad pipe girth welds incorporating improved crack driving force solutions. **Engineering Fracture Mechanics**, v. 148, p. 383-405, 2015.

23 CHONG, T.-V. S. *et al*. Effects of elevated temperatures on the mechanical properties of nickel-based alloy clad pipelines girth welds. **Engineering Fracture Mechanics**, v. 152, p. 174-192, 2016.

24 XU, L. Y.; JING, H. Y.; HAN, Y. D. Effect of welding on the corrosion behavior of X65/Inconel 625 in simulated solution. **Welding in the World**, v. 62, n. 2, p. 363-375, 2018.

25 XU, L. *et al*. Insights into the intergranular corrosion of overlay welded joints of X65-Inconel 625 clad pipe and its relationship to damage penetration. **Corrosion Science**, v. 160, n. 108169, p. 1-15. 2019.

26 CIESLAK, M. J.; HEADLEY, T. J.; FRANK, R. B. Welding metallurgy of custom age 625 PLUS alloy. **Welding Journal (Miami, Fla)**, v. 68, n. 12, p. 473s-482s, 1989.

27 SANDHU, S. S.; SHAHI, A. S. Metallurgical, wear and fatigue performance of Inconel 625 weld claddings. **Journal of Materials Processing Technology**, v. 233, p. 1-8, 2016.

28 BRUSCHI, R. From the Longest to the Deepest Pipelines. *In*: INTERNATIONAL OFFSHORE AND POLAR ENGINEERING CONFERENCE, 22., 2012, Rhodes. **Proceedings**. Rhodes: International Society of Offshore and Polar Engineers, 2012. p. 8-23.

29 WANG, Y. *et al*. Advances in deepwater structure installation technologies. **Underwater Technology**, v. 34, n. 2, p. 83-91, 2017.

30 BRUSCHI, R. *et al*. Pipe technology and installation equipment for frontier deep water projects. **Ocean Engineering**, v. 108, p. 369-392, 2015.

31 LIN, S. *et al*. Effect of cyclic plastic deformation on microstructure and mechanical properties of weld metals used for reel-lay pipeline steels. **Materials Science and Engineering: A**, v. 737, p. 77-84, 2018.

32 TOGUYENI, G. A.; BANSE, J. Mechanically lined pipe: installation by reel-lay. *In*: OFFSHORE TECHNOLOGY CONFERENCE, 2012, Houston. **Proceedings**. Houston: Offshore Technology Conference, 2012. p 1-15.

33 CHAUDHURI, J.; PIGLIAPOCO, M.; PULICI, M. The medgaz ultra deep water pipeline project. *In*: OFFSHORE TECHNOLOGY CONFERENCE, 2010, Houston. **Proceedings**. Houston: Offshore Technology Conference, 2010. p 1-10.

34 DNVGL. DNVGL ST F101: **Submarine Pipeline Systems**. Oslo. p. 520. 2017.

35 DNV. JIP: **Lined and Clad Pipeline Materials: Guidelines for Design and Construction of Clad and Lined Pipelines**. Oslo. 2007.

36 CIESLAK, M. J. The welding and solidification metallurgy of Alloy 625. **Welding Journal**, v. 70, n. 2, p. 49-56, 1991.

37 HODGE, F. G. The history of solid-solution-strengthened Ni alloys for aqueous corrosion service. **JOM**, v. 58, n. 9, p. 28-31, 2006.

38 AGARWAL, D. C.; HERDA, W. R. The “C” family of Ni-Cr-Mo alloys’ partnership with the chemical process industry: The last 70 years. **Materials and Corrosion**, v. 48, n. 8, p. 542-548, ago. 1997.

39 MISHRA, A. K.; SHOESMITH, D. W. Effect of alloying elements on crevice corrosion inhibition of nickel-chromium-molybdenum-tungsten alloys under aggressive conditions: an electrochemical study. **Corrosion**, v. 70, n. 7, p. 721-730, fev. 2014.

40 AMERICAN WELDING SOCIETY. AWS A5.28/A5.28M:2015: **Specification for Low-Alloy Steel Electrodes and Rods for Gas Shielded Arc Welding**. Miami. p. 40. 2015.

41 AMERICAN WELDING SOCIETY. AWS A5.11/A5.11M:2018: **Specification for Nickel and Nickel-Alloy Welding Electrodes for Shielded Metal Arc Welding**. Miami. p. 40. 2015.

42 LIPPOLD, J. C. Centerline cracking in deep penetration electron beam welds in type 304L stainless steel. **Welding Journal (Miami, Fla)**, v. 64, n. 5, p. 127s-136s, 1985.

43 SUN, Y. *et al*. Characterization and formation mechanism of periodic solidification defects in deep-penetration laser welding of NiCrMoV steel with heavy section. **The International Journal of Advanced Manufacturing Technology**, v. 100, n. 9, p. 2857-2866, 2019.

44 SILVA, C. C. *et al*. Assessment of microstructure of alloy Inconel 686 dissimilar weld claddings. **Journal of Alloys and Compounds**, v. 684, p. 628-642, 2016.

45 GORHE, D. D. *et al*. Electrochemical methods to detect susceptibility of Ni-Cr-Mo-W alloy 22 to intergranular corrosion. **Metallurgical and Materials Transactions A**, v. 36, n. 5, p. 1153-1167, 2005.

46 YANG, Y. K.; KOU, S. Mechanisms of Macrosegregation Formation near Fusion Boundary in Welds Made with Dissimilar Filler Metals. **Materials science and technology - Association for iron and steel technology**, v. 5, p. 3201, 2007.

47 ANDREWS, K. W. The Calculation of Transformation Temperatures and Austenite-Ferrite Equilibria. in Steels. **Journal of the Iron and Steel Institute**, v. 184, p. 414-427, 1956.

48 KANG, B. Y.; KIM, H. J.; HWANG, S. K. Effect of Mn and Ni on the variation of the microstructure and mechanical properties of low-carbon weld metals. **ISIJ International**, v.

40, n. 12, p. 1237-1245, 2000.

49 WANG, P.; KUMAR, K. S. Dynamic deformation response of a high-strength, high-toughness Fe–10Ni–0.1C steel. **Materials Science and Engineering: A**, v. 519, n. 1, p. 184-197, 2009.

50 KAUFMAN, L.; COHEN, M. The martensitic transformation in the iron-nickel system. **JOM**, v. 8, n. 10, p. 1393-1401, 1956.

51 YANG, H.-S.; BHADESHIA, H. K. D. H. Austenite grain size and the martensite-start temperature. **Scripta Materialia**, v. 60, n. 7, p. 493-495, 2009.

52 BISS, V.; CRYDERMAN, R. L. Martensite and retained austenite in hot-rolled, low-carbon bainitic steels. **Metallurgical and Materials Transactions B**, v. 2, n. 8, p. 2267-2276, 1971.

53 KRAUSS, G. Martensite in steel: strength and structure. **Materials Science and Engineering: A**, v. 273-275, p. 40-57, 1999.

54 MORSDORF, L. *et al*. Multiple mechanisms of lath martensite plasticity. **Acta Materialia**, v. 121, p. 202-214, 2016.

55 MINÁ, É. M. *et al*. Novel proposal for dissimilar girth welding of API 5L X65 steel pipe with an internal Alloy 625 cladding using both low alloy steel and Alloy 22 combined filler metals. **Materials Science and Engineering: A (under review)**, 2020.

56 MORRIS, J. W. Stronger, Tougher Steels. **Science**, v. 320, n. 5879, p. 1022-1023, 2008.

61 TANAKA, M. *et al*. Effects of Ni and Mn on brittle-to-ductile transition in ultralow-carbon steels. **Materials Science and Engineering: A**, v. 682, p. 370-375, 2017.

57 YAO, Z. *et al*. Effects of Ni and Cr on Cryogenic Impact Toughness of Bainite/Martensite Multiphase Steels. **Metals and Materials International**, v. 25, n. 5, p. 1151-1160, 2019.

58 YOU, Y.; SHANG, C.; SUBRAMANIAN, S. Effect of Ni addition on toughness and microstructure evolution in coarse grain heat affected zone. **Metals and Materials International**, v. 20, n. 4, p. 659-668, 2014.

59 MORRIS J.W., J. *et al*. The limits of strength and toughness in steel. **ISIJ International**, v. 41, n. 6, p. 599-611, 2001.

60 MORITO, S.; NISHIKAWA, J.; MAKI, T. Dislocation density within lath martensite in Fe-C and Fe-Ni alloys. **ISIJ International**, v. 43, n. 9, p. 1475-1477, 2003.

61 SHIUE, R. K.; LAN, K. C.; CHEN, C. Toughness and austenite stability of modified 9Cr–1Mo welds after tempering. **Materials Science and Engineering: A**, v. 287, n. 1, p. 10-16, 2000.

62 KIM, S.-H.; KANG, C.-Y.; BANG, K.-S. Weld metal impact toughness of electron beam welded 9% Ni steel. **Journal of Materials Science**, v. 36, n. 5, p. 1197-1200, 2001.

63 MORITO, S. *et al*. The morphology and crystallography of lath martensite in alloy steels. **Acta Materialia**, v. 54, n. 19, p. 5323-5331, 2006.

64 MORITO, S. *et al*. The morphology and crystallography of lath martensite in Fe-C alloys. **Acta Materialia**, v. 51, n. 6, p. 1789-1799, 2003.

65 TAKAKI, S.; KAWASAKI, K.; KIMURA, Y. Mechanical properties of ultra fine grained

steels. **Journal of Materials Processing Technology**, v. 117, n. 3, p. 359-363, 2001.

66 SONG, R.; PONGE, D.; RAABE, D. Mechanical properties of an ultrafine grained C–Mn steel processed by warm deformation and annealing. **Acta Materialia**, v. 53, n. 18, p. 4881-4892, 2005.

67 KIMURA, Y. *et al*. Inverse temperature dependence of toughness in an ultrafine grain-structure steel. **Science**, v. 320, n. 5879, p. 1057-1060, may. 2008.

68 KITAHARA, H. *et al*. Crystallographic features of lath martensite in low-carbon steel. **Acta Materialia**, v. 54, n. 5, p. 1279-1288, 2006.

69 SWARR, T.; KRAUSS, G. The effect of structure on the deformation of as-quenched and tempered martensite in an Fe-0.2 pct C alloy. **Metallurgical Transactions A**, v. 7, n. 1, p. 41-48, 1976.

70 INOUE, T. *et al*. The fracture of a low carbon tempered martensite. **Transactions of the Japan Institute of Metals**, v. 11, n. 1, p. 36-43, 1970.

71 MORRIS JR, J. W. *et al*. Microstructure and cleavage in lath martensitic steels. **Science and technology of advanced materials**, v. 14, n. 14208, p. 1-9, 2013.

Chapter 10

New proposal for joint welding of API 5L X65 steel pipe internally cladded with Alloy 625 combining different filler metals: Alloy 59 and low alloy steel

10.1 Abstract

The present study developed and evaluated a new design for the joint welding of an API 5L X65 steel pipe internally cladded with Alloy 625 using Alloy 59 and AWS ER100S-G steel. The 1st and 2nd passes deposited the Ni-based Alloy 59, in order to give good corrosion resistance similar to the Alloy 625 cladding. The low alloy steel (LAS) was used to fill the joint from the 3rd to the 10th passes and provide a yield strength (YS) overmatch in comparison to the API 5L X65 steel pipe. The microstructure and mechanical properties of the welded joint were assessed. Scanning electron microscopy techniques were used to analyze the microstructure, while the mechanical properties were assessed by transverse tensile, transverse all-weld, bending, microhardness map, hardness profile, and Charpy-V tests. The welded joint did not show any solidification cracks, only shrink porosities. The YS overmatch was sufficient for the API 5L X65, X70 and X80 steels. The resultant weld had a complex microstructure, in which the 1st and 2nd passes exhibited a γ-FCC matrix with secondary phases, while the 3rd and 4th weld passes showed a martensitic matrix with retained austenite (A_{ret}) and cubic carbides. The 5th weld pass exhibited a bainitic matrix with martensite, martensite-austenite (MA) microconstituents and carbides. The other passes of the welded joint showed an acicular ferrite (AF) matrix with MA particles. The energy absorbed for the LAS weld passes diluted with Alloy 59 in the impact toughness assay was 63 J.

10.2 Introduction

Dissimilar welding is a powerful manufacturing technique that combines materials from different classes, and is used to combine the best properties of selected materials in order to manufacture specific equipment and/or components[1–7]. Industries, such as the oil & gas industry, have been using dissimilar welding to manufacture risers based on steel pipes with internal CRA claddings[8–11]. The CRA cladding is commonly manufactured using a Ni-based alloy, and the Alloy 625 is the alloy most frequently used for this welding overlay[12–14], as it gives an extended life to the component at a good cost-benefit[10]. Initially designed for

weldability and high creep resistance for high thermal service, Alloy 625 has shown excellent resistance to corrosion in various environments since its development in the 60's[15]. Nonetheless, the welding overlay procedure to perform the dissimilar cladding of the steel pipe with the Ni-based alloy is well established. The challenge begins on welding procedure to join the risers.

Usually, the welding procedure recommends the same Ni-based alloy used on the internal cladding of the pipe for the joint, in order to avoid metallurgical problems caused by the mixing of different materials[16–18]. In addition, for the same reason a low dilution with the steel pipe is recommended[16]. Thus, it is possible to join pipes without solidification defects, especially cracks[16]. Naturally, the mechanical properties of the joint must be similar to the Ni-based alloy used. However, this will reduce the applicability of these pipes, especially for welding of HSLA steel pipes, such as API 5L X65, X70 and X80 steels, where a high yield strength is required[16,18].

Nowadays, the most attractive riser installation process is the reel lay method. Different from the traditional methods such as S-lay and J-lay, the reel lay method joins or welds the pipes at an onshore unit close to the docks. This enables high quality weldments with good productivity and easy inspection. After welding, the pipeline is spooled onto a large diameter drum on a pipe-laying vessel for transportation. Subsequently the pipeline is unspooled offshore during the installation of the subsea pipeline. During the bending and unbending deformation or spooling and unspooling steps about 2% of plastic deformation is introduced into the pipe, including the welds[19]. Considering that the welding process may introduce some defects such as porosity, shrink porosity, solidification cracks and reheat cracks as well[20], the reel lay process requires high quality welding with excellent mechanical properties.

The general recommendation is that a girth weld must have a YS overmatch of about 100 MPa in comparison to the standard minimum yield strength (SMYS) of the base metal[21]. Nonetheless, the DNVGL ST F101 standard, that sets the rules for the installation of pipelines by the reel lay process[22], has established that the YS of a girth weld must be at least equal to the maximum YS of the base metal minus 20 MPa. This severe overmatch criterion is defined to increase the safety of the component, since the pipeline will experience about 2% of deformation during the reel lay installation. Therefore, it is necessary to select materials that will provide the mechanical properties required along with good weldability. According to the literature Alloy 625 weld metal only has sufficient yield strength overmatch for API 5L X65 steel (550 MPa) after word hardening caused by the bending and unbending steps during the

reel lay installation process. A DNV report classifies this kind of girth weld as a 'partially overmatch' and recommends that this is taken into account in all calculations[23]. Beside this, the Alloy 625 is reported to be an alloy with high solidification crack susceptibility[24], especially for dissimilar welding.

The incorporation of Fe through dilution with the steel pipe makes the nucleation of eutectic phases such as Laves possible, and this would impair the weld metal through the nucleation of solidification cracks[12]. Thus, new solutions are clearly needed to make the reel lay process viable for the installation of rigid risers with internal cladding.

An alternative to carry out the girth welding of steel pipes with internal CRA cladding is to use LAS, in order to obtain the overmatch of the mechanical properties. Nonetheless, a mixture of alloys from different classes of materials may promote metallurgical defects. Therefore, good metallurgical compatibility of the LAS with the Ni-based cladding alloy is necessary. In general, the mixture of steel and Ni-based alloys may cause solidification cracking due to the nucleation of eutectic phases at the final stage of solidification, especially in the case of Alloy 625[12,13,24–26]. Cieslak *et al*. evaluated the solidification cracks of Alloy 625 weld metal varying the fraction of Si, C and Nb[26]. The authors highlighted high solidification crack susceptibility characterized by wider fusion/solidification due to nucleation of the eutectic phases such as NbC, Laves and M_6C at the final stage of solidification[26]. In this case, the addition of Nb showed a more deleterious effect than that of Si and C[26]. Therefore, a concise selection of materials is necessary to mix with LAS in order to avoid solidification defects.

Other Ni-based alloys may substitute the Alloy 625 in order to overcome this challenge, offering similar or better oxidation and corrosion resistance. The Ni-based Alloy 59 appears as a good option. Alloy 59 was first designed in 1990 in order to improve corrosion resistance of some components used in coal-fired power stations. The more common Ni-based alloys such as Alloy 625, Alloy C276 and Alloy 22 were not capable of maintaining the integrity of these components under such corrosive environments[15]. Alloy 59 was developed based on the Ni-Cr-Mo ternary system without the addition of any other alloying elements such as W, Cu, Nb and Ti[27]. Thermodynamic simulation was used to design the Alloy 59 along with good thermal stability. This meant that the alloy was designed to exhibit a very low precipitation of deleterious phases that notably impair corrosion resistance[27]. The very high Cr and Mo confer the Ni-Cr-Mo alloys with excellent corrosion resistance due to the spontaneous formation of a stable nanometric oxide layer on their surfaces[28]. Lou *et al*.[29] assessed the Alloy 59 under H_2SO_4 acid solution and highlighted its fast and stable passivation in a large field of potential

range from 0 to 0.9V. This strong passivation was due to the formation of Cr_2O_3, $Cr(OH)_3$ and $Ni(OH)_2$ with support from Mo oxides from range of Mo(VI) and Mo(IV)[29].

Previous chapters have demonstrated through thermodynamic simulation that Alloy 59 has good metallurgical compatibility when diluted with API 5L X65 steel, considering that no eutectic phases were predicted in the solidification simulation. The same tendency was predicted in another study, that assessed the deposition and consequent dilution of AWS ER 100S-G steel with Alloy 59, in which again no low melting point phases were predicted in the solidification simulation. Moreover, an experimental study evaluated the deposition of 100S-G steel on Alloy 59 cladding, in which the authors highlighted low solidification crack susceptibility of the weld metal, even when a very high dilution of approximately 50% was applied.

Based on this background concerning the engineering challenge, the present study using a new design, manufactured and evaluated a girth weld of a riser internally cladded with Alloy 625 for subsequent pipeline installation by the reel lay process. The complex dissimilar girth welding was performed using two filler metals from different classes of materials: Alloy 59 and AWS ER100S-G steel. The Ni-based Alloy 59 was used for the root and hot passes in order to assure a corrosion resistance similar or superior to the inner cladding of the riser. The 100S-G was selected to fill the largest part of the joint, in order to provide an overmatch of mechanical properties in comparison to the API 5L X65 steel pipe, attending the DNVGL ST F101 requirements. All the microstructure and mechanical properties of the welded joint were assessed.

10.3 Experimental procedure

The welding of the joint was performed on an API 5L X65 steel pipe internally cladded with Alloy 625. The 1st and 2nd passes of the welded joint were done with Ni-based Alloy 59, in order to secure a corrosion resistance similar or superior to the Alloy 625 cladding. The greater part of the joint, from the 3rd to the 10th pass, was filled using the AWS ER100S-G steel (LAS). The 100S-G steel was selected to provide an overmatch of the mechanical properties in comparison with the API 5L X65 steel for the welded joint[30,31]. A schematic drawing of the proposed welded joint is shown in Figure 10-1. Table 10-1 gives the chemical composition of all materials used in the present study. The chemical compositions were acquired from optical spectroscopy measurements.

The welded joint was manufactured by the pulsed gas metal arc welding process (GMAW-P). All weldments were performed on an industrial robotic workbench with a weld torch, providing accuracy of movement. The filler metals used were the AWS ER NiCrMo-13 (Alloy 59) and AWS ER 100S-G steel (LAS), both with a diameter of 1.2 mm and under 100%Ar and 98%Ar + 2%CO_2 shielding gases, respectively. Figure 10-2 exhibits the workbench used for the joint welding. Table 10-2 gives the main welding parameters of each pass used to fill the weld joint. The welding speed was reduced from the 1st pass onward in order to deposit one weld pass by weld layer to fill the weld groove. This led to a continuous increase in welding heat input.

Figure 10-1. Schematic drawing of the proposed welded joint.

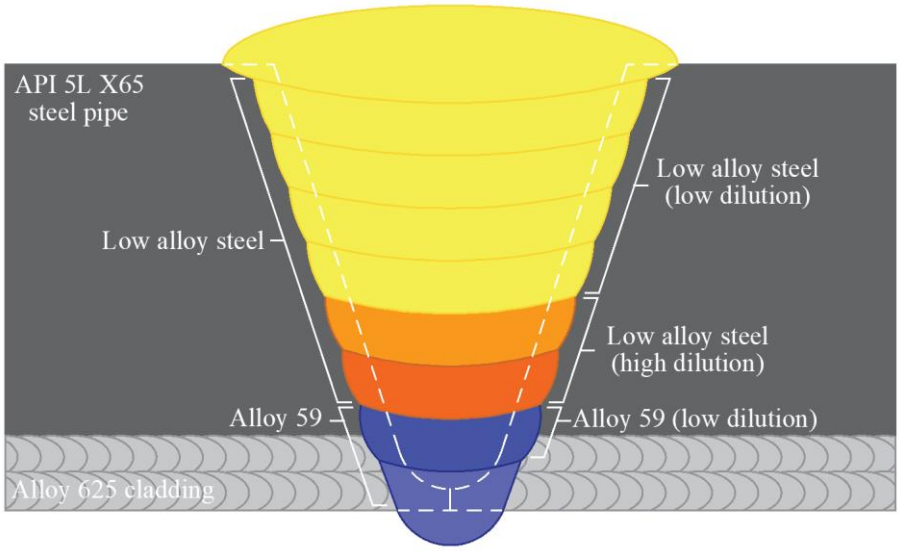

Source: Developed by the author.

Table 10-1. Chemical compositions of the materials used in the dissimilar joint welding.

Chemical composition of materials												
Alloy	Al	C	Cr	Cu	Fe	Mn	Mo	Ni	P	S	Si	Ti
Alloy 59 (AWS ER NiCrMo-13)	-	0.015	22.78	0.05	0.77	0.23	15.4	60.42	0.015	0.005	-	0.01
API 5L X65 steel pipe	0.04	0.11	0.12	0.18	97.51	1.17	0.14	0.34	0.012	0.004	0.28	-
AWS ER100S-G steel	-	0,04	0.12	0.11	96.47	1.37	0.38	0.82	0.055	0.014	0.62	0.13

Source: Developed by the author.

Macrographic and micrographic analyses were made of the welded joint, after the surface of the transverse cross-sections of the welded joint were prepared by conventional metallography. The samples were etched using 2% nital and 10% acid chromic solutions to revel the microstructure of the LAS and Ni-based alloy passes, respectively. The microstructure was assessed using scanning electron microscopy (SEM) techniques.

The mechanical behavior of the welded joint was evaluated following the recommendations of DNVGL ST F101[22]. Two transverse tensile and four bending tests were performed in order to verify the integrity of the welded joint. These tests are useful to verify if the welding procedures adopted were suitable. Rupture in the fusion zone without evidence of defects may indicate that an unsuitable filler metal was used, while defects such as lack of fusion, porosity, shrink porosities and solidification cracks could be the result of incorrect welding parameters. Figures 10-3a and 10-3c show a schematic image of the bending and transverse tensile test samples.

Figure 10-2. Industrial robotic workbench with a) welding torch. The welding torch position b) before and c) after a welding pass.

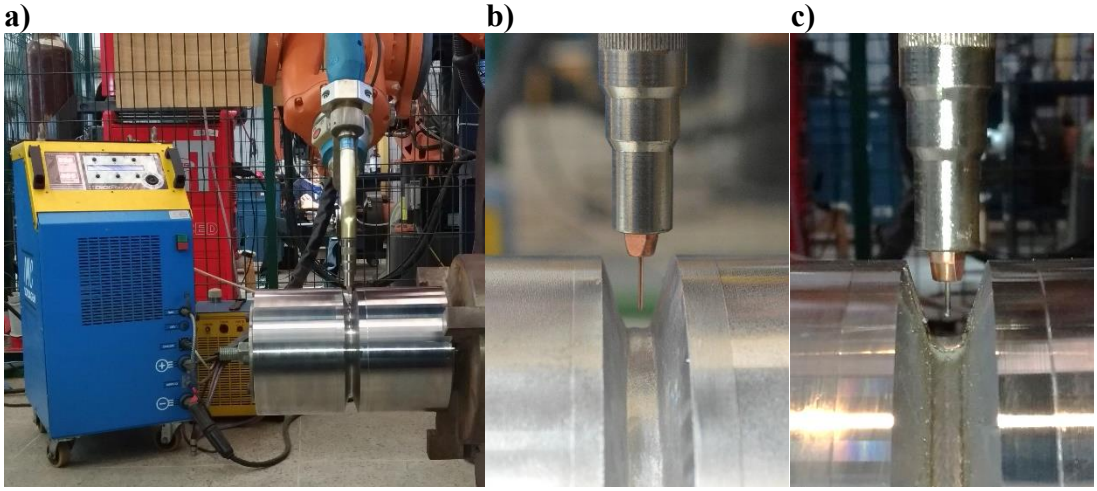

Source: Developed by the author.

Table 10-2. Main welding parameters used for each weld pass.

Welding parameters										
Passes	Alloy	I_p (A)	I_b (A)	t_p (s)	t_b (s)	S_w (cm/min)	U (V)	S_{wf} (m/min)	A_t (mm)	HI_w (kJ/mm)
1st pass	Alloy 59	300	90	2.2	4.4	45	20.9	7.2	0.6	0.50
2nd pass	Alloy 59	300	90	2.2	4.4	40	21.4	7.0	2.2	0.58
3rd pass	100S-G	300	90	2.2	4.4	35	21.6	5.5	3.7	0.65
4th pass	100S-G	300	90	2.2	4.4	35	20.1	5.5	4.7	0.62
5th pass	100S-G	300	90	2.2	4.4	25	20.2	5.5	5.5	0.88
6th pass	100S-G	300	90	2.2	4.4	18	20.2	5.5	6.0	1.23
7th pass	100S-G	320	100	2.2	4.4	15	21.7	5.8	6.5	1.75
8th pass	100S-G	320	100	2.2	4.4	14	21.9	5.8	7.0	1.75
9th pass	100S-G	320	100	2.2	4.4	13	22.2	5.8	7.5	1.89
10th pass	100S-G	320	100	2.2	4.4	12	22.6	5.8	8.4	2.11

Source: Developed by the author.

The yield strength of the welded joint was assessed using the transverse all weld tensile test and was performed following the recommendations of DNVGL RP F108[32]. Two

samples of each one of the four different regions of the welded joint were evaluated. The root-hot passes (1st – 2nd), high dilution LAS passes (3rd – 4th), low dilution LAS passes (5th – 6th) and filling region (7th – 8th) were all assessed. These tests are important to obtain the main mechanical properties of this complex dissimilar welded joint. Figure 10-3b shows a diagram of the specimen.

Figure 10-3. Schematic draw of specimens: a) bending, b) transverse all-weld tensile, c) transverse tensile and d) Charpy-V with notch at the 3rd weld pass.

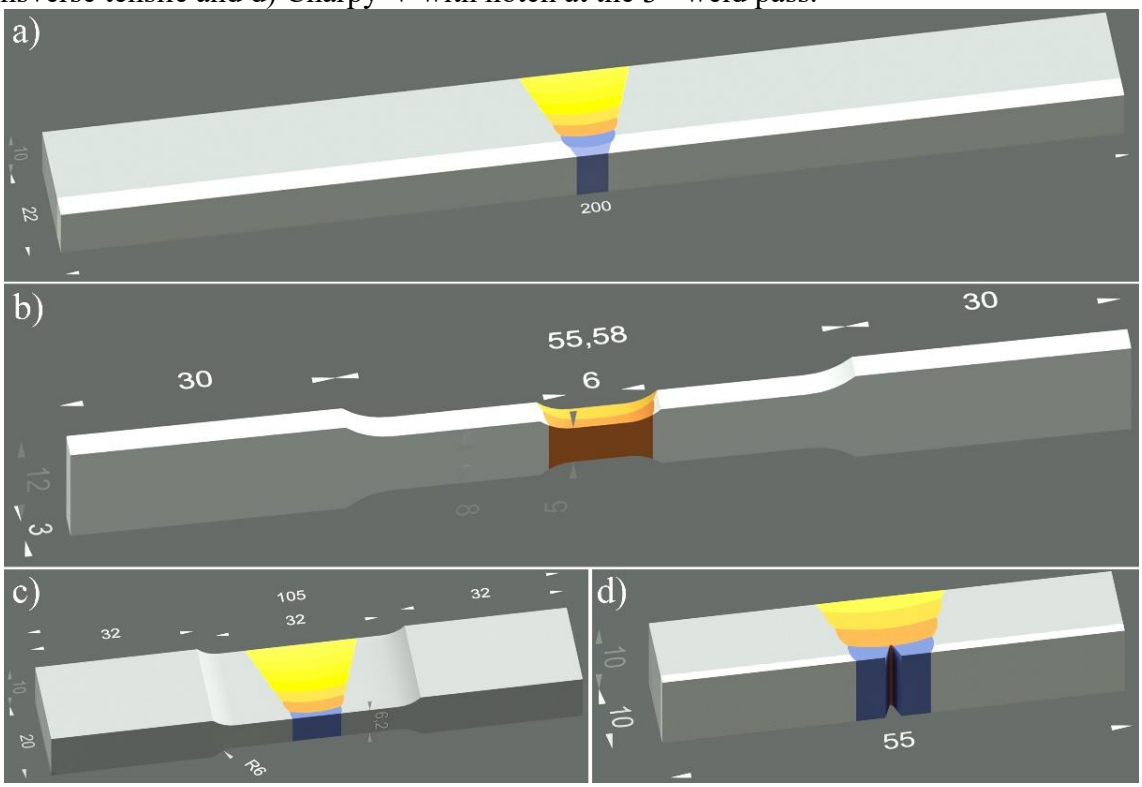

Source: Developed by the author.

The hardness of the welded joint was assessed through a microhardness map and hardness profile. The microhardness map was made using a 100 gf load with 300 μm spacings between the indentations giving a good spatial resolution. The hardness profile was made along of weld passes with a 10 kgf load and 1 mm spacings between indentations.

The toughness of the welded joint was assessed by Charpy-V test. Five Charpy-V impact tests were performed with the notch positioned at the beginning of the 3rd pass in order to assess the effect of dilution on the toughness of the first 100S-G pass deposited on the Ni-based Alloy 59 pass. A schematic drawing of the Charpy-V impact samples is shown in Figure 10-3d.

10.4 Results and Discussion

10.4.1 Weldability of welded joint

An import characteristic to be considered for dissimilar welding is the weldability of the system (filler metal and base metal). Weldability is the ease in which a weld is made without defects, and producing the desired properties. One of the main factors of weldability is the 'wetting' between filler metal and base metal. Wetting has been highlighted due to its potential to create weld defects. A good wetting enables the welding of narrow gap grooves, where the bevel angle is very small. On the other hand, a bad wetting impairs the fusion and the filling of the edges of the joint, causing a lack of fusion along the side wall[33].

Based on the above the proposed joint welding of a riser using 100S-G steel and Alloy 59 showed good wetting, the combination of these alloys showed good wetting. The deposition of Alloy 59 showed good wetting when deposited on the Alloy 625 cladding, producing a concave feature along the edges of the pass. The same characteristic was observed for the deposition of 100S-G steel on the Alloy 59 pass. This good wetting was obtained even when using a low welding heat input. This shows the good weldability characteristic of this new design for dissimilar girth welding of a CRA cladded riser and enables the use of other welding parameters without impairing the weldability. Low and high welding heat inputs (HI_w) can be used with the aim to avoid metallurgical problems or undesired mechanical properties. When, the wetting of the welding system is bad, normally, it is necessary to use a high HI_w in order to improve the wetting by reducing the surface tension. The macrograph of the welded joint displayed in Figure 10-4 demonstrates this good weldability.

This macrograph provides information about this complex dissimilar welded joint. The API 5L X65 steel pipe was cladded by two layers of Alloy 625. The 1st (root) and 2nd passes were deposited using Alloy 59 showed a similar contrast of the Alloy 625 cladding. Next, the 3rd pass was not etched sufficiently by the regents because the high dilution of 100S-G steel with Alloy 59 pass caused the incorporation of a large amount of Ni, Cr and Mo, which possibly made this new alloy relatively inert to chromic acid and nital. Moreover, the 4th pass was partially etched if compared with the subsequent 100S-G steel passes, indicating the influence of dilution.

No defects such as lack of fusion, porosity and solidification cracks were observed. Each weld pass was deposited keeping a low depth-to-width (D/W) rate. During the welding the solidification grains (SG) grew normal to the solid-liquid interface, following the direction

of the thermal gradient[34]. Furthermore the shape of the weld pool pass has a significant influence on the size and direction of growth of the SG. The low D/W promoted an elliptical weld pool shape and, consequently caused the SG to grow from the base in the direction of the welding surface. This prevented the SG meeting at the weld centerline, reducing the accumulation of elements segregated during solidification. On the other hand a high D/W pass gives the weld pool a teardrop shape, and this cause an intense microsegregation at center of welding leading to weld centerline solidification cracks[34,35].

Figure 10-4. Macrograph of the transverse cross-section of the welded joint and the microstructure of main passes.

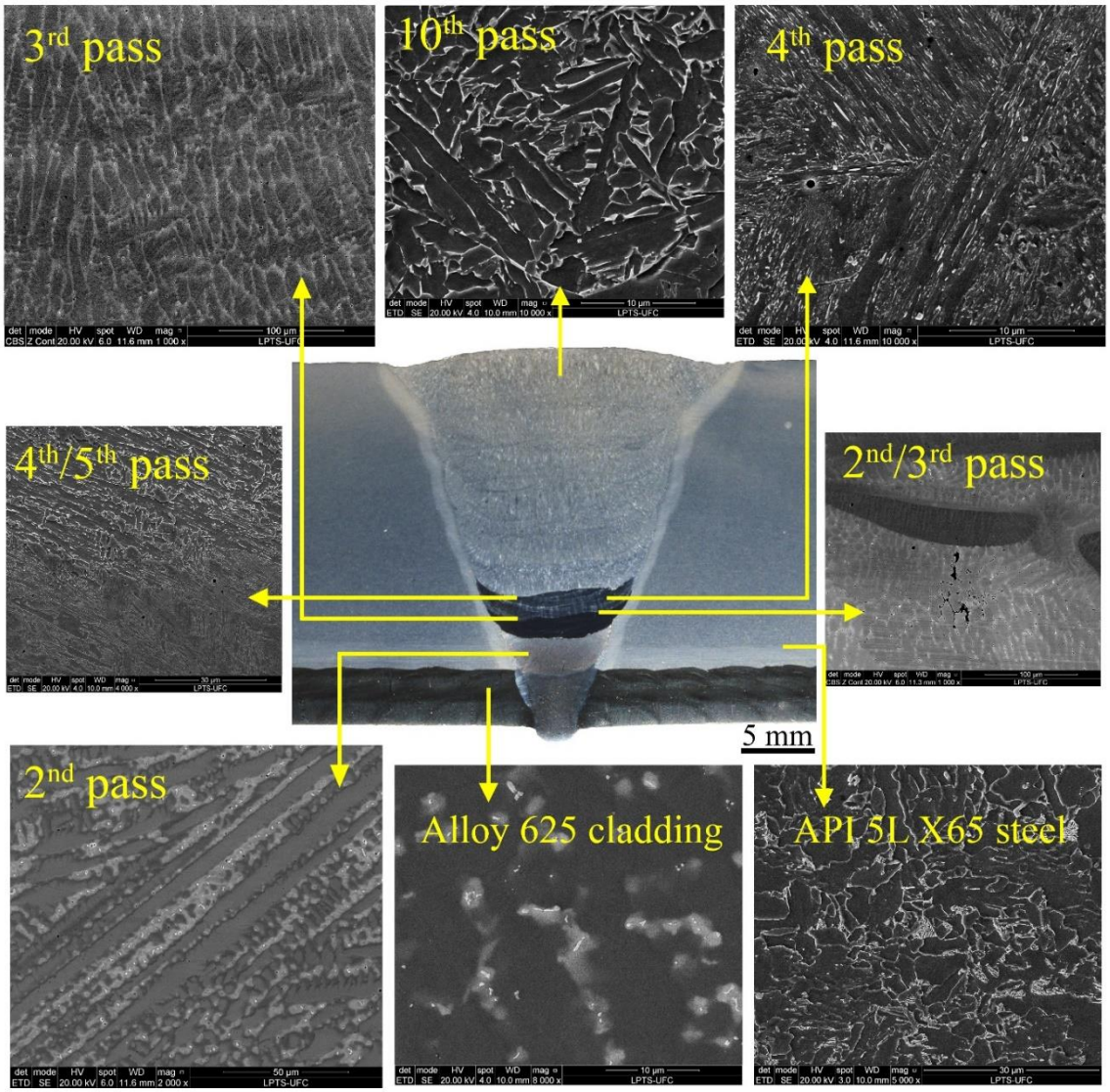

Source: Developed by the author.

The absence of solidification cracks followed the tendency predicted by studies in previous chapters of thermodynamic simulations of the solidification of these dissimilar welds.

According to these studies, the dilution of Alloy 59 with API 5L X65 steel showed good welding compatibility. The results of thermodynamic simulation for the solidification of Alloy 59 show a low solidification temperature range, even for a high dilution level, in which only a low fraction of σ phase and M_6C were predicted in equilibrium with the γ-cfc matrix. Based on these results the study concluded a low solidification crack susceptibility for welding Alloy 59 with API 5L X65 steel. Using the same method, the solidification simulation of 100S-G steel deposited on Alloy 59 was assessed by thermodynamic simulation. The study pointed out a low solidification crack susceptibility, considering the prediction of only a small fraction of M_6C at the final stage of solidification. Even for a high dilution level the increase of Ni, Cr and Mo were not enough to predict, by simulation, the nucleation of the σ phase. Furthermore, an experimental study of welding 100S-G steel on Alloy 59 cladding reveled aspects of solidification cracking, corroborating with the results of the present study. The high dilution obtained on single weld beads, approximately 50%, caused the addition of a high fraction of alloying elements, which did not promote a significant fraction of secondary phases. No cracks were observed in this study, and only a few shrink porosities were observed in the fusion zone localized between the SG, especially in the macrosegregation regions rich in Alloy 59. Moreover, the study highlighted an opposite behavior for the dilution of 100S-G steel with Alloy 625 cladding, in which a large fraction of secondary phases were observed at the interdendritic regions due to the intense segregation of Nb and Mo. These precipitates caused the formation of cracks due to their low melting points, that increase the susceptibility to solidification cracks considerably. All these studies support the low solidification crack susceptibility observed in the present study.

The chemical compositions of the 1st to the 6th weld passes of the welded joint are presented in Figure 10-5. The Ni fraction, predominant in the Ni-based alloys, was reduced from the 3rd pass onward due to dilution with the 100S-G steel. The evolution of the chemical composition clearly shows that there is a transition from the Ni-based alloy to the low alloy steel. Probably, the 3rd and 4th pass can be classified as high alloy steels due to the strong incorporation of Ni, Cr and Mo, of approximately 24 wt% and 10 wt% of these alloying elements, respectively. These elements enable an increase of the oxidization and corrosion resistance of the alloy[28], and also increase the strength by solid solution and quenching.

Nb is an alloying element commonly added to Ni-based alloys in order to increase the strength of the alloy and stabilize the carbon content. However, the Nb content in the weld passes decreased to almost zero in the 1st pass. Nb has a low solubility in a γ-Ni matrix and a

high affinity with C, Si and Fe. Thus, only a small fraction of Nb leads to eutectic reactions such as γ + NbC and/or γ + Laves phase. According to Dupont *et al.*[36], eutectic reactions will occur depending of the C content able to react with Nb. Ni-based alloys with high C content will show γ nucleation followed by the γ + NbC reaction at final stage of solidification. While, Ni-based alloys with low C content have the tendency to form Laves phase. The NbC phase different from Laves phase has good mechanical effects, blocking dislocation motion, increasing the strength, improving the creep resistance and preventing ductility dip cracks[40–42]. The small concentrated particles located at the solidification grain boundary act as a pinning point on the matrix[40]. On the other hand, the Laves phase has a very low melting point, which helps extend the solidification temperature range causing the formation of solidification cracks during the final stage of solidification[12,13,26,41–43]. Therefore, two weld passes of the Nb-free Ni-based alloy (Alloy 59) were designed for the root and hot passes in order to dilute the Nb present in the Alloy 625 cladding. Thus, the first 100S-G steel pass diluted with the second Alloy 59 pass will incorporate only Ni, Cr and Mo. This decision was important to minimize the solidification crack susceptibility of the 3rd pass of the welded joint.

Figure 10-5. Chemical composition of the 1st, 2nd, 3rd, 4th, 5th and 6th passes of the welded joint. The arrows indicate the scale side.

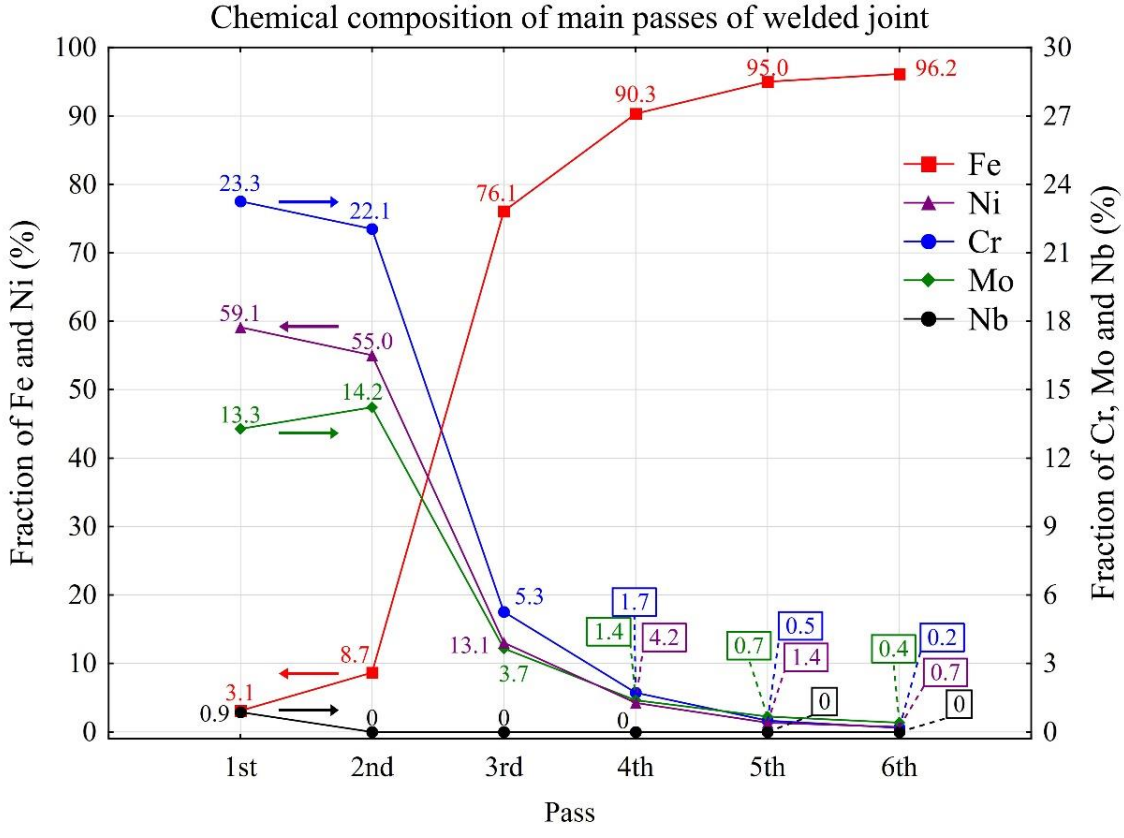

Source: Developed by the author.

10.4.2 Microstructural analysis

The microstructure of the welded joint was assessed using SEM techniques in order to understand and provide support for the discussion of the mechanical properties obtained. In general, the microstructure of the 1st and 2nd passes of the Alloy 59 exhibited features similar to other Ni-based alloys from the Ni-Cr-Mo class[13,44–46]. Figure 10-6 shows the microstructures of the 2nd weld pass. Here a dendritic microstructure with its respective interdendritic region was seen along with a very small fraction of precipitates. The low HI_w led to a fast cooling rate, which minimized the microsegregation of the alloying elements during solidification. Moreover, the development of the Alloy 59 must be taken into account. As mentioned, the conception of Alloy 59 was based on a Ni-Cr-Mo ternary system so as to result in a very low microsegregation of alloying elements during solidification[27]. Thus, Alloy 59 shows an almost negligible precipitate fraction in the as welded condition. This feature enables the use of Alloy 59 in several different corrosive environments, and even for high temperature service due to its good thermal stability[15,27,47]. Moreover, according to Heubner and Köhler[48], based on a time-temperature-sensitization diagram of Alloy 59, more time is necessary to sensitize this alloy in comparison to other alloys of the same family such as Alloy 276, Alloy C4 and Alloy 22. The authors believe that sensitization was due to μ, P and M_6C nucleation similar to what has been reported for Alloy C276[48]. On the other hand, the previous thermodynamic study predicted the solidification path based on the classical model of Scheil-Gulliver[30], which did not predicted any μ and P phases:

$$L \rightarrow L + \gamma \rightarrow L + \gamma + \sigma \rightarrow L + \gamma + \sigma + M_6C$$

Thus, probably, the precipitates observed in the 2nd pass were originally from solidification, since the liquid metal solidified quickly and, therefore, there was only a short time for solid transformations during cooling, and probably the particles are composed of σ phase and M_6C[30]. Even so, the reheat provided by the subsequent passes may have induced to solid transformations, which may have dissolved the precipitates in the γ phase or led to the nucleation of other TCP phases such as the μ and P phases.

Figure 10-7 shows the microstructure of the 3rd weld pass. Shrink porosities were observed close to the solidification interface between the 2nd and 3rd passes (Figure 10-7a). These solidification defects occurred in a filler-deficient region at the solidification interface. During the welding, a small volume of base metal melts (Alloy 59 pass), however, the fast

solidification did not allow enough time for it to mix with the 100S-G steel filler metal. In addition, this melted layer of the base metal is located close to the solid-liquid interface, in a region that in terms of mechanical fluids means that the fluid will exhibit a low velocity, and thus impair its mixture with the weld metal[49]. This rich region of the base metal has a relatively smaller liquidus temperature (T_L) than LAS, in other words, its solidification occurs after the bulk of the weld metal, inducing the formation of shrink porosities easy. According to the literature, dissimilar welding of materials with significant differences in liquidus temperatures leads to the occurrence of macrosegregation. For this specific case, where the T_{LW} (weld metal) is higher than the T_{LB} (base metal) the most common macrosegregations are related to rich regions of the base metal along the fusion boundary[50,51].

Figure 10-6. Microstructure of a) solidification interface between steel pipe and the 2nd Alloy 59 pass and b) the bulk of microstructure of the 2nd pass.

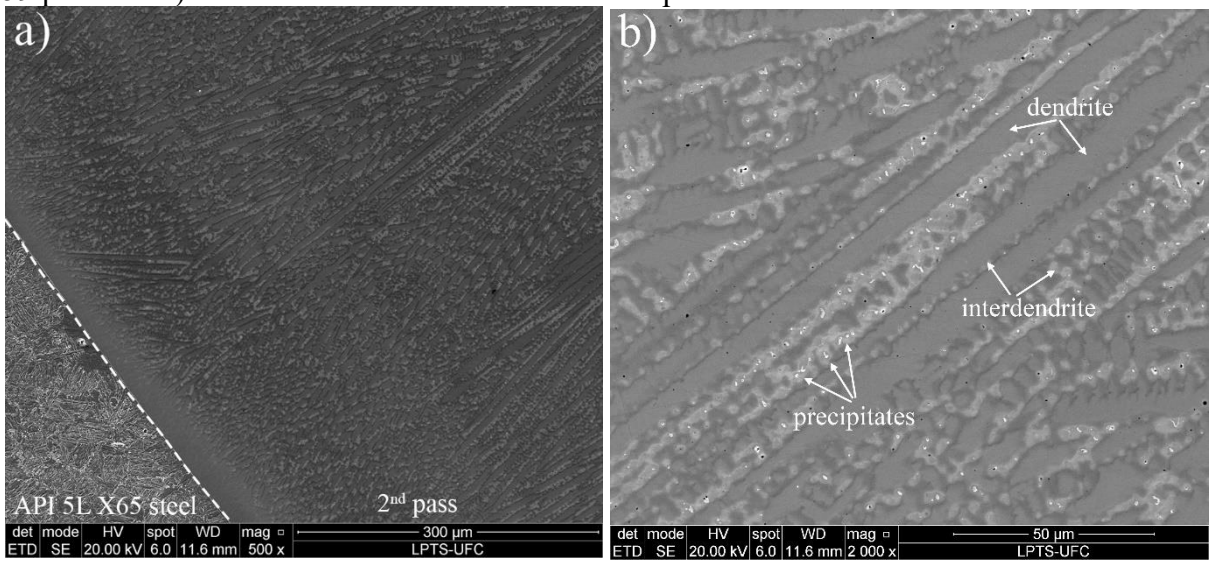

Source: Developed by the author.

The bulk of the 3rd weld pass did not show any solidification cracks. On the other hand, the microstructure was strongly affected by the dilution of 100S-G steel (3rd pass) with the Alloy 59 pass (2nd pass) due to the incorporation of a high fraction of alloying elements such as Ni, Cr and Mo. Figure 10-7b shows the microstructure with evidence of segregation at the intercellular region. Moreover, straight lines with a 45º in relationship to the direction of the cell growth of the cells were observed. This feature is typical of diffusionless solid transformations. Probably, this microstructure is formed by a martensitic matrix due to its good quenching ability caused by the incorporation of Ni, Cr and Mo. The low HI_w used to deposit this weld pass also contributed to the martensitic transformation, since the weld pass experienced a fast cooling rate, which provided the shear stress indispensable for diffusionless

transformations. Nonetheless, the high Ni content, about 13%, may lead to the formation of retained austenite, even for a high cooling rate, especially for rich regions of a filler metal, where the Ni content is slightly higher than the bulk of the weld metal.

Figure 10-7. Microstructure of the 3rd pass highlighting a) the fusion boundaries between passes and shrink porosities at the begin of the 3rd pass and, b) the bulk of the microstructure of the 3rd pass exhibiting a shear microstructure at the core of the cell.

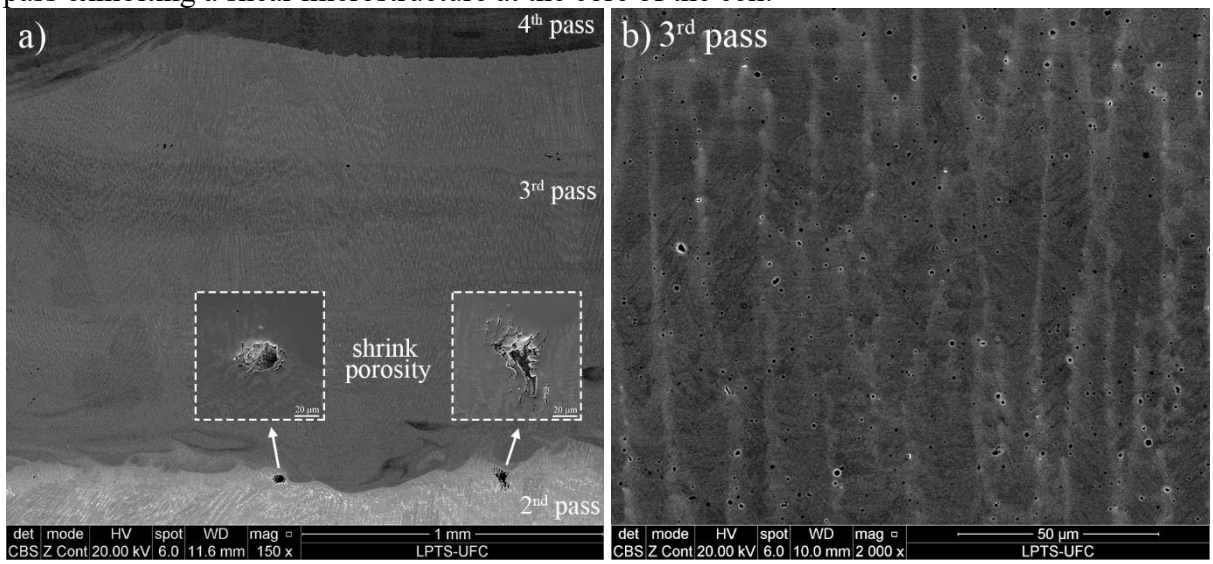

Source: Developed by the author.

Thermodynamic simulations were carried out in order to provide more information about the martensite transformation. Figure 10-8 shows the equilibrium simulation performed. The 3rd weld pass started the solidification as γ-FCC. Some carbides and other TCP phases like μ and Laves phases were predicted as the material cooled. This may explain the presence of shrink porosities observed at the interface between the 2nd and 3rd weld passes, since Laves phase represent a eutectic phase with a very low melting point[12,26,40,52]. In fact, at 606°C the γ-FCC becomes unstable in detrimental of the nucleation of α-BCC. Nonetheless, the fast cooling prevents the diffusion of elements, which impairs the transformation of γ-FCC to α-BCC. In addition, the high thermal gradient causes a high contraction stress, which causes the shear of the γ-FCC lattice, thus transforming it into martensite.

A second etching was done only to assess the microstructure of the 3rd weld pass. This time a higher concentration of HNO_3 was used for a longer period. The severe etching aggressively eroded the steel pipe and the LAS weld passes from the 4th weld pass onward. Figure 10-9 shows a macrograph using light microscopy imaging. The huge formation of macrosegregations along the weld pass can be clearly seen. The dark regions represent the rich regions of the filler metal, since this was more seriously corroded by the etching, whereas the

light regions have a higher concentration of the base metal. According to the literature these macrosegregations are a result of an incomplete mixture of the materials and represents an inherent phenomenon of dissimilar welding[53].

Figure 10-8. Equilibrium simulation of the phase fraction of the 3rd weld pass.

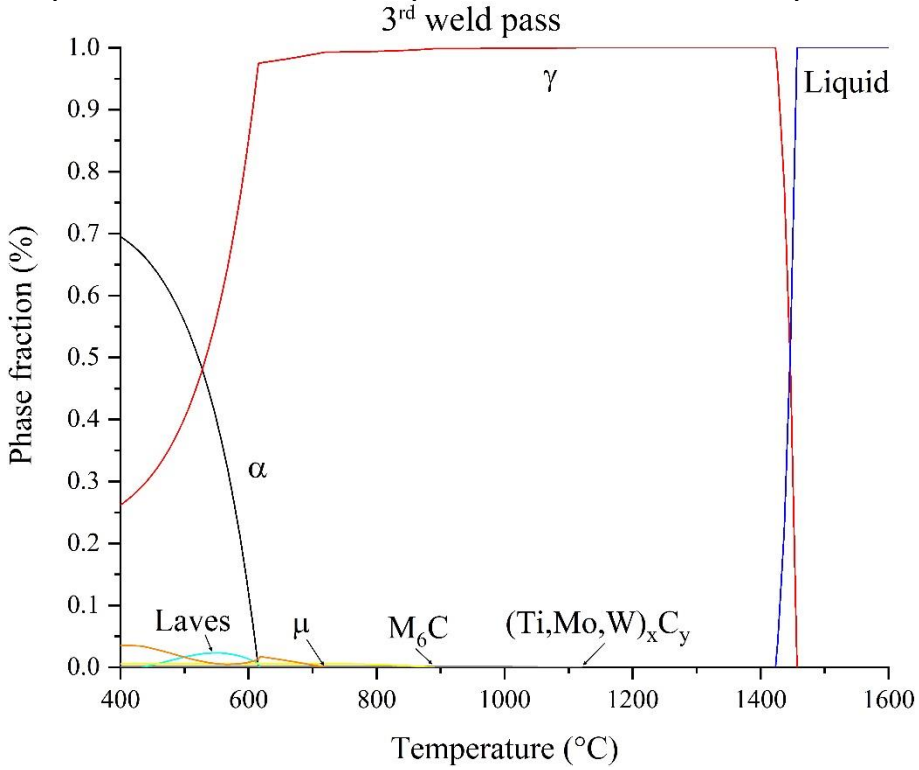

Source: Developed by the author.

Figure 10-9. Macrosegregations observed in the 3rd weld pass after severe etching.

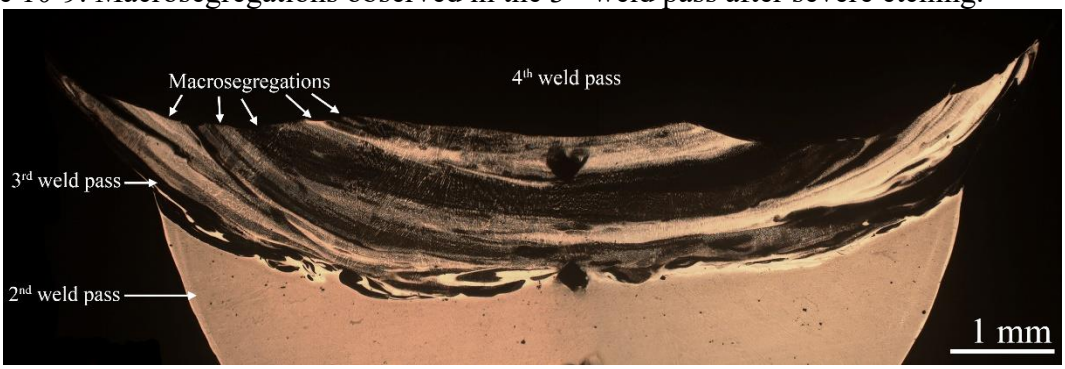

Source: Developed by the author.

Yang and Kou[50] evaluated the macrosegregation phenomenon, assessing various Cu-Ni alloys. Sheets of Cu-30Ni and pure Cu and pure Ni wires were used to create different mixtures. The authors divided the phenomenon in two different mechanisms, based on the liquidus temperature of the mixed materials. When the base metal has a lower liquidus temperature in comparison with the filler metal and consequently their resultant mixture, which

is the case of the deposition of the first LAS weld pass on the Alloy 59 weld pass. In this case here, the arc welding causes a significant penetration into the base metal, melting a considerable portion that is pushed into the bulk of the weld metal and then cools quickly before a total mixture of the materials occurs. In such cases, where the base metal has a lower liquidus temperature, it is virtually impossible to have a total mixture.

A rich region of the filler metal was selected to assess the microstructure, since the second etching was more revealing. Figure 10-10 shows the microstructure of the 3rd weld pass. The severe etching revealed a shear microstructure typical of diffusionless transformations like martensite. This feature was observed in the full weld pass, but some blocks were observed at the interdendritic core, which are probably A_{ret}. The microsegregation during solidification caused a concentration of Ni, Mn and C that caused a local reduction of the martensite start (M_S) temperature. In general, the addition of alloying elements causes a reduction of M_s and the martensite final (M_F) temperature, especially with the elements that increase the stabilization field of γ-FCC. The MS temperature of the dendrite core and A_{ret} particles were investigated based on the Andrews[54] model (Equation 1). Table 10-3 shows the chemical composition obtained by EDS analyses. In fact, the A_{ret} particle observed at the interdendritic region is rich in Ni, Mn and Mo, while the dendrite has a chemical composition similar to the bulk of the weld metal. This was reflected in the M_S temperature of A_{ret} and dendrite, which exhibited 91°C and 262°C, respectively. Probably the M_F temperature of the A_{ret} particle is below or close to room temperature. Kaufman and Cohen[55] investigated the M_S and M_F temperatures of alloys of the Fe-Ni system by dilatometry. The M_S and M_F obtained for the alloys Fe-14.5Ni, Fe-19Ni and Fe-27.75Ni were 350°C and 230°C, 210°C and 103°C, 120°C and 25°C, respectively. Note that addition of Ni caused the reduction of both M_S and M_F. In addition, the ΔT for full martensite transformation varied from 95 – 120°C. Therefore, it is reasonable to suppose that the M_F of the A_{ret} particle is below or close to room temperature, which hinders full martensite transformations.

$$M_S(°C) = 539 - 423wt\%C - 30.4wt\%Mn - 17.7\ wt\%Ni - 12.1\ wt\%Cr - 7.5\ wt\%Mo \qquad (1)$$

The bulk microstructure of the 4th weld pass is presented in Figure 10-11. A microstructure feature typical of martensite was seen here, where different packets grew from the same austenitic grain, and probably converged at the center of the grain. In addition, several very small particles were observed following the same direction as the lath martensite. Beside these particles, which are probably A_{ret}, there were some carbides. In fact, the literature reported

the occurrence of A_{ret} in high Ni steels. Shiue *et al*.[56], who evaluated the 9Ni-1Mo steel, when welded and posteriorly submitted to tempering treatment, identified by selected area electron diffraction (SAED) the presence of the A_{ret} between lath martensite, showing the classical crystallographic relationship of Kurdjumov–Sachs and Nishiyama–Wasserman. According to literature, the formation mechanism of the A_{ret} is related to a short range diffusion of elements rejected by martensite, which concentrates at the interlath of martensite, thus stabilizing the γ-FCC[57].

Figure 10-10. Microstructure of the 3rd weld pass observed after severe etching, evidencing the shear microstructure of martensite with A_{ret} at the interdendritic region plus TiC dispersed along the weld pass.

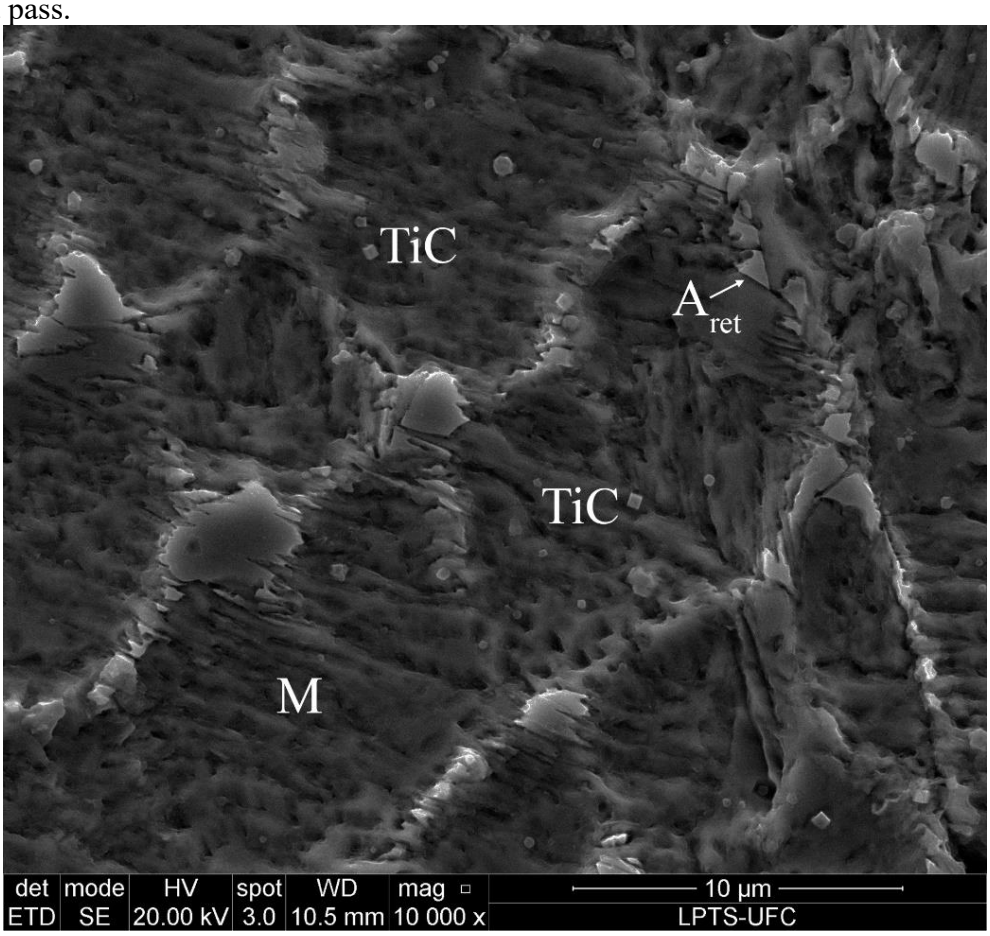

Source: Developed by the author.

Table 10-3. EDS chemical composition of the dendrite core (D_{core}), A_{ret} and cubic carbide characterized as Ti(C,N).

Chemical composition of phases of the 3rd weld pass											
Phases	Al	Cr	Fe	Mg	Mn	Mo	Ni	Nb	Si	Ti	V
D_{core}	-	4.3	83.9	-	1.6	1.7	8.3	-	0.2	-	-
A_{ret}	-	4.6	69.8	-	4.4	9.4	10.0	1.1	0.8	-	-
Ti(C,N)	2.2	4.7	71.4	0.5	1.0	2.9	7.8	0.4	0.4	8.5	0.3

Source: Developed by the author.

Figure 10-12 shows the bulk microstructure of the 5th weld pass. The microstructure was based on a bainitic matrix with the presence of martensite and carbides dispersed along the weld pass. Other particles of martensite-austenite (MA) microconstituents were observed as stringers and blocks. This time, the reduction of alloying elements not only increased the M_S, but also had a significant effect on shifting the time temperature transformation curve of bainite and other diffusional transformations. In addition, the HI_w used to deposit this weld pass was slightly higher and, certainly this must be considered, since there was more time for the diffusional transformation to occur. Thus, the majority of the γ-FCC was transformed into bainite (B), while some regions experienced a martensite transformation. During transformation of these phases the concentration of Ni, Mn and C caused the formation of MA particles[56,57]. According to the literature this microconstituent causes a strengthening of the matrix, but is also detrimental to the toughness of materials[58].

Figure 10-11. Microstructure of the 4th weld pass highlighting the martensite (M) matrix with a large amount of MA particles as stringer well distributed along the weld metal.

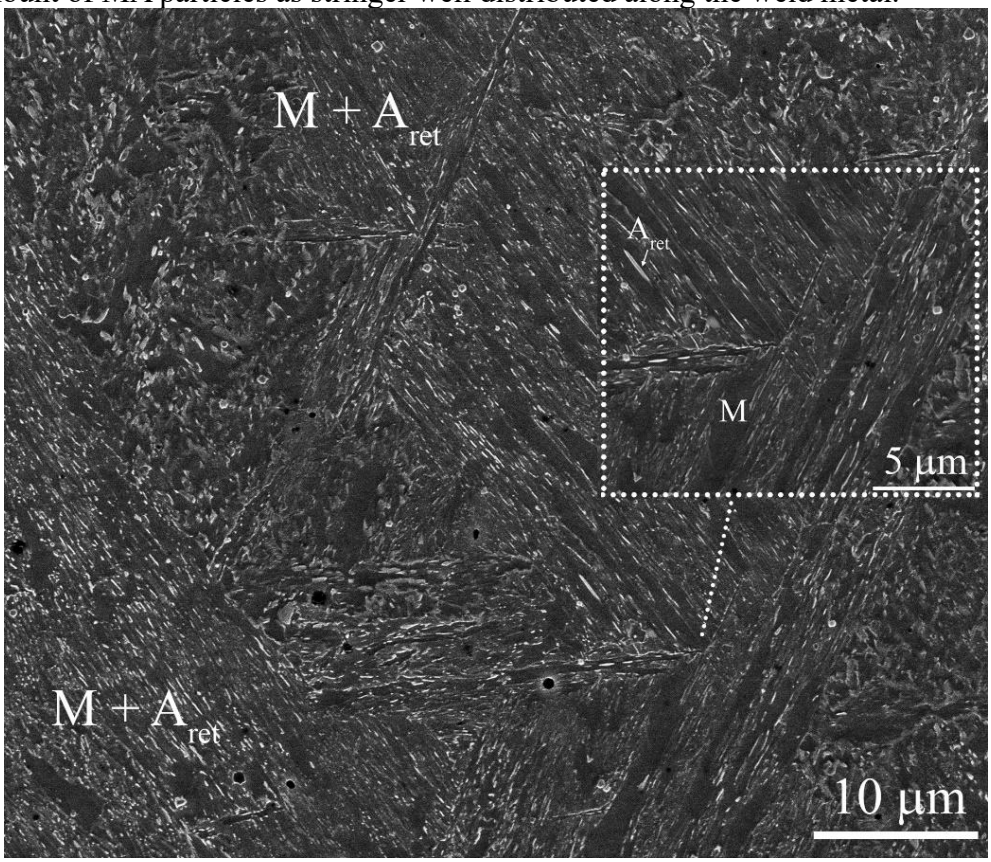

Source: Developed by the author.

The incorporation of Ni, Cr and Mo from the mixture of the first three 100S-G passes with the 2nd Alloy 59 pass slowly reduced until there was only a negligible incorporation

of these elements into the 6th weld pass onward (Figure 10-5). For this reason, the microstructure of these passes showed a similar microstructure. Thus, the microstructure of last weld pass was assessed in order to comprehend the microstructure of the second half of the welded joint. The microstructure of the 10th weld pass is shown in Figure 10-13, which demonstrated an acicular ferrite (AF) matrix with a large fraction of finely dispersed MA particles. The reduction of the alloying elements and the decrease in the cooling rate made the formation of an AF matrix possible, while the addition of C from the dilution with the API X65 steel pipe combined with Ni, Mn, Cr and Mo favored the formation of a large amount of MA particles. Normally this microconstituent has a high hardness that impedes the dislocation motion through it. Moreover, large primary austenitic grains that naturally reduce the toughness of steels was observed.

Figure 10-12. The bulk microstructure of the 5th weld pass, showing the bainitic matrix with martensite, MA particles and carbides distributed along the weld pass.

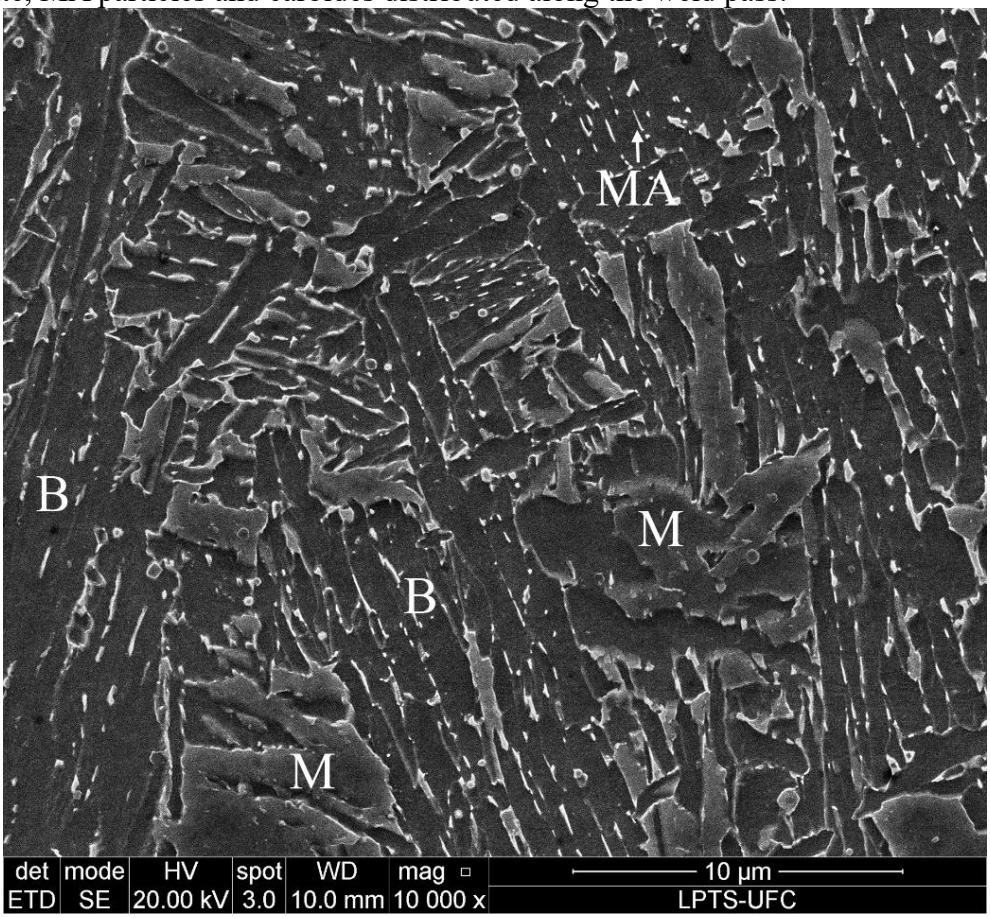

Source: Developed by the author.

Figure 10-13. a) The bulk microstructure of the 10th weld pass. b) The microstructure composed by acicular ferrite (AF) matrix and MA like block and stringer.

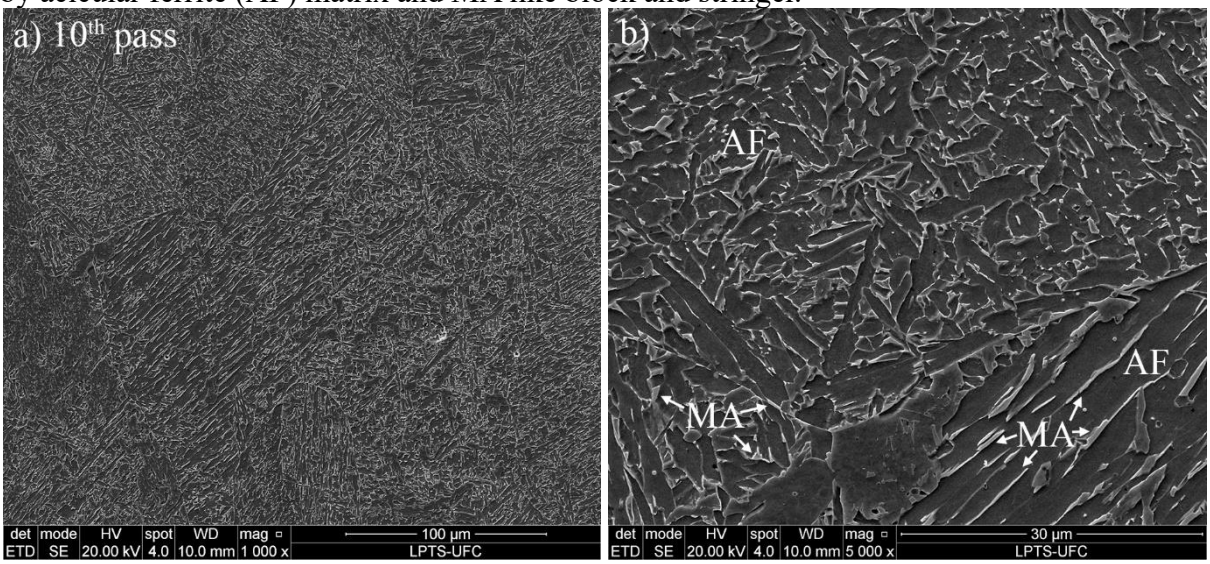

Source: Developed by the author.

10.4.3 Mechanical evaluation

10.4.3.1 Bend testing

The bending test evaluated the integrity of the welded joint, similar to the transverse tensile test. Figure 10-14 shows the four samples tested by the bending test. All the welded joint samples were approved in the four tests, considering that only small defects, less than 1 mm, were observed in two samples. One small defect was observed close to the wall bevel due to oxidation of the previous pass that was not perfectly removed. The defect observed in the bulk of the weld pass close to the top of the welded joint, possibly occurred due to the high weaving amplitude used. The welding parameter was defined in order to keep one weld pass by weld layer. When the arc welding moves from one side of the bevel to the other, the weld pool solidifies and forms an oxide layer on the surface that impairs the fusion of the weld metal when the arc welding torch returns from the previous region. However, it is important to highlight that these small defects are commonly observed in joint welds and they have a low mechanical effect on the performance of the component. The DNVGL ST F101 standard[22] standard considers the joint approved when defects do not exceed 3 mm. Therefore, the welded joint was also approved in all the bending samples assessed.

Figure 10-14. Bending specimens after test. All samples were approved.

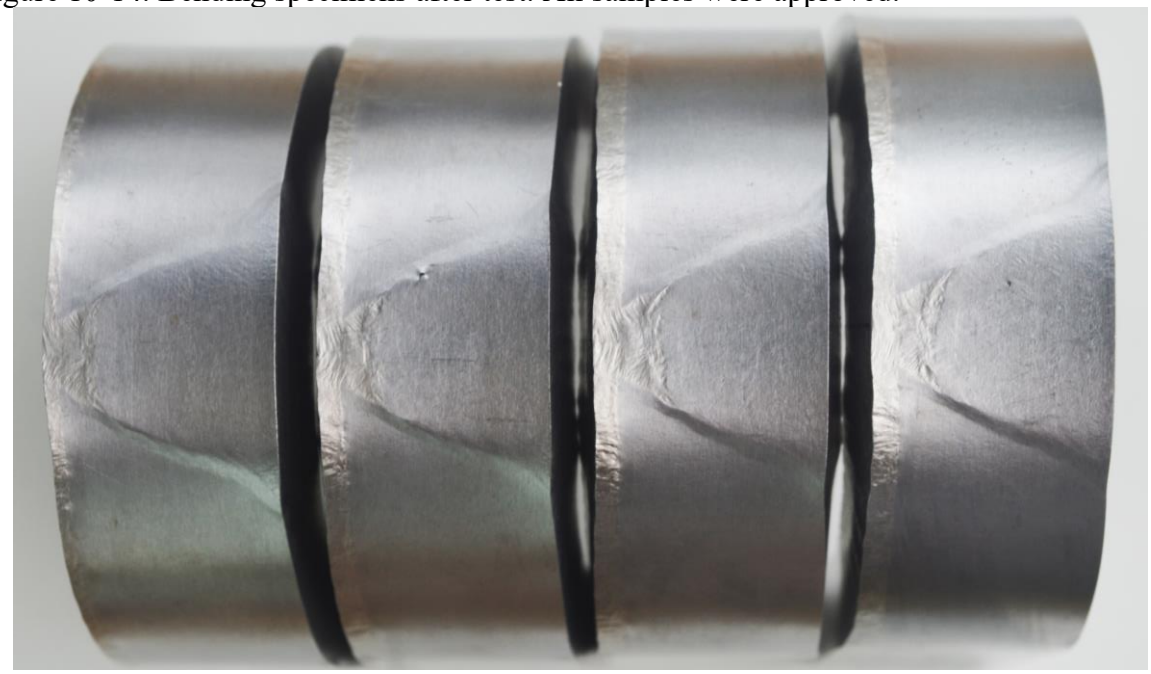

Source: Developed by the author.

10.4.3.2 Tensile testing

Transverse tensile tests with all passes of the welded joint plus the API 5L X65 steel base metal were performed in order to verify the ultimate tensile strength of the joint and discover where the rupture would occur in the samples. Two samples were taken from welded pipe for this analyze. Figure 10-15 shows the samples after the tests.

Figure 10-15. Transverse tensile specimens after test. All samples showed a collapse on the API 5L X 65 steel pipe.

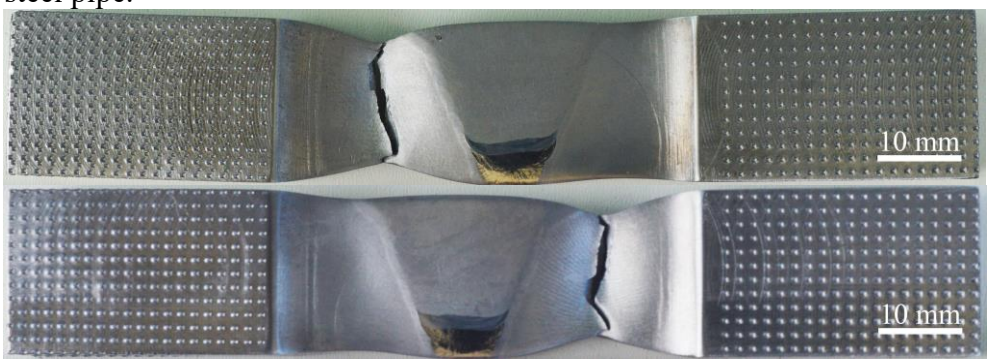

Source: Developed by the author.

All the samples exhibited a rupture at the base metal relatively far from the heat affected zone, in other words, all the welded joint samples were approved. This result was only possible as there were no solidification cracks in the welding passes. The average ultimate tensile strength was 642.4 MPa. The result exceeded the minimum tensile strength required by

the API 5L standard for the API 5L X65 PSL2[31]. The fracture located at the base metal with no relevant defects on the surface of the weld means that the ultimate tensile strength of the weld overmatched the base metal.

The transverse tensile test and bending test also pointed out that the welding procedures adopted for this joint welding were successful. The filler metals used to perform the joint welding were able to overmatch the ultimate tensile strength of the steel pipe. Moreover, the good metallurgical compatibility between the filler metals and the base metal associated with the welding parameters selected, enabled the welded joint to be manufactured without any defects capable of impairing the mechanical properties of the welded joint.

The mechanical properties of the weld metal were assessed though transverse all-weld tensile tests. Four different positions of the welded joint were investigated because dissimilar welding produces weld passes with significantly different chemical compositions and microstructures as shown previously. Table 10-4 shows the YS, ultimate tensile strength, elongation and the local of rupture. The results obtained represent an approximation of the mechanical properties of the fusion zone of the respective regions, considering that there is a mixture of weld passes and a small portion of API 5L X65 steel pipe at the radius fillet of the samples.

Table 10-4. Mechanical properties of the welded joint obtained by transverse all-weld tensile tests. The letters W and R mean that rupture occurred at the weld metal and radius fillet, respectively.

Transverse all welding tensile test					
region (weld pass)	specimen	yield strength (MPa)	tensile strength (MPa)	elongation (%)	rupture
2nd	1	559.9	798.9	29.7	W
	2	542.1	816.4	32.0	W
3rd - 4th	1	793.6	915.6	23.0	R
	2	828.3	896.6	21.4	R
5th - 6th	1	782.7	830.7	23.4	W
	2	800.0	856.7	23.9	W
7th - 8th	1	720.2	761.5	23.5	W
	2	711.7	760.6	22.4	W

Source: Developed by the author.

The results obtained revealed that a good overmatch of the mechanical properties was achieved. Actually, the overmatch was more than that required for the API 5L X65 steel pipe. Only the 2nd pass did not exceed the YS required, but this weld pass is not taken into account for the mechanical overmatch requirements, considering that it is located virtually

along the same line as Alloy 625 cladding. The good mechanical properties obtained was enough to attend the general overmatch requirements not only for API 5L X65 steel, but also for the API 5L X70 and X80 steels.

The success of this novel proposal for joint welding of rigid riser steel pipes with an internal Ni-based Alloy 625 cladding using two filler metals, a Ni-based alloy and a low alloy steel, opens up new perspectives for dissimilar joint welding of such components. The use of a low alloy steel figures as an ideal solution to provide an overmatch of the mechanical properties of high strength low alloy steel pipes, opening the possibility to weld joints with other steel pipes such as API 5L X90 and X100. Currently, the joint welding of these HSLA pipes are done using LAS without difficulties, but when the steel pipe has an internal Ni-based cladding, the metallurgical problems do not allow the use of a low alloy steel.

10.4.3.3 Microhardness and hardness tests

The microhardness map was made in a region covering the 2nd, 3rd, 4th, 5th, and 6th weld passes and the API 5L X65 steel pipe in order to assess the resistance of the welded joint to the penetration of an indenter. The microhardness map was made using a 100 gf load with 300 μm spacings between indentations, which gave a good spatial resolution. Figure 10-16 shows the microhardness map of the welded joint. The scale bar was from 250 HV to 400 HV.

The API 5L X65 steel pipe showed a microhardness less than 250 HV, while the Alloy 625 cladding exhibited a microhardness of approximately 285 HV. The same result of the CRA cladding was observed for the 2nd weld pass. On the other hand, the 3rd and 4th passes showed a greater hardness. The incorporation of Ni, Cr and Mo from the dilution with the Alloy 59 caused a strong hardening by solid solution and quenching, considering the martensitic matrix observed in these weld passes. Although the 3rd pass showed a more complex microhardness, since some regions showed a microhardness above 400 HV, while other softer regions presented a microhardness similar to the API 5L X65 steel pipe, that is below 250 HV. Probably these softer regions are composed of regions rich in the base metal as discussed previously, which concentrate more alloying elements from mixing with Alloy 59. The addition of alloying elements, in turn, also increases the hardening by solid solution and quenching, but the Ni effect is complex and must also be considered. Several authors have studied the Ni effect in martensite transformation and its mechanical properties[59–64]. Zeng investigated the hardness of alloys from the Ni-Fe and Fe-C systems. With very low carbon content, below 0.002 wt%, the alloys Fe-1.8Ni, Fe-3.7Ni, Fe-5.5Ni, Fe-7.6Ni and Fe-31Ni exhibited virtually equal

hardness of approximately 262.3 HV. In contrast, the hardness increased quickly with small additions of carbon. Morsdorf *et al*.[57] explained that C has an important role in the mechanical properties of martensitic materials, since it is possible obtain a material strength with high toughness with very low carbon content, whereas the addition of carbon is harmful to the toughness of materials.

Figure 10-16. Microhardness map of the welded joint, evaluating the 2nd, 3rd, 4th, 5th, 6th weld passes and the API 5L X65 steel pipe.

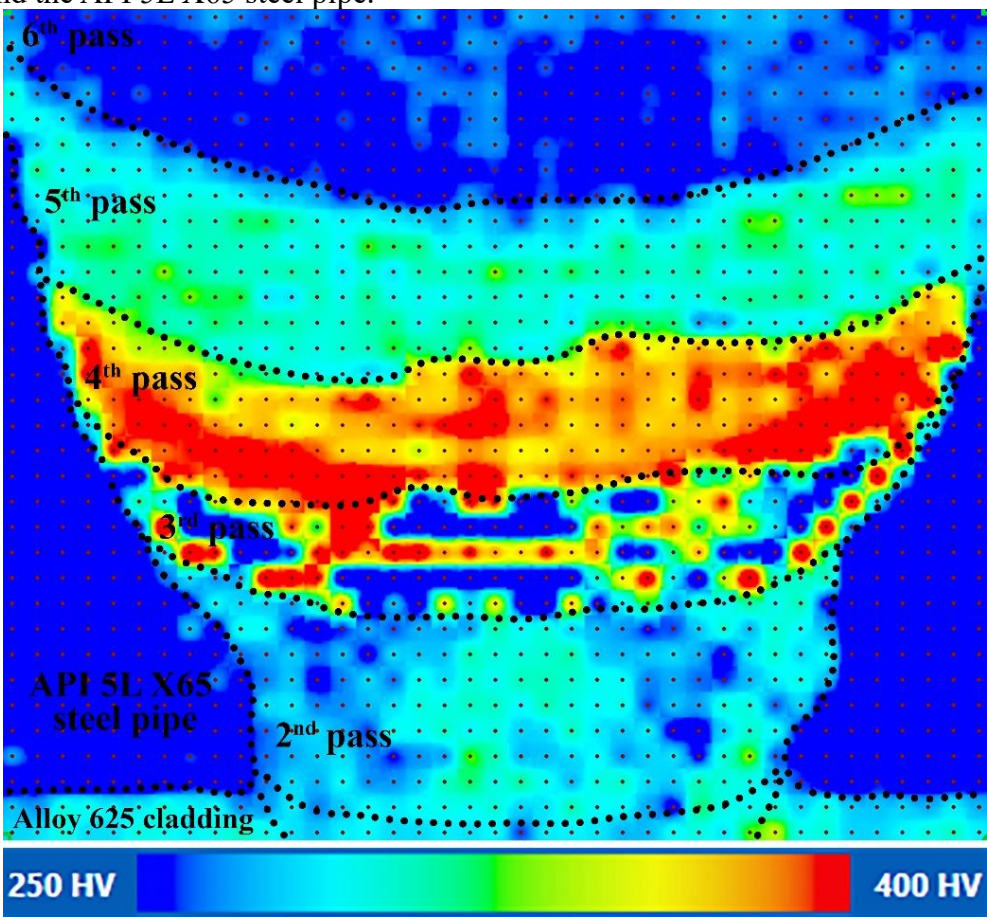

Source: Developed by the author.

The microhardness of the 4th pass varied from approximately 350 HV to 400HV. The reduction of Ni content because of the minimization of the dilution effect reduces the field of γ-FCC in terms of thermodynamic stabilization, thus favoring hardening by quenching through the martensitic transformation, considering that the M_S temperature increases with the reduction of alloying elements in general. Moreover, this weld pass experienced a higher dilution with the steel pipe, which increased the carbon content.

In general, the 5th weld pass showed a microhardness softer than the high dilution weld passes like the 3rd and 4th. The average was about 285 HV, similar to the 2nd Alloy 59 weld

pass. The reduction of alloying elements from dilution with Alloy 59 decreased the hardening by solid solution and quenching, which corroborates with the bainitic matrix observed in Figure 10-12. The softening effect was also observed for the 6th pass, where the microhardness was similar to the API 5L X65 steel pipe. Probably from the 6th pass onward the microhardness of the passes will follow the characteristics of 100S-G steel.

The hardness profile was executed along the passes, starting at the root pass until the last welded joint pass, in order to obtain a general overview of the hardness profile of the weld passes. The hardness indentations were made using a 10 kgf load with 1 mm spacings between indentations. Figure 10-17 shows the hardness profile performed along all the weld passes of the welded joint. A wide range of hardness values was observed, varying from 221 HV to 376 HV. This demonstrates the differences of the weld passes, corroborating with the microstructure and microhardness map discussed previously.

Figure 10-17. Hardness profile of the welded joint along the weld passes.

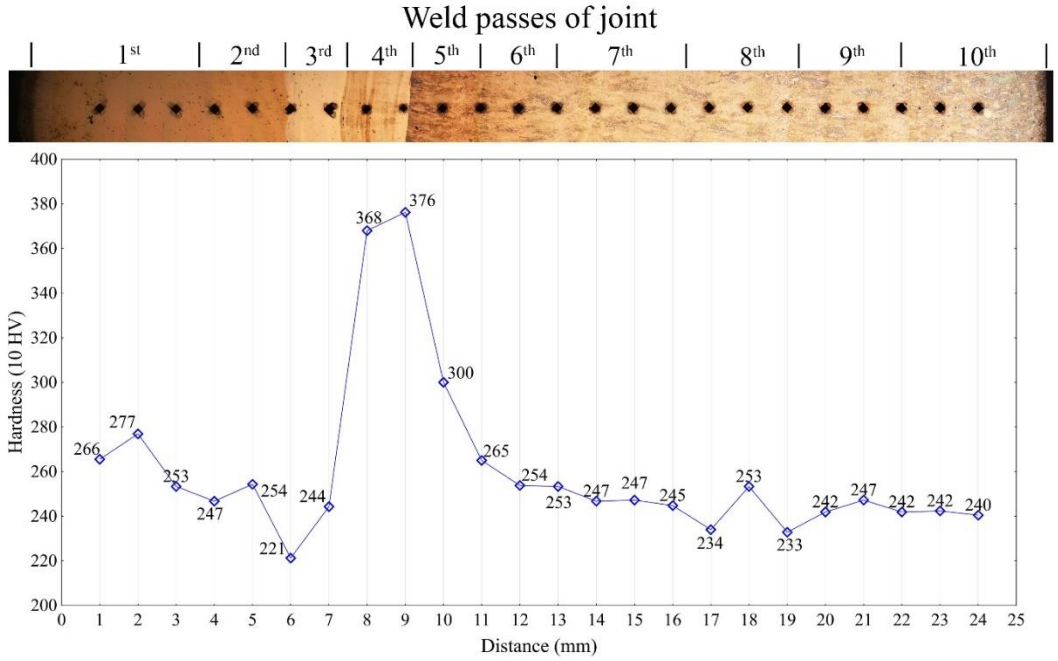

Source: Developed by the author.

The austenitic passes based on dilution of the Alloy 59 passes with the steel pipe and Alloy 625 cladding of the pipe showed a hardness varying from 247 HV to 277 HV. The 3rd weld pass, in turn, exhibited a very low hardness (221 HV) on the solidification interface between the 2nd and 3rd passes and, at the core of the pass (244 HV). As expected, the high Ni content in the 3rd weld pass caused a softening of the martensitic matrix. On the other hand, a drastic reduction of Ni content in the 4th pass kept the martensite pass very hard, varying from 368 HV to 376 HV. The 5th weld pass exhibited a considerable reduction, varying from 265 HV

to 300 HV on the fusion boundary between the 5th and 6th weld passes and the core of the 5th pass, respectively. The 6th weld pass forward showed a very low hardness, with an average of 250 HV.

The hardness profile demonstrated the high complexity of the welded joint. From a macro point of view, the welded joint has a hard layer, of about 3 mm, located at final of the first portion of three of the welded joint. This hard layer is confined between two soft regions, one of which is the 1st and 2nd weld passes and other is the steel passes of the 6th to the 10th weld passes. This shows the difficulties involved to assess the global mechanical behavior of such dissimilar welds.

10.4.3.4 Impact toughness

Certainly, the toughness represents an important mechanical property when designing components or equipment, especially for complex application such as risers, where the pipeline is to be used under severe environmental conditions. The impact toughness test is the most common toughness test that offers the absorbed energy during the dynamic load. The dissimilar region of the welded joint, in other words, the 3rd weld pass was evaluated for impact toughness. The notch was positioned at the beginning of the weld pass close to the interface between the 2nd and 3rd weld passes. Moreover, it is also important to investigate the impact toughness of the main part of the welded joint that is the 100S-G steel weld passes that only experienced a dilution with the steel pipe. This result was obtained in study of a previous chapter, which used the same welding procedures with only one essential difference: the Ni-based Alloy 22 was used as the filler metal for the 1st and 2nd weld passes of the joint, however, the same LAS was used to fill the joint. In this study the impact toughness with the notch positioned in the 7th pass of the joint was performed and this result can probably be considered as a good approximation. The fractographs of the impact toughness tests for both conditions are shown in Figures 10-18a and 10-18b.

The sample with the notch positioned at the 3rd weld pass showed a region with a matte surface feature near the notch. This feature is typical of a ductile fracture and corresponds to the 3rd weld pass of the welded joint. Probably the high amount of Ni incorporated from the dilution with the Alloy 59 pass provided the good toughness to this weld pass. On the other hand, this ductile region changed quickly to a brittle region as of the 4th weld pass onward, in which shiny surface features were seen, and which are typical of brittle materials which fracture

is based in cleavage. In contrast, the sample with the notch in the 7th weld pass showed a brittle feature in all weld passes covered.

Figure 10-18. The Charpy-V samples after tests. Macrograph of a) notch in the 7th weld pass (previous chapter) and b) notch in the 3rd weld pass samples. Micrograph of c) 3rd weld pass samples highlighting fracture features.

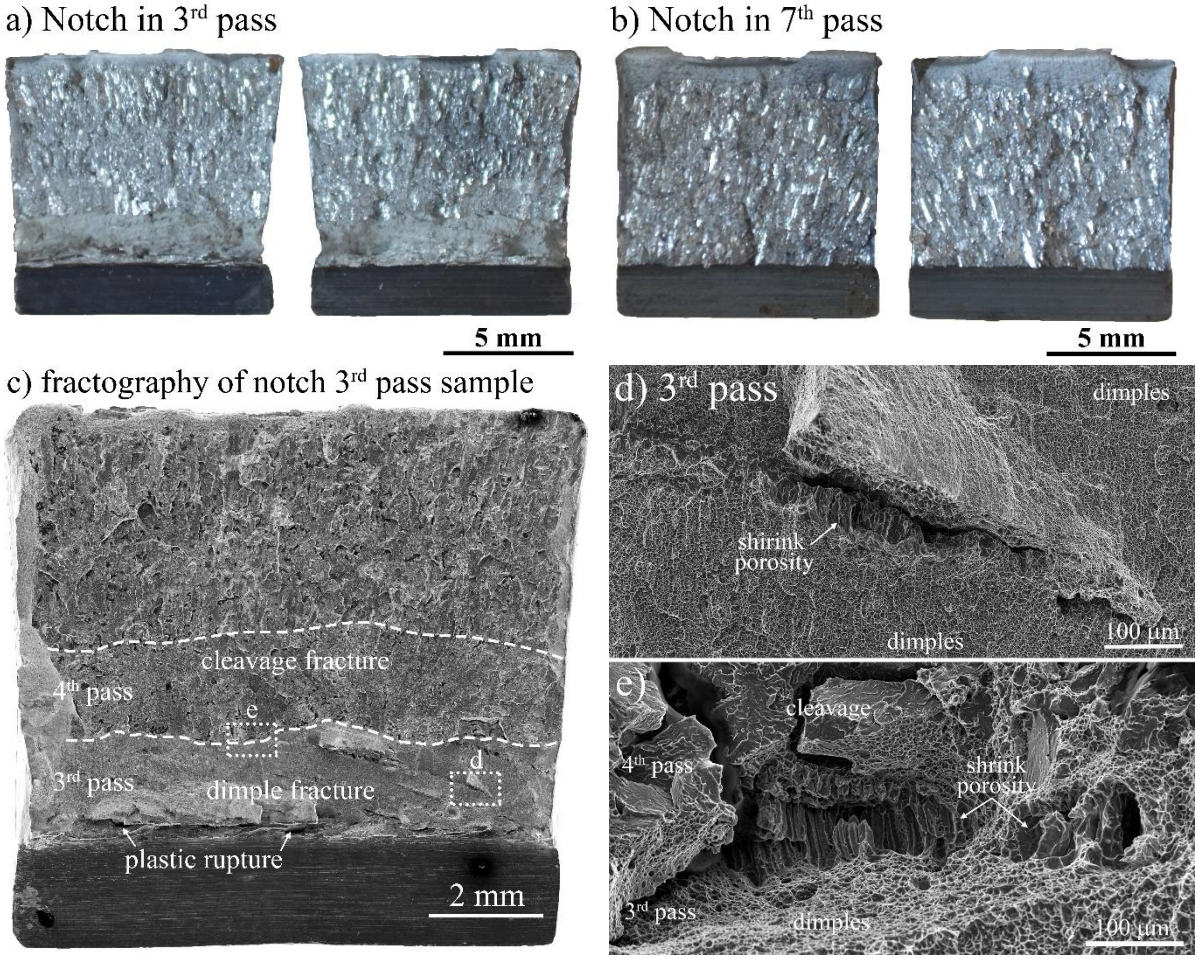

Source: Developed by the author.

The SEM fractographs of the sample with the notch positioned at the 3rd weld pass is displayed with more details in Figure 10-18c. Here the interface between the 3rd and 4th weld passes, and some discontinuities distributed in the 3rd weld pass can be seen. The 4th weld pass showed a flat surface indicating an abrupt rupture, while the 3rd weld pass exhibited a tortoise surface with propagation of a plastic rupture displayed as the defects. More details are displayed in Figures 10-18d and 10-18e. Here, the 3rd pass had a fracture based in dimples with the presence of shrink porosities. However, no evidence of a cleavage fracture was detected for the 3rd weld pass, therefore, it is reasonable to conclude that the macrosegregations observed in the 3rd weld pass did not cause a brittle region. In contrast, the interface between the weld passes

revealed a transition from ductile fracture in the 3rd weld pass to a brittle fracture in the 4th weld pass. Shrink porosities were also observed at the interface.

Table 10-5 exhibits the energy absorbed results for the samples with the notch positioned on the 3rd weld pass, including the results obtained in the previous chapter. The absorbed energy of the samples tested which included the 3rd and 4th weld passes, was considerably greater than the samples with only the lowest dilution pass; more than four times on average. The ductile behavior of the 3rd pass was responsible for this large increase in absorbed energy, of about 63 J. Probably, the high Ni content present in the 3rd pass was responsible for this behavior, while the reduction of Ni associated with the presence of Cr, Mo and more carbon from the dilution with the steel pipe led to a fragile fracture for the 4th weld pass onward. The microstructure of the 4th weld pass presented in Figure 10-11 explains this brittle behavior, considering the martensitic matrix with several A_{ret} particles finely distributed along the grain boundaries of packets, blocks, sub-blocks and laths.

Table 10-5. The impact toughness of the welded joint with the notch positioned in the 3rd and 7th passes.

Impact toughness of welded joint (J)	
Notch in 3rd pass	63.3 ± 6.4
Notch in 7th pass	14.3 ± 1.3

Source: Developed by the author.

Zeng[64] studied the different low carbon Fe and observed that the addition of Ni increased the misorientation of the grains of the blocks and sub-blocks, which means that Ni causes the grain refining of martensite. Probably, this result supports the better toughness observed for the 3rd weld pass in comparison to the 4th weld pass. Nonetheless, the carbon content must be taken in consideration for this analysis. As previously mentioned, carbon affects the mechanical properties of martensite[57]. According to the literature, the Fe-C system has at least a two times greater dislocation density compared to Fe-Ni and, in some cases, this difference may exceed an order of magnitude[61]. This higher number of dislocation supports the strain at the first moment, but progresses quickly to the formation of a tangle of dislocation, which evolves to complex dislocation interactions like jogs, junctions and locks[65], which in the last stage exceed the ability of material to strain.

According to study of a previous chapter a very low energy of approximately 14 J was absorbed by the samples with the notch positioned at the 7th weld pass for similar welded joints as in this work. This poor toughness was attributed to the fact that the LAS weld passes were assessed below their ductile-to-brittle transition temperature (DBTT), of -15°C. The

dilution of 100S-G steel with the steel pipe caused a reduction of the increase of Mn and C present in weld metal, while the Ni fraction was diluted. Tanaka *et al*.[63] investigated the Ni and Mn effect on DBTT of low carbon steels, and these authors highlighted that the microstructural and also crystallographic effect of both elements is hard to explain, but in fact, Ni reduces the DBTT while Mn cause the opposite effect. Kang *et al*.[60] also concluded that steels containing a high Ni fraction have a better toughness, but the combination of high Ni and Mn cause a reduction of toughness of the steel.

10.5 Conclusion

Based on the results shown in the present study, it was concluded that:

- The new design for joint welding of rigid risers internally cladded using two different filler metals, Alloy 59 and 100S-G steel can be successfully manufactured without solidification cracks.
- The welded joint attended the minimum YS overmatch required for welding of API 5L X65 steel. The YS overmatch was also sufficient for welding API 5L X70 and X80 steels for posterior installation by the reel lay method.
- The dilution between the steel pipe, Alloy 59 and 100S-G steel created a complex microstructure, in which the Alloy 59 weld passes exhibited a γ-FCC matrix with precipitates, whereas the first two LAS weld passes showed a martensitic matrix with A_{ret} and cubic carbides. The third LAS weld pass showed a bainitic matrix with MA particles and carbides. The other LAS weld passes of the welded joint showed an AF matrix with the presence of MA particles.
- The 100S-G steel pass strongly diluted with Alloy 59 exhibited a good impact test, at -15°C, of approximately 63 J, but this performance could be better if it were not for the brittle feature of the 4^{th} weld pass. Even so, this result is considerable better than the performance reported for the 100S-G steel weld passes diluted with API 5L X65 steel, which showed only 14 J of absorbed energy, at -15°C.

REFERENCES

1 SILVA, C. C. *et al*. Austenitic and ferritic stainless steel dissimilar weld metal evaluation for the applications as-coating in the petroleum processing equipment. **Materials & Design**, v. 47, p. 1-8, 2013.

2 SUN, Z.; ION, J. C. Laser welding of dissimilar metal combinations. **Journal of Materials Science**, v. 30, n. 17, p. 4205-4214, 1995.

3 BALDRIDGE, T. *et al*. Laser cladding of Inconel 690 on Inconel 600 superalloy for corrosion protection in nuclear applications. **Optics and Lasers in Engineering**, v. 51, n. 2, p. 180-184, 2013.

4 SILVA, C. C. *et al*. A Study on the Effect of the Interpass Temperatures in Properties and Microstructures of the Alloy 625 Dissimilar Fusion Zone. **Materials Science Forum**, v. 783-786, p. 2816-2821, 2014.

5 SARAIVA, D. L. *et al*. Application of low Ms temperature consumable to dissimilar welded joint. **Materials Science and Technology**, v. 30, n. 9, p. 1057-1062, jul. 2014.

6 KOURDANI, A.; DERAKHSHANDEH-HAGHIGHI, R. evaluating the properties of dissimilar metal welding between Inconel 625 and 316L stainless steel by applying different welding methods and consumables. **Metallurgical and Materials Transactions A**, v. 49, n. 4, p. 1231-1243, 2018.

7 SAEDI, A. H.; HAJJARI, E.; SADROSSADAT, S. M. Microstructural characterization and mechanical properties of TIG-welded API 5L X60 HSLA steel and AISI 310S stainless steel dissimilar joints. **Metallurgical and Materials Transactions A**, v. 49, n. 11, p. 5497-5508, 2018.

8 DUPONT, J. N.; BABU, S.; LIU, S. Welding of materials for energy applications. **Metallurgical and Materials Transactions A**, v. 44, n. 7, p. 3385-3410, 2013.

9 SILVA, C. C. *et al*. Evaluation of the corrosion resistant weld cladding deposited by the TIG cold wire feed process. **Materials Science Forum**, v. 783-786, p. 2822-2827, 2014.

10 MOHAMMADI ZAHRANI, E.; ALFANTAZI, A. M. Hot corrosion of Inconel 625 overlay weld cladding in smelting off-gas environment. **Metallurgical and Materials Transactions A**, v. 44, n. 10, p. 4671-4699, 2013.

11 MINÁ, É. M. *et al*. The effect of dilution on microsegregation in AWS ER NiCrMo-14 alloy welding claddings. **Metallurgical and Materials Transactions A: Physical Metallurgy and Materials Science**, v. 47, n. 12, 2016.

12 DUPONT, J. N. Solidification of an alloy 625 weld overlay. **Metallurgical and Materials Transactions A**, v. 27, n. 11, p. 3612-3620, nov. 1996.

13 SILVA, C. C. *et al*. New insight on the solidification path of an alloy 625 weld overlay. **Journal of Materials Research and Technology**, v. 2, n. 3, p. 228-237, 2013.

14 DAI, T.; LIPPOLD, J. Characterization of the interface of an Alloy 625 overlay on steels using nanoindentation. **Journal of Materials Engineering and Performance**, v. 27, n. 7, p. 3411-3418, 2018.

15 HODGE, F. G. The history of solid-solution-strengthened Ni alloys for aqueous corrosion service. **JOM**, v. 58, n. 9, p. 28-31, 2006.

16 JONES, R. L. *et al*. Reeled clad SCR weld fatigue qualification. *In*: OFFSHORE TECHNOLOGY CONFERENCE, 2011, Houston. **Proceedings**. Houston: Offshore Technology Conference, 2011. p 1-13.

17 SOUZA, R. F.; RUGGIERI, C. Fracture assessments of clad pipe girth welds incorporating improved crack driving force solutions. **Engineering Fracture Mechanics**, v. 148, p. 383-405, 2015.

18 CHONG, T.-V. S. *et al*. Effects of elevated temperatures on the mechanical properties of nickel-based alloy clad pipelines girth welds. **Engineering Fracture Mechanics**, v. 152, p. 174-192, 2016.

19 LIN, S. *et al*. Effect of cyclic plastic deformation on microstructure and mechanical properties of weld metals used for reel-lay pipeline steels. **Materials Science and Engineering: A**, v. 737, p. 77-84, 2018.

20 CROSS, C. E. On the origin of weld solidification cracking. *In*: BÖLLINGHAUS, T.; HEROLD, H. **Hot Cracking Phenomena in Welds**. Heidelberg: Springer Berlin Heidelberg, 2005. p. 3-18.

21 SMITH, S. N.; CLOUGH, T. Deepwater Pipeline Installation by Reel-lay Method. *In*: OFFSHORE TECHNOLOGY CONFERENCE, 2010, Houston. **Proceedings**. Houston: Offshore Technology Conference, 2010. p 1-12.

22 DNVGL. DNVGL ST F101: **Submarine Pipeline Systems**. Oslo. p. 520. 2017.

23 DNV. JIP: **Lined and Clad Pipeline Materials: Guidelines for Design and Construction of Clad and Lined Pipelines**. Oslo. 2007.

24 LIPPOLD, J. C. *et al*. Weld solidification cracking in solid-solution strengthened ni-base filler metals BT. *In*: BÖLLINGHAUS, T. *et al*. **Hot Cracking Phenomena in Welds II**. Heidelberg: Springer Berlin Heidelberg, 2008. p. 147-170.

25 CIESLAK, M. J.; HEADLEY, T. J.; FRANK, R. B. Welding metallurgy of custom age 625 PLUS alloy. **Welding Journal (Miami, Fla)**, v. 68, n. 12, p. 473s-482s, 1989.

26 CIESLAK, M. J. The welding and solidification metallurgy of Alloy 625. **Welding Journal**, v. 70, n. 2, p. 49–56, 1991.

27 AGARWAL, D. C.; HERDA, W. R. The “C” family of Ni-Cr-Mo alloys’ partnership with the chemical process industry: The last 70 years. **Materials and Corrosion**, v. 48, n. 8, p. 542–548, ago. 1997.

28 GRAY, J. J.; ORME, C. A. Electrochemical impedance spectroscopy study of the passive films of alloy 22 in low pH nitrate and chloride environments. **Electrochimica Acta**, v. 52, n. 7, p. 2370-2375, 2007.

29 LUO, H. *et al*. Characterization of electrochemical and passive behaviour of Alloy 59 in acid solution. **Electrochimica Acta**, v. 135, p. 412-419, 2014.

30 AMERICAN WELDING SOCIETY. AWS A5.28/A5.28M: **Specification for Low-Alloy Steel Electrodes and Rods for Gas Shielded Arc Welding**. Miami. p. 40. 2015.

31 AMERICAN PETROLEUM INSTITUTE. API specification 5L: **Specification for Line Pipe**. Washington. p. 180. 2013.

32 DNVGL. DNVGL RP F108. **Assessment of flaws in pipeline and riser girth welds**.

Oslo. p. 130. 2017.

33 MIN, D. *et al*. Welding of quenched and tempered steels with high-spin arc narrow gap MAG system. **The International Journal of Advanced Manufacturing Technology**, v. 55, n. 5, p. 527-533, 2011.

34 LIPPOLD, J. C. Centerline cracking in deep penetration electron beam welds in type 304L stainless steel. **Welding Journal (Miami, Fla)**, v. 64, n. 5, p. 127s-136s, 1985.

35 SUN, Y. *et al*. Characterization and formation mechanism of periodic solidification defects in deep-penetration laser welding of NiCrMoV steel with heavy section. **The International Journal of Advanced Manufacturing Technology**, v. 100, n. 9, p. 2857-2866, 2019.

36 DUPONT, J. N. *et al*. Solidification of Nb-bearing superalloys: part I. reaction sequences. **Metallurgical and Materials Transactions A**, v. 29, n. 11, p. 2785-2796, 1998.

37 RAMIREZ, A. J.; LIPPOLD, J. C. High temperature behavior of Ni-base weld metal: Part II – Insight into the mechanism for ductility dip cracking. **Materials Science and Engineering: A**, v. 380, n. 1, p. 245-258, 2004a.

38 RAMIREZ, A. J.; LIPPOLD, J. C. New insight into the mechanism of ductility-dip cracking in Ni-base weld metals. *In*: **Hot Cracking Phenomena in Welds**. Heidelberg: Springer Berlin Heidelberg, 2005. p. 19-41.

39 RAMIREZ, A. J.; LIPPOLD, J. C. High temperature behavior of Ni-base weld metal: Part I. Ductility and microstructural characterization. **Materials Science and Engineering: A**, v. 380, n. 1, p. 259-271, 2004.

40 SILVA, C. C. *et al*. Mechanical properties and microstructural characterization of aged nickel-based Alloy 625 weld metal. **Metallurgical and Materials Transactions A: Physical Metallurgy and Materials Science**, v. 49, n. 5, p. 1653-1673, may. 2018.

41 HU, Y. L. *et al*. Effect of Ti addition on cracking and microhardness of Inconel 625 during the laser solid forming processing. **Journal of Alloys and Compounds**, v. 711, p. 267-277, 2017.

42 DUPONT, J. N.; ROBINO, C. V.; MARDER, A. R. Solidification and weldability of Nb-bearing superalloys. **Welding Journal (Miami, Fla)**, v. 77, n. 10, p. 417-431, 1998.

43 SOHRABI, M. J.; MIRZADEH, H.; RAFIEI, M. Solidification behavior and Laves phase dissolution during homogenization heat treatment of Inconel 718 superalloy. **Vacuum**, v. 154, p. 235-243, 2018.

44 MINÁ, E. M. *et al*. Effect of dilution on the microstructure of AWS ERNiCrMo-14 alloy in overlay welding by the TIG process with cold wire feed. **Welding International**, v. 32, n. 2, p. 130-138, 2018.

45 SILVA, C. C. *et al*. Assessment of microstructure of alloy Inconel 686 dissimilar weld claddings. **Journal of Alloys and Compounds**, v. 684, p. 628-642, 2016.

46 CIESLAK, M. J.; HEADLEY, T. J.; ROMIG, A. D. The welding metallurgy of HASTELLOY alloys C-4, C-22, and C-276. **Metallurgical Transactions A**, v. 17, n. 11, p. 2035–2047, nov. 1986.

47 KIRCHHEINER, R.; KÖUHLER, M.; HEUBNER, U. Nicrofer 5923 hMo, ein neuer hochkorrosionsbeständiger werkstoff für die chemische industrie, die umwelttechnik und verwandte anwendungen. **Materials and Corrosion**, v. 43, n. 8, p. 388-395, ago. 1992.

48 HEUBNER, U.; KÖHLER, M. Das zeit-temperatur-ausscheidungs- und das zeit-temperatur-sensibilisierungs-verhalten von hochkorrosionsbeständigen nickel-chrom-molybdän-legierungen. **Materials and Corrosion**, v. 43, n. 5, p. 181–190, may. 1992.

49 KOU, S.; WANG, Y. H. Weld pool convection and its effect. **Welding Journal (Miami, Fla)**, v. 65, n. 3, p. 63s-70s, 1986.

50 YANG, Y. K.; KOU, S. Macrosegregation in Cu–30Ni welds made with dissimilar filler metals. **Science and Technology of Welding and Joining**, v. 13, n. 4, p. 318-326, may. 2008.

51 YANG, Y. K.; KOU, S. Macrosegregation mechanisms in arc welds made with dissimilar filler metals. **Science and Technology of Welding and Joining**, v. 15, n. 1, p. 15-30, jan. 2010.

52 CIESLAK, M. J. *et al*. A melting and solidification study of alloy 625. **Metallurgical Transactions A**, v. 19, n. 9, p. 2319-2331, 1988.

53 SOYSAL, T. *et al*. Macrosegregation in dissimilar-metal fusion welding. **Acta Materialia**, v. 110, p. 149-160, 2016.

54 ANDREWS, K. W. The Calculation of Transformation Temperatures and Austenite-Ferrite Equilibria. in Steels. **Journal of the Iron and Steel Institute**, v. 184, p. 414-427, 1956.

55 KAUFMAN, L.; COHEN, M. The Martensitic Transformation in the Iron-Nickel System. **JOM**, v. 8, n. 10, p. 1393-1401, 1956.

56 SHIUE, R. K.; LAN, K. C.; CHEN, C. Toughness and austenite stability of modified 9Cr–1Mo welds after tempering. **Materials Science and Engineering: A**, v. 287, n. 1, p. 10-16, 2000.

57 MORSDORF, L. *et al*. Multiple mechanisms of lath martensite plasticity. **Acta Materialia**, v. 121, p. 202-214, 2016.

58 BISS, V.; CRYDERMAN, R. L. Martensite and retained austenite in hot-rolled, low-carbon bainitic steels. **Metallurgical and Materials Transactions B**, v. 2, n. 8, p. 2267-2276, 1971.

59 YAO, Z. *et al*. Effects of Ni and Cr on Cryogenic Impact Toughness of Bainite/Martensite Multiphase Steels. **Metals and Materials International**, v. 25, n. 5, p. 1151-1160, 2019.

60 KANG, B. Y.; KIM, H. J.; HWANG, S. K. Effect of Mn and Ni on the Variation of the Microstructure and Mechanical Properties of Low-carbon Weld Metals. **ISIJ International**, v. 40, n. 12, p. 1237-1245, 2000.

61 MORITO, S.; NISHIKAWA, J.; MAKI, T. Dislocation Density within Lath Martensite in Fe-C and Fe-Ni Alloys. **ISIJ International**, v. 43, n. 9, p. 1475-1477, 2003.

62 KIM, S.-H.; KANG, C.-Y.; BANG, K.-S. Weld metal impact toughness of electron beam welded 9% Ni steel. **Journal of Materials Science**, v. 36, n. 5, p. 1197-1200, 2001.

63 TANAKA, M. *et al*. Effects of Ni and Mn on brittle-to-ductile transition in ultralow-carbon steels. **Materials Science and Engineering: A**, v. 682, p. 370-375, 2017.

64 ZENG, T. On the martensitic structure and hardness in as-quenched Fe-Ni alloys. **Journal of Alloys and Compounds**, 2017.

65 WICKHAM, L. K.; SCHWARZ, K. W.; STÖLKEN, J. S. Rules for Forest Interactions between Dislocations. **Physical Review Letters**, v. 83, n. 22, p. 4574-4577, nov. 1999.

Chapter 11

The summary of the thesis

11.1 Conclusions

Based on the results obtained and presented in this thesis on developing a new approach to manufacturing dissimilar girth welds of rigid risers with overmatching requirements aiming at installation by the reel-lay method, it was concluded that:

- The main objective of this thesis has been achieved, since the approach allow to manufacture three welded joins of API 5L X65 cladded by Alloy 625 using two fillers metals, providing the minimum yield strength overmatch required, that is 580 MPa and, the welded joints integrity was assured in terms of solidification cracks observed.

Some specific objectives also were achieved:

- The thermodynamic simulation study provided support to understand the mixing effect of Ni-based alloys and low alloy steels on solidification. In fact, the mix of low alloy steel and Ni-based alloys with Nb addition, that was the case of alloy 625 and alloy 680, resulted in the prediction of eutectic phases rich in Nb that expanded the solidification temperature range. The alloys 22, 686 and 59 had the lowest solidification temperature range among the evaluated alloys, even in dilution condition with steel;
- The experimental study on mixing of LAS with N-based alloys 625, 22, 686 and 59 claddings evidenced the harful effect of Nb on susceptibility to solidification crack. For Alloy 625, conditions showed large cracks regardless of the welding heat input used. For alloys 22, 686 and 59, condition exhibited only a few minor discontinuities, especially at high heat input, where the microsegregation commonly is favored. Probably this contradiction was due the hypothesis that welds experienced a lower thermal solid stress contraction.
- The three dissimilar girth welds produced with alloys 22, 686 and 59 for the first two weld pass, filled by LAS in all cases, achieved the minimum YS overmatch requirement, not only for API 5L X65 steel, but also for API 5L X70 and X80 steels. No solidification crack was observed under these conditions, while in the condition produced using Alloy 625 showed numerous cracks in

the first two LAS weld passes, which were detrimental to the mechanical properties of the welded joint.

- A complex microstructure was produced by dissimilar girth welding. The first two Ni-based alloy weld passes showed a γ-FCC matrix. The subsequent LAS weld passes showed a martensitic matrix with A_{ret} and cubic carbides. The third LAS weld pass showed a bainitic matrix with martensite, martensite-austenite (MA) and carbides. The others LAS weld passes exhibited an acicular ferrite (AF) matrix with MA particles as blocks and stringers. The welded joints showed a brittle behavior in toughness tests, at -15°C.

Chapter 12

Main contributions of the Thesis

- The present Thesis demonstrated possible and advantageous to joint pipe with internal cladding of Ni-based alloy using two different filler metals, in order to achieve the mechanical properties required to reel lay installation process. The new procedure kept the cladding properties and avoided solidification cracks;
- Using the thermodynamic software, it was possible to establish a systematic study to select materials with good metallurgical compatibility, considering solidification aspects, especially the qualitative and quantitative information about predicted phases. The evaluation method correctly pointed out the high susceptibility to solidification cracks for mixture of the low alloy steel with the Alloy 625 and the opposite tendency for mixture with the 22, 686 and 59 alloys;
- The welded joint filled by the Alloy 625 and the low alloy steel failed from mechanical point of view due to presence of large solidification cracks into dissimilar weld passes;
- The welded joints, which combined the 22, 686 and 59 alloys with the low alloy steel, demonstrated a great applicability. The small defects observed into dissimilar weld passes was not enough to impair the mechanical properties of the welding joints.